UNIVERSITÉ DE SHERBROOKE
Faculté de génie
Département de génie civil

DEVELOPMENT AND STRUCTURAL TESTING OF NEW BASALT FIBER-REINFORCED-POLYMER (BFRP) BARS IN RC BEAMS AND BRIDGE-DECK SLABS

ÉTUDE DU COMPORTEMENT STRUCTURAL DE POUTRES ET DE DALLES DE PONTS EN BÉTON ARMÉ D'UNE NOUVELLE ARMATURE À BASE DE FIBRE DE BASALTE SOUS CHARGE STATIQUE

Thèse de doctorat
Spécialité: Génie civil

Fareed Mahmoud ELGABBAS

A dissertation submitted in partial fulfillment
of the requirements for the degree of
Doctor of Philosophy
(Civil Engineering)

Jury: Prof. Brahim BENMOKRANE, Directeur de recherche
Prof. Abdeldjelil BELARBI, Examinateur
Prof. Amir FAM, Examinateur
Prof. Sébastien LANGLOIS, Rapporteur

Sherbrooke (Québec) Canada Avril 2016

ABSTRACT

The advances in fiber-reinforced-polymer (FRP) technology have spurred interest in introducing new fibers, such as basalt FRP (BFRP), which has the potential to offer an efficient solution when implemented in concrete structure, such as corrosion resistant, durable and cost-effective.

Furthermore, the available design codes and guides do not provide any recommendations for the use of BFRP bars since fundamental studies and relevant applications are still limited. Therefore, investigations are needed to characterize and understand the behavior of BFRP bars in concrete members. Consequently, the main objectives of this experimental investigation are to evaluate the short- and long-term characteristics of newly developed BFRP bars, as well as evaluate the structural performance of these new bars as internal reinforcement for concrete beams and bridge-deck slabs to introduce these new reinforcing bars to the design codes and guides.

The experimental tests were completed through three parts. The first part was conducted on three newly developed BFRP bars and tendons to investigate their physical and mechanical properties. Durability and long-term performance were assessed by conditioning the BFRP bars in an alkaline solution simulating the moist concrete environment to determine their suitability as internal reinforcement for concrete elements. Thereafter, the properties were assessed and compared with the unconditioned (reference) values. The second part of this study was conducted on seven full-scale edge-restrained concrete bridge-deck slabs simulating actual slab-on-girder bridge-deck that is commonly used in North America to evaluate the performance of concrete bridge-deck slabs reinforced with BFRP and steel bars. The deck slabs measured 3000 mm long × 2500 mm wide × 200 mm deep. The slabs were tested up to failure under single concentrated load acting on the center of each slab simulating the footprint of sustained truck wheel load. The punching shear capacities were predicted using the available provisions, and compared with the experimental results. The third part of this study included testing of fourteen concrete beams of 3100 mm long × 200 mm wide × 300 mm deep to investigate the flexural behavior and serviceability performance of sand-coated and ribbed BFRP bars in concrete beams. The beams were tested under four-point bending over a clear span of 2700 mm until failure. The results are introduced and discussed in

terms of cracking behavior, deflection, flexure capacity, and failure modes. In addition, the bond-dependent coefficient (k_b) of the BFRP bars was determined and compared with the recommendations of the current FRP design codes and guides.

The findings of this study concluded the feasibility of producing BFRP bars meet the requirements of the current FRP standards. Also, the test results revealed that the BFRP bars had good mechanical behavior and could be placed in the same category as grade II and grade III GFRP bars. Moreover, the behavior of the concrete bridge-deck slabs and beams reinforced with BFRP bars was quite similar to the counterparts reinforced with glass- and carbon-FRP bars and the available FRP provisions are applicable for BFRP bars. The beam test results yielded an average bond-dependent coefficient (k_b) of 0.76±0.03 and 0.83±0.03 for the sand-coated and ribbed BFRP bars, respectively.

Keywords: Fiber-reinforced polymer (FRP); basalt; physical and mechanical properties; durability; restrained bridge-deck slab; punching shear; beams; flexure; deflection; crack width; bond-dependent coefficient (k_b).

RÉSUMÉ

L'avancée de la technologie des PRF a suscité l'intérêt de l'introduction de nouvelles fibres, comme la fibre de basalte, qui a un potentiel d'offrir une solution efficace, lorsqu'utilisée dans les structures en béton, soit sur la résistance à la corrosion, la durabilité et la rentabilité. En outre, les codes et les guides disponibles, ne fournissent pas de recommandations pour l'utilisation de barres en PRFB puisque les recherches passées dans ce domaine sont limitées. Donc, des travaux de recherche sont nécessaires pour caractériser et comprendre le comportement des barres de PRFB dans les éléments en béton armé. En conséquence, les objectifs principaux sont d'évaluer les caractéristiques à court et long terme des barres de PRFB nouvellement développées, ainsi que d'évaluer les performances structurales de ces nouvelles barres comme renforcement interne dans les poutres et les dalles de pont et d'introduire ce nouveau renforcement dans les codes et les guides de dimensionnement.

Les tests expérimentaux ont été faits en trois parties. La première partie porte sur le développement de trois nouvelles barres et tendons en PRFB pour déterminer leurs propriétés physiques et mécaniques. Les performances à long terme et de durabilité ont été réalisées en conditionnant les barres de PRFB dans une solution alcaline simulant les conditions humides dans le béton pour déterminer la compatibilité comme renforcement interne dans les éléments en béton. Par la suite, les propriétés ont été déterminées et comparées avec des spécimens non conditionnés (référence). La seconde partie a porté sur sept dalles de pont en béton armé grandeur réelle avec les bords restreints, simulant les tabliers de pont les plus utilisés en Amérique du Nord, pour évaluer la performance des dalles renforcées de PRFB et d'acier. Les dalles mesurent 3000 mm de long × 2500 mm de large × 200 mm d'épaisseur. Les dalles ont été testées jusqu'à la rupture sous une charge concentrée au centre de celles-ci simulant l'empreinte d'une roue d'un camion. Les capacités en poinçonnement sont prédites en utilisant les exigences réglementaires disponibles, et sont comparées aux résultats expérimentaux. La troisième partie de cette étude portait sur les essais de 14 poutres en béton de 3100 mm de long × 200 mm de large × 300 mm de profond pour examiner le comportement en flexion et les performances en service des barres de PRFB avec deux états de surfaces: fini sablé et crénelé. Les poutres ont été testées en flexion en quatre points avec une portée

libre de 2700 mm jusqu'à la rupture. Les résultats sont introduits et discutés en terme : du comportement de la fissuration, des flèches, de la capacité en flexion et des modes de ruptures. De plus, le coefficient d'adhérence (k_b) des barres de PRFB est déterminé et comparé avec les recommandations des codes et guides actuels.

Les résultats sont introduits et discutés en terme : du comportement de la fissuration, des flèches, de la capacité en flexion et des modes de ruptures. De plus, le coefficient d'adhérence des barres de PRFB est déterminé et comparé avec les recommandations des codes et guides actuels. Les résultats de l'étude concluent sur la viables pour la production des barres de PRFB pour respecter les exigences des codes actuelles. Également, les résultats d'essai indiquent que les barres de PRFB ont de bonnes propriétés mécaniques et peuvent être placées dans la même catégorie que les barres de PRFV, soit grade III. De plus, le comportement des poutres et des dalles de pont renforcées de PRFB est similaire que pour un renforcement en PRFV et PRFC et les exigences réglementaires sont applicables pour les barres de PRFB.

ACKNOWLEDGEMENTS

First of all, I thank GOD who guided and helped me to finish this work in the proper shape.

I wish to take the opportunity to express my sincere thanks and gratitude to my parents, my family and my wife who encouraged and supported me during the completion of this work. I doubt that I will ever be able to convey my full appreciation, but I owe them my endless gratitude.

I would like to express my appreciation and gratitude to my supervisors, Professor Brahim BENMOKRANE from University of Sherbrooke, for offering me the opportunity to work on such a challenging subject. I am so proud to work with him. All of the guidance, insight, helpful advice, and constant encouragement provided throughout the course of the dissertation are greatly appreciated. I owe him an unbelievable amount of gratitude for his prominent role in helping me to achieve one of the greatest accomplishments in my life.

I would like to express extremely grateful to Professor Amr ABDELRAHMAN, Department of Civil Engineering, Ain Shams University, Egypt, for his experienced advice, guidance and valuable suggestions, continuous and deep encouragement through my life. He taught me to be responsible for myself and my acts. I am very lucky to know a humble person like him.

I would also like to acknowledge and thank Dr. Ehab AHMED for his constant cooperation, continuous encouragement, consulting, guidance, and friendship.

I wish to acknowledge the financial support of the Natural Sciences and Engineering Research Council of Canada (NSERC) and the Fonds de la recherche du Québec en nature et technologies (FRQ-NT). I would like to thank MagmaTech (FRP manufacturer in the United Kingdom) and ASA.TEC (Austria) for providing the BFRP reinforcement.

Sincere words of thanks must also go to Mohamed SHAMANDY for his help during the construction of specimens. Also, I would also like to thank all my colleagues in the Civil Engineering Research Group for their support and valuable discussions.

Last but never the least, I wish to extend my deepest love and appreciation to my wife ♥NORAN♥ for her kindness, devotion, continuous patience, understanding, sacrifice, and prayers throughout this research. She was always there to give me the push for this challenge.

TABLE OF CONTENTS

LIST OF FIGURES

LIST OF TABLES

BIBLIOGRAPHY

During this research work the candidate published the following papers in journals and conferences:

PUBLISHED OR ACCEPTED ARTICLES IN REFEREED JOURNALS

1. **Elgabbas, F.**, Vincent, P., Ahmed, E., and Benmokrane, B. (2016). "Experimental Testing of Basalt-Fiber-Reinforced Polymer Bars in Concrete Beams." *Journal of Composite: Part B*, 91, 205-218.

2. **Elgabbas, F.**, Ahmed, E., and Benmokrane, B. (2016). "Experimental Testing of Concrete Bridge Deck Slabs Reinforced with Basalt FRP Bars under Concentrated Loads." *ASCE Journal of Bridge Engineering*, DOI: 10.1061/(ASCE)BE.1943-5592.0000892 , 04016029.

3. **Elgabbas, F.**, Ahmed, E., and Benmokrane, B. (2015). "Physical and Mechanical Characteristics of New Basalt-FRP Rods for Reinforcing Concrete Structures." *Journal of Construction and Building Materials*, 95, 623-635.

4. Benmokrane, B., **Elgabbas, F.**, Ahmed, E., and Cousin, P. (2015). "Characterization and Comparative Durability Study of Glass/Vinylester, Basalt/Vinylester, and Basalt/Epoxy FRP Bars." *ASCE Journal of Composite for Construction*, 19 (6), 04015008.

SUBMITTED ARTICLES IN REFEREED JOURNALS

5. **Elgabbas, F.**, Ahmed, E., and Benmokrane, B. (2015). "Flexural Behavior of Concrete Beams Reinforced with Ribbed Basalt-FRP Bars under Static Load." Submitted to *Journal of Composites for Construction*. (December 2015).

ARTICLES IN REFEREED CONFERENCES

1. **Elgabbas, F.**, Ahmed, E., and Benmokrane, B. (2016). "Flexure Performance of Concrete Beams Reinforced with Sand-Coated Basalt and Glass FRP Bars." Proc. of The 7^{th}

International Conference on Advanced Composite Materials in Bridges and Structures [*ACMBS 2016*], Vancouver, British Columbia, Canada, August 24-26, 6 pp.

2. **Elgabbas, F.**, Ahmed, E., and Benmokrane, B. (2016) "Flexural Behavior & Bond-Dependent Coefficient of Basalt- and Glass-FRP Bars in RC Beams." Proc. of *Annual Conference of the Canadian Society for Civil Engineering* [*CSCE 2016*], London, Ontario, June 1-4, 6 pp.

3. **Elgabbas, F.**, Ahmed, E., and Benmokrane, B. (2015). "Laboratory Testing of Edge-Restrained Concrete Bridge-Deck Slabs Reinforced with Basalt-FRP Bars." Proc. of the *5th International Conference on Construction Materials: Performance, Innovations and Structural Implications* [*ConMat 2015*], Whistler, BC, Canada. August 19-21, 10 pp.

4. **Elgabbas, F.**, Ahmed, E., and Benmokrane, B. (2014). "*Development and Characterization of Basalt FRP Reinforcing Bars for Concrete Structures*." Proc. of the *7th International Conference on FRP Composites in Civil Engineering* [*CICE 2014*], Vancouver, Canada. August 20-22, 6 pp.

5. **Elgabbas, F.**, Ahmed, E., and Benmokrane, B. (2013). "Basalt FRP Reinforcing Bars for Concrete Structures." Proc. of the *4th Asia-Pacific Conference on FRP in Structures* [*APFIS 2013*], Melbourne, Australia. December 11-13, 8 pp.

POSTER PRESENTATIONS (NSERC RESEARCH CHAIR MEETING)

1. **Elgabbas, F.**, Ahmed, E., and Benmokrane, B. (2015). "Characterization of Newly Developed Basalt Fiber-Reinforced Polymer (BFRP) Bars." May 1st, Université de Sherbrooke, Quebec.

2. **Elgabbas, F.**, Ahmed, E., and Benmokrane, B. (2015). "Basalt FRP Reinforcing Bars for Concrete Bridge Deck Slabs." May 1st, Université de Sherbrooke, Quebec.

SELECTED TECHNICAL REPORTS

1. **Elgabbas, F.,** Ahmed, E., and Benmokrane, B. (2014). "Testing of Concrete Bridge Deck Slabs Reinforced with Basalt FRP Bars under Concentrated Loads." Technical Report. September, 25 pp.

2. **Elgabbas, F.**, Ahmed, E., and Benmokrane, B. (2014). "Flexure Test of Concrete Beams Reinforced with BFRP, GFRP and Steel Bars." Technical Report. September, 20 pp.

3. Ahmed, E., **Elgabbas, F.**, and Benmokrane, B. (2013). "Field Testing of the Hybrid-Reinforced Continuous Concrete Bridge on Chemin Dunant: Bridge P-15604." Technical Report Submitted to Ministry of Transportation of Quebec, Canada. May, 31 pp.

4. **Elgabbas, F.**, Ahmed, E., and Benmokrane, B. (2013). "Transverse Shear Strength, Flexure Properties and interlaminar Shear Strength (Short-Beam Shear Strength) of Vinylester and Epoxy Basalt and Glass Fiber-Reinforced Polymer of Bars of Size 6 mm: Reference, 1000-hr, 3000-hr and 5000-hr Alkaline Conditioned specimens." Technical Report. April, 32 pp.

5. **Elgabbas, F.**, Ahmed, E., and Benmokrane, B. (2013). "Tensile Properties, Flexure Properties, Transverse Shear Strength, Interlaminar Shear Strength (Short-Beam Shear Strength) and Bond Strength of Vinylester and Epoxy Basalt and Glass Fiber-Reinforced Polymer of Bars of Size 6 mm and BASA-Prestress Fiber-Reinforced Polymer (FRP) Bars of Size 7 mm and: Reference, 1000-hr, 3000-hr, and 5000-hr Alkaline Conditioned Specimens." Technical Report, May, 71 pp.

6. **Elgabbas, F.**, Ahmed, E., and Benmokrane, B. (2013). "Bond Strength of Magmatic Basalt Fiber-Reinforced Polymer (BFRP) Bars of Sizes 10 and 12 mm." Technical Report. January, 9 pp.

7. **Elgabbas, F.**, Ahmed, E., and Benmokrane, B. (2013). "Tensile Properties, Transverse Shear Strength, Interlaminar Shear Strength (Short-Beam Shear Strength) and Bond Strength of BASA Basalt Fiber-Reinforced Polymer (BFRP) Bars of Size 8 and 12 mm (Codes 43 and 51): Reference, 1 and 3 Months Alkaline-Conditioned Specimens." Technical Report. May, 62 pp.

CHAPTER 1
INTRODUCTION

1.1 Background and Problem Definition

Deterioration of reinforced concrete (RC) structures due to the corrosion of embedded steel reinforcement bars is a well-known and well-documented problem, particularly where deicing salts are routinely used, such as concrete deck slabs and parking garages. The same problem of steel corrosion was observed in marine structures where the chlorides and seawater are available. Therefore, routine maintenance is needed to counter this deterioration. The cost of repair, rehabilitation, strengthening of steel reinforced concrete structures, or delaying and detouring traffic can be high, which has been estimated to be twice the original construction cost, Boyle and Karbhari (1994).

On the other hand, most of the RC bridges are designed for a service life not less than 50 years before major rehabilitation or replacement. Due to the premature deterioration of the bridges, the actual service life had been recorded and found to be 43 years (Transportation for America 2013). There are approximately 583,000 bridges in the United States, about 15% of these bridges are structurally deficient because of steel corrosion. The annual total direct costs were estimated to be $8.3 billion USD, including $3.8 billion USD to replace deficient bridges over the next 10 years and $2 billion for maintenance of concrete bridge-decks (Koch et al. 2002).

Many techniques such as epoxy-coated steel bars and high performance concrete are used to avoid the corrosion. However, it was found that such remedies might not eliminate the problem of corrosion of steel reinforcement in the concrete structures. ACI 440.1R (2015) reported that when epoxy-coated steel bars were implemented in harsh weather conditions, these bars still corroded. Therefore, finding new non-corrosive materials such as fiber-reinforced polymer (FRP) composite that can fulfill the above problem is a must, especially in harsh environmental conditions. FRPs have clear advantages such as high strength, light weight, good resistance to fatigue and corrosion,

ease of forming, in comparison with steel elements (Wu et al. 2007; Bakis et al. 2002). FRP bars consist of continuous fibers of glass (GFRP), aramid (AFRP), carbon (CFRP), or a combination of these (hybrid FRP), impregnated and bound by a resin matrix through a pultrusion, braiding, or weaving manufacturing process. Each of these fiber types is linearly elastic to failure.

Recently, continuous effort in development and innovation of the FRP technology is devoted towards using new types of fibers, such as basalt fibers, in addition to the commonly used glass and carbon fibers. Basalt-FRP (BFRP) has been assured to have advantages in achieving the goal of enhancing safety and reliability of structural systems compared with the conventional FRP composites (Wu et al. 2012).

Basalt fiber is inorganic fibers like glass fibers fabricated from basalt rocks through the melting process. The basalt fibers have high tensile strength and modulus, better chemical resistance, extended operating temperature range, better environmental friendliness when compared to E-glass. Moreover, BFRP has a good impact resistance, and fire with less poisonous fumes. Therefore, basalt fibers are ideally suited for applications requiring high temperatures, chemical resistance, durability, mechanical strength and low water absorption (InfoMine Research Group 2007). In addition, the basalt fibers do not need any other additives in the single producing process, adding special benefit in cost. These advantages make basalt fiber a promising alternative to glass fiber as a reinforcement material in aerospace, metallurgical, chemical, building industries and so on (Mingchao et al. 2008). BFRP composite is expected to provide benefits that are comparable or superior to other types of FRP while being significantly cost effective (Parnas et al. 2007; Wang et al. 2012; Wei et al. 2010a; Lopresto et al. 2011).

On the other hand, North American design codes and guidelines such as CAN/CSA S806 (2012), CAN/CSA S6 (2014) and ACI 440.1R (2015) have been developed to allow engineers to design structural element with the advanced composite materials as GFRP, CFRP and AFRP. However, these codes are not reflecting any recommendations or design procedure for the BFRP bars as reinforcing materials for concrete structures since there are very few researches investigated the physical, mechanical and durability characteristics as well as structural performances of BFRP bars (Mingchao et al. 2008; Scheffler et al. 2009; Wei et al. 2010&2011; Shi et al. 2011a&b; Bi et al. 2011; Wang et al. 2012&2014; Elgabbas et al. 2014; Ovitigala and Issa 2013; El Refai et al. 2014a&b; El Safty et al. 2014; Dhand et al. 2015; Benmokrane et al. 2015; Wu et al. 2015a&b;

Altalmas et al. 2015). Consequently, the main objectives of this experimental investigation are to evaluate the short- and long-term characteristics of newly developed BFRP bars, as well as evaluate the structural performance of these new bars as internal reinforcement for reinforced concrete beams and bridge-deck slabs, in terms of serviceability (deflection and crack width) and nominal resistance, and to introduce these new reinforcing bars to the design codes. Moreover, compare the calculated bond-dependent coefficient (k_b) of sand-coated and ribbed BFRP bars with the recommendations of the current FRP design codes and guidelines. The outcome of this study is expected to provide engineers with more confidence in using FRP bars made with basalt fibers for safe and economic reinforced concrete structures in aggressive environments. Also, this study will be as a step forward towards introducing BFRP composite materials into the available FRP standards and guidelines, such as ACI 440.6M (2008), CAN/CSA S807 (2010), and CAN/CSA S806 (2012) CAN/CSA S6 (2014), and ACI 440.1R (2015).

1.2 Research Objectives

This research project aims at evaluating the feasibility of manufacturing a new generation of FRP bars using basalt fibers (BFRP) and evaluating the use of these bars as internal reinforcement for structural concrete elements, with an emphasis on concrete beams and concrete bridge-deck slabs. This study consists of three parts, designed to evaluate the short-and long-term characteristics and structural performance of newly developed BFRP bars. Part I concerned the physical and mechanical properties as well as the durability performance of BFRP bars and tendons under severe environmental conditions. Part II concerned the structural performance evaluation of seven full-scale restrained bridge-deck slabs reinforced with BFRP bars under truck wheel load. Part III concerned the flexural behavior and serviceability performance evaluation of fourteen concrete beams reinforced with different types and ratios of BFRP and steel bars. This study is expected to introduce these new materials to the FRP design codes and guidelines and enrich the FRP industry. The specific objectives of the current investigation are to:

a. Investigate physical and mechanical properties of newly developed BFRP bars and compare their characteristics with the current requirements of the FRP specifications.
b. Evaluate the durability of BFRP bars under the effect of harsh environmental conditions using accelerated aging technique (alkaline solution at high temperature).

c. Evaluate the structural performance of full-scale restrained concrete bridge deck slabs reinforced with BFRP bars under concentrated loads simulating the truck wheel loads and evaluate their performance in the light of the Canadian Highway Bridge Design Code (CHBDC) requirements.
d. Compare the structural performance of concrete bridge deck slabs reinforced with BFRP reinforcing bars against bridge deck slabs reinforcement with GFRP and CFRP bars, from literature, with similar axial stiffness.
e. Investigate the flexural behavior and serviceability performance of concrete beams reinforced with BFRP bars under static loads.
f. Investigate the cracking behavior and evaluate the bond dependent coefficient (k_b) of sand-coated and ribbed BFRP bars and compare the values with current design codes.
g. Investigate the immediate deflection of concrete beams reinforced with BFRP bar and compare the measured deflection against those values predicted using FRP codes and guides.
h. Evaluate the applicability/accuracy of the current FRP design approaches on BFRP-RC beams and bridge deck slabs at service and ultimate load levels (SLS and ULS).
i. Provide design recommendations and limits for the BFRP reinforcing bars on the material level and when employed in RC elements.

1.3 Methodology

This experimental study was designed to achieve the aforementioned objectives of this research. The study comprised three parts summarized as follows:

Part I: Characterization of BFRP Bars

This part was conducted on three newly-developed BFRP bars and tendons to investigate their physical, mechanical, and durability characteristics. The tests were conducted in accordance to CAN/CSA S807 (2010) and ACI 440.6M (2008). This part was divided into three phases. Phase I focused on physical characterization of the BFRP bars. The physical properties determined in this phase served as references for physical properties after conditioning. Phase II focused on mechanical characterization of the BFRP bars. The tensile strength, tensile modulus of elasticity, ultimate tensile strain, transverse-shear strength, flexural strength, flexural modulus of elasticity, interlaminar-shear strength, and bond strength were determined according to the appropriate test

methods. The test results also served as references for calculating the residual strengths after conditioning. Phase III assessed the durability and long-term performance of the conditioned BFRP bars. The durability was assessed by immersing the BFRP specimens in an alkaline solution at high temperature for different lengths of time (up to 3000 h at 60 °C) designed to simulate a concrete environment so as to validate the performance of the BFRP bars as internal reinforcement for concrete elements. Changes in the physical and mechanical characteristics were assessed by comparing the characteristics of the conditioned BFRP bars to the reference ones from Phases I and II.

Part II: Concrete Bridge-Deck Slabs Reinforced with BFRP Bars

This part included six full-scale edge-restrained concrete bridge-deck slabs simulating a slab-on-girder bridge-deck commonly used in North America and one full-scale unrestrained concrete deck slab to evaluate the performance of concrete bridge-deck slabs reinforced with BFRP bars. The deck slabs measured 3000 mm long × 2500 mm wide × 200 mm thick. The slabs were tested up to failure over a center-to-center span of 2000 mm under single concentrated load acting on the center of each slab over a contact area of 600 mm × 250 mm to simulate the footprint of sustained truck wheel load (87.5 kN CL-625 truck), as specified in Canadian Highway Bridge Design Code (CHBDC). The test parameters investigated herein were: (i) reinforcement type (BFRP and steel); (ii) BFRP bar size (12 and 16 mm); (iii) reinforcement ratio in each direction (0.4% to 1.2%); and (iv) edge-restraining (restrained or unrestrained [free]). The crack width, deflection, and strains of both of reinforcing bars and concrete were observed and recorded up to failure. In addition to the crack pattern and mode of failure were remarked. The punching shear capacities were predicted using the available equations and provisions and compared with the experimental results.

Part III: Concrete Beams Reinforced with BFRP Bars

This part included casting and testing of twelve rectangular concrete beams of 3100 mm long × 200 mm wide × 300 mm deep reinforced with BFRP bars and two beams reinforced with steel bars to investigate the flexural behavior and serviceability performance of concrete beams reinforced with sand-coated and ribbed BFRP bars. The beam specimens were designed in accordance with Annex S of CSA S806 (2012) and tested under four-point bending over a clear span of 2700 mm until failure. The main variables considered in this part were: (i) reinforcement type (BFRP and steel); (ii) bar size (8 mm to 16 mm); (iii) reinforcement ratio; (iv) axial stiffness; and (v)

reinforcing bar configuration (sand-coated and ribbed). The cracking moments, flexure capacities, deflection responses and cracks width of the tested beams reinforced with BFRP and steel bars were predicted using the available equations and provisions and compared with the experimental results. Moreover, the bond-dependent coefficient (k_b) of the BFRP bars were evaluated and compared with the recommendations of the current FRP design codes and guidelines.

1.4 Organization of the Dissertation

This dissertation consists of eight chapters. The following is a brief description of each:

Chapter 1: This chapter defines the problem and summarizes the main objectives and originality of the research program. The methodology followed to achieve these objectives is also introduced.

Chapter 2: This chapter introduces a review of the relevant literature. Firstly, the chapter provides a review of FRP composite materials in general (mainly referred to carbon, glass and aramid) followed by a review about basalt-FRP in particular. After that, it provides a brief review of the experimental and theoretical studies carried out using steel and FRP reinforcing bars and grids as an internal reinforcement for concrete deck slabs. In addition, the chapter provides a summary of the design methods of concrete bridge-deck slabs as specified in CHBDC (CAN/CSA S6 2014). Finally, the literature review will be directed to provide a review about the experimental and theoretical studies carried out on concrete beams reinforced with FRP bars.

Chapter 3: This chapter describes in details the experimental program conducted at the structural laboratory of University of Sherbrooke to develop a better understanding of basalt fiber-reinforced polymer (BFRP) bars. In this chapter, the details of test specimens, configurations, test setups, and instrumentations are given.

The subsequent four chapters respectively correspond to four technical papers that have either been accepted or submitted for publication in scientific journals:

Chapter 4: This chapter presents the first paper in this dissertation entitled “Physical and Mechanical Characteristics of New Basalt-FRP Bars for Reinforcing Concrete Structures”. This chapter includes the complete physical and mechanical characterization of different BFRP bars. It also included long-term durability characterization using accelerated aging techniques in different

chemical solutions at high temperatures for certain periods of time in accordance with ACI 440.6M (2008) and CAN/CSA S807 (2010). [**Reference:** Elgabbas, F., Ahmed, E., and Benmokrane, B. (2015) "Physical and Mechanical Characteristics of New Basalt-FRP Bars for Reinforcing Concrete Structures." *Journal of Construction and Building Materials*, 95, 623–635.]

Chapter 5: This chapter presents the second paper in this dissertation entitled "Experimental Testing of Concrete Bridge-Deck Slabs Reinforced with Basalt-FRP Bars under Concentrated Loads". This chapter presents an investigation of the behavior of edge-restrained concrete bridge-deck slabs reinforced with BFRP bars. The tests included six full-scale edges-restrained concrete deck slabs simulating actual slab-on-girder bridge-deck commonly used in North America and one full-scale unrestrained concrete deck slab. The deck slabs measured 3000 mm long × 2500 mm wide × 200 mm thick. The slabs were tested up to failure over a center-to-center span of 2000 mm under single concentrated load acting on the center of each slab over a contact area of 600 mm × 250 mm to simulate the footprint of sustained truck wheel load (87.5 kN CL-625 truck) as specified in Canadian Highway Bridge Design Code. [**Reference:** Elgabbas, F., Ahmed, E., and Benmokrane, B. (2016). "Experimental Testing of Concrete Bridge Deck Slabs Reinforced with Basalt FRP Bars under Concentrated Loads." *ASCE Journal of Bridge Engineering*, DOI: 10.1061/(ASCE)BE.1943-5592.0000892 , 04016029.]

Chapters 6 and 7: These chapters present the third and fourth papers in this dissertation entitled "Experimental Testing of Basalt-Fiber-Reinforced Polymer Bars in Concrete Beams" and "Flexural Behavior of Concrete Beams Reinforced with Ribbed Basalt-FRP Bars under Static Load". These chapters present an experimental study aimed at determining the bond-dependent coefficient (k_b) and investigating the structural performance of newly developed sand-coated and ribbed BFRP bars in concrete beams. A total of fourteen concrete beams measured 3100 mm length × 200 mm width × 300 mm depth were constructed and tested up to failure. Six beams were reinforced with 10, 12, 16 mm BFRP bars with sand-coated surface (Described in details in **Chapter 6**), as well as six beams were reinforced with 8, 12, and 16 mm BFRP bars with ribbed surfaces and two reference beams were reinforced with 10M and 15M steel bars (Described in details in **Chapter 7**). The main difference between chapters 6 and 7 are the mechanical properties and surface configuration of basalt FRP bars. The beam specimens were designed in accordance with Annex S of CAN/CSA S806 (2012) and tested under four-point bending over a clear span of

2700 mm until failure. It is worth mentioning that the materials presented in chapter six are collaborative joint research work between the author of this dissertation during his doctorate studying and a master's degree student through his master studying at University of Sherbrooke (Vincent 2013). [**Reference:** Elgabbas, F., Vincent, P., Ahmed, E., and Benmokrane, B. (2016). "Experimental Testing of Basalt-Fiber-Reinforced Polymer Bars in Concrete Beams." *Journal of Composite: Part B*, 91, 205-218. **Elgabbas, F.**, Ahmed, E., and Benmokrane, B. (2015). "Flexural Behavior of Concrete Beams Reinforced with Ribbed Basalt-FRP Bars under Static Load." Submitted to *Journal of Composites for Construction*. (December 2015).]

Chapter 8: This chapter presents a general conclusion of the results drawn from the work presented in this dissertation. Recommendations for future research are also given.

CHAPTER 2
LITERATURE REVIEW

2.1 Introduction

The deterioration of metals due to corrosion is a natural phenomenon. Like other natural hazards such as earthquakes, floods or severe weather disturbances, corrosion can cause dangerous and expensive damage to everything from automobiles, home appliances, and drinking water systems to pipelines, bridges, and public buildings.

The corrosion of steel reinforcement is the most common source of concrete structural deterioration, particularly in severe weather conditions where deicing salts are required or structures located by seawater. The U.S. Federal Highway Administration (FHWA) released a breakthrough study entitled "*Corrosion Costs and Preventive Strategies in the United States*" on the direct costs associated with the metal corrosion in nearly every U.S. industry sector, from infrastructure and transportation to production and manufacturing (Koch et al. 2002). The results of the study showed that the total annual direct cost of corrosion in the U.S. is estimated about $276 billion, which is approximately 3.1% of the nation's gross domestic product (GDP). Moreover, the indirect cost of corrosion is conservatively estimated to be equal to the direct cost which brings the cost of corrosion to $552 billion (i.e., 6% of the GDP). Evidences of the large indirect corrosion costs are: (1) lost productivity because of outages, delays, failures, and litigation, (2) taxes and overhead on the cost of the corrosion portion of goods and services, and (3) indirect costs of non-owner/operator activities. In addition, Transportation for America (2013) reported that one out of every nine bridges that U.S. motorists cross each day is likely to be deteriorating to some degree. Nearly 66405, or 11.5%, of the bridges nationwide are rated "structurally deficient" according to government standards. In Canada, the direct costs of corrosion are estimated as $23.6 billion, which represents about 2-4% of the global national product (GNP) (Ghali et al. 2007). Therefore, finding

new non-corrosive materials to be sustainable, environmentally friendly and financially feasible structures became a must challenge for the civil engineers.

Fiber-reinforced-polymer (FRP) material with non-corrosive nature is identified as one of the promising materials for the structural applications. At the beginning FRP material was expensive and it was limited to niche markets such as space shuttles and air industry (in the 1960s), overtime it became cheaper and spread to other industries such as sporting goods (in 1980s-1990s) and then towards the infrastructure industry (Ovitigala 2012). The FRP materials have emerged as an alternative material to steel reinforcing bars in concrete structures, especially that located in corrosive environments, due to their non-corrosive nature (Iyer and Sen 1991; Erki and Rizkalla 1993; Benmokrane et al. 2002; Benmokrane and El-Salakawy 2002), high strength and stiffness-to-weight ratios, resistance to corrosion and chemical attack, controllable thermal expansion, damping characteristics and electromagnetic neutrality (Nanni 1993; Nanni and Dolan 1993; Benmokrane and Wang 2001).

Since FRP is a linear elastic brittle material, the design guidelines for the concrete elements with steel reinforcement became not valid for FRP materials. Worldwide research efforts in this field through professional organizations have resulted in the publication of several codes and guidelines for the design of concrete structures using FRP materials. The design and construction guidelines (ACI 440.1R 2015; CAN/CSA S6 2014; CAN/CSA S806 2012; the JSCE design recommendations 1997) allow the use of glass, carbon, and aramid FRP bars (GFRP, CFRP, and AFRP), while AASHTO (2009) allows the use of glass FRP (GFRP) bars. The FRPs have been used in many demonstration projects and field applications, such as bridge-decks (Hill et al. 2003; Nanni and Faza 2002; El-Salakawy et al. 2003a; Phillips 2004; Benmokrane et al. 2004a; 2006; 2007; Ahmed et al. 2014a), bridge barriers (El-Salakawy et al. 2003b; Matta and Nanni 2009; Ahmed and Benmokrane 2011; Ahmed et al. 2013a&b; Azimi et al. 2014; Khederzadeh and Sennah 2014), bridge piers (De Luca et al. 2010), parking garages (Benmokrane et al. 2004b; El-Gamal et al. 2009; Benmokrane et al. 2012), water-treatment plants (Mohamed and Benmokrane 2014), and concrete pavement (Eddie 1999; Katz 2004; Benmokrane et al. 2008). Most of these projects focused on the use of GFRP bars due to their relatively low cost compared to other FRPs (carbon and aramid).

Recently, continuous effort in development and innovation of the FRP technology is devoted towards using new types of fibers, such as basalt fibers, in addition to the commonly used glass and carbon fibers. Basalt fibers-reinforced-polymers (BFRPs) have become available commercially at a price comparable to E-glass (Ross 2015; BFCMTD 2015; Kameny Vek 2015; Serbescu et al. 2015), which are significantly lower than S-glass or carbon fibers and currently attracting the interest of research communities (Fahmy et al. 2009; Ericson 2012; Quagliarini et al. 2012; Li et al. 2012). Numerous studies have been investigated the traditional FRP products manufactured with vinylester or epoxy resin to determine the effect of environmental conditions (water, salts, alkalis and high temperature) on their physical and mechanical properties (Mouritz et al. 2004; Wang 2005; Zou et al. 2008; Robert et al. 2009; Benmokrane et al. 2015). Few studies, however, investigated the characteristics and durability performance of BFRP under a real and simulated harsh environmental conditions (Mingchao et al. 2008; Scheffler et al. 2009; Wei et al. 2010&2011; Shi et al. 2011a&b; Bi et al. 2011; Wang et al. 2012&2014; Elgabbas et al. 2014; Ovitigala and Issa 2013; El Refai et al. 2014a&b; El Safty et al. 2014; Dhand et al. 2015; Benmokrane et al. 2015; Wu et al. 2015a&b; Altalmas et al. 2015). Moreover, the available design codes (ACI 440.1R 2015; CAN/CSA S6 2014; CAN/CSA S806 2012) and material specifications (ACI 440.6M 2008; CAN/CSA S807 2010) have been developed to allow engineers to design structural element with the advanced composite materials as GFRP, CFRP and AFRP. However, these codes are not reflecting any recommendations or design procedure for structural elements reinforced with BFRP bars because the fundamental studies and the relevant applications are still limited due to the relatively recent development compared with other FRP composites. Therefore, BFRP bars are still not used in the United States and Canada like the aforementioned FRP. In spite of that and as a result of the expected similarity between BFRP bars as the other common GFRP materials, the available design codes and specifications were used to evaluate the characteristics and structural performance of the newly developed BFRP bars.

This chapter introduces a review of the relevant literature. Firstly, the chapter provides a review of FRP composite materials in general (mainly referred to carbon, glass and aramid) followed by a review about basalt-FRP in particular. After that, it provides a brief review of the experimental and theoretical studies carried out using steel and FRP reinforcing bars and grids as an internal reinforcement for concrete deck slabs. In addition, the chapter provides a summary of the design methods of concrete bridge-deck slabs as specified in CHBDC (CAN/CSA S6 2014). Finally, the

literature review will be directed to provide a review about the experimental and theoretical studies carried out on concrete beams reinforced FRP reinforcement.

2.2 Fiber-Reinforced-Polymers (FRPs)

Fiber-reinforced polymers and plastics (FRPs) are a composite material made of a polymer matrix reinforced with fibers, as shown in **Figure 2–1**. The fibers are usually glass, carbon, aramid, or basalt. The polymer is usually an epoxy or vinylester. Since FRP composite is a combination of two or more different materials (fiber and resin) with a distinct interface between them, the constituent materials maintain their separate identities in the composite. Yet their combination produces properties and characteristics that are different from those of the constituents and highly dependent on the cohesion between the fibers and resin, as shown in **Figure 2–2**. The resin system acts as a matrix bonding the fibers together and spreading the applied load to the composite between each of the individual fibers. The resin system also protects the fibers from the abrasion and impact damage as well as the severe environmental conditions, such as water, salts, and alkalis, which affect the durability of FRP products (SP System 1998).

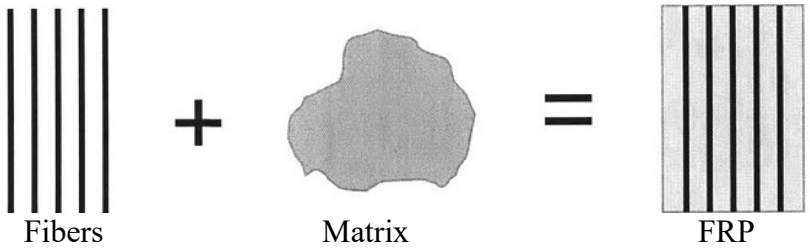

Figure 2–1: Formation of fiber reinforced polymer composite

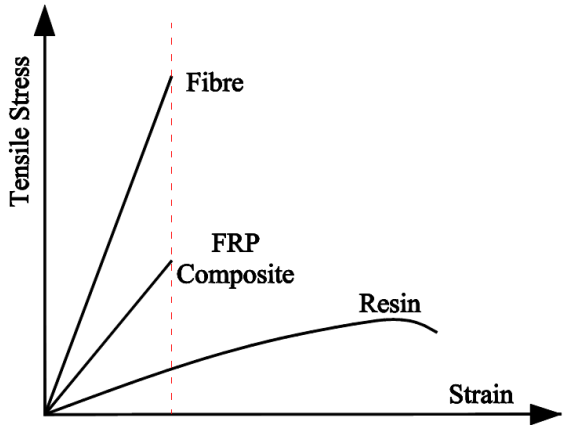

Figure 2–2: Stress-strain relationships for fibers, matrix, and FRP composite

The FRP composites are available with a wide range of mechanical properties (tensile strength, tensile modulus of elasticity, shear strength, flexure strength and bond strength) and made with high-tensile-strength fibers such as carbon, glass, aramid, and basalt. Moreover, FRPs can be produced as bars, ropes, tendons, and grids in a wide variety of shapes and surface configurations, as well as varied characteristics (Erki et al. 1993; *fib* 2007). **Figure 2–3** shows some products of FRP composites. There are many forms of FRP applications, such as FRP sheets and plates for strengthening the structure by attaching them externally to the structure using epoxy or vinylester resin, discontinuous FRP fibers mixed with the concrete, and FRP bars for strengthening using near surface mounted technique (NSM) or as internal reinforcements. This study mainly focuses on the FRP bars as internal reinforcements for concrete structures.

FRP reinforcing bars are typically made using the pultrusion process. In this method, the fibers are impregnated with resin, pulled through a die that compacts and hardens the material, and then cut to a prescribed length.

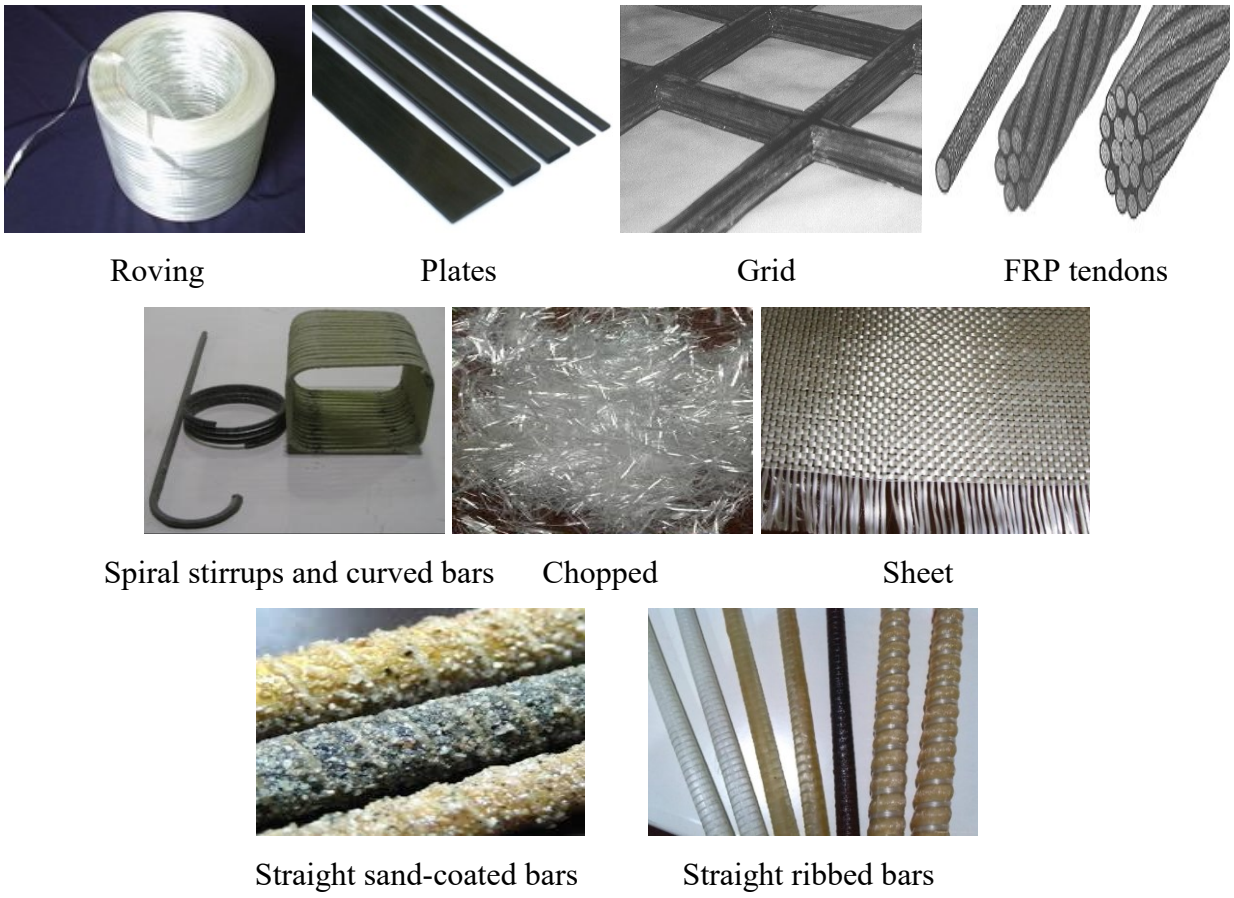

Figure 2–3: Different FRP products

FRP like any other materials have many advantages as well as disadvantages. Therefore, it is important to analyze case by case before it is used. These advantages and disadvantages are given below (Ovitigala 2012).

2.2.1 Advantages of FRP

a. The FRP materials possess a considerable higher strength-to-weight and modulus-to-weight ratios in comparison to steel (Karbhari 2007). The specific weight is nearly one fourth of the steel. Therefore, it is easy handling and transporting.
b. High mechanical performance/price ratio (Brik 2003).
c. High corrosion resistance (Nanni and Dolan 1993; Karbhari 2007).
d. Low thermal and electric conductivity.
e. High fatigue resistance. Schwartz (1997) mentioned that the inhomogeneity in the microstructure could provide mechanisms for high-energy absorption on a microscopic scale that is the reason for increasing the fatigue resistance of the FRP.
f. The anisotropic nature of the FRP material can be an advantage if the fibers are selectively provided in the direction of higher stresses or provided to increase the stiffness in the required direction.
g. Very good damping property.

2.2.2 Disadvantages of FRP

a. Usually high costs associated with the fabrication and the raw materials.
b. The properties are dominated in fiber direction. For instance, the tensile strength of the carbon fiber perpendicular to the fiber axis is 10 times less than the strength parallel to the longitudinal axis (Schwartz 1997).
c. Due to lower elastic modulus, large deflections and crack widths at service load occur compared to steel bars.
d. After manufacturing as a bar, it is difficult to bend as needed due to brittleness. Therefore, bending of FRP bars should be carried out before the resin is fully cured.
e. The transverse and off-axis properties are significantly reduced as the temperatures approach the so-called glass-transition temperature (T_g) of the polymer matrix. Once this limit is crossed, there can be observed significant drop in the strength and the modulus of the material due to thermal softening.

f. The anisotropy of the FRP material makes the design and analysis of the structure more difficult, especially in seismic design. This will be a main factor since FRP does not yield until failure and low ductility demand for rigorous analysis and design methodologies.
g. May be susceptible to fire depending on matrix type and concrete cover thickness.
h. Low durability of some glass and aramid fibers in an alkaline environment.

2.3 Basalt-FRP Bars: Background and Review

Basalt fiber-reinforced polymers (BFRPs) are the most recent FRP composites that have been developed within the last decades and assured to have advantages in achieving the goal of enhancing safety and reliability of structural systems compared with the conventional carbon, glass and aramid FRP composites. Since antiquity basalt is used as crushed rock in construction and Romans recognized its strength and durability and used it in road construction as flagstone. Basalt is an inorganic-natural material that is found in volcanic rocks originated from frozen lava, with a melting temperature comprised between 1500 and 1700 °C (Militký and Kovačič 1996; Militký et al. 2002; Ross 2015). The molten rocks are then extruded through small nozzles to produce continuous filaments of basalt fibers of diameters ranging from 13 to 20 µm (Pantanik 2009). Basalt fibers became available for the use as a reinforcement for concrete structures and found to have acceptable mechanical properties (Banibayat and Patnaik 2015).

The superior properties of basalt fibers (Patnaik et al. 2004) combined with a cost-effective manufacturing process have led to development of BFRP bars that are suitable as internal reinforcement for concrete structures (Brik 1997&2003; Sim et al. 2005; Patnaik 2011&2013; Banibayat and Patnaik 2015; Dhand et al. 2015). Moreover, BFRP bars have gathered attention as a replacement for the other FRPs due to its energy-saving, environmentally friendly, natural green fiber (Wu et al. 2011), high temperature resistance (Brik 2003; Sim et al. 2005), freeze-thaw performance (Wu et al. 2010; Shi et al. 2011a&b), and ease of manufacture (Brik 1997; Sim et al. 2005). It has also been shown to perform better in acidic environments than GFRP (Wei et al. 2010; Wu et al. 2012). However, like GFRP, BFRP has a low elastic modulus relative to steel and undergoes degradation from alkali solutions (Sim et al. 2005). Moreover, basalt fibers can be used for very low temperatures (i.e. about -200 °C) up to the comparatively high temperatures (i.e. in the range of 600 to 800 °C) (Sim et al. 2005; Deák and Czigány 2009; Scheffler et al. 2009;

Morozov et al. 2001; Cao et al. 2009; Wu et al. 2012). The basalt fibers also have better fatigue performance (Wu et al. 2010), over five times of strength and around one third of density than commonly used low-carbon steel bars, as shown in **Figure 2–4** (Wu et al. 2012). In addition, it has good insulation, anti-radiation, and sound wave-transparent properties (Wu et al. 2011). BFRP is successfully used for fire (Parnas et al. 2007; Basaltex 2015) and begun to be used in national defense industry, aerospace, civil construction, transport infrastructure, energy infrastructure, petrochemical, fire protection, automobile, shipbuilding, water conservation and hydropower, ocean engineering and other fields (Wu et al. 2012). **Table 2–1** shows typical values of the physical and mechanical properties of the common used fibers compared to basalt fiber (Kameny Vek 2015).

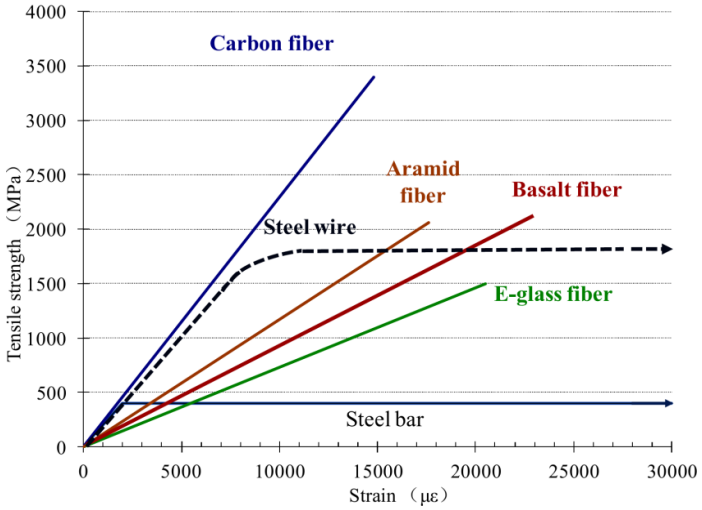

Figure 2–4: Stress-strain curve of various FRP (Wu et al. 2012)

Table 2–1: Comparative characteristics between basalt and other fibers (Kameny Vek 2015)

Capability		Basalt fiber	E-glass fiber	S-glass fiber	Carbon fiber
Tensile strength (MPa)		3000-4840	3100-3800	4020-4650	3500-6000
Elastic modulus (GPa)		79.3-93.1	72.5-75.5	83-86	230-600
Elongation at break (%)		3.1	4.7	5.3	1.5-2.0
Diameter of filament (μm)		6-21	6-21	6-21	5-15
Temperature of application (°C)	Minimum	-260	-50	-50	-50
	Maximum	+500	+380	+300	+700
Price (USD/kg)		2.5	1.1	1.5	30

Basalt is chemically rich with oxides of magnesium, calcium, sodium, potassium, silicon and iron, along with traces of alumina. Parnas et al. 2007 stated that the chemical composition of basalt fibers closely resembles that of the commonly used E- and S-glass fibers, except that basalt contains a high ratio of iron, which yields its brown color, as shown in **Table 2–2**. Besides the chemical compositions, the mechanical properties of basalt fibers from different sources are also different (Subramanian et al. 1977; Artemenko 2003; Sim et al. 2005), probably due to different chemical components and processing conditions, such as drawing temperature. The tensile strength of basalt fibers tends to increase between 1.5 to 2.9 GPa with increasing drawing temperatures between 1200~1375 °C. This is due to increasing proportions of crystal basalt nuclei at lower temperatures, as proved by scanning electron microscopy (SEM), while the Young's modulus varies between 78 and 90 GPa from different sources (Subramanian et al. 1977). **Figure 2–5** shows different products of basalt fibers. In this research the bar shape is of the most interest.

Table 2–2: Chemical components comparison between different fibers (Parnas et al. 2007)

Chemical Composition (%)	Basalt	E-Glass	S-Glass
Silicon Dioxide, SiO_2	48.8-51.0	52-56	64-66
Aluminum Oxide, Al_2O_3	14.0-15.6	12-16	24-26
Iron Oxide, $FeO+Fe_2O_3$	7.3-13.3	0.05-0.40	0-0.3
Calcium Oxide, CaO	10.0	16-25	0-0.3
Magnesium Oxide, MgO	6.2-16.0	0-5	9-11
Sodium Oxide & Potassium Oxide, $Na_2O + K_2O$	1.9-2.2	0-2	0-0.3
Titanium Oxide, TiO_2	0.9-1.6	0-0.8	--
MnO	0.10-0.16	--	--
Fluorides	--	0-1	--
Boron Oxide	--	5-10	--

(a) BFRP bars

(b) BFRP plate (c) BFRP Grid (d) BFRP sheet

(e) BFRP roving (f) BFRP sections

Figure 2–5: Products of basalt-FRP composites

Sukhanov et al. (2004) investigated the mechanical properties and the chemical resistance of basalt fibers subjected to various aggressive media and compared the investigation with glass fiber. Comparative investigations indicated that the resistance of some basalt fibers in alkaline solution (5% NaOH) exceeding the resistance of the widespread alkali-free E-glass fibers. This indicates the possible and prospective use of basalt fiber reinforced composites for concrete reinforcement and producing bridge members. In addition, the basalt fiber endurance in acids is higher than E-

glass. The investigation results of mechanical properties of basalt fiber reinforced produced by different techniques (press molding, winding, and pultrusion) show that basalt plastics properties are much higher than those of similar fiber glass.

Sim et al. (2005) investigated the applicability of the basalt fiber as a strengthening material for structural concrete members through various experimental works for durability, mechanical properties, and flexural strengthening. In addition, the elevated temperature performance of basalt fibers was evaluated. The authors reported that when the fibers were immersed in an alkali solution, both the basalt and glass fibers lost their volumes and strengths with a reaction product on the surface; however the carbon fiber did not show significant strength reduction. For the accelerated weathering test, the basalt fiber provided better resistance than the glass fiber. However, the basalt fiber kept about 90% of the normal temperature strength after exposure at 600 ºC for 2 hours, whereas the carbon and the glass fibers did not maintain their volumetric integrity. In the tests for flexural strengthening evaluation, the basalt fiber improved both the yielding and the ultimate strength of the beam specimen up to 27% depending on the number of layers applied. Based on the investigation, the authors suggested that the basalt fiber could be good alternative fiber reinforcement among glass and carbon fibers in moderate structural strengthening and rehabilitation that required high resistance to fire.

Parnas et al. (2007) conducted an experimental study to determine if BFRP composites were feasible, practical, and a beneficial alternative for transportation applications. They concluded that the chemical composition of basalt fibers was close to glass fibers, except that the basalt contains a high ratio of iron oxide, conferring its brown color. They found no significant differences in stiffness or strength between basalt-fabric-reinforced-polymer composites and glass composites reinforced with a fabric of similar weave. Moreover, they found that the strength and stiffness of the basalt epoxy reinforced composites were no greater than the glass epoxy reinforced material. Aging results indicated that the interface region in basalt composites might be more sensitive to environmental damage than in glass composites. The basalt–epoxy interface, however, might also be more durable than the glass–epoxy interface in tension–tension fatigue, because basalt composites have a longer fatigue life.

Mingchao et al. (2008) studied the chemical durability and mechanical properties of basalt fiber and its epoxy resin composites. The basalt yarns were boiled for 3 hours in distilled water, sodium hydroxide and hydrochloric acid. The yarns mass loss and strength declines in hydrochloric acid were more severe than in sodium hydroxide, showing that the alkali resistance of the basalt fiber was better than acid resistance. In addition, the flexural properties and surface morphologies of the composites were investigated after being immersed in 8 kinds of chemical mediums for 15, 30 and 90 days at room temperature. After each period of immersion, the flexural properties were determined by a three-point flexural test. In acid mediums, the flexural strength and flexural modulus declined in the same way. In alkaline mediums, the flexural modulus kept close to the original value while the flexural strength declined gradually. Even after being immersed in the strong-alkali of sodium hydroxide and ammonia for 90 days, the residual strength was about 70% of originals. The results also showed that the interface formed between basalt fiber and epoxy resin is better than that of glass fiber and epoxy resin.

Adhikari (2009) studied the mechanical properties (tensile strength, rupture strain and modulus of elasticity) of the BFRP bars and their applicability as internal reinforcement in reinforced concrete beams. The reinforcement bars were 3.0, 5.0 and 7.0 mm diameter with the volume fraction of 44%, 52% and 41%, respectively. **Table 2–3** presents the average tensile properties and bond strength of the tested BFRP bars. The test results obtained were fairly consistent and satisfactory. The standard deviations for the tensile strength were found to be varying from 7.0 to 7.9%. The distribution of rupture strains was found to be more variable, varying between 6.0 to 13.7%, the maximum being in the case of 3 mm bar which was related to the probable non-uniformity of the distribution of fibers in the case of small sized bars. In addition, four pullout cylinder tests were conducted for each size of BFRP bars to evaluate the bond-strength. It was concluded that the embedment length of 10 inches was sufficient for the 3 mm basalt bar to develop full tensile strength. Compared with the results for the 5.0 and 7.0 mm basalt bars, it can be observed that the embedment length can be reduced to 7 or 8 inches in the case of 3 mm basalt-FRP bars. In the case of 5 and 7 mm bars, it was evident that the provided embedment of 10 inches was insufficient to develop their full tensile strength and the authors proposed an equation to predict the embedment length of these bars. In addition, the bond behavior of BFRP and GFRP bars were studied by Bi et al. (2011) and Ovitigala and Issa (2013). The study revealed that BFRP bars showed bond stress-slip behavior similar to that of GFRP bars.

Table 2–3: Mechanical properties and bond strength of BFRP bars (Adhikari 2009)

Bar size (mm)	Tensile strength (MPa)	Elastic modulus (GPa)	Rupture strain (mm/mm)	Bond strength (MPa)
3.0	2317±181	86.0	0.0279	4.1±0.22
5.0	2201±154	86.3	0.0272	6.7±0.41
7.0	2079±153	88.5	0.0241	7.3±0.90

Wei et al. (2010) studied the effects of treatment with acidic (HCl) and alkaline (NaOH) media for different times on basalt and glass fibers. They examined post-treated fibers in terms of their strength maintenance ratio and mass loss ratio. They observed that the tensile strength of the fibers decreases with increasing treatment time. It seems that in the same acid environment, the effect of the treatment time on the strength reduction of the basalt fibers is not as obvious as that for the glass fibers. As for alkali environment, the variation of the strength with treating time is almost the same for basalt and glass fibers. For the basalt fibers the acid resistance is much better than the alkali resistance, but for the glass fibers the acid resistance is similar to the alkali resistance. They concluded that amongst these solutions, alkaline conditions were the most corrosive for basalt. The rate of corrosion depends on several intrinsic and extrinsic factors like temperature, fiber composition, aging time, solution composition, pH and size of the fibers. On the whole, the chemical stability of the basalt fibers is better than the glass fibers especially in an acidic environment.

Wei et al. (2011) reinforced basalt and glass fibers in an epoxy resin to study composite degradation in seawater. They observed that the mass gain change of the BFRP and GFRP composites after being immersed in seawater is a combination of two effects: water absorption and soluble material extraction. At the initial stage the water absorption is predominant, and at the late stage the soluble material extraction may play a major role. The tensile and bending strengths decrease with increasing immersion time, indicating that the material has experienced some forms of physical damage and/ or irreversible chemical degradation. The penetrated water may cause the matrix to swell and break, and the soluble material extraction at the interface may damage the coherence between the matrix and the fiber. All these effects make the properties of the composite deteriorate. Moreover, the tensile strength and bending results of seawater treated composites indicated a decreasing trend, based on the time of treatment. They observed that BFRC expressed anti-seawater

corrosion properties similar to GFRP. They concluded that by effectively lowering the content of Fe^{2+} ions within the basalt fibers, one can achieve better and improved stability of composites in seawater environments.

Ovitigala (2012) sought to determine the mechanical properties of BFRP bars by testing five specimens of each of the five different bar sizes: 6, 10, 13, 16 and 25 mm. The tensile strength slightly decreased as the bar diameter increased, with values of 160.2 ksi (110.4 MPa), 162.6 ksi (1121.0 MPa) and 156.9 ksi (1081.7 MPa) for the 6 mm, 10 mm, and 13 mm bars, respectively. All bar diameters exhibited brittle failure by rupture of the fibers. Similarly, the modulus of elasticity of each bar size was also determined and found to decrease with the increase of the bar diameter, except for the 6 mm bars. The minimum value of 7260 ksi (50.0 GPa) was obtained from the 25 mm bars, while the 8 mm bars had the greatest modulus of 8022 ksi (55.3 GPa). As expected, the linear stress-strain curve continued until failure for all specimens. The ultimate strain at failure was as high as 20588 μs for the 13 mm bars and 21171 μs for the 6 mm bars.

Li et al. (2012) studied the durability and fatigue performances of basalt fiber/epoxy FRP reinforcing bars exposed to hygrothermal and alkaline environment. The bare basalt fiber (no resin protection) immersed in these environments, exhibited a severe degradation of tensile properties, due to significant corrosion of the fibers as revealed by scanning electron microscopy. However, the BFRP bars evidenced better durability when subjected to the same conditions. For distilled water immersion for six months, despite of remarkable fluctuation in the original two weeks, the tensile strength of BFRP bars showed a little bit increase (~4%) at 20 °C, but decreased by 26% at 40 °C, 38% at 60 °C and 49% at 80 °C, respectively. As believed, the increase of the strength at 20 °C is due to post-curing effect. Immersed in alkali, BFRP bars showed much pronounced degradation in both strength and modulus. At relatively low temperatures (e.g., 20 °C and 40 °C), the tensile strength firstly increased by about 4% and then decreased. The increase can be assigned to the post-curing effect. At relatively higher temperatures, the tensile strength dramatically reduced in the first month and then slows down. After six months immersion, the reductions of the tensile strengths were 13%, 37%, 56% and 56% at four testing temperatures, respectively. It is worth noting that the reduction of the tensile strength is much higher than that immersed in distilled water. Moreover, the fatigue performance of basalt fiber reinforcing bars was investigated before and after ageing in alkaline solution. The fatigue life of aged samples was remarkably reduced

compared to the control samples. From unaged to aged S-N curve, the fatigue resistance moved backward to the original point. For example, at stress level of 0.5, the fatigue life fell down from 102000 circles to only 7000 circles (93% cut off from the initial).

Wang et al. (2012) studied the degradation of tensile properties of BFRP and the related hybrid FRP tendons under salt solution. The researchers concluded that: i) the degradation of tensile strength of BFRP tendons was proportional to the increase of stress level, while the corresponding modulus was relatively constant; ii) the BFRP tendons under the stress level of $0.6f_u$ after 63 days aging maintained the tensile strength of more than 90%, which showed a good resistance to salts corrosion; iii) hybrid B/CFRP tendons showed even better resistance to salt corrosion in comparison to BFRP but the positive hybrid effect was only observed for the tendons under low stress level ($0.3f_u$); iv) the degradation of hybrid B/SFRP tendons was larger than that of the other FRP tendons, which was mainly caused by the corrosion of steel wires inside.

The tensile properties of BFRP bar of 8 mm diameter and 60% fiber content, pultruded with a vinylester, has been verified under the temperature up to 300 °C by Wu et al. (2012). The results showed that the bar was able to maintain about 85% of its tensile strength due to the high T_g of vinylester (around 120 °C). It was also indicated that the pultruded FRP had a good homogeneity and could achieve high residual strength. To further clarify the mechanism of tensile degradation of BFRP under elevated temperatures, the basalt fiber bundles were tested under the temperatures up to 500 °C, subjected to different conditions, tension under heating and after heating. The degradation of tensile strength of basalt fibers showed, in general, below 200 °C the tensile strength stayed constant and gradually decreased between 200 °C and 300 °C, and noticeably dropped after 300 °C, and finally reached the minimum at 500 °C. In general, the tensile strength of basalt fibers degraded faster when they were tensioned under heating compared with those tensioned after heating.

El Refai (2013) investigated the durability of a novel BFRP bar-anchor system. The BFRP bars were exposed to saline and alkaline solutions for ten weeks before being anchored and tested under static and fatigue loading. Unconditioned basalt, glass, and carbon specimens were also tested and served as controls. The authors concluded that:

a. Conditioning of the BFRP bars in saline and alkaline solutions resulted in a decrease of 7% and 9%, respectively, in the tensile strength of the bar-anchor systems. No noticeable changes in the modulus of elasticity of the NaCl-conditioned specimens were observed, but the NaOH-conditioned specimens exhibited an average decrease of 11% in their modulus. Therefore, the alkaline solution was more aggressive in damaging the BFRP bars than the saline solution.
b. The fatigue test results showed that the applied stress range primarily affected the fatigue life of the bar-anchor system. In addition, continuous immersion of the BFRP bars in the alkaline solution increased its tendency to fracture prematurely in the anchor zone. The fatigue limit (stress range) of the BFRP bar-anchor system was determined to be 4% of its ultimate capacity, compared with 3% and 10% of the glass and carbon systems, respectively.
c. The fatigue performance of the BFRP bar-anchor system is poorer than that of the CFRP system, the former can still be considered in applications involving low to moderate levels of fatigue loading to avoid the high cost of carbon fiber composites.
d. Finally, basalt fibers might be a good alternative to traditional glass fibers in manufacturing FRP composites. The durability and fatigue performance of BFRP bar-anchor systems could be enhanced by improving the manufacturing quality of the BFRP bars in terms of the fiber, matrix, and fiber/matrix interface.

Vincent et al. (2013) characterized newly developed BFRP bars and evaluated their bond-dependent coefficient (k_b). The investigation included physical and mechanical characterization of sand-coated BFRP bars of 10, 12, and 16 mm diameters. In addition, three beams reinforced with BFRP bars of the same diameters were constructed and tested to evaluate the bond-dependent coefficient and compared the results with the current design recommendations of the FRP design codes and guidelines. The test results confirmed that the developed BFRP bars meet the requirements of the ACI 440.6M (2008) and CAN/CSA S807 (2010) concerning their physical and mechanical properties, as well as, the modulus of elasticity of the BFRP bars close to that of GFRP bars of grade I. In addition, the measured bond-dependent coefficient for the tested BFRP bars was 0.74. This value is very close to that of the CAN/CSA S6.1S1 (2010) for sand-coated FRP bars ($k_b = 0.8$). Consequently, the predicted crack widths using CAN/CSA S6.1S1 (2010) provisions were very close to the experimentally measured ones.

Wang et al. (2014a) studied the degradation of the tensile properties of prestressed basalt FRP and hybrid basalt/carbon FRP tendons in a marine environment, as well as addressed the prestressing effect and hybrid effect on degradation. The characteristics of prestressed hybrid FRP tendons in a marine environment simulated by a salt solution. The authors concluded that BFRP tendon showed superior resistance to salt corrosion. The degradation rate of the tensile strength is nonlinearly proportional to the prestressing ratios, whereas the elastic modulus remains constant regardless the prestressing ratios and aging duration. The tensile properties degradation of BFRP tendons mainly lie in the interfacial deterioration instead of the fibers themselves. In addition, the prestressing accelerated strength degradation of BFRP tendons as well as decreased the variation of the strength retention after aging, which can be explained by the straightening effect of fibers in FRP under sustained loads. Moreover, hybridization decreased the degradation rate of non-prestressed B/CFRP tendon due to the contribution of carbon fibers to the strength, whereas for prestressed B/CFRP, the controlling factor of degradation transfers from the carbon fibers to the relatively weak interface between the two kinds of fibers and the resin, consequently resulting in faster degradation. Finally, simultaneous degradations of strength and modulus in the hybrid B/SFRP were caused by the corrosive steel wires in FRP.

El Refai et al. (2014b) investigated the effect of five different accelerated environments (tap water, seawater, elevated temperature, elevated temperature followed by tap water, and elevated temperature followed by seawater) on the bond stress-slip response, adhesion to concrete, and bond strength of two types of BFRP bars (sand-coated and helically grooved) and one type of GFRP bar. The authors concluded that all specimens failed in pullout mode by the interlaminar shear between the bar layers for basalt specimens and by shearing of the surface ribs in the glass specimens. The bond stress-slip response was governed mainly by the surface treatment of the bar and its manufacturing quality, regardless of the type of fiber used. Furthermore, the sand-coated BFRP bars showed higher bond strength, higher adhesion to concrete, and less slip at peak stress than the helically grooved BFRP bars. Exposure to elevated temperatures of up to 80 °C had a minor effect on the bond strength of the tested bars, regardless of the fiber material. In addition, immersion in aqueous solutions enhanced the adhesion stresses at early stages of pullout loading. Nevertheless, such environments had a detrimental effect on the bond strength at later stages depending on the bar material's moisture absorption. Finally, the test results demonstrated the great promise BFRP bars show as reinforcing materials.

Wang et al. (2014b) investigated the creep behavior of newly developed basalt fiber reinforced polymer (BFRP) tendons for prestressing application. Furthermore, the creep rupture stress was predicted based on statistical analysis. The results show that the creep strain to time relationship of BFRP tendons depends highly on the stress level applied. The creep rate of BFRP tendons under low levels of stress remains in low and steady values. Meanwhile, the residual strength of BFRP after 1000 h of sustained load still reaches approximately 95% of its initial tensile strength and the corresponding coefficient of variation (CV) is much less than the original CV. For prestressing application, the creep rupture stress limit for BFRP tendons can be adopted up to 52% of its tensile strength according to the reliability based analysis.

Wu et al. (2015a) investigated the degradation of the tensile properties of basalt fibers and epoxy-based composites in various corrosive environments, including alkaline, acid, salt and water solutions. Accelerated experiments were conducted at temperatures of 25 °C and 55 °C and the variation in tensile properties was studied by means of tensile testing, mass loss weighing, scanning electron microscope imaging and energy spectrum analysis. The degradation of carbon and glass fibers and their composites was also tested for comparison. The findings of the experimental tests were as follows:

a. Basalt fibers exhibited relatively little resistance to corrosion in alkaline and acid solutions, but strong resistance to corrosion in salt and water solutions.
b. Degradation of basalt fibers in both salt and water solutions was induced by local etching of the fibers, while in alkaline solutions, the degradation is caused by large-area pitting of the fiber, resulting in complete loss of tensile strength. In acid solutions, the damage or change in the chemical composition of the fibers is the major reason for the degradation of the tensile strength.
c. BFRP composites exhibited greater improvement in their tensile strength retention under different types of corrosion than basalt fibers, primarily due to the protection of the matrix. However, this improvement was limited by the degradation of the interface between the fibers and the matrix. The elastic modulus of BFRP composites was unaffected by exposure to the corrosive environments.
d. Basalt fibers and their composites exhibit similar resistance to water, salt and alkaline corrosion, but less resistant to acid corrosion than glass fibers and their composites. Carbon

fibers and their composites were resistant to all types of corrosion tested in the study. The corrosion resistance of basalt-FRP composites can be improved by modifying the matrix and the coupling agent.

Wu et al. (2015b) assessed the residual tensile properties of unstressed and stressed BFRP bars exposed to four types of simulated harsh environments: alkaline solution, salt solution, acid solution, and deionized water at 25, 40, and 55 °C. Microstructural analysis by scanning electronic microscopy (SEM) was also performed to reveal the inherent degradation mechanism of BFRP bars in an alkaline environment. The residual tensile strength of unstressed BFRP bars exposed to an alkaline solution was used to predict long-term performance based on the Arrhenius theory. The authors concluded that the effect on the durability of BFRP bars exposed to acid, salt, and deionized water was less than that for bars exposed to alkaline solution. While the elastic modulus of the BFRP bars was quite stable and nearly unaffected by all four types of solutions and sustained stress levels applied. The tensile-strength reductions for an unstressed BFRP bar after conditioning in alkaline solution for 63 days were 31.5 and 6.0% at 55 and 25 °C, respectively. Moreover, after immersion in 40 °C for 42 days, the tensile strength of the BFRP bar was reduced by 5.5, 5.5, and 4.2% over bars immersed in deionized water, salt, and acid solutions, respectively, under the same conditions. In addition, the effects of sustained stress on the degradation of BFRP bars were not obvious when the stress level was less than 20% of ultimate strength, but the degradation processes accelerated when the stress exceeded this level. Finally, the predicted exposure time for the unstressed BFRP bar immersed in a simulated alkaline solution to produce a 50% reduction in strength at 20.3, 14.0, and 5.7 °C, which represent the annual temperatures of areas with northern latitudes 30°, 40°, and 50° (which represents an area with a northern latitude of 50°), respectively, were 4.2 years, 7.4 years, and 16.1 years.

Banibayat and Patnaik (2015) performed creep rupture tests on BFRP reinforcing bars of 4.3 mm diameter at load levels ranged between 25% and 80% of the corresponding ultimate tensile strength. Simulated environmental conditions using an alkaline solution with pH of 13 were used. The tests were conducted at an elevated temperature of 60 °C. An alkaline environment was used to simulate exposure of the FRP bars to the alkaline environment of concrete, and the elevated temperature was used to accelerate the degradation process. The ultimate creep rupture strength coefficients for basalt-FRP bars were determined to be approximately 18% for 50 years' service

life and 28% for 5 years' service life. The ACI 440.1R (2006) approach of using one creep rupture strength limit corresponding to 50 year service life, regardless of the length of the service life leads to conservative designs for structural elements (such as seawalls) that may be designed for 5 to 10 years of service life. Finally, the million hours (114 year) creep coefficient of BFRP bars was estimated to be 13%, which is marginally smaller than that for other AFRP materials.

Benmokrane et al. (2015) investigated the physical, mechanical, and durability characteristics of three different types of FRP bars made of basalt and glass fibers with vinylester and epoxy resins. First, their physical and mechanical properties were assessed. Then, a comparative durability study was performed under alkaline exposure simulating a concrete environment. The alkaline exposure was achieved by immersing the bars in an alkaline solution for up to 5000 h at 60 °C. Thereafter, the properties were assessed and compared with the unconditioned (reference) values. The authors found that the Glass/Vinylester bars exhibited the best bond between the fibers and resin, flexural strength, flexural modulus of elasticity, and interlaminar shear strength, which is governed by the fiber/matrix interface. In addition, they showed the lowest moisture uptake. In contrary, the unconditioned Basalt/Vinylester bars exhibited the lowest transverse-shear strength, flexural strength, interlaminar shear strength, and worst fiber/resin interface. The transverse-shear strength of the Basalt/Vinylester bars was significantly affected by accelerated aging (reduced by 33% after 5000 h), while the Glass/Vinylester and Basalt/Epoxy bars were slightly affected by accelerated aging (reduced by 10% and 9%, respectively, after 5000 h). Moreover, the flexural strength of the Basalt/Vinylester and Basalt/Epoxy bars was significantly affected by accelerated aging (reduced by 37% and 39%, respectively, after 5000 h), while the Glass/Vinylester bars were slightly affected by accelerated aging (reduced by 7% after 5000 h). The interlaminar shear strength of the Basalt/Vinylester and Basalt/Epoxy bars was affected by accelerated aging (reduced by 22% and 14%, respectively, after 5000 h), while the Glass/Vinylester bars were slightly affected by accelerated aging (reduced by 5% after 5000 h). The fiber-resin interface plays a significant role in controlling the degradation due to conditioning. Finally, the Glass/Vinylester FRP bars showed superior durability in the alkaline environment at elevated temperature compared to the Basalt/Vinylester and Basalt/Epoxy bars. The results confirmed that the two types of fiber (glass and basalt) and resins (vinylester and epoxy) used in this study were not affected by the conditioning.

Lu et al. (2015) thermally aged a pultruded unidirectional BFRP plate at 135 and 300 °C for 4 hours, and subsequently immersed in distilled water or strong alkaline solution (simulating concrete pore water, pH = 12.6-13.0) for 3 months. The variation of the tensile and interlaminar shear properties of the BFRP plates was studied. Thermal aging exhibited a slight effect on both the longitudinal tensile properties and the interlaminar shear strength, although thermal decomposition of the resin matrix started at 300 °C and brought in a high void content (4.8%). FTIR and DMTA results indicated that thermal aging lead to post-curing and oxidation of the resin matrix, leading to an increase of the glass transition temperatures. Thermal aging accelerated the degradation of the BFRP plates in distilled water or alkaline solution at 20, 40 and 60 °C. In the studied hash immersion conditions at 60 °C alkaline solution for 3 months, the un-aged, 135 and 300 °C aged BFRP samples showed reduction in the tensile strength by 43.2, 62.3 and 74.1%, respectively. The higher the thermal aging and immersion temperatures, the more deterioration of the mechanical properties occurred. Alkaline solution immersion showed more adverse effects compared to the distilled water. The detrimental effects of the thermal aging were attributed to the formation of voids and cracks through which water or alkaline solution tended to easily penetrate into the BFRPs.

Serbescu et al. (2015) examined the degradation of BFRP bars after exposure to accelerated environmental conditions and proposed a methodology to predict their long-term design strength. A total of 132 BFRP specimens comprising two types and seven different diameters were tested in tension after conditioning in pH9 and pH13 solutions at 20, 40, and 60 °C for 100, 200, 1000; and 5000 hours. The tested BFRP bars exhibited a tensile strength ranged from 972 to 1481 MPa while the elastic modulus varied from 34 to 47 GPa. The lowest strength retention of 69% was observed for bars exposed to pH9 solution at 60 °C for 5000 hours. Despite some strength deterioration, the elastic modulus of the tested bars increased by an average of 6.5% (this can be attributed to post curing of the resin matrix). In addition, they were estimated to retain about 72% and 80% of their strength after 100 years exposure to concrete and mortar environment, respectively.

2.4 Bridge-Deck Slabs: Background and Review

2.4.1 General

The most common type of bridges built in highways is concrete deck slabs constructed on steel or prestressed girders. The concrete deck slabs deteriorate faster than any other bridge elements because of direct exposure to harsh environmental conditions such as freeze-thaw cycles, wet-dry cycles, de-icing chemicals, and traffic loads, which result in corrosion of steel reinforcement. The magnitude of deck cracking and delamination due to the corrosion is a major problem when measured in rehabilitation costs and traffic disruption (Yunovich and Thompson 2003). In Quebec, half of the maintenance budget of the Ministry of Transportation is spent on concrete structures damaged by corrosion of steel (El-Salakawy et al. 2003a).

Fiber-reinforced polymers (FRP) reinforcing bars with non-corrosive nature are beneficial for improving the durability of these bridge-decks and reduce – if not eliminating – the maintenance and repair cost (ACI 440.1R 2015; ISIS-M3 2007). The service life of concrete deck slabs reinforced with steel bars expected to be 25 years before requiring replacement. However, the service life of the panels with FRP reinforcement is usually expected to be at least 75 years (i.e. the period of use of the bridge) (O'Connor et al. 2003; Wu et al. 2012).

On the other hand, one of the usual characteristics of the slab constructed on girder bridges is composite action between the girders and deck slab that contributes to increase both of the longitudinal flexural strength and stiffness (Edalatmanesh and Newhook 2012). Therefore, this composite action is recommended to enhance stiffness and economy of structures. To ensure composite action between the deck slabs and steel or concrete girders, shear connectors are fixed to the top surface of girders, as shown in **Figure 2–6**.

Moreover, it is well established that restrained concrete bridge-deck slabs (slab-on-girder type) fail in the punching shear failure mode under the effect of concentrated wheel loads because of the effects of compressive membrane action (Hewitt and Batchelor 1975; Batchelor et al. 1978; Fang et al. 1990; Kuang and Morely 1993; Thorburn and Mufti 2001; Graddy et al. 2002; El-Gamal et al. 2005; Newhook et al. 2011; Edalatmanesh and Newhook 2012; Zheng et al. 2012a&b; 2013; Zheng et al. 2014; 2015). This arching action is a result of the lateral restraining forces applied to

the deck slab due to the continuity of the slabs and the monolithic action of the supporting girders. The compressive membrane action significantly increases the carrying capacity of these deck slabs compared to that of the slab in pure flexure (Hon et al. 2005).

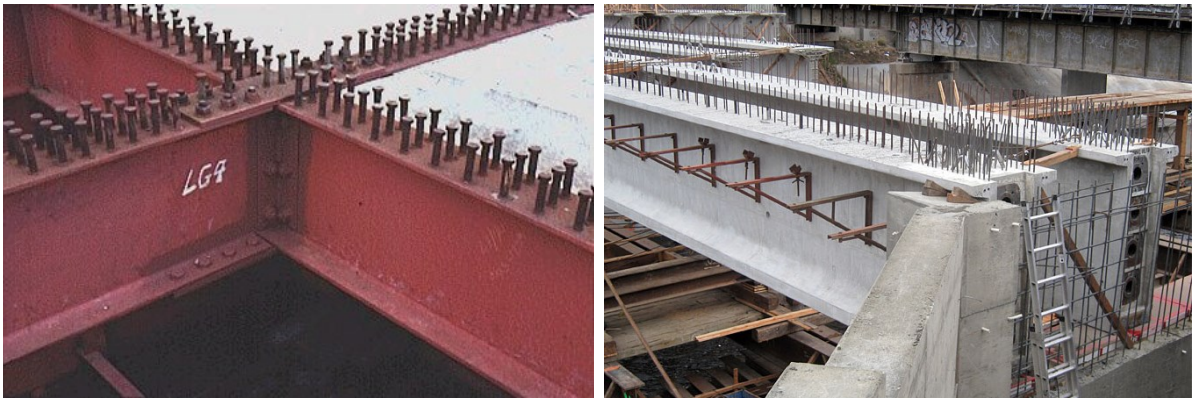

Figure 2–6: Steel shear connectors fixed to the top flange of steel and concrete girders

2.4.2 Review about FRP-RC Bridge-Deck Slabs

The punching shear behavior of steel-RC deck slabs system has been extensively studied (Hweitt 1972; Hewitt and Btchelor 1975; Perdikaris and Beim 1988; Kuang and Morely 1993; Mufti and Newhook 1998) and several code provisions have been established. These provisions cannot be directly applied for FRP-RC slabs due to the significant difference in the mechanical and physical properties between steel and FRP bars. In the past decade, few researchers studied the behavior of restrained concrete deck slabs reinforced with glass and carbon FRP bars (Hassan and Rizkalla 2004; El-Gamal et al. 2005a&b; 2007; El-Ragaby et al. 2007; Bouguerra et al. 2011; Zheng et al. 2012a&b; 2013). It has been demonstrated some modifications in the available provisions to be convenient to the slabs reinforced with FRP bars.

One of the early studies on the punching shear of FRP-reinforced concrete slabs was conducted by Ahmed et al. (1993). They tested six simply supported square concrete slabs under central concentrated loads. All concrete slabs were 690 × 690 × 80 mm. Four of the slabs were reinforced with 3-D carbon fiber fabric, and two were reinforced with conventional mild steel. For the four CFRP slabs, two were fabricated with column stubs and the other two slabs without the column stub. The reinforcement ratios in the three directions for the CFRP slabs were 0.95%. For the two slabs reinforced with steel, the reinforcement ratios in the X and Y directions were 1.18% and 1.35%, respectively. They concluded that all test slabs failed in punching shear before reaching the

design flexural capacity and the punching shear behavior of the tested FRP-reinforced slabs were different from the slabs reinforced with conventional steel. The FRP-RC slabs exhibit a significant non-linear behavior and a reduction in the stiffness in the post cracking stage, and also showed a post-maximum load deformation softening response.

Banthia et al. (1995) tested four concrete slabs measured 600 × 600 × 75 mm to study the behavior of concrete slabs reinforced with FRP grids. Three slabs reinforced with FRP grids (NEFMAC) were tested and compared to a similar slab reinforced with conventional steel reinforcement. Normal strength, high strength and normal strength concrete with fiber were used to manufacture the slabs. It was concluded that the ultimate loads supported by slabs reinforced with FRP were equal to or higher than that supported by the companion slab reinforced with steel. It was observed, however, that because of the brittle nature of fracture in the FRP, slabs reinforced with such grids were less energy absorbing than one reinforced with steel. In this context, the use of fiber-reinforced concrete appeared to be promising. The ultimate loads supported by slabs were compared to those predicted by the various code equations. It appeared that not many changes were needed to these equations when applying them to slabs reinforced with FRP grids.

Bakht et al. (2000) presented different types of straps as externally transverse reinforcements for steel-free deck slabs. This type of slab derives its strength from its internal arching action, which is harnessed longitudinally by making the slab composite with the girders, and transversely by restraining the relative transverse movement of the top flanges of adjacent girders. The slab included fully studded straps, partially studded straps, cruciform straps, FRP bars and diaphragms. Three models of steel-free slabs with different straps were tested to failure under monotonic loading. An additional specimen was tested under 1000 cycles of pulsating load between 0 and 88 kN prior to the static testing. The results of the latter static testing indicated that the forces in straps increased, due to shakedown in the slab. The authors concluded that the modes of failure of the steel-free deck slabs were mostly punching shear failure as expected, but the actual failure loads were more than 10 times the theoretical failure load. The very large differences between the theoretical bending and actual failure loads confirmed that the transverse confining systems employed were effective in forcing the deck slab to act in arching. It was shown that the steel-free deck slab, in addition to being more durable than slabs with steel reinforcement, can also prove to be more economical.

Hassan et al. (2000) studied the behavior of two full-scale models of a portion of a highway bridge-deck slab reinforced with FRP reinforcement under concentrated loads through a 225 × 575 mm steel plate. The first slab was reinforced totally with CFRP bars, and the second slab was reinforced with hybrid GFRP and steel bars. Each model consisted of three continuous spans of 1800 mm each and two cantilevers, to simulate the effect of a truck wheel load, with overall dimensions of 7200 × 3000 × 200 mm, as shown in **Figure 2–7**. The applied load was cycled three times every 200 kN. Load–deflection behavior, crack patterns, strain distribution, and failure mode were reported. The test results confirmed that the ultimate load carrying capacity of continuous full-scale bridge-deck slab models is more than seven times the service load specified by the AASHTO Code (1996) and the failure is due to punching shear. The presence of top reinforcement in continuous bridge-deck slabs has a negligible effect on the punching shear capacity. In addition, to satisfy serviceability and ultimate capacity requirements for span-to-depth ratios ranging between 9 and 15, the use of 0.3% CFRP (fiber volume ratio of 60% or more) as top and bottom reinforcement in each direction was recommended. For GFRP reinforcements (fiber volume ratio of 60% or more), using 1.2% for the bottom reinforcement and 0.6% for the top reinforcement in the transverse direction, as well as 0.6% as top and bottom reinforcement ratios in the longitudinal direction, achieves the code requirements.

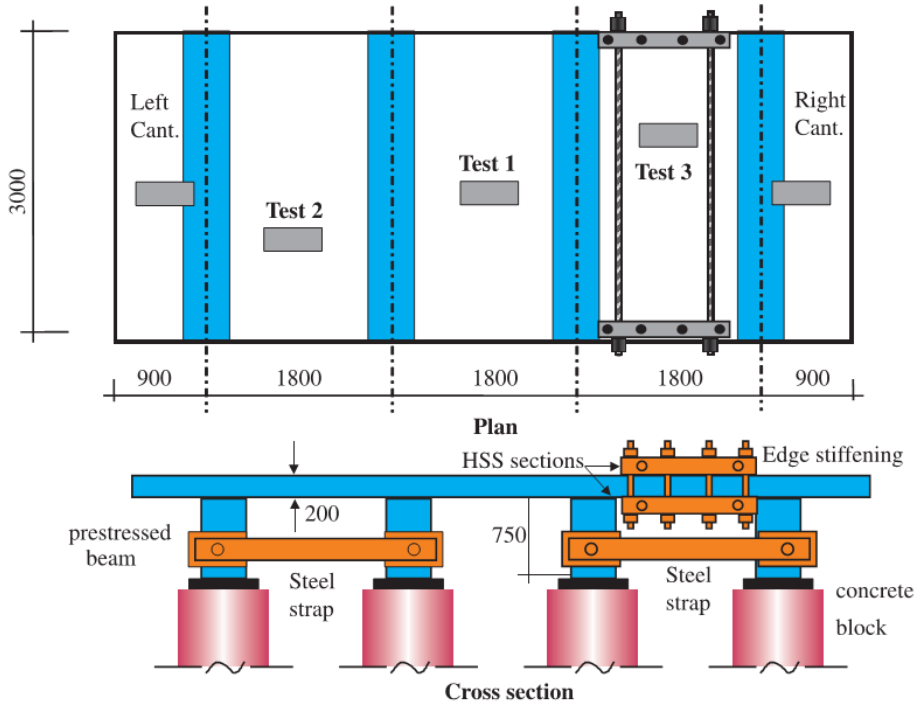

Figure 2–7: Full-scale bridge-deck panel (Hassan et al. 2000)

Khanna et al. (2000) carried out an experimental study to investigate the influence of each layer of reinforcement (steel and glass FRP) on the behavior of conventionally reinforced concrete deck slabs. The test model was a 12000 mm long × 175 mm thick slab cast compositely on two steel girders spaced at 2000 mm. The slab model was conceptually divided into four segments (3000 mm long each), as shown in **Figure 2–8**. Each segment had a different reinforcement configuration. The first segment contained isotropic steel reinforcement in two layers. The second contained only the bottom layer of steel reinforcement. The third contained only the bottom transverse steel bars. The last segment contained only bottom transverse GFRP bars having the same axial stiffness as those of the steel bars in the third segment. Each segment was tested under concentrated load over an area measured 250 × 500 mm, simulating the dual tire footprint of a typical commercial vehicle, according to the Ontario Highway Bridge Design Code (OHBDC). The test results showed that all segments failed in the punching-shear mode at similar load values. Also, it was confirmed that only the bottom transverse reinforcement influences the load carrying capacity and deflection behavior of a reinforced concrete deck slab. Moreover, the stiffness of the bottom transverse reinforcement, rather than its strength, is of paramount importance. Finally, the results indicated the validation and competitiveness of the proposed FRP design compared to the conventional steel design.

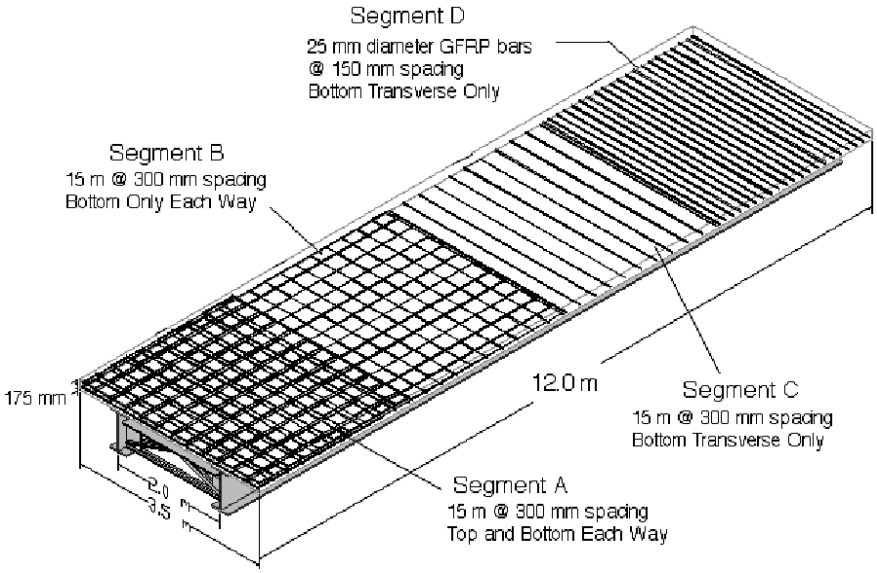

Figure 2–8: Full-scale bridge-deck panel (Khanna et al. 2000)

Rahman et al. (2000) tested a full-scale model of a bridge-deck slab reinforced with a mesh of CFRP with a reinforcement ratio of 0.3%. The slab dimensions were 6000 mm each side and 185

mm thick. It was supported on three steel girders spaced at 2000 mm (center-to-center). The model had two 2000 mm continuous spans and 1000 mm cantilevers on both sides, as shown in **Figure 2–9**. The slab was first loaded monotonically at six positions at three stages (using two concentrated loads at each span on a footprint of 150 × 250 mm) to crack the concrete. Then it was loaded cyclically in three stages of 4 million cycles each at a frequency of 5 Hz, with the load varying between 0 and 100 kN in the first two stages and between 0 and 125 kN in the last stage. The authors observed that the overall behavior of the slab under the service load was satisfactory, the deflection was small (about L/800), and the stresses in the reinforcement were approximately 7% of its ultimate strength. It was confirmed that the failure mode was punching shear and the minimum ultimate load capacity of the slab was more than five times the maximum wheel load of 100 kN. In addition, the deterioration in the slab's structural performance under a simulated 50 years of service loading, indicated by the increase in slab deflection and stress in the FRP reinforcement during the course of cyclic loading, is negligible.

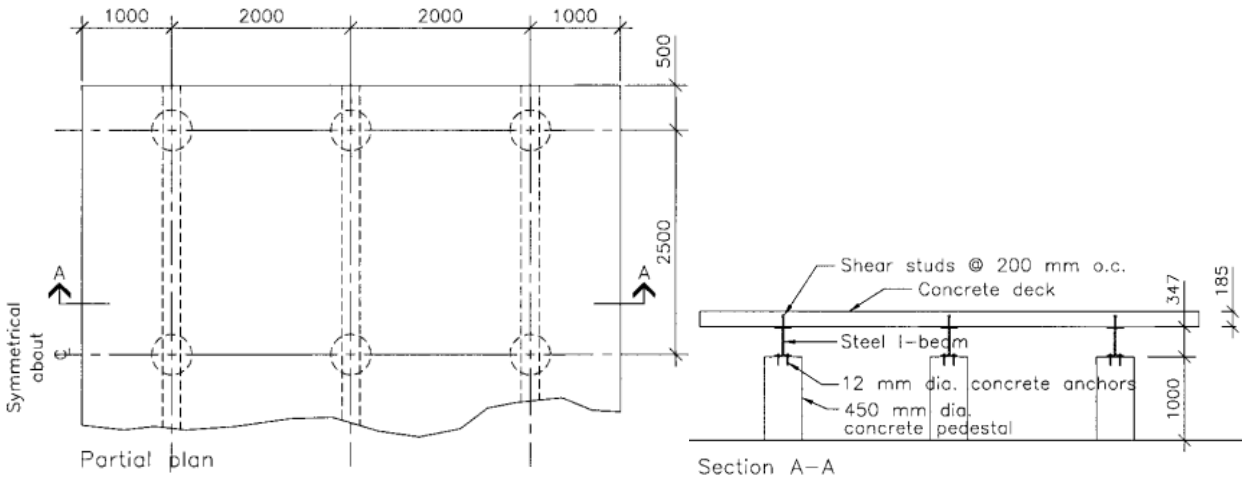

Figure 2–9: Plan and cross section of tested bridge-deck (Rahman et al. 2000)

Thorburn and Mufti (2001) presented a design procedure for an externally restrained highway bridge-deck. The method has been developed, based on the Canadian Limit States design philosophy, considering both the strength and serviceability requirements. Transverse steel straps, placed below the concrete slab (**Figure 2–10**), eliminate the deleterious effects of corrosion on the concrete. Further, the straps can be designed to provide the restraint necessary to promote the development of internal arching in the concrete slab in response to a concentrated load. The capacity of an externally restrained composite bridge-deck, with no internal steel reinforcing, will

be limited by the formation of a local punching failure if sufficient external reinforcement has been provided.

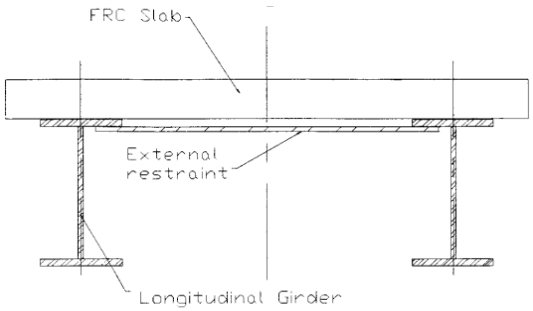

Figure 2–10: Section of externally reinforced slab-on-girder bridge with FRP deck slab (Thorburn and Mufti 2001)

El-Salakawy et al. (2003a) tested a new bridge for service performance using standard truckloads. The bridge is located in the Municipality of Wotton, Quebec, Canada. The bridge is a girder type with four main girders simply supported over a span of 30.6 m. One half of the concrete deck slab was reinforced with carbon and glass FRP bars, and the other half with conventional steel bars. The design of the reinforced concrete deck slab was made according to the Canadian Highway Bridge Design Code. The bridge was well instrumented at critical locations for long-term internal temperature and strain data collection using fiber optic sensors. The construction details and the results of the field tests and remote monitoring for the bridge-deck slab showed that under the same real service and environmental conditions, very similar behavior was obtained from the sand-coated FRP and steel bars. No obstacles to construction were encountered due to the use of the FRP bars. The FRP bars withstood normal on-site handling and placement problems. In addition, the maximum tensile strain values in concrete were very small (10-25 μs) and well below the cracking strain of concrete, which is 132 μs for normal-weight concrete (f_c'= 37 MPa, E_c = 28 GPa). While the maximum tensile strains in FRP and steel bars were 15 and 16 μs, respectively. These values are less than 0.13% of the ultimate strain of the FRP material. Moreover, the flexural design methods (CAN/CSA S6 2000) for concrete bridge-deck slabs supported on girders and with span to depth ratios of less than 15 seem to be conservative. Deflections of the bridge-deck slab and girders were less than 5 and 10 mm, respectively, well below the CHBDC and AASHTO allowable limits. Finally, the empirical design method (CAN/CSA S6 2000) for concrete bridge-deck slabs supported on girders and with a span to depth ratios of less than 15, the following FRP

reinforcement ratios were recommended: 0.6% of CFRP reinforcement in the bottom transverse direction and 0.6% of GFRP reinforcement in all other directions. This is valid for carbon and glass FRP composite bars with a modulus of elasticity of at least 110 and 40 GPa, respectively.

Hassan and Rizkalla (2004) presented results of nonlinear finite element formulation of typical concrete bridge-decks reinforced with different types and configurations of FRP bars to study their effectiveness under service and ultimate limit states. Based on the results of the finite element analysis and possibility of constructing concrete bridges using FRP reinforcing bars, the proposed GFRP bottom transverse reinforcement ratio shall not be less than 1.2%. The top and bottom longitudinal GFRP reinforcement as well as the top transverse reinforcement shall not be less than 0.6% to resist shrinkage and temperature stresses. Using the proposed values for the reinforcement ratios will ensure that the deflections under service load level is well below the limiting value required by the AASHTO code. The maximum tensile stresses in the bottom and top transverse GFRP bars at service load level were 17 MPa and 16 MPa, respectively, which are less than 20% of the ultimate tensile strength of the rebars. Consequently, creep rupture problem of GFRP bars is not a concern. The failure mode of continuous bridge-deck slabs, having a span-to-depth ratio of 10 or less is due to punching shear. In addition, the presence of top transverse reinforcement in bridge-deck slabs has a negligible effect on the punching shear capacity.

Hon et al. (2005) carried out an experimental program and nonlinear finite element modeling for assessing the restraint stiffness that exists for the slab of typical beam-and-slab bridge-decks and the strength enhancement due to compressive membrane action. The tested specimen consisted of a slab with a transverse span of 600 mm and a depth of 75 mm. The slab in each specimen was designed to be identical, so that the effects of the boundary conditions could be properly evaluated. The longitudinal edge beam span of all of the specimens was 3000 mm. The boundary conditions consisted of edge beams of varying widths, and transverse end diaphragms. A small gap was formed between the slab and the diaphragm to ensure that the slab spanned in one-way action. Some specimens had an adjacent slab on the other side of the edge beam to increase the horizontal translational restraint stiffness that existed for the loaded slab. **Figure 2–11** shows typical geometry of the tested specimens. They concluded that the compressive membrane action enhanced the deck strength above that determined using a normal flexural and punching shear strength theory. The results indicated that a significant amount of compressive membrane action can be expected to

develop transversely in the slabs of actual beam-and-slab bridge-decks. The stiffness and strength of the slabs can then be expected to be significantly higher than that predicted using methods that do not incorporate the enhancing effects of compressive membrane action. Hon et al. (2005) described two requirements for developing a compressive membrane action in a reinforced concrete slab. First, some form of horizontal translational restraint must exist for the slab. In the case of a beam-and-slab bridge-deck, this consists of the longitudinal beams, the adjacent slabs, and the surrounding slab area. The other condition is related to the strain compatibility along the length of the slab, in that the net tensile strain along a longitudinal fiber must be non-zero if there is no horizontal restraint. The presence of a rigid horizontal restraint (at the depth of a longitudinal fiber that would have had non-zero net tensile strain) forces the strain back to zero, which induces membrane forces in the slab. If the restraint is less than rigid, the net longitudinal strain will not be zero and a lesser amount of membrane action will develop in the slab. The compressive membrane action develops transversely in the slab because cracks develop at mid-span and at the slab ends. This causes an extension in the longitudinal fibers of the slab, which is restricted by the horizontal restraint. In this case, the concrete in the surrounding beams and adjacent slabs provide the horizontal restraint. Therefore, the two conditions necessary for compressive membrane action to develop are satisfied. Approximate methods to account for compressive membrane action have been developed by previous researchers. These methods require knowledge of the restraint stiffness that exists for the slab, and this is not known with much certainty. Hence, compressive membrane action is usually not taken into account when determining the strength of reinforced concrete slabs. The reinforcement has a dual purpose: it provides for both local flexural resistance and global confinement required to develop arching effects (Holowka et al. 1980; Fang 1985).

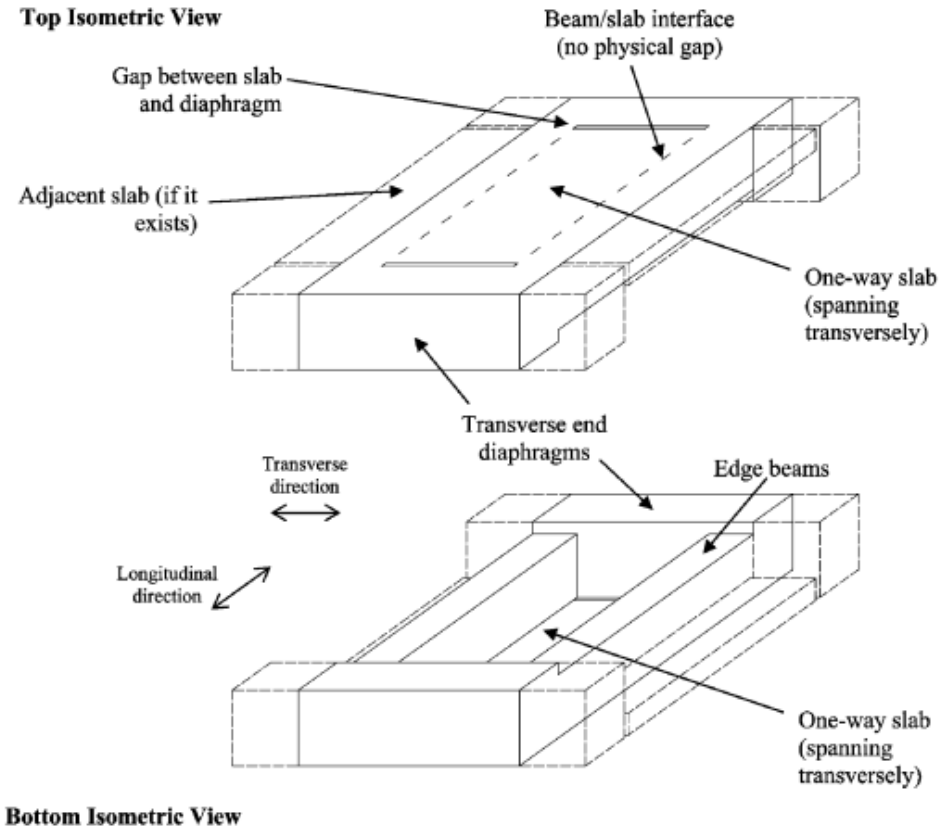

Figure 2–11: Typical specimen in experimental program (Hon et al. 2005)

El-Gamal et al. (2005; 2007) investigated the effect of the bottom transverse GFRP and CFRP reinforcement ratio and type on the behavior of edge-restrained concrete bridge-deck slabs reinforced with FRP bars. The investigation was conducted on full-scale bridge-deck slabs of 3000 mm long × 2500 mm wide × 200 mm thick. The deck slabs were constructed and tested under monotonic concentrated load. One deck slab was reinforced with steel bars, one deck slab was constructed using plain concrete without any reinforcement and the others were reinforced with GFRP and CFRP bars. The deck slabs were supported on two steel girders spaced at 2000 mm (center-to-center) and restrained at the longitudinal ends by bolting the concrete slabs to the supporting steel girders through holes in the slabs. Also, they proposed a new model to predict the punching shear capacity of two-way concrete slabs reinforced with FRP or steel reinforcement. This model takes into consideration a new parameter to give better agreement with the experimental results. Based on the experimental and theoretical results, the following conclusions were drawn:

1. The restrained deck slabs were failed due to punching shear of carrying capacities more than three times the factored design load as specified by the CHBDC. The plain concrete deck slab,

however, behaved differently and failed at a lower load level, which was less than 25% of the failure loads of the other tested slabs.

2. Neither the top reinforcement assembly nor the bottom longitudinal reinforcement has a major effect on the measured deflections or strains.
3. The maximum measured deflection at the service load level was below the allowable code limits (L/800). In addition, the increase of the FRP reinforcement ratio has an insignificant effect on the deflection behavior.
4. The recorded cracking load was higher than the service load. For the pre-cracked slabs, however, the maximum measured crack widths at the service load level were less than 0.4 mm, which is below the allowable code limits.
5. The ratios of the strains at service load to strains at failure were less than 5 and 10% for bars and concrete, respectively.
6. The proposed model, given by Eqn. (2-1), showed good agreement with the available test results.

$$V_c = V_{c,ACI\,318} \times \alpha = 0.33\sqrt{f'_c}\, b_{o;0.5d}\, d \times \alpha \qquad (2\text{-}1)$$

$$\alpha = 0.5\left(\rho_f\, E_f\right)^{1/3}\left(1 + 8d/b_o\right) \qquad (2\text{-}1a)$$

Where α is a new parameter which is a function of the flexural stiffness of the tensile reinforcement ($\rho_f E_f$), b_o is the perimeter of the applied load, and d is the effective depth of the slab.

Jacobson and Bank (2005) performed a series of punching shear tests on deck slab specimens reinforced with double layer glass/vinylester FRP pultruded grids having varying dimensions, support conditions, and end restraint conditions using a patch load that simulated the tire contact area of an HS-20 design truck double wheel. Punching shear was the mode of failure identified in all of the tested slabs. The punching shear capacity of the slab specimens was shown to be enhanced by introducing edge restraint to the specimens. In each case, the punching shear failure plane acted through the non-mechanically connected overlap splice between adjacent reinforcement cages. This confirmed the notion that the simple overlap splice would be the most structurally vulnerable aspects of the FRP reinforcement system, due to a lack of physical reinforcement continuity.

However, the punching shear failure occurred at loads many times greater than the HS-20 service load.

Benmokrane et al. (2006) presented the design method, construction details, and test results for the GFRP-reinforced concrete deck of the Morristown Bridge on Route 100 which is located in Vermont, United States. The bridge is a single span steel girder with integral abutments spanning 43.90 m. The concrete deck is a 230 mm depth and continuous over girders spaced at 2.36 m. The entire concrete deck slab was reinforced with GFRP bars in two identical layers at the top and the bottom. The bridge was tested for service performance using standard truck loads. The construction procedure and field test results under actual service conditions revealed that GFRP rebar provides very good and promising performance. In addition, the FRP bars withstood normal on site handling and placement with no problems and their light weight made them easy to carry and easier to place. Also, the maximum tensile strains in the GFRP bars were 8 μs and 31 μs, at the top and bottom, respectively. These values represent less than 0.19% of the ultimate strain of the GFRP and suggest that the AASHTO flexural design method overestimates the calculated design moments (service and ultimate). The small measured strains either in GFRP bars or in concrete compared to the expected values according to the flexural design moments suggest that the behavior of the deck slab under concentrated wheel loads is arching action and the failure mode is punching shear.

El Ragaby (2007) concluded that the primary structural action of deck slabs resists concentrated loads is a complex internal membrane stress state referred to the internal arching (the arching action theory). This action activated after top and bottom cracks over the supports and at mid-span, respectively, penetrated through the deck slab depth. The arching action is sustained by in-plane membrane forces that developed as a result of lateral confinement. This lateral confinement is provided by the surrounding concrete slab, supporting elements, internal reinforcement and rigid appurtenances. All of these components act compositely with the slab to create internal membrane compressive forces. The failure of the internal compressive dome (arch) usually occurs as a result of overstraining around the perimeter of the wheel footprint (punching shear failure).

Seliem et al. (2008) described the behavior of concrete bridge-decks reinforced with newly developed high-performance steel that is characterized by its high strength and enhanced corrosion-resistance in comparison with conventional ASTM A61S (2006) Grade 60 steel. The study included testing of three full-scale bridge-decks with a span-depth ratio of 12.5. It was concluded that the

ultimate load-carrying capacity of the three bridge-decks was approximately 10 times the service load prescribed by the AASHTO specifications. In addition, punching shear was the primary mode of failure for the three bridge-decks. Due to continuity used in the test models, flexural-shear failure was observed as a secondary mode of failure. Finally, the cracking load of the tested bridge-decks was more than twice the service load prescribed by the AASHTO specifications. Hence, under service load level, the three bridge-decks behaved as uncracked sections.

Ahmed and Benmokrane (2010) investigated the use of two GFRP products in the design of GFRP bridge-deck slabs using two concrete strengths. Through this investigation, it was concluded that increasing the modulus of elasticity of GFRP bars reduces the required reinforcement amount and therefore reduces the cost.

Bouguerra et al. (2011) experimentally investigated the behavior of FRP-reinforced concrete bridge-deck slabs under concentrated loads. Eight full-scale restrained deck slabs measuring 3000 mm long × 2500 mm wide and different thickness (150, 175 and 200 mm) were constructed using normal and high strength concrete. The slabs were reinforced with GFRP, CFRP, and steel bars with different reinforcement ratios in the bottom transverse direction. The slabs were tested using the same setup of El-Gamal et al (2005). All deck slabs failed in punching shear. It was confirmed that the bottom transverse reinforcement ratio was the main parameter affecting crack widths. In addition, the punching capacity of the tested deck slabs ranged from 1.74 to 3.52 times the factored load specified by CAN/CSA S6 (2006). The punching capacities of the tested slabs were significantly affected by the slab thickness and the concrete compressive strength. Finally, the ACI 440.1R (2006) punching strength equation greatly underestimated the capacity of the tested slabs with an average experimental-to-predicted punching capacity ratio of 3.17.

Zheng et al. (2012a&b) studied the structural behaviors of GFRP reinforced concrete slabs with lateral restraint stiffness. A series of experimental tests were carried out to investigate the influences of some structural variables on the response of one-third scaled concrete bridge-deck models, including supporting beam sizes, reinforcement percentages and reinforcing materials. The laterally restrained slabs, such as those in bridge-deck slabs, exhibit arching action or compressive membrane action (CMA) which has a beneficial influence on the service behavior such as the deflection, cracks widths, and ultimate capacity. Without consideration of CMA, the current design standard cannot predict ultimate strengths and deflections of the laterally restrained concrete slabs

accurately. Because of the existing of CMA, the reinforcement percentages could not influence ultimate strengths in GFRP reinforced concrete bridge-deck slabs significantly. However, the increasing of lateral restraint stiffness and concrete compressive strength could enhance the loading capacities obviously. GFRP reinforcement in laterally restrained slabs can produce both economical and durable concrete designs.

Zheng et al. (2013) presented a numerical study of the structural behavior of concrete bridge-deck slabs under static and dynamic traffic loads and an investigation of compressive membrane action (CMA) inside slabs. The deck slabs were reinforced with GFRP bars. Non-linear finite element analysis (NLFEA) models were established. Experimental data from one-span bridge structures by the author and other researchers are used to validate and calibrate the proposed FEM models. In the simulation of behavior of GFPR reinforced concrete bridge-deck slabs under traffic loads, a field test using calibrated truckloads of Cooshire-Eaton Bridge in Canada was used to validate the accuracy of proposed numerical models in dynamic analysis. NLFEA results indicate that the compressive membrane action has a sufficient effect on ultimate behavior and serviceability of GFRP reinforced concrete bridge-deck slabs with low reinforcement percentages. However, current design standards of FRP reinforced concrete structures, such as ACI 440-1R (2006), underestimate the behavior of the bridge-deck slabs under the ultimate and serviced load level. In addition, the punching failure was the common failure mode and the punching effect became stronger with the increasing compressive membrane action. During the entire moving truck loading procedure in NLFEA, the maximum stress of concrete slabs was less than 5% of ultimate strengths of concrete material and the maximum tensile stress of GFRP bars was less than 1% of ultimate stress. The largest deflection of deck slabs was smaller than the limit value (span/800).

Ahmed et al. (2014a) presented the construction details and the live-load field testing of the hybrid-reinforced Sainte Catherine overpass located on Highway 410 (Sherbrooke, Quebec). These hybrid-reinforced slab-on-girder bridges are simply supported over a single span of 43.4 m. The concrete deck slabs of 200 mm thick are continuous over four spans of 2.65 m each, with an average overhang of about 1.0 m on both sides. The deck slabs were reinforced with GFRP reinforcing bars in the top mat and with galvanized steel bars in the bottom mat. The bridge was tested for service performance with three calibrated truck loads prior to placement of the asphalt layer to check for flexural cracks. It was concluded that the field tests yielded very small strains in the GFRP

reinforcing bars, which clarified the arch-action effect in the restrained hybrid-RC bridge-decks and the maximum tensile strain in the top transverse GFRP bars was less than 1% of the ultimate tensile strain of the GFRP bars. Nevertheless, it is lower than the strains expected by the flexural design method. This result suggests that the CHBDC flexural design method overestimates the calculated design moments. The very small measured strains in the GFRP reinforcing bars indicate the presence of arching action between the girders in the restrained hybrid-reinforced-concrete bridge-decks. In the unlikely occurrence of field failure, the mode would be punching shear. Moreover, when hybrid-reinforced-concrete bridge-decks meet the CHBDC requirements concerning the empirical design method, they could be designed accordingly, which could save significant amounts of transverse reinforcement. Finally, the tests confirmed that the behavior of hybrid-reinforced-concrete bridge-decks is similar to that totally reinforced with FRP or steel bars. This hybrid concept may be a viable solution for concrete bridge-decks with extended service life.

Zheng et al. (2014) experimentally and theoretically studied the punching strength and failure mode of concrete deck slabs reinforced with GFRP bars, including arching action contribution to punching failure. The experimental study included static tests on a series of one-third scale deck specimens. The structural behavior, including punching capacity, failure mode, strain and deflection were discussed and used to investigate the influence of arching action. The test results revealed that increasing the lateral restraint stiffness resulted in higher punching strengths and lower GFRP reinforcement strain. This is due to the enhancement of aching action. In addition, the failure mode of deck slabs was varied from flexural punching failure to shear punching failure by the higher contribution of arching action. The flexural behavior was dominant in the test specimens with low reinforcement percentage and small external restraint stiffness.

Ahmed and Benmokrane (2014) investigated the effect of using GFRP reinforcing bars of different grades on the required reinforcement amount for concrete bridge-deck slabs and cantilever overhangs designed according to the CHBDC (CAN/CSA S6S1 2010) using the empirical and the flexural design methods for the interior deck slabs and the flexural design method for the cantilever overhangs. The author concluded that in the empirical method, increasing the slab thickness increased the required reinforcement in all directions, while increasing the elastic modulus of FRP bars decreased the bottom transverse reinforcement. The design of deck slabs using the flexural method was governed in most cases by the crack width limit. Thus, increasing the elastic modulus

of the GFRP reinforcement decreased the required GFRP reinforcement amount. In addition, it was recommended to use small diameter bars at closer spacing, rather than big diameter bars at larger spacing, assuming the properties of the bars are the same, to control the crack width.

Mara et al. (2014) examined the cost efficiency and sustainability of FRP solutions in relation to other conventional bridge concepts. An existing composite (steel–concrete) bridge with a concrete deck that had deteriorated was selected for this purpose. Two scenarios are studied and analyzed; the total replacement of the entire bridge superstructure and the replacement of the concrete deck with a new deck made of GFRP. The analyses prove that FRP decks contribute to potential cost savings over the life cycle of bridges and a reduced environmental impact.

2.4.3 Design Approaches of Concrete Bridge-Deck Slabs in Accordance to CHBDC

The Canadian Highway Bridge Design Code (CHBDC) (CAN/CSA S6 2014) specifies two different design theories for the design of concrete bridge-deck slabs reinforced with steel and FRP reinforcing bars (Section 8 and Section 16). The following is a description of those design methods:

2.4.3.1 The Empirical Design Method

The empirical design method applies to concrete deck slabs of nearly uniform thickness and supported on girders, stringers, or floor beams. When proportioned in accordance with the empirical design method of Clause 8.18.4, these deck slabs need not be analyzed, except for negative transverse moments due to loads on the deck slab overhang and the barrier walls, and for longitudinal moments in continuous-span bridges. The following general conditions should be satisfied in the concrete deck slab, as specified in Clause 8.18.4.1 in the CAN/CSA S6 (2014):

a. The deck slab is composite with the supporting beams, which are parallel to each other, and the lines of supports for the beams are also parallel to each other.
b. The ratio of the spacing of the supporting beams (S_e) to the thickness of the slab is less or equal to 18.0. The spacing of the supporting beams used in calculating this ratio is taken parallel to the direction of the transverse reinforcement.
c. The spacing of the supporting beams does not exceed 4.0 m and the slab extends sufficiently beyond the external beams to provide full development length for the bottom transverse reinforcement.

d. When the supporting beams or their lines of supports are not parallel to themselves, engineering judgment shall be used to determine whether the empirical design method for the design of the deck slab is to be adopted.

In case of full-depth cast-in-place deck slab, and for empirical design method application, the deck slabs should be satisfied the previous condition specified by Clause 8.18.4.1 in addition to the following conditions specified by Clause 8.18.4.2:

a. As shown in **Figure 2–12**, the deck slab contains two orthogonal assemblies of reinforcement, near the top and bottom of the slab, respectively, with ρ in each direction in each assembly being at least 0.003, except as specified in Item (c).
b. When the slab is supported on parallel beams, the reinforcement bars closest to the top and bottom of the slab are laid perpendicular to the axes of the supporting beams or are laid on a skew parallel to the lines of beam supports.
c. The reinforcement ratio, ρ, may be reduced to 0.002 where deck slabs with the reduced reinforcement can be satisfactorily constructed and the reduction of ρ below 0.003 is approved.
d. Where the transverse reinforcing bars are placed on a skew, the reinforcement ratio for these bars is not less than $\rho/cos2\theta$, where θ is the skew angle.
e. Where the unsupported length of the edge-stiffening beam, S_e, exceeds 5.0 m, the reinforcement ratio, ρ, in the exterior regions of the deck slab is increased to 0.006, as shown in **Figure 2–13**.
f. The spacing of the reinforcement in each direction and in each assembly does not exceed 300 mm.

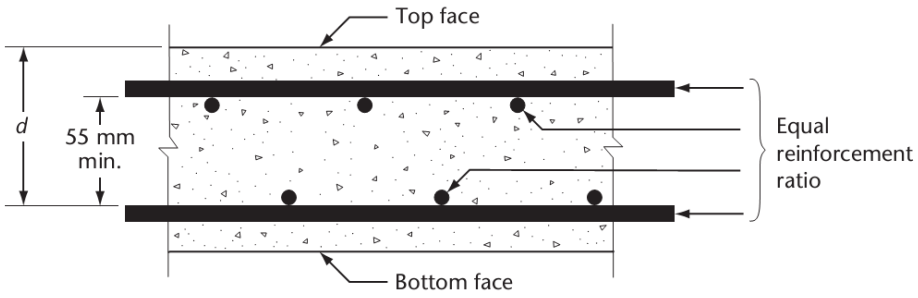

Figure 2–12: Reinforcement details of cast-in-place deck slab (Clause 8.18.4.2)

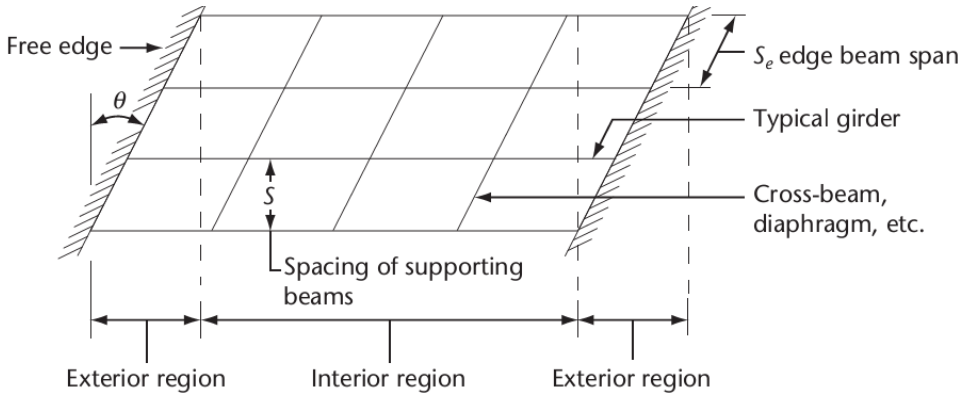

Figure 2–13: Reinforcement details of cast-in-place deck slab (Clause 8.18.4.2)

In addition, for the empirical design method to apply, a full-depth cast-in-place deck slab should satisfy the conditions specified by Clause 8.18.4.2 (for steel reinforcement) and Clause 16.8.8.1 (for FRP reinforcement) in addition to those of Clause 8.18.4.1. Clause 16.8.8.1 "Design by empirical method" mandates the following:

a. The deck slab shall contain two orthogonal assemblies of FRP bars, with the clear distance between the top and bottom transverse bars being at least 55 mm and the slab thickness not less than 175 mm.
b. For the transverse FRP bars in the bottom assembly, the minimum area of cross-section in mm^2/mm shall be $500d_s/E_{FRP}$.
c. The longitudinal bars in the bottom assembly and the transverse and longitudinal bars in the top assembly shall be of GFRP with a minimum of 0.0035.

2.4.3.2 Flexural Design Method

In the flexural design method, concrete deck slabs shall be analyzed for positive and negative bending moments resulting from loads applied on the slabs. The analysis shall consider the bending moments induced in the longitudinal direction that agree with the assumptions used in the analysis of the transverse bending moments. The cantilever portions of concrete deck slabs shall be analyzed for transverse negative bending moments resulting from loads on the cantilever portions of the slabs or horizontal loads on barriers and railings. The cantilever portions of concrete deck slabs may be analyzed using Clause 5.7.1.6 while the deck slabs are analyzed using Clause 5.7.1.7. The design of sections, however, should be conducted according to Section 8 when steel bars are used and Section 16 when FRP reinforcing bars are used.

The longitudinal reinforcement provided by Clause 8.18.7 of the CAN/CSA S6 (2014), both top and bottom when the main reinforcement is perpendicular to traffic shall be $120/(S)^{0.5}$, up to a maximum of 67% of the transverse reinforcement. In addition, as mandated by Clause 16.8.8.2 the spacing of the reinforcement in each direction shall not exceed 300 mm and the diameter of the reinforcement shall not be less than 15 mm.

When the concrete deck slabs are designed according to the flexural design method for CL-625 truck, the design bending moments are determined based on a maximum wheel load of 87.5 kN. The design service load for the deck slabs is taken as $1.4 \times 0.9 \times 87.5 = 110.25$ kN, where 1.4 is the impact coefficient and 0.9 is the live-load combination factor, while the design factored load is taken as $1.4 \times 1.7 \times 87.5 = 208.25$ kN, where 1.7 is the live-load combination factor.

2.5 Concrete Beams Reinforced with FRP Bars

The flexural response of FRP reinforced concrete were reported by Benmokrane et al. (1996) and other investigators. They concluded that at low load level, the crack pattern and spacing in FRP-RC beams were similar to that reinforced with steel bars. As load increases, however, there are more and wider cracks with greater penetration depth in FRP-RC elements than in traditional steel-RC elements, for comparable reinforcement ratios. This behavior is expected, since FRP has a much lower modulus of elasticity compared with traditional steel reinforcement. The moment-curvature diagrams of lightly reinforced FRP beams are clearly bi-linear, with the bend point at the crack initiation moment level. Experimental strain distributions clearly demonstrated the perfect bond between FRP reinforcing bars and the surrounding concrete. In addition, GFRP reinforced concrete beams were analyzed by Vijay and GangaRao (2001), different modes of failure were compared. The compression controlled failure mode presented not only higher flexural strength, but also a more ductile failure than the tension controlled failure mode. This result was consistent with ACI 440.1R (2001) suggested design criteria.

Alsayed et al. (2000) concluded that the flexural capacity of the beams reinforced by GFRP beams can be accurately predicted using the ultimate design theory (when failure occurs due to crushing of concrete in the compression side) which is also applicable to design of concrete beams reinforced by steel bars (over reinforced sections). In addition to the assumptions used in steel reinforced beam design, the tensile behavior of the FRP reinforcement is linearly elastic until failure. There

is no yield point until failure of the FRP and hence it doesn't provide early warning of failure of the member. Therefore, if concrete member is under reinforced with FRP, the FRP reinforcement would rupture before crushing of concrete occurs and the failure of the member would be sudden and catastrophic. Bank (2006) stated that the crushing of the concrete can be regarded to be less brittle than the rupture of the FRP reinforcement bar. Therefore, concrete crushing failure is not catastrophic compared to the FRP rupture failure. In addition, Nanni (1993) stated that the concrete crushing failure mode is marginally more desirable for flexural members reinforced with FRP reinforcing bars. However, ACI 440.1R (2006) accepted both failure modes (FRP rupture and concrete crushing) for the design of flexural members reinforced with FRP bars if strength and serviceability criteria are satisfied. However, for both under reinforced and over reinforced cases, there is an early warning of failure due to extensive cracking and large deflections due to the significant elongation of FRP reinforcement before rupture.

Adhikari (2009) studied the applicability of using BFRP bars as internal reinforcement in concrete beams. The reinforcement bar diameters were 3.0, 5.0 and 7.0 mm with the volume fraction of 44%, 52% and 41%, respectively. A total of fifteen different beams of 8" width × 7" height × 84" total length (203.2 × 177.8 × 2133.6 mm) were constructed and reinforced with BFRP and steel bars. The beams were tested to failure in four-point bending over a clear span of 60" (1524 mm). It was observed that the ACI 440.1R (2006) can predict the moment strength of BFRP reinforced beams with reasonable accuracy. It was also found that the strain-compatibility method can provide a slightly better approximation of the moment strength than the ACI method depending on the reinforcement ratio of the different beams. From the load-deflection analysis, it was observed that the Branson's equation for the effective moment of inertia of the cracked section predicted larger stiffness for the BFRP reinforced sections. Therefore, leading to underestimation of the deflection values. Similarly, it was observed that the ACI 440.1R (2006) under predicted the stiffness of the BFRP reinforced beams, thus leading to the overestimation of the deflection values. It was also observed that the degree of overestimation of the deflection values was reduced with increasing reinforcement ratios. Hence, it can be concluded that reinforcement ratio should be also incorporated into the computation of the stiffness of the BFRP reinforced beams.

Ovitigala (2012) investigated the bond strength of BFRP bars based on the flexure-bond test method. The test was carried out on twenty hinged concrete beams, as shown in **Figure 2–14**,

using five different BFRP bar diameters (6, 10, 13, 16 and 25 mm) with different bonded lengths ($5d_b$, $10d_b$, and $15d_b$). It is worth mentioning that many researchers stated that this test procedure simulate the real flexural behavior, since the reinforcement bar is forced to pull out by applying the forces as same as flexural beams. The author concluded that the bond characteristics of BFRP bars are better than the GFRP bars and almost the same as steel reinforcement. Twenty times the bar diameter ($20d_b$) can be considered as the development length for BFRP reinforced flexure specimens, since all the BFRP bars failed by rupture without slippage. As well as the average bond stress increased when the bonded length decreased for the same diameter of BFRP bar specimens, and increased when the diameter of the BFRP bar decreased for the same development length.

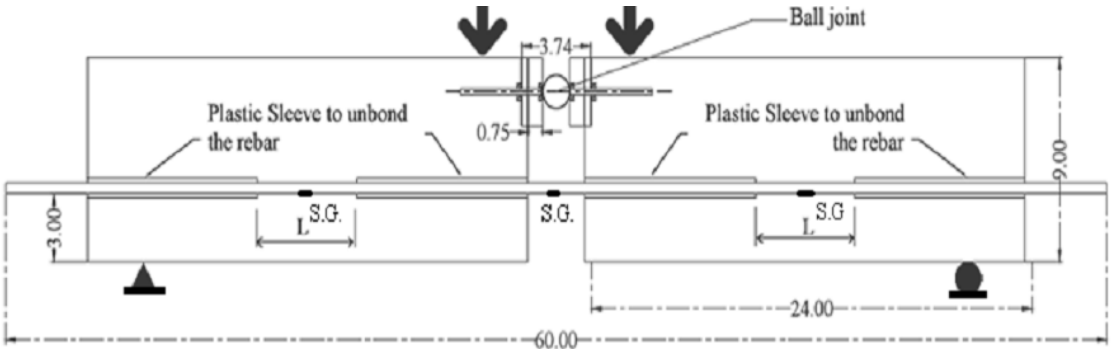

Figure 2–14: Flexural bond strength specimens (Dimension in inches)

Ovitigala (2012) investigated the flexure behavior of eight BFRP-RC beams of 8" width × 12" height × 144" total length (203.2 × 304.8 × 3657.6 mm). The beams were cast using normal-weight concrete. All beams were designed for over reinforced condition and tested in flexure over clear span of 120" (3048.0 mm), as recommended by the ACI 440.1R (2006) for deflection control (span-to-depth ration of 10). The beams failed by crushing of the concrete at the mid span on compression face, as expected for over reinforced condition. The following conclusions were drawn from the experimental study:

a. The ultimate flexural capacities of BFRP-RC beams predicted by ACI 440.1R (2006) were conservative due to the use of lower values in strength reduction factors. ACI 440.1R (2006) predicted nominal moment capacities were around 0.82 to 0.93 of the experimental moment capacity depending on the reinforcement area.

b. When the area BFRP reinforcement increased seven times (from 3 bars of 10 mm diameter to 3 bars of 25 mm diameter), the deflection was reduced by 63% and moment capacity was increased by 90%.
c. Serviceability criteria (deflection limits) can be achieved by increasing the area of BFRP reinforcement. However, the ultimate failure would be brittle in nature without prior warning due to lower deflection when the area of BFRP reinforcement increased. Therefore, establishing the maximum FRP reinforcement area would be much more important. The maximum FRP reinforcement area limit was proposed by limiting the strain in the BFRP bars to be greater than or equal to 5000 με.
d. Bischoff (2007) rational model and the ACI 440.1R (2006) model were found to be the most reliable models for predicting effective moment of inertia. Bischoff's (2007) model predicts the deflection at 40% and 60% of the ultimate load more accurately than ACI 440.1R (2006) model. However, both models provided better results at ultimate because I_e in ACI 440.1R (2006) was taken as I_{cr} and Bischoff's (2007) model also consider I_e at ultimate as I_{cr}.

El-Nemr et al. (2013) investigated the flexural behavior and serviceability performance of twelve full-scale GFRP-RC beams and two steel-RC beams fabricated with normal- and high- strength concrete (NSCs and HSCs). The beam specimens measured 4250 mm long × 200 mm wide × 400 mm deep. The beams were tested to failure in four-point bending over a clear span of 3750 mm. Three GFRP products with moduli of elasticity ranging from 48.7 to 69.0 GPa with sand-coated and helically grooved surface textures were employed. The following conclusions have been drawn:

a. All the GFRP-RC beams showed typical bi-linear behavior until failure. Both NSC and HSC evidenced reduced stiffness after cracking. The NSC and HSC beams showed similar behavior until failure.
b. FRP-RC beams showed very sharp increases in reinforcement strains at cracking due to poor energy absorption at cracking.
c. Increasing the reinforcement ratio and concrete strength resulted in a larger number of cracks and smaller crack widths. Beams reinforced with sand-coated GFRP bars produced larger numbers of cracks and smaller crack widths than those reinforced with helically-grooved

GFRP bars. In addition, the crack width is proportional to the bar diameter for both of the NSC and HSC beams reinforced with GFRP bars.

d. ACI 440.1R (2006) and ACI 440-H yielded un-conservative deflection values at the $0.3M_n$ and $0.67M_n$ (Where M_n is the nominal moment). At $0.3M_n$ the experimental-to-predicted deflection ($\delta_{exp}/\delta_{pred}$) of ACI 440.1R (2006) and ACI 440-H were 1.17±0.38 and 1.13±0.22, respectively.
e. Both CAN/CSA S806 (2012) and ISIS (2007) yielded conservative deflection predictions. At $0.3M_n$, the experimental-to-predicted deflection of CAN/CSA S806 (2012) and ISIS (2007) were 0.76±0.12 and 0.80±0.11, respectively.
f. The bond coefficient (k_b) value of 1.4 provided by ACI 440.1R (2015) is very conservative for both of sand-coated and helically-grooved GFRP bars in NSC and HSC. While a k_b of 0.8 provided by CAN/CSA S6 (2014) yielded very un-conservative predictions, on average, for sand-coated and helically-grooved GFRP bars in NSC and HSC.

Rizkalla (2013) studied the flexural behavior of concrete members reinforced with BFRP reinforcing bars. A total of six one-way concrete slabs of 3658 mm length × 610 mm wide × 152 mm deep reinforced with varying BFRP reinforcement ratios and tested in four-point bending configuration to failure. Load, deflection and strain data were recorded during testing and compared to the predicted values recommended by the design guidelines of ACI 440.1R (2006). Test results indicated that the measured loads at failure compared well with nominal flexural capacities predicted using ACI 440.1R (2006) equations and detailed layered-sectional analyses. The measured short-term deflections at service load level were higher than the values predicted by ACI 440.1R (2006). Mid-span deflections at service load level were also predicted using a numerical method of integrating curvature along the span length and compared well with the measure values. Test results indicate that the ACI 440.1R (2006) equations can be used safely to predict the nominal moment capacity of concrete flexural members reinforced with BFRP bars. However, it was found that the ACI 440.1R (2006) method underestimated the deflection at service load level by 20% to 60%.

Urbański et al. (2013); Lapko and Urbański (2015) investigated the flexure performance of simply supported concrete beams measured 80 mm wide × 120 mm width × 1200 mm length and reinforced with BFRP bars. A comparative analysis of experimental and theoretical results was

presented. The tested beams have been made of concrete class C30/37 and reinforced with BFRP bars of 8 mm diameter and 39.05 GPa tensile modulus of elasticity. The authors concluded that:

a. The BFRP-RC beams revealed a linear relationship between loading forces and concrete and reinforcing bar strains as well as deflections. The failure of BFRP-RC beams did not occur suddenly due to transformation of the beam into a tie system because of flexural basalt reinforcement remained unbroken. The carrying capacity of tested BFRP-RC beams was much greater than the of steel-RC beams.
b. Deflections and crack width of BFRP-RC beams were significantly higher (average of 3 to 4 times and 3 times, respectively) than the reference beam, due to the much lower modulus of BFRP bars compared to steel bars. Therefore, both of the deflection and crack widths can be a major factor in the designing the BFRP-RC beams.
c. For beams with flexural reinforcement ratio greater than the balanced reinforcement ratio, values of deflections calculated from the modified Branson equation (ACI 440.1R 2006) are lower compared to the experimental values in the initial phase of the load (after three cycles of loading–unloading). For the load ranged from 20 to 30% of critical load, the differences were estimated in the range of 26–87%.
d. The values of deflections obtained on the basis CAN/CSA S806 (2002) are characterized by a better convergence with the experimental values in the initial level of load (the differences between theoretical and experimental deflections were between 9% and 47%).
e. The basalt rebars having full resistance against corrosion may be good alternative for the reinforcement of concrete structures, like RC bridge girders subjected to environmental attack.

Tomlinson et al. (2015) evaluated the flexural and shear performances of concrete beams reinforced with BFRP bars and stirrups. Nine concrete beams of 150 mm wide × 300 mm height × 3100 mm total length were tested in four-point bending over clear span of 2900 mm and shear span of 1100 mm to examine the effect of BFRP flexural reinforcement ratios and stirrups on the structural performance. The beams were reinforced by either BFRP or steel stirrups, and some had no shear reinforcement. The following conclusions were reached:

a. The ultimate and service loads increased with increasing of flexural reinforcement ratio for all shear reinforcement types, while the service load levels were not affected by stirrup type. On

the other hand, load-deflection responses within the service load range were not noticeably affected by shear reinforcement type.

b. Beams without stirrups and those with BFRP stirrups failed in shear, with the former reaching 55–58% of ultimate flexural capacity and the latter failing by stirrup rupture at 90–96% of flexural capacity. Beams with steel stirrups failed in flexure. The ultimate shear capacities increased as the BFRP flexural reinforcement ratio increased.

c. The beams with BFRP flexural reinforcement and BFRP or steel stirrups had significantly higher strengths (2.6–2.9 times) than control steel-reinforced counterparts having the same reinforcement ratio ρ. The strength increase in tension-controlled BFRP beams was similar to the ratio of the BFRP to steel ultimate strengths. In compression-controlled sections, the ratio was lower as the FRP did not reach its ultimate strength. The steel-reinforced beams consistently had a flexural tension failure.

2.6 Deformability and Minimum Reinforcement

Deformability (ductility) is important to ensure large deformations and providing warning of impending failure and is obviously important in seismic where the ability to absorb energy is of prime importance. Deformability can be defined as the capacity of the structure element to absorb energy without suffering failure, and is generally related to the amount of inelastic deformation that takes place before a complete failure. In other words, it could be represented as the ability to sustain inelastic deformations without loss of its load-carrying capacity prior to failure. In steel reinforced structures, the deformability is defined as the ratio of post yield deformation to yield deformation which it usually comes from steel. Due to the linear stress-strain relationship of FRP bars, the traditional definition of deformability cannot be applied to structures reinforced with FRP reinforcement (Kassem et al. 2011). Several methods, such as the energy-based method and the deformation-based method have been proposed to calculate the deformability factor for FRP reinforced structures, but the later used by the CHBDC (CAN/CSA S6 2014) is most common (Jaegar et al. 1995; Thériault and Benmokrane 1998; Kassem et al. 2011). The CHBDC (CAN/CSA S6 2014) (Clause 16.8.2.1) stated that the deformability performance factor, J, shall be at least 4.0 for rectangular sections and 6.0 for T-sections (Clause 16.8.2.1). The deformability performance factor calculated as follows:

$$j = \frac{\psi_u M_u}{\psi_c M_c} \tag{2-2}$$

where M is the bending moment and ψ is the curvature. The subscripts u and s refer to ultimate limit state and service limit state, which is assumed, corresponds to a concrete strain equal to 0.001, respectively. The strain of 0.001 is considered the beginning of inelastic deformation of concrete (Thériault and Benmokrane 1998).

Wang and Belarbi (2005) argued that there are two approaches to increase the deformability of beams reinforced with FRP bars. The first approach is by using hybrid FRP bars, which were found in previous studies that their deformability index are close to that of beams reinforced with steel, but this approach is limited in application due to its complicity and high cost of manufacturing. The other approach is to improve the property of concrete with use of over reinforcement so that failure is in concrete crush rather than by bar rupture.

According to Section 16 in the CHBDC (CAN/CSA S6 2014), the design of flexural members reinforced with FRP bars should consider the following:

a. The factored resistance, M_r, shall be at least 50% greater than the cracking moment, M_{cr}. This requirement may be waived if the factored resistance, M_r, is at least 50% greater than the factored moment, M_f. If the ultimate limit state (ULS) design of the section is governed by FRP rupture (under reinforced section), M_r shall be greater than 1.5 M_f (Clause 16.8.2.2).
b. When the maximum tensile strain in FRP reinforcement under full service loads exceeds 1500 με, the crack width has to not exceed 0.5 mm for members subjected to aggressive environments and 0.7 mm for other members (Clause 16.8.2.3). The crack width calculated as follows:

$$W_{cr} = 2\frac{f_{FRP}}{E_{FRP}}\frac{h_2}{h_1}k_b\sqrt{d_c^2 + \left(s/2\right)^2} \tag{2-3}$$

The value of k_b shall be determined experimentally, but in the absence of test data may be taken as 0.8 for sand-coated and 1.0 for ribbed FRP bars. In calculating d_c, the clear cover shall not be taken greater than 50 mm.

c. The maximum stress in FRP bars under loads at service limit state (SLS) shall not be more than $F_{SLS} f_{FRPu}$, where F_{SLS} is 0.35 for AFRP bars, 0.25 for GFRP bars, and 0.65 for CFRP bars. (Clause 16.8.3).

2.7 Summary

Many studies of FRP composites have focused on the carbon, aramid and glass FRP composites. Recently, BFRP bars have emerged as a promising alternative to conventional glass fiber-reinforced polymer (GFRP) materials. However, North American codes do not recognize the BFRP bars as reinforcing materials for concrete structures. Only a limited number of studies have been conducted to date on BFRP bars do not provide confidence to potential users of the material. As a result, there is lack of knowledge on the performance of the bars in concrete. Therefore, investigations are needed to characterize and understand the durability and structural performance of different products of BFRP bars in concrete members.

This research aims at evaluating the feasibility of manufacturing a new generation of BFRP bars with different mechanical properties and surface configuration, as well as evaluating the use of these bars as internal reinforcement for structural concrete elements, with an emphasis on concrete beams and concrete bridge-deck slabs. The experimental studies presented herein will contribute to advancing the state-of-the-art and extend the current data which will lead to introducing such new fibers to the current FRP codes and guidelines.

CHAPTER 3
EXPERIMENTAL PROGRAM

3.1 Introduction

This chapter describes in detail the experimental program conducted at the structural laboratory of University of Sherbrooke to develop a better understanding of basalt fiber-reinforced polymer (BFRP) bars. The experimental program consists of three parts, designed to evaluate the short-and long-term characteristics and structural performance of newly developed BFRP bars. Part I concerned with physical and mechanical properties as well as the durability performance of BFRP bars and tendons under harsh environmental conditions (alkaline solution at high temperature). Part II concerned with the structural performance evaluation of restrained bridge-deck slabs reinforced with steel and BFRP bars with different reinforcement ratios under truck wheel load. Part III concerned with the flexural behavior and serviceability performance evaluation of concrete beams reinforced with different types and ratios of BFRP bars. **Table 3–1 s**ummarizes the methodology to achieve the aforementioned objectives. The specific test procedure, specimen details and materials used to carry out this research are presented in this chapter.

Table 3–1: Summary of the objectives and methodology

Part	Objectives	Methodology
I	Evaluate the short and long-term characteristics of newly developed BFRP bars and tendons.	Testing of three different products of newly developed BFRP bars and tendons to evaluate the physical and mechanical properties (Phase I and Phase II, respectively) as well as to assess the durability and long-term performance of BFRP bars and tendons under the effect of harsh environmental conditions using accelerated aging technique (alkaline solution at high temperature) (Phase III).
II	Investigate the performance of concrete bridge-deck slabs reinforced with BFRP bars at service and factored load levels under wheel loads.	Testing of seven full-scale concrete deck slabs measuring 3000 mm long × 2500 mm wide × 200 mm thick and reinforced with steel and BFRP bars of different reinforcement ratios and bar diameters. The slabs were tested under concentrated load simulating the footprint of a sustained truck wheel load (87.5 kN-CL-625 truck), as specified by CHBDC (CAN/CSA S6S1 2010).
III	Investigate the flexural behavior and serviceability performance of concrete beams reinforced with BFRP bars under static loads.	Testing of fourteen concrete beams measuring 200 mm wide × 300 mm height × 3100 mm long reinforced with steel and BFRP bars of different reinforcement ratios, surface configurations and bar diameters under four-point load.

3.2 Part I: Short and Long-Term Characterization of BFRP Bars

The first part of the current study involved three different products of newly developed BFRP bars and tendons: types A, B, and C. This part was divided into three phases. Phase I focused on physical characterization of the BFRP bars. The physical properties determined in this phase served as references for physical properties after conditioning. Phase II focused on mechanical characterization of the BFRP bars. The tensile strength, tensile modulus of elasticity, ultimate

tensile strain, transverse–shear strength, flexural strength, flexural modulus of elasticity, interlaminar-shear strength, and bond strength were determined according to the appropriate test methods. The test results also served as references for calculating the residual strengths after conditioning. Phase III assessed the durability and long-term performance of the conditioned BFRP bars. The durability was assessed by immersing the BFRP specimens in an alkaline solution at high temperature (60 °C) for different lengths of time (3000 hours for Type A and 2160 hours for Types B and C) designed to simulate a concrete environment so as to validate the performance of the BFRP bars as internal reinforcement for concrete elements. Changes in the physical and mechanical characteristics were assessed by comparing the characteristics of the conditioned BFRP bars to the reference ones from Phases I and II.

Furthermore, a pilot investigation was also conducted to evaluate the effects of chemicals on the basalt fibers used in manufacturing the BFRP bars tested herein. The tests were conducted according to Owens Corning (2011) guide for glass fibers.

3.2.1 Material Properties and Tested Specimens

Three types of BFRP bars were used in this part. Type A has a 7 mm diameter with a woven surface (manufactured for prestresing purpose), while Types B and C have a 8 mm diameter with a deformed surface with helical ribs. The BFRP bars were made of continuous basalt fibers impregnated in vinylester resin according to the pultrusion process. They were provided by the manufacturer with an expected tensile modulus close to 50 and 60 GPa, simulating grade II and III GFRP bars [CAN/CSA S807 (2010)]. **Table 3–2** describes the BFRP bars used in this part of the study, and **Figure 3–1** shows their surface configurations. The basalt fibers used herein were known ASA.TEC (produced by Asamer Basaltic Fibers GmbH, Austria). The fibers were produced from volcanic material with organic surface coating and had a diameter of 10-19 μm.

Table 3–2: Details of tested BFRP bars

Type	d_b (mm)	A_f [a] (mm²)	Surface Configuration
A	7.0	38.46	Woven Surface
B and C	8.0	50.24	Ribbed Surface

[a] Nominal cross section area.

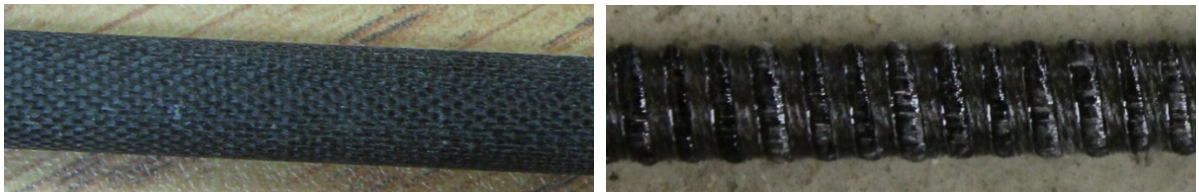

Type A Types B and C

Figure 3–1: Tested BFRP bars

3.2.2 Test Procedures

3.2.2.1 Phase I: Physical Characterization

The physical properties of the reference (unconditioned) BFRP bars were conducted in accordance with ACI 440.6M (2008) and CAN/CSA S807 (2010) and the relevant ASTM standards. The relative density was determined according to ASTM D792 (2008), fiber content according to ASTM D3171 (2011), transverse coefficient of thermal expansion according to ASTM E831 (2012), water absorption according to ASTM D570 (2010), cure ratio according to ASTM D5028 (2009), and glass-transition temperature (T_g) according to ASTM D3418 (2012). In addition, microstructural analysis was performed for all three types of BFRP specimens using scanning electron microscopy (SEM) for both unconditioned (reference) and conditioned specimens to assess changes and/or degradation. Since BFRP bars are not included in any FRP standard yet, the physical properties of the investigated BFRP bars and tendons were compared to the specified limits for FRP bars.

The moisture uptake at saturation was determined for the BFRP bars. The test was carried out in accordance with ASTM D570 (2010). Five 100 mm long specimens of each type of BFRP were cut, dried, and weighed. They were then immersed in water at 50 °C for 3 weeks. The samples were periodically removed from the water, surface dried, and weighed. The water content as a percentage of weight was calculated by Eq. (3-1).

$$W = \frac{(P_s - P_d)}{P_d} \times 100 \qquad (3\text{-}1)$$

Where P_s and P_d are the bar weights in the saturated and dried states, respectively. The percentage of moisture uptake was calculated. The gain in mass was corrected to account for specimen mass loss due to a possible dissolution phenomenon. This correction was achieved by completely drying

the immersed specimens in an oven at 100 °C for 24 h and comparing their masses to their initial masses.

Differential scanning calorimetry (DSC) is used to obtain information about the thermal behavior and characteristics of polymer materials and composites, such as the glass-transition temperature (T_g) and curing process. In this study, 30 to 50 mg specimens from both the unconditioned and conditioned specimens were sealed in aluminum pans and heated in a TA Instruments DSC Q10 calorimeter to 200 °C at a rate of 20 °C/min. The glass-transition temperature (T_g) was determined in accordance with ASTM D3418 (2012).

3.2.2.2 Phase II: Mechanical Characterization

The mechanical characterization included testing of representative BFRP specimens to determine their tensile strength in accordance with ASTM D7205 (2011), transverse-shear testing a in accordance with ASTM D7617 (2011), flexural properties in accordance with ASTM D4476 (2009), interlaminate shear strength (short-beam shear test) in accordance with ASTM D4475 (2008), and bond strength using the pullout test in accordance with ACI 440.3R (2012), B.3 Test Method and CAN/CSA S806 (2012), Annex G. The mechanical properties reported herein were calculated using the nominal cross-sectional areas.

Tensile Properties of the Reference BFRP Bars

The tensile properties of the investigated BFRP bars were determined by testing five representative specimens for each type in accordance with ASTM D7205 (2011). The specimens were cut to the desired lengths and prepared by installing the steel tube (anchors) with expansive cement grout commercially known as Bustar Expansive grout. The specimens were instrumented with a 200 mm LVDT to capture specimen elongation during testing. The tests were conducted with a Baldwin testing machine in which the applied load and specimen elongation were electronically recorded during the test. **Figure 3–2** shows the test setup. The tensile strength and tensile modulus of the BFRP bars were determined with Eqns. (3-2) and (3-3), respectively,

$$f_u = \frac{F_u}{A} \tag{3-2}$$

where f_u is the tensile strength (MPa), F_u is the tensile capacity (N), and A is the nominal cross-sectional area of the BFRP bar (mm^2).

$$E = \frac{F_1 - F_2}{(\varepsilon_1 - \varepsilon_2)A} \tag{3-3}$$

where E is the tensile modulus of elasticity (MPa); A is the nominal cross-sectional area (mm^2); F_1 and ε_1 are the load and corresponding strain, respectively, at approximately 50% of the ultimate tensile capacity; and F_2 and ε_2 are the load and corresponding strain, respectively, at approximately 25% of the ultimate tensile capacity.

It should be mentioned that the design of FRP-reinforced members is based on guaranteed tensile strength (the mean tensile strength minus three times the standard deviation in according to ACI 440.1R (2006)). While the design tensile modulus of elasticity for FRP reinforcement, E, shall be the same as the mean tensile modulus.

Figure 3–2: Typical test setup for tensile tests

Transverse-Shear Strength of the Reference BFRP Bars

Transverse-shear tests were conducted according to ASTM D7617 (2011). The setup consisted of a 230 × 100 × 110 mm steel base equipped with lower blades spaced at 50 mm face to face, allowing for the double transverse-shear failure of the specimen caused by an upper blade, as shown in **Figure 3–3**.

For each type of BFRP bar, five unconditioned specimens of 200 mm length were tested under laboratory conditions with an MTS 810 testing machine equipped with a 500 kN load cell. A displacement-controlled rate of 1.3 mm/min was used during the test, which yielded between 30 and 60 MPa/min until specimen failure. The loading was performed without subjecting the test specimens to any shock. The transverse-shear strength was calculated with Eq. (3-4):

$$\tau_u = \frac{P_s}{2A} \tag{3-4}$$

where τ_u is the transverse-shear strength (MPa), P_s is the failure load (N), and A is the nominal cross-sectional area of the BFRP bar (mm²).

Figure 3–3: Typical test setup for transverse-shear tests

Interlaminar-Shear Strength of the Reference BFRP Bars (Short-Beam Shear Test)

The short-beam shear test was conducted on five specimens of each type of BFRP bar according to ASTM D4475 (2008) in order to calculate the interlaminar-shear strength, which is governed by the fiber–matrix interface. The tests were carried out with a 500-kN MTS 810 testing machine. The distance between the shear planes was set to 6 times the nominal diameter of the FRP bars. **Figure 3–4** shows the test setup. A displacement-controlled rate of 1.3 mm/min was used during the test. The applied load was recorded with a computer-monitored data-acquisition system. The interlaminar-shear strength, S_u, of the FRP bars was calculated with Eq. (3-5).

$$S_u = 0.849\frac{P}{d^2} \tag{3-5}$$

where S_u is the interlaminar-shear strength (MPa), P is the shear failure load (N), and d is the bar diameter (mm).

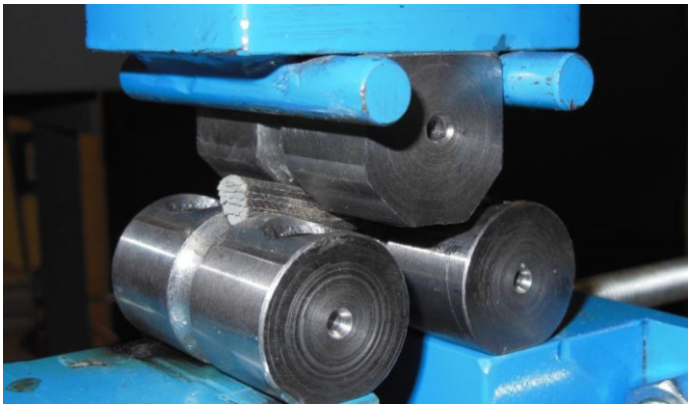

Figure 3–4: Typical test setup for short-beam test

Flexural Properties of the Reference BFRP Bars (Three-Point Flexural Test)

The flexure test was conducted on five specimens of each type of BFRP bars of 180 mm long according to ASTM D4476 (2009), as shown in **Figure 3–5**. The specimens were tested under laboratory conditions on an MTS 810 testing machine equipped with a 500 kN load cell. The specimens were tested over a simply supported span equal to 20 times the bar diameter. The specimens were loaded at the mid-span with a circular nose and ends rested on two circular supports that allowed the specimens to bend. A displacement-controlled rate of 3.0 mm/min was used during the test. The rate of loading occurred without subjecting the test specimen to any shock. The applied load and deflection were recorded during the test on a computer- monitored data-acquisition system.

The flexural strength of tested FRP specimens was calculated with Eq. (3-6). Flexural modulus of elasticity is the ratio, within elastic limit, of stress to corresponding strain. It was calculated with Eq. (3-7):

$$f_u = \frac{PLC}{4I} \tag{3-6}$$

$$E = \frac{PL^3}{48IY} \tag{3-7}$$

where f_u is the flexural strength in the outer fibers at mid-span (N/mm^2), P is the failure load (N), L is the clear span (mm), I is the moment of inertia (mm^4), C is the distance from the centroid to the extremities (mm), E is the flexural modulus of elasticity in bending (N/mm^2), and Y is the mid-span deflection at load P (mm).

The maximum outer-fiber strain (ε_u) was calculated from Eq. (3-8).

$$\varepsilon_u = \frac{f_u}{E} \tag{3-8}$$

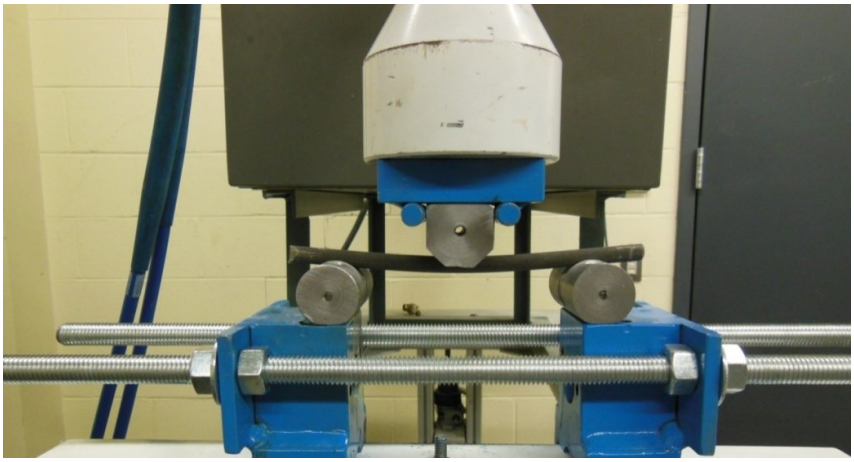

Figure 3–5: Typical test setup of flexure test

Bond Strength of the Reference BFRP Bars (Pullout Test)

The bond strength of the BFRP bars was assessed with the pullout test. The pullout tests were carried out in normal-strength concrete with a designated strength of 35 MPa after 28 days according to the ACI 440.3R (2012), B.3 Test Method and CAN/CSA S806 (2012), Annex G. The bonded length was kept constant at $5d_b$, where d_b is the nominal diameter of FRP bars. The pullout blocks measured 200 × 200 × 200 mm. **Figure 3–6** shows the geometry of the pullout specimens and test setup.

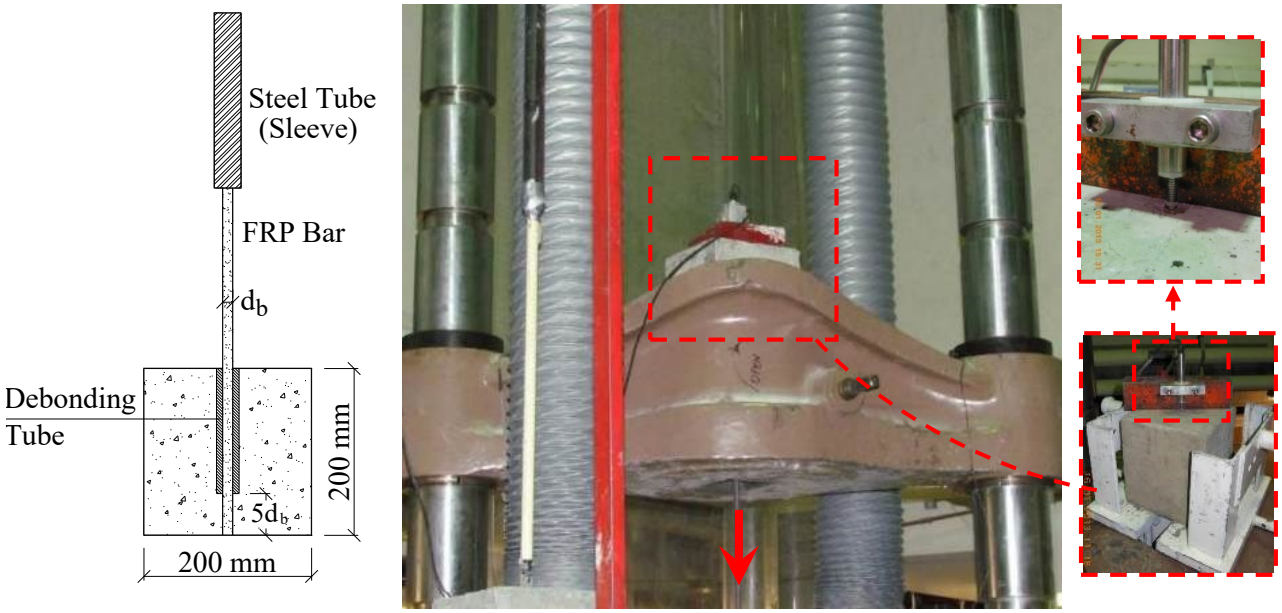

(a) (b)

Figure 3–6: Pullout test: (a) Specimen geometry; (b) Test setup

3.2.2.3 Phase III: Durability Study and Long-Term Performance Assessment

This phase was conducted to assess the durability and long-term performance of the BFRP bars conditioned in an alkaline solution simulating concrete pore solution. Accelerated aging tests were conducted in accordance with ASTM D7705 (2012). The conditioning of the BFRP bars included a combined exposure to an alkaline environment and elevated temperature. Immersion in an aqueous media (alkaline solution) at high temperature accelerates degradation. The alkaline solution was prepared to have a composition representative of the pore water inside Portland-cement concrete, specifically, 118.5 g of $Ca(OH)_2$, 0.9 g of NaOH, and 4.2 g of KOH per liter of deionized water. The solution had a pH of 12.6-13.0, which is representative of a mature concrete pore solution. The three types of BFRP bars were immersed in this solution at 60 °C. The BFRP specimens were conditioned for different lengths of time (1000 and 3000 h for BFRP Type A; 720 and 2160 h for BFRP Types B and C). The conditioning time started once the solution had reached the prescribed temperature.

The BFRP specimens were placed in hermetically sealed stainless-steel containers to prevent excessive evaporation and reaction of atmospheric CO_2 with calcium hydroxide. The containers were placed in an environmental chamber adjusted to the prescribed temperature (60 °C) under isothermal conditions. The FRP bars were weighed and their diameters measured throughout the

conditioning period to monitor water absorption and eventually characterize the mass and diameter changes. Specimens of each type of BFRP bar were removed from the solution and tested to determine their physical and mechanical properties after the exposure periods at 60 °C. Similar to as in Phase I, the effects of conditioning on the glass-transition temperatures (T_g) and chemical composition were also assessed with differential scanning calorimetry (DSC) and Fourier transform infrared spectroscopy (FTIR), respectively. The microstructure of all types of the BFRP bars was investigated with scanning electron microscopy (SEM) for both conditioned and unconditioned cases to assess changes and/or degradation. In addition, the mechanical properties of the conditioned specimens were assessed with tests similar to those in Phase II. The results for the conditioned specimens were compared to those of the reference ones. The change in the properties was selected as an indicator on the degradation of the BFRP materials.

3.2.2.4 Chemical Resistance Evaluation of Bare Basalt Fibers

Chemical resistance tests were conducted on the basalt fibers utilized in manufacturing the tested BFRP bars, in parallel to the main study conducted herein to investigate the physical and mechanical characteristics of new BFRP bars. These tests were conducted to clarify the effect of the different chemicals on the bare basalt fibers. The tests were conducted following Owens Corning (2011) guide for evaluating the chemical resistance of glass fibers. Basalt fibers were heated to 540 °C overnight to remove any sizing and provide a proper clean surface for chemical-resistance investigation. Samples were then cut and carefully weighed before immersion in different corrosive aqueous solutions at 96 °C for 1 (24 h) and 7 days (168 h). The solutions were deionized water, an acidic solution (10% HCl), a saline solution (10% NaCl), and an alkaline solution (3.2 g NaOH per liter). After conditioning, the samples were thoroughly washed, dried, and weighed again. Furthermore, the conditioned fibers were then analyzed using SEM to detect any changes in microstructure.

3.3 Part II: Performance Evaluation of Concrete Bridge-Deck Slabs Reinforced with BFRP Bars under Concentrated Loads

The second part of the current study presents an experimental study aimed at investigating the structural performance of restrained bridge-deck slabs reinforced with BFRP bars and subjected to concentrated load at the center of the slab on an area equivalent to a wheel load (87.5 kN-CL-625

truck), as specified by the CHBDC (CAN/CSA S6 2014). This section provides full description of the experimental work related to this part.

3.3.1 Material Properties

***Reinforcing bars*:** BFRP bars of 12 and 16 mm diameters were used in this study. The BFRP bars were fabricated using a pultrusion process in a vinylester resin with fiber content of 79.2% and 80.0% for 12 and 16 mm bars, respectively. The basalt fibers used herein were known ASA.TEC (produced by Asamer Basaltic Fibers GmbH, Austria). The bars had a deformed surface with helical ribs to increase the bond between the bar surface and surrounding concrete. The tensile properties of the BFRP bars were determined by testing five representative specimens of each diameter according to ASTM D7205 (2011). The tensile modulus of elasticity was 69.3 and 64.8 GPa for BFRP bars of 12 and 16 mm diameter, respectively. On the other hand, 15M steel bars were used for the reference slab. **Table 3–3** provides the properties of the reinforcing bars.

Table 3–3: Tensile properties, bond strength and surface configurations of the reinforcing bars

RFT Type	d_b (mm)	A_f [a] (mm²)	E_f (GPa)	f_{fu} (MPa)	ε_{fu} (%)	f_b (MPa)	Surface configuration
BFRP	12	113.1	69.3±0.5	1760±39	2.54±0.10	17.7±1.3	Ribbed Surface
	16	201.1	64.8±3.3	1724±64	2.67±0.17	16.8±1.4	
Steel [b]	15M	200.0	200.0	f_y [c]=450	ε_y [c]=0.20	--	Ribbed Surface

[a] Nominal cross-sectional area.

[b] Tensile properties of steel bars were provided by the manufacturer.

[c] f_y and ε_y are yield strength and strain of steel bars, respectively.

Notes: properties calculated based on the nominal cross-sectional area.

Concrete: The slabs were constructed using ready-mix normal-weight concrete with 28-days target compressive strength of 40 MPa. The mix proportion for a cubic meter of concrete was 350 kg of cement, 813 kg of natural sand, and 1032 kg of aggregate of size ranges between 5-20 mm (20 mm maximum nominal size), 155 liter water (water/cement ratio of 44%) and air entrainment ratio of 5-8%. The designed slump of the concrete was 80±30 mm. Once the concrete was poured, the concrete was compacted using electrical vibrator and leveled manually. After two hours, curing process started by covering the concrete surface with wet burlap and polythene sheet for ten days.

The concrete compressive strength for each batch was determined by testing three 150 × 300 mm cylinders in accordance with ASTM C39 (2015). In addition, the tensile strength was determined from split-cylinder testing on three 150 × 300 mm cylinders in accordance with ASTM C496 (2011). **Table 3–4** shows the concrete compressive and the tensile strengths on the day of slab testing.

Table 3–4: Mechanical properties of concrete

Casting No.	Slab No.	f'_c (MPa)	f_t (MPa)
1	S1-S and S2-B	48.81±1.43	4.70±0.17
2	S3-B and S4-B	42.20±1.58	4.24±0.06
3	S5-B, S6-B and S7-B	47.90±1.14	4.44±0.09

3.3.2 Test Specimens

This part of the experimental program included testing of seven full-scale concrete deck slabs measuring of 3000 mm long × 2500 mm wide × 200 mm thick and span of 2000 mm (center to center), as shown in **Figure 3–7**. The test specimens were designed to simulate the deck slabs of a actual bridge (Wotton Bridge, Quebec, Canada) (El-Salakawy et al. 2003a) and were in agreement with the past tests conducted at the University of Sherbrooke with GFRP and CFRP bars (El-Gamal et al. 2005). Six slabs were provided with two holes 27 mm in diameter spaced 160 mm apart with a 250 mm pitch in the longitudinal direction at the restrained edges. One slab had no holes on the edges to be simply supported during the test. The concrete cover —constant for all the slabs— was equal to 30 and 25 mm at the top and bottom, respectively, as specified in Clause 16.4.4 of CAN/CSA S6 (2014). The slab thickness was selected to keep the supporting beams spacing to slab thickness ratio less than 18, as specified in Clause 8.18.4.1 of CAN/CSA S6 (2014), and to represent the most commonly used size of concrete bridge-deck slabs in Canada. Slabs length, however, was selected to avoid one-way shear before punching failure and to include the slab area affected by the wheel load. This area was assumed to be based on the outer diameter of the wedge formed during punching failure (El-Gamal et al. 2005). The test parameters investigated herein were: (i) reinforcement type [steel and BFRP bars]; (ii) BFRP bar size [12 mm and 16 mm]; (iii) reinforcement ratio in each direction [0.4% up to 1.2%]; and (v) edge restraining [restrained and

unrestrained (free)]. For comparisons, two slabs reinforced with GFRP and CFRP (El-Gamal et al. 2005) with the same dimensions and loading procedure were presented.

Table 3–5 summaries the reinforcement details. The first slab (S1-S) was reinforced, top and bottom, with 15M steel bars each 150 mm in the main direction (transverse direction) and reinforced, top and bottom, with 15M steel bars each 225 mm, in the secondary direction (longitudinal direction). The slab had a reinforcement ratio of 0.80% in the bottom transverse direction. The slab's reinforcement was designed to simulate the deck slabs of Wotton Bridge, Quebec, Canada (El-Salakawy et al. 2003a). The second slab (S2-B) was reinforced with 16 mm BFRP bars arranged exactly as S1-S (same reinforcement ratio of BFRP and steel). The amount of reinforcement in this slab (S2-B, 16 mm @150 mm) satisfies the CHBDC's empirical and flexural design methods (CAN/CSA S6 2014), assuming that the material safety factor and the stress level in the BFRP bars at service load level are the same as GFRP bars as provided in Appendix A. The third slab (S3-B) was designed to have the same reinforcement ratio and approximately the same axial-reinforcement stiffness of slab S2-B by replacing the 16 mm BFRP bars with 12 mm BFRP bars. The fourth slab (S4-B) had the same bottom reinforcement as S2-B but without top reinforcement. The fifth slab (S5-B) was designed to have approximately the same axial reinforcement stiffness as slabs G-S2 and C-S2 (El-Gamal et al. 2005). The last two slabs (S6-B and S7-B) were reinforced with the same BFRP bars: 16 mm spaced 300 mm in the orthogonal direction, top and bottom (minimum reinforcement in accordance with CAN/CSA S6 (2014). All the slabs were edge-restrained except S7-B which was simply supported (free). **Figure 3–7** to **Figure 3–14** show the geometry and the reinforcement details of the tested deck slabs.

Table 3–5: Reinforcement details of the tested bridge-deck slabs

Slab ID[a]	Bottom Reinforcement						Top Reinforcement					
	Transverse direction			Longitudinal direction			Transverse direction			Longitudinal direction		
	RFT[c]	ρ (%)	$\rho \times E$ (MPa)	RFT[c]	ρ (%)	$\rho \times E$ (MPa)	RFT[c]	ρ (%)	$\rho \times E$ (MPa)	RFT[c]	ρ (%)	$\rho \times E$ (MPa)
S1-S	15M@150	0.80	1606	15M@225	0.59	1184	15M@150	0.83	1655	15M@225	0.61	1225
S2-B	16 @150	0.80	520	16 @225	0.59	383	16 @150	0.83	536	16 @225	0.61	396
S3-B	12 @85	0.79	523	12 @125	0.58	383	12 @85	0.81	539	12 @125	0.60	395
S4-B	16 @150	0.80	520	16 @225	0.59	383	--	--	--	--	--	--
S5-B	16 @100	1.20	780	16 @170	0.78	507	16 @105	1.18	766	16 @120	1.15	743
S6-B	16 @300	0.40	260	16 @300	0.44	288	16 @300	0.41	268	16 @300	0.46	297
S7-B[b]	16 @300	0.40	260	16 @300	0.44	288	16 @300	0.41	268	16 @300	0.46	297

[a] Slab number (S1 to S7) followed by reinforcement type (S: steel; B: basalt FRP).

[b] Simply supported slab.

[c] Bar diameter and spacing in mm (diameter in mm @ spacing in mm).

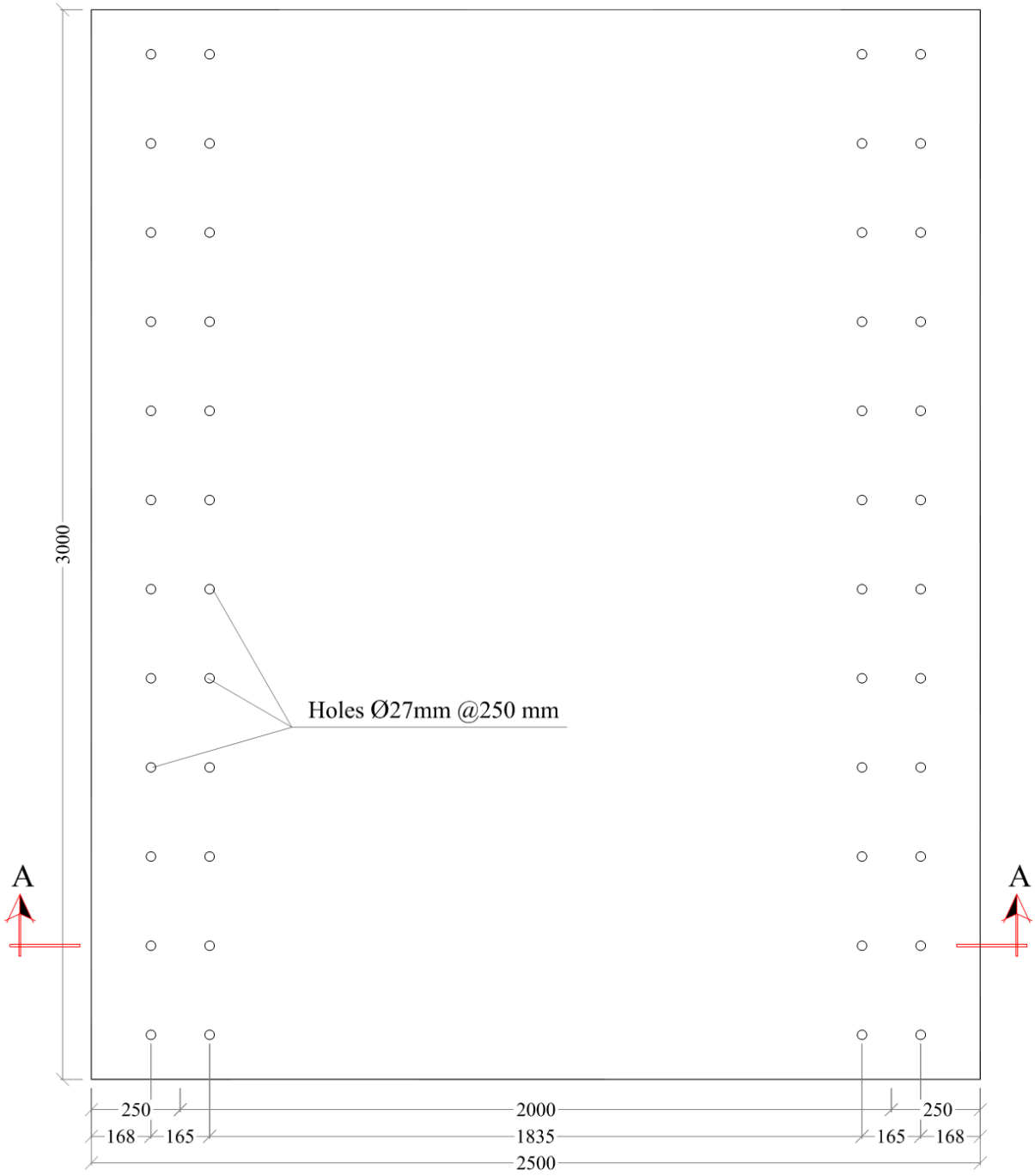

(a) Plan

(b) Section (A-A)

Figure 3–7: Geometry of the tested deck slabs (Dimensions in mm)

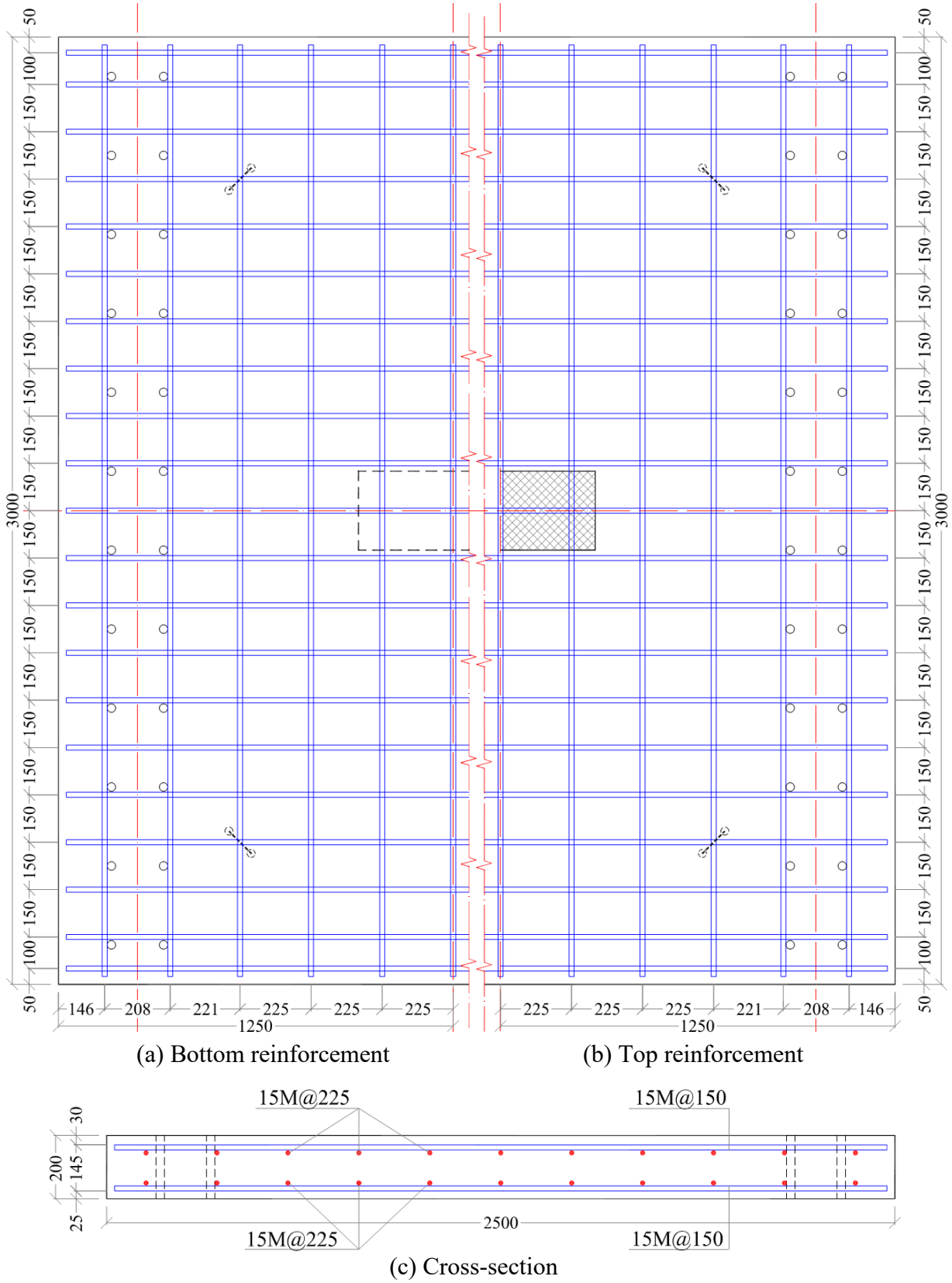

(a) Bottom reinforcement (b) Top reinforcement

(c) Cross-section

Figure 3–8: Reinforcement details of slab S1-S

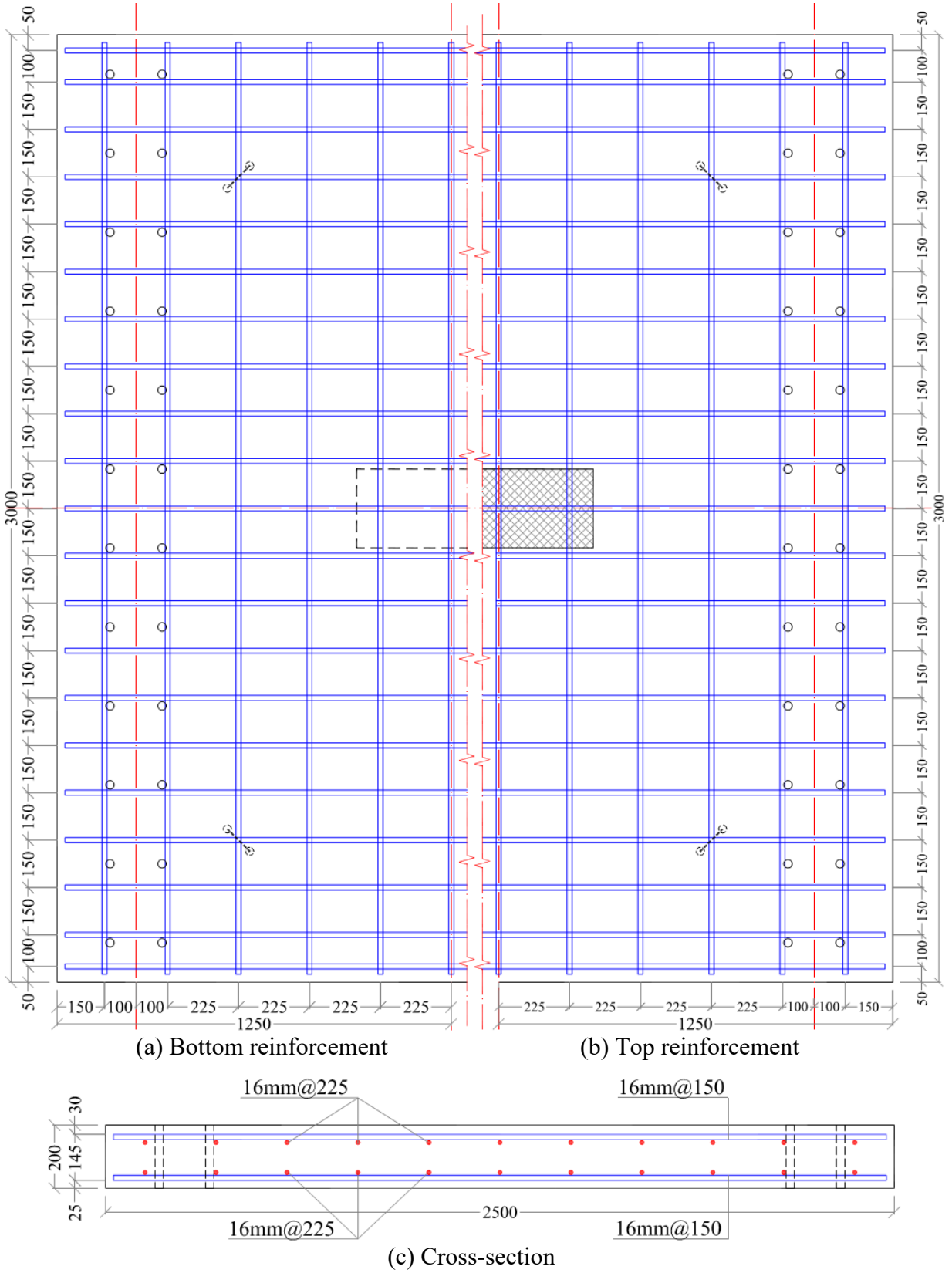

(a) Bottom reinforcement (b) Top reinforcement

(c) Cross-section

Figure 3–9: Reinforcement details of slab S2-B

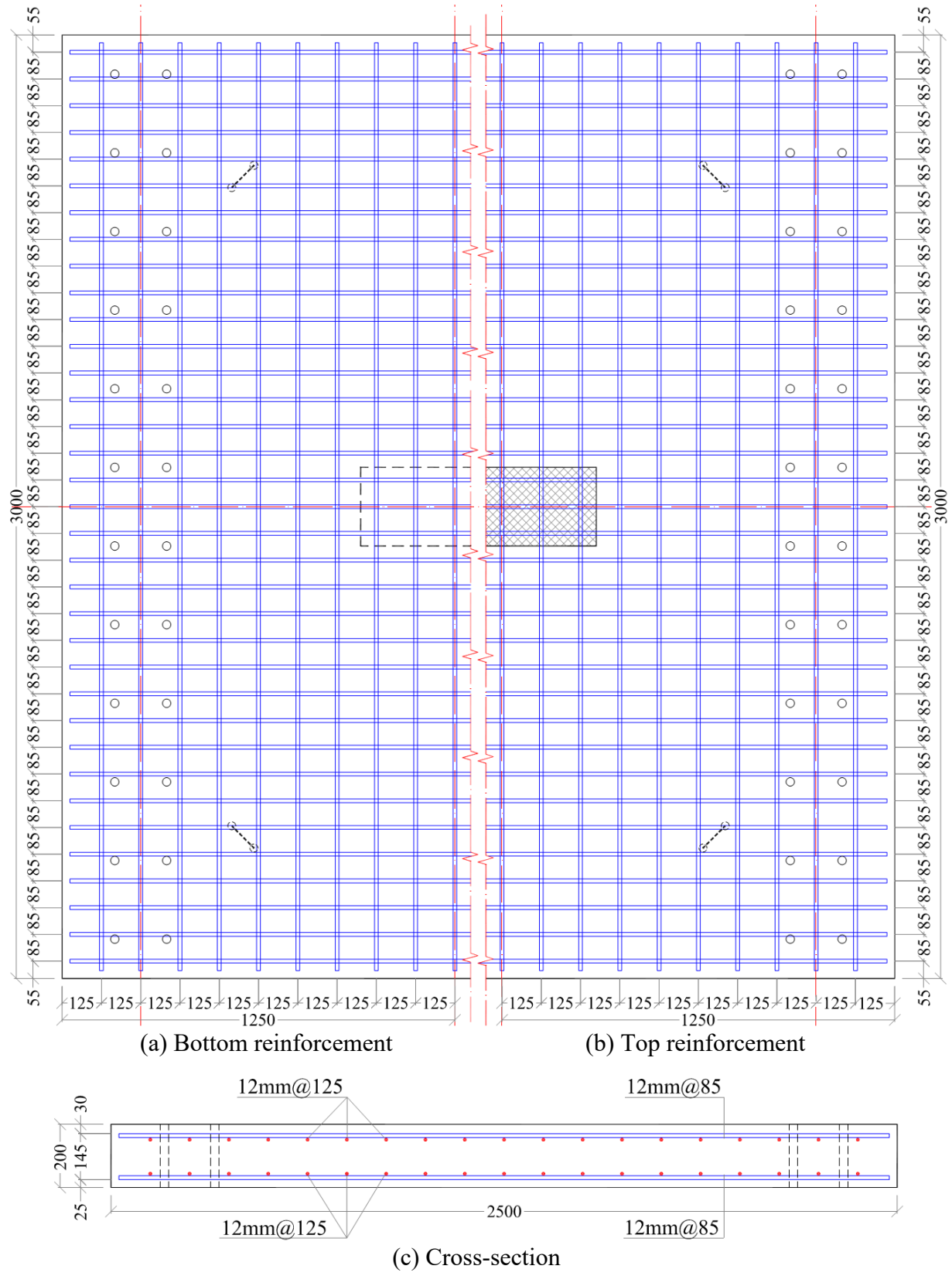

Figure 3–10: Reinforcement details of slab S3-B

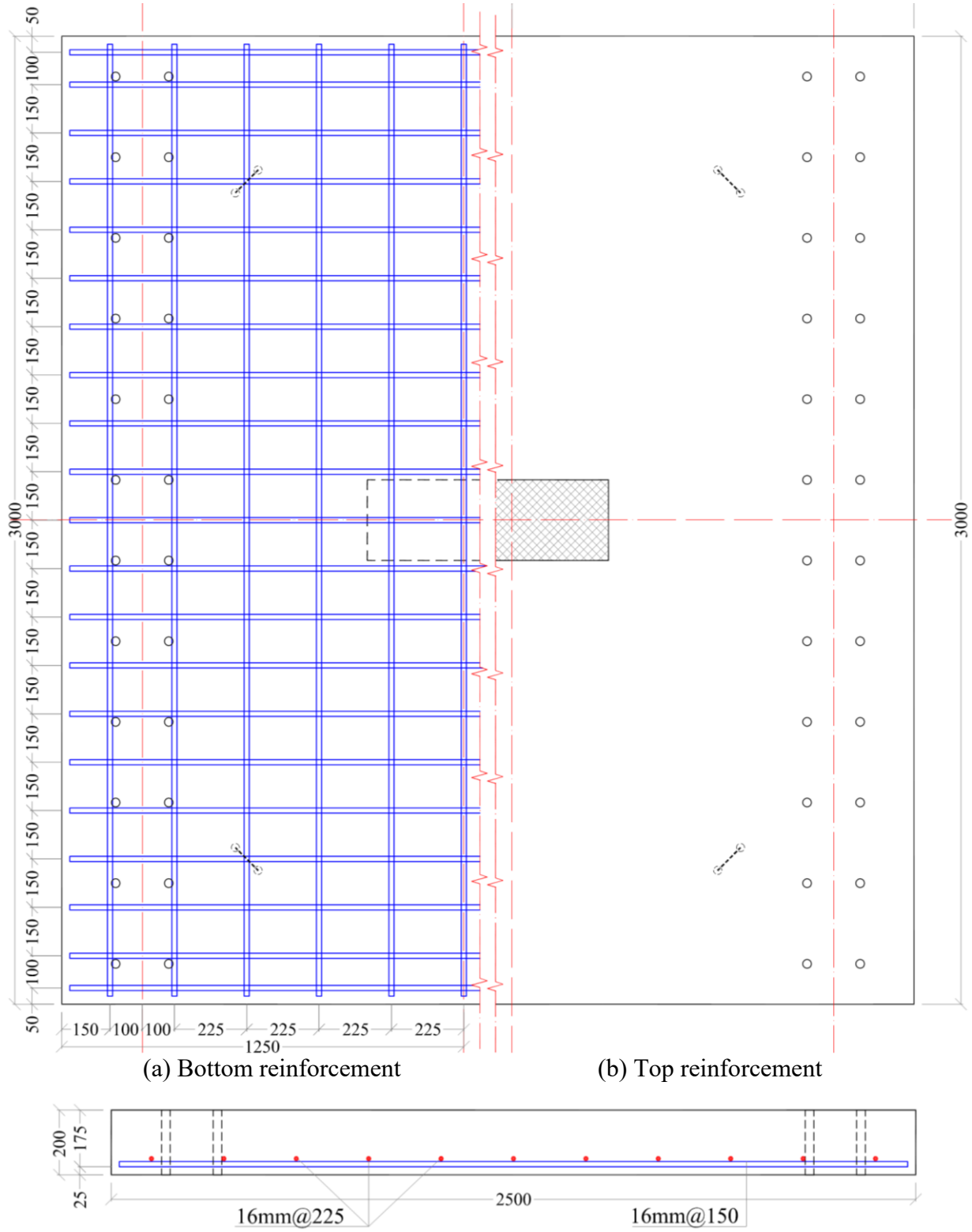

(a) Bottom reinforcement (b) Top reinforcement

(c) Cross-section

Figure 3–11: Reinforcement details of slab S4-B

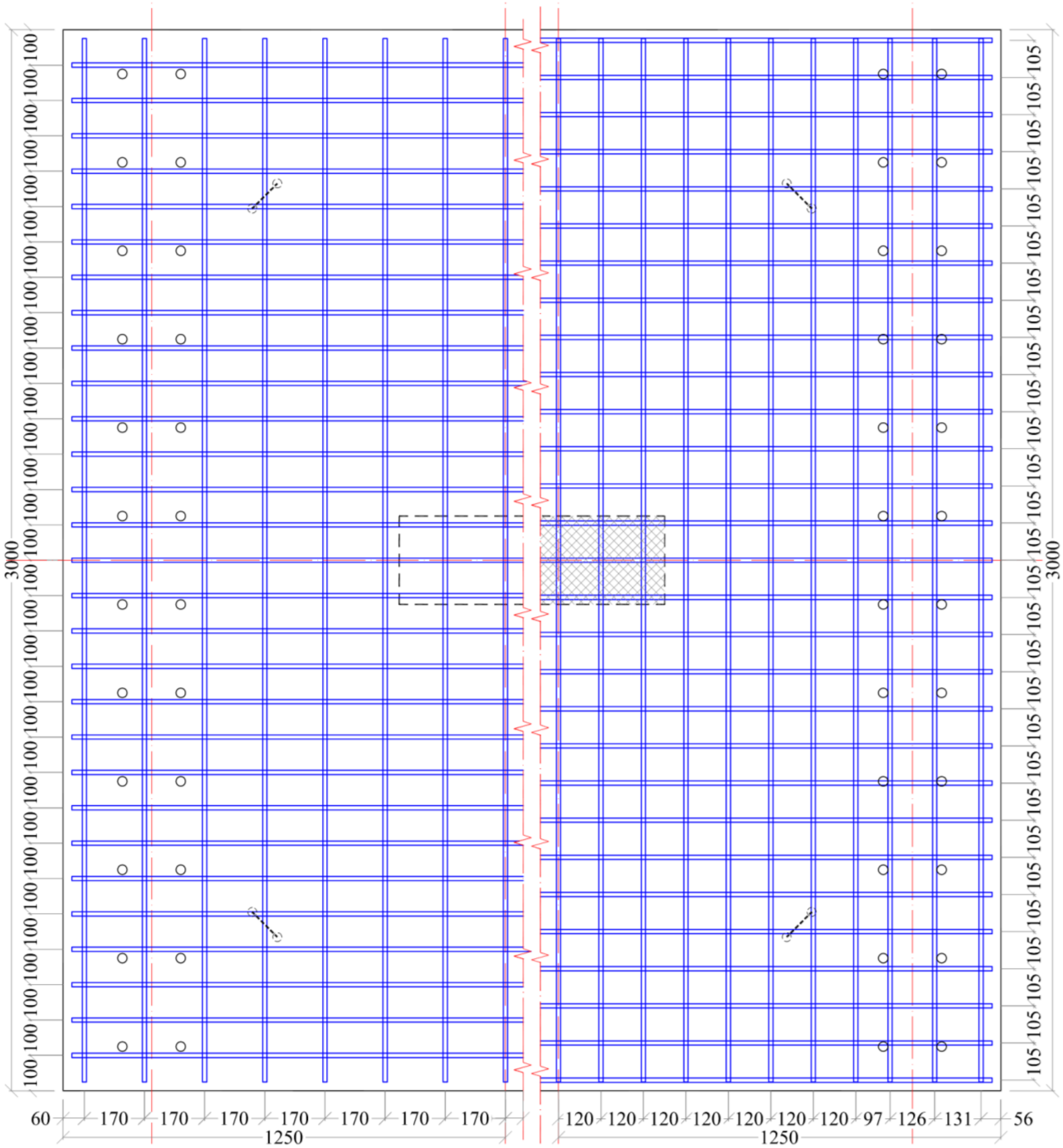

(a) Bottom reinforcement

(b) Top reinforcement

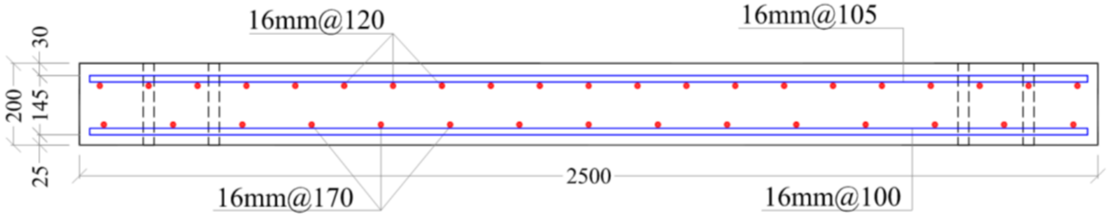

(c) Cross-section

Figure 3–12: Reinforcement details of slab S5-B

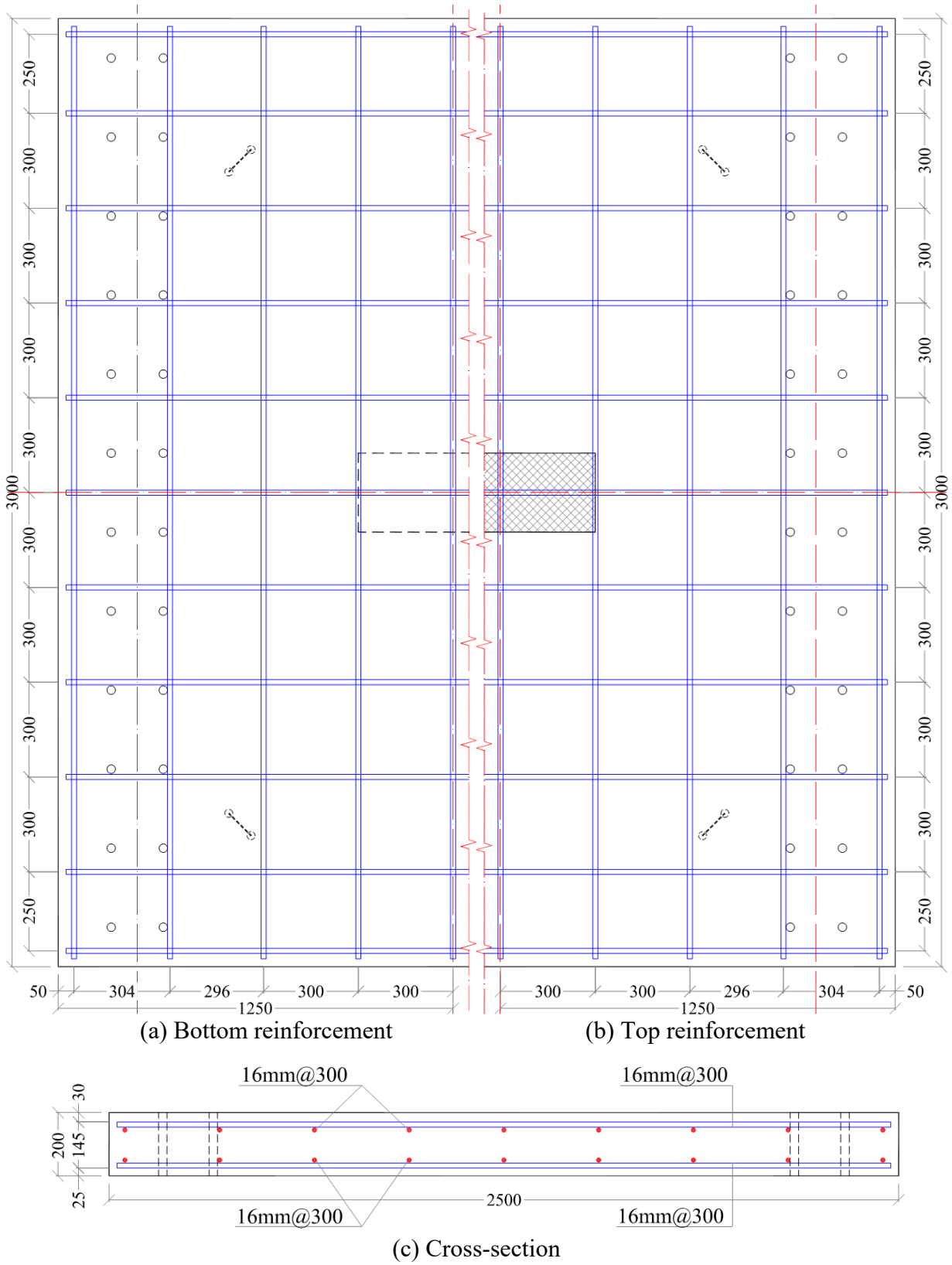

(a) Bottom reinforcement (b) Top reinforcement

(c) Cross-section

Figure 3–13: Reinforcement details of slab S6-B

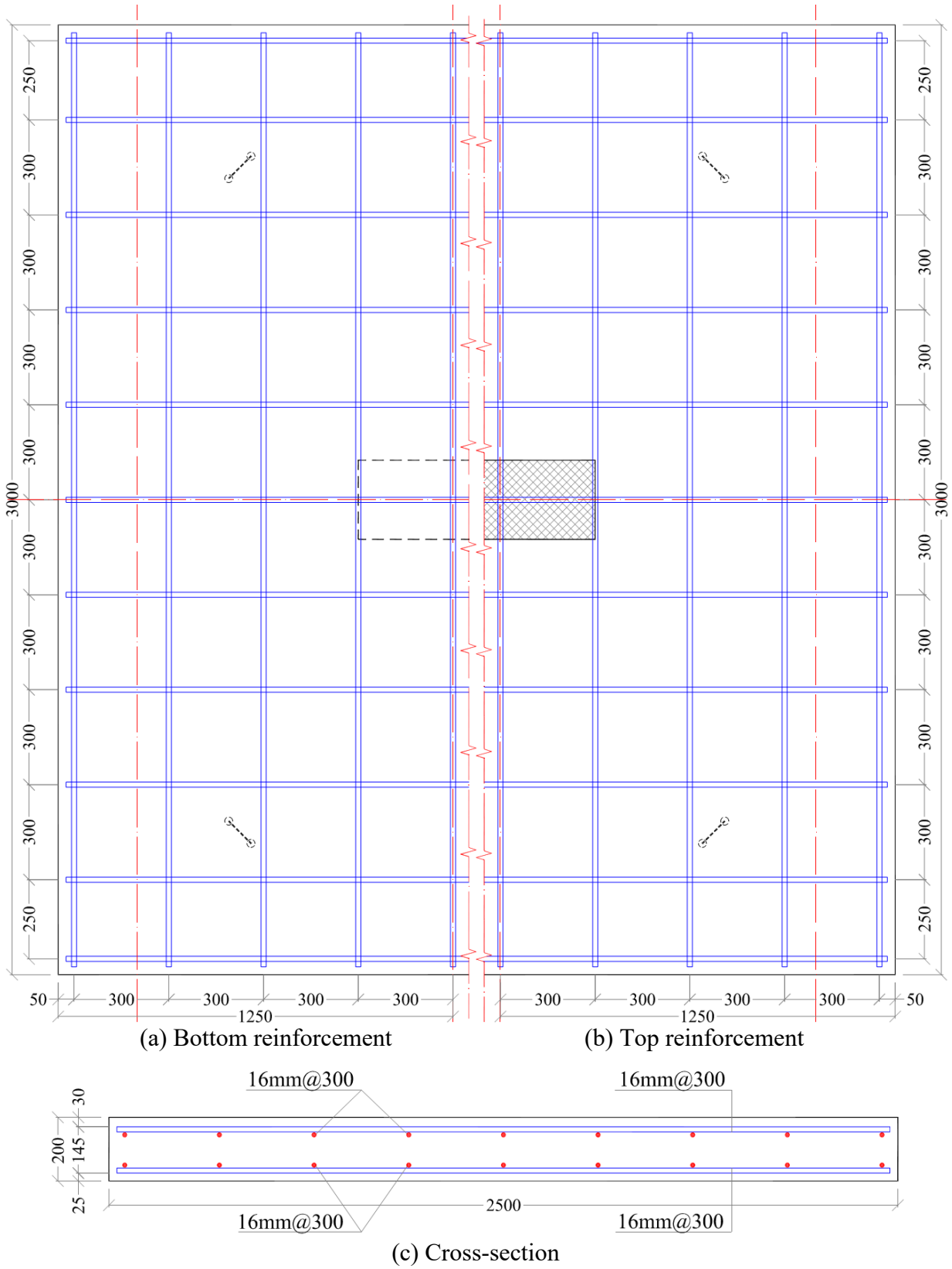

Figure 3–14: Reinforcement details of slab S7-B

3.3.3 Preparation of the Specimens

3.3.3.1 The Formwork

Two wooden formworks were fabricated and used for casting the slabs. Each formwork was provided with two rows of holes (spaced at 250 and 160 mm in the longitudinal and transverse directions, respectively) at each longitudinal side of the formwork's base. Two plates of wood, provided with holes at the same positions as those in the base of the formwork, were fixed at the top of the formwork. Plastic tubes were inserted through the holes in the top plates and in the base of the formwork. A few hours following casting the concrete, the plastic tubes were removed. Four steel angles were tied diagonally at the top of the formwork to support the sides. Before placing the cages, the formwork was painted with oil to protect the formwork and to facilitate the de-molding of the specimens from the formwork after concrete hardening. **Figure 3–15** and **Figure 3–16** shows a schematic drawing and a photo for the formwork, respectively.

3.3.3.2 Preparing of the Reinforcement and Concrete Casting

Steel and BFRP bars were cut to the required lengths and arranged together to form both the top and bottom reinforcement layers. Plastic tie-wraps were used to tie the reinforcing bars together to keep the spacing and orientation of the bars as required. Plastic and steel chairs were used to ensure the concrete cover of the bottom and top reinforcement, respectively. The strain gauges were installed on the surface of the reinforcing bars after assembling the cages. Then the two reinforcement layers were placed in their position inside the formwork. **Figure 3–17** shows assembled cages made of BFRP bars, while **Figure 3–18** shows the cages inside the formwork ready for concrete casting.

A normal-weight ready mixed concrete with 28-days target compressive strength of 40 MPa was used. Once the concrete was poured, the concrete was compacted using electrical vibrator and leveled manually. After two hours, curing process started by covering the concrete surface with wet burlap and polythene sheet for ten days. After that, the slabs were removed from the forms and kept in the ambient temperature until testing. Nine standard cylinder specimens (150 × 300 mm) from each batch were prepared during concrete casting. The standard cylinders were subjected to the same environmental conditions as their correspondent slabs. The concrete compressive strength and tensile strength for each batch was determined by testing three standard cylinders at the same

day of slab testing. **Figure 3–19** to **Figure 3–22** show the casting, surfacing, curing and de-molding of the concrete deck slabs, respectively. While **Figure 3–23** shows the deck slab after construction.

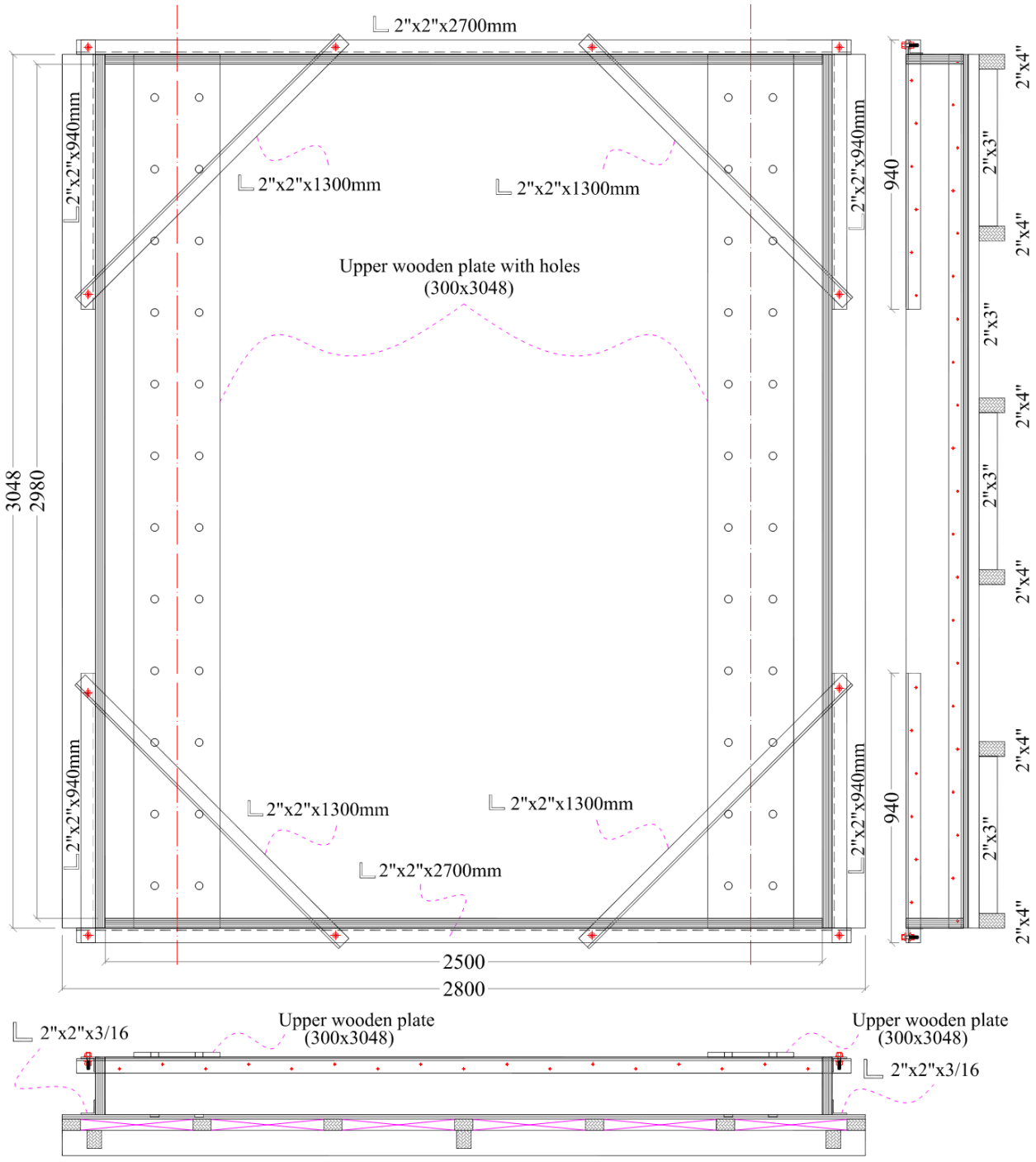

Figure 3–15: Schematic drawing for the formwork

Figure 3–16: The wooden formwork

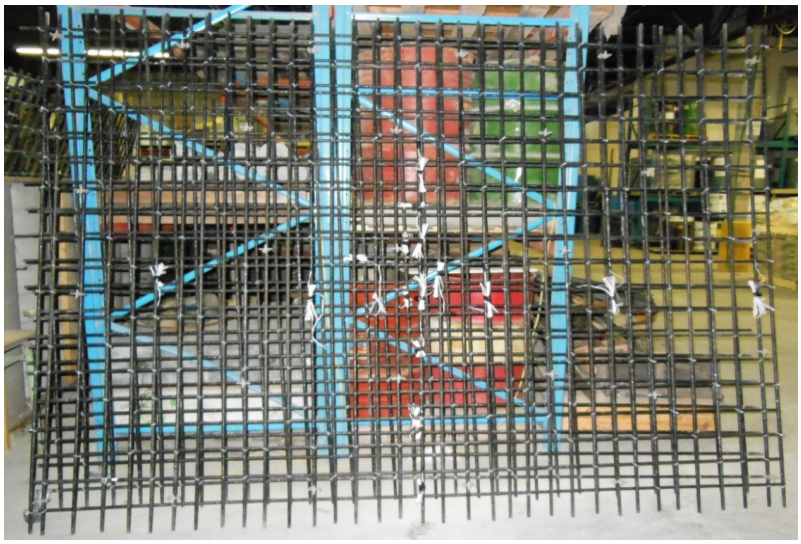

Figure 3–17: Assembled cages

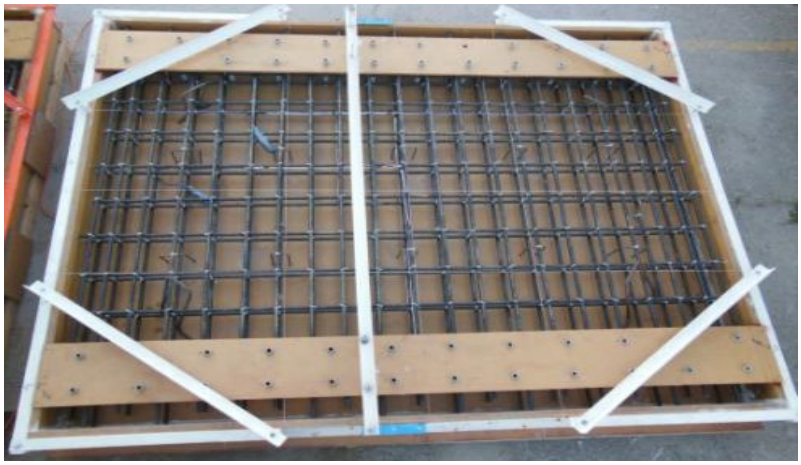

Figure 3–18: Cages inside the formwork (before concrete casting)

Figure 3–19: Deck slabs during concrete casting

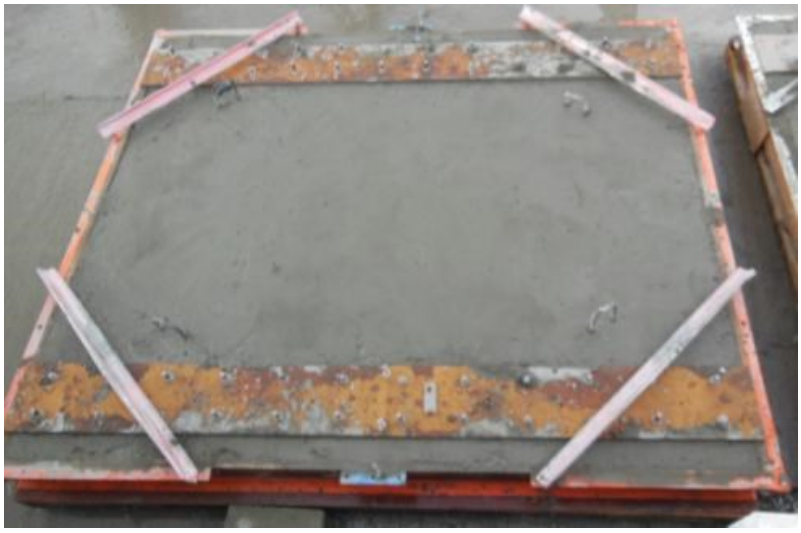

Figure 3–20: Deck slabs after concrete casting and surfacing

Figure 3–21: Curing of the concrete deck slabs

Figure 3–22: De-molding of the concrete deck slabs

Figure 3–23: Concrete deck slabs after de-molding

3.3.4 Instrumentations

Figure 3–24 to **Figure 3–28** show the internal and external instrumentation that used for slab testing. Deflections were monitored using seven Linear Variable Differential Transducers (LVDTs), with a precision of 0.001 mm, installed at the top surface of the deck slabs (D1 to D7), as shown in **Figure 3–24**. This figure also shows that two LVDTs (D8 and D9) were installed at both sides of the slabs to monitor any movement of the slab edges during the testing. Moreover, six electrical strain gauges of 6 mm length were used to measure strains at different positions on the steel cross frame at the top and bottom, as shown in **Figure 3–24** (Section A-A). The concrete compressive strains at different locations on the top surface of the slabs were measured using four electrical strain gauges of 60 mm length. **Figure 3–25** shows the location of the concrete strain gauges on the top surface of deck slab. Several electrical strain gauges of 6 mm length were also installed on the reinforcing bars to record the strains. **Figure 3–26** and **Figure 3–27** show the typical position of strain gauges on the top and bottom reinforcing bars, respectively. The initial crack widths were measured using 50X handheld microscope. High- precision LVDTs (0.001 mm) were installed at the position of the first three cracks to record the crack-width propagation with load increasing, as depicted in **Figure 3–28.** An automatic data acquisition system connected to a computer was used to monitor loading, deflections and strains in concrete and reinforcing bars.

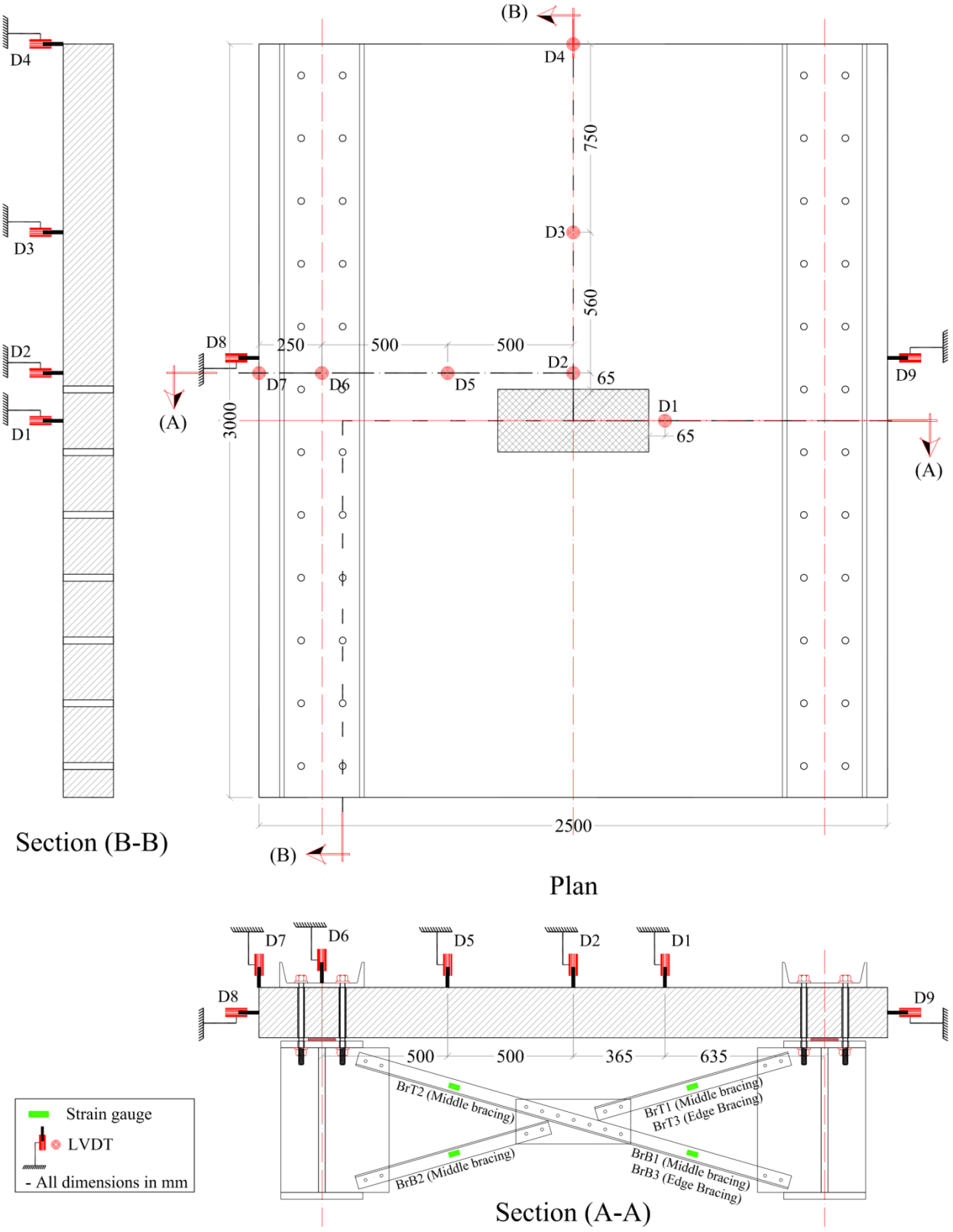

Figure 3–24: Typical locations of the LVDTs on the deck slabs and strain gauges on the cross frames

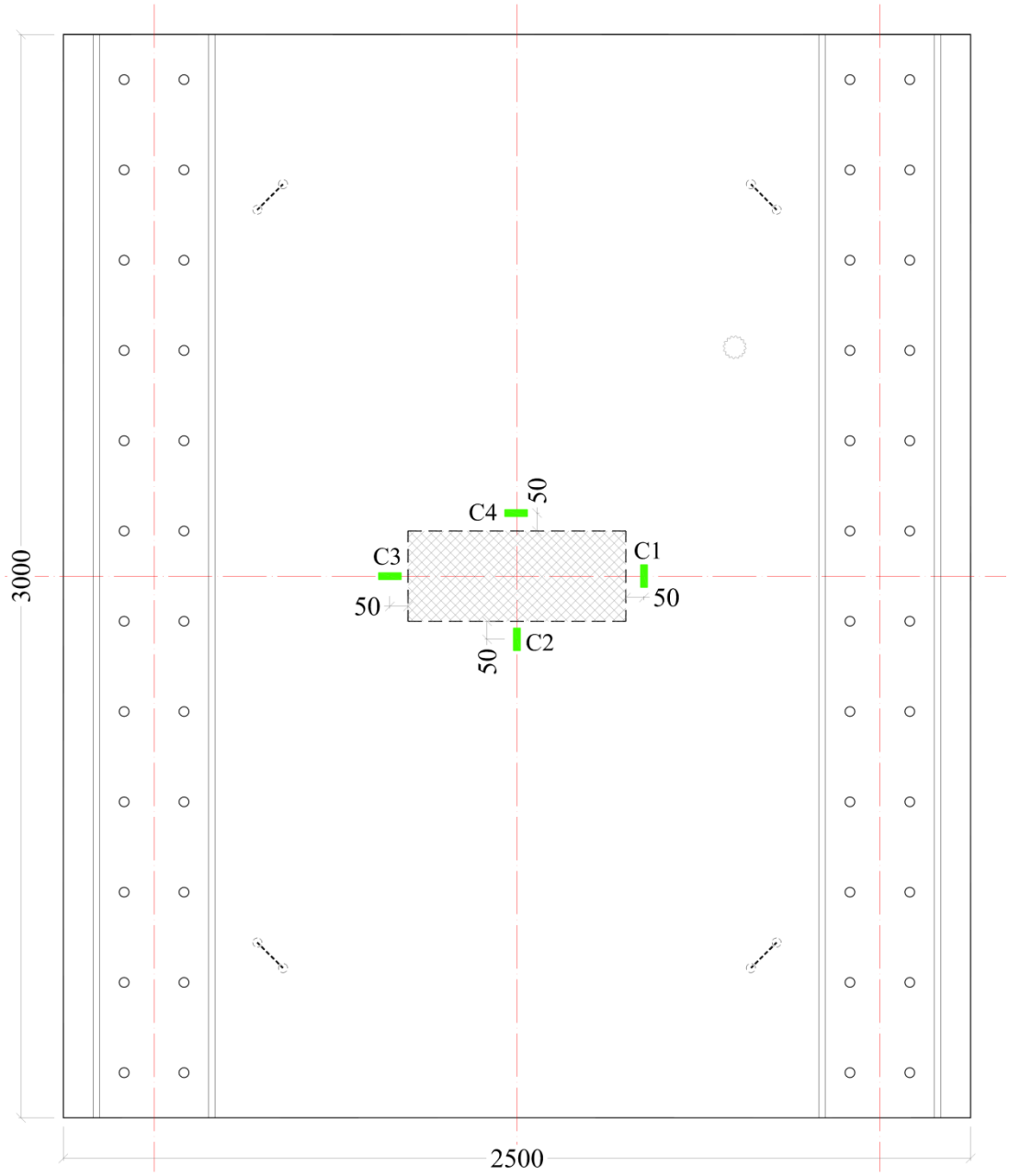

Figure 3–25: Typical location of strain gauges on the top surface of concrete deck slabs

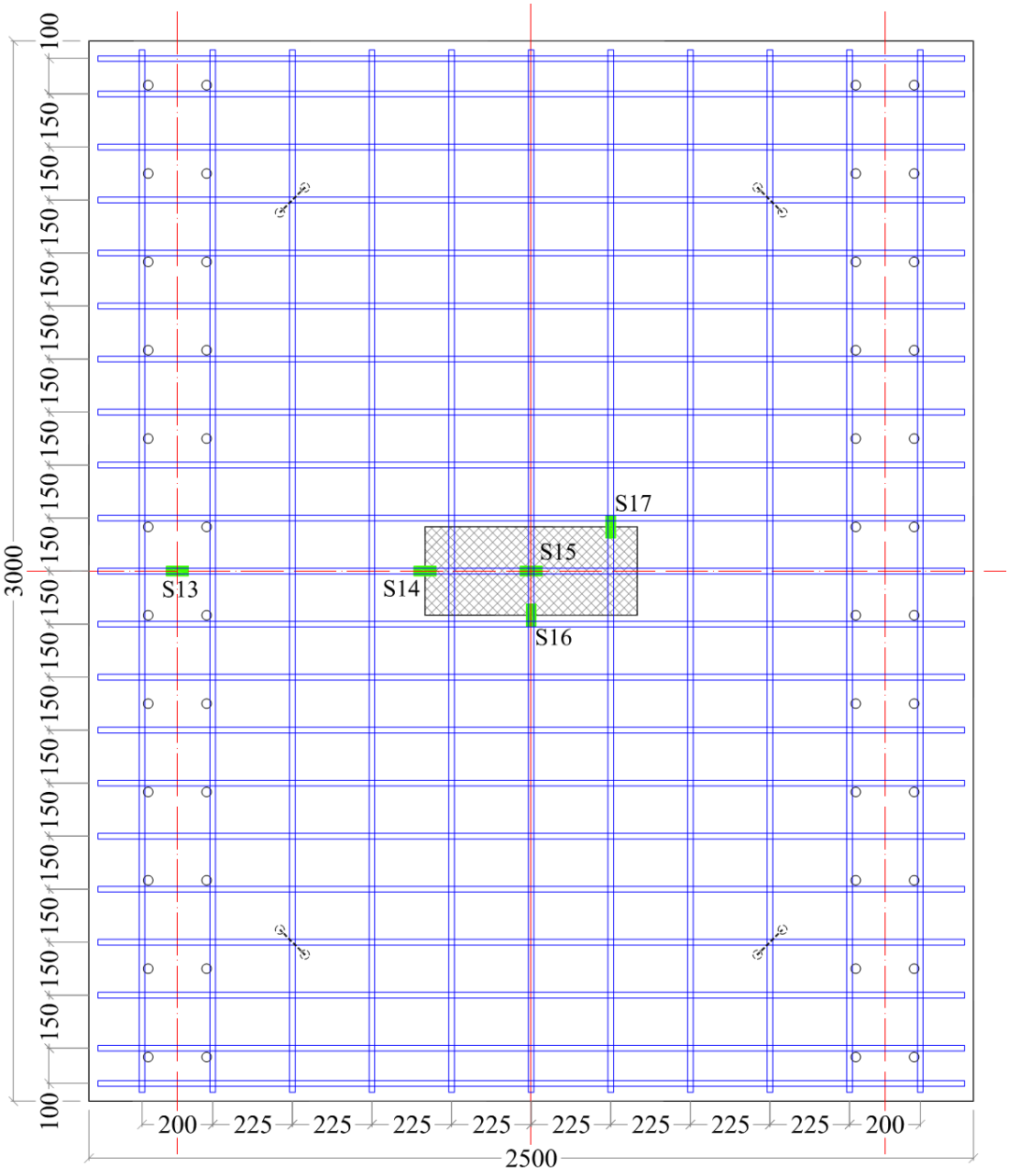

Figure 3–26: Typical location of strain gauges on the top reinforcing bars

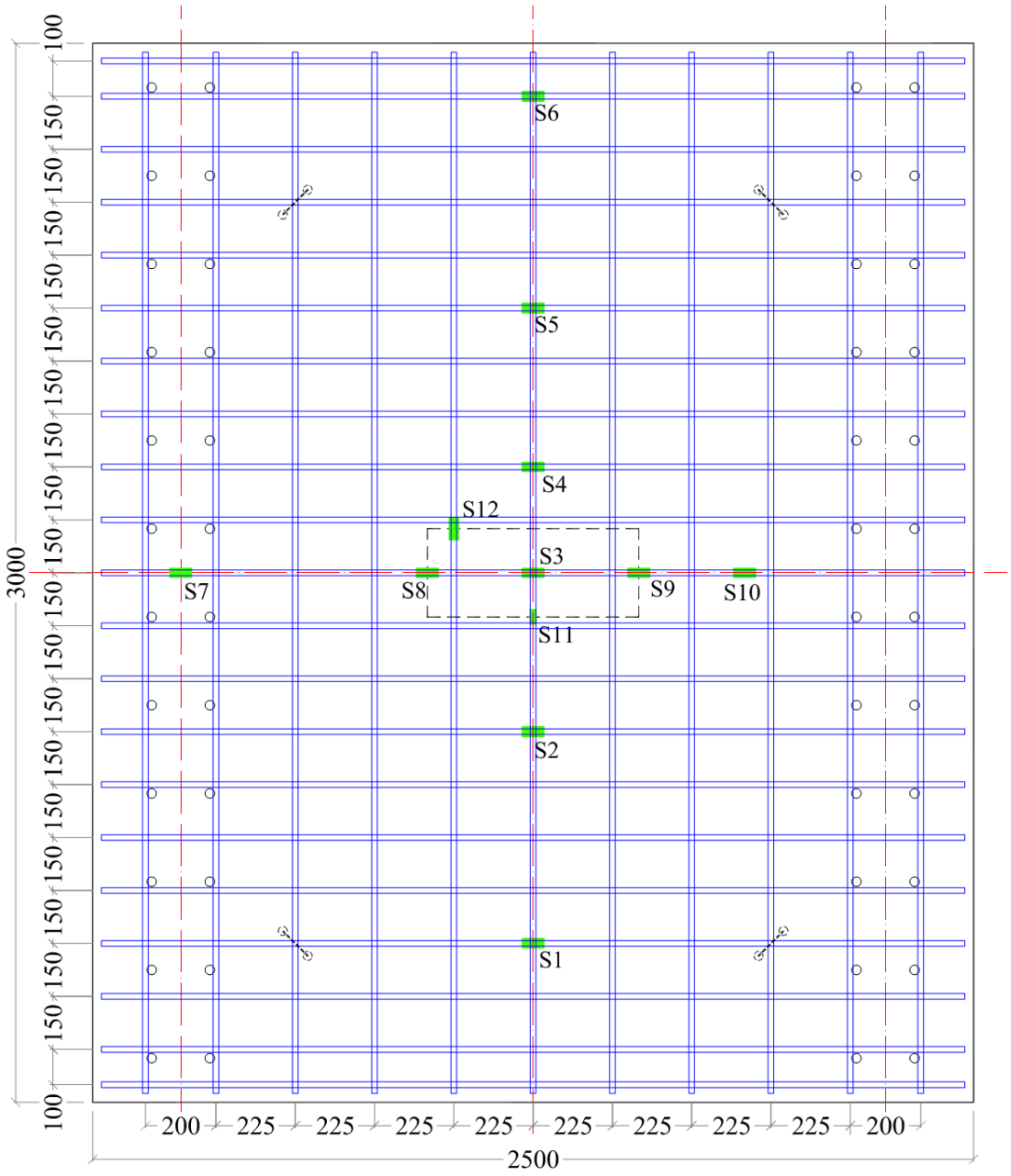

Figure 3–27: Typical location of strain gauges on the bottom reinforcing bars

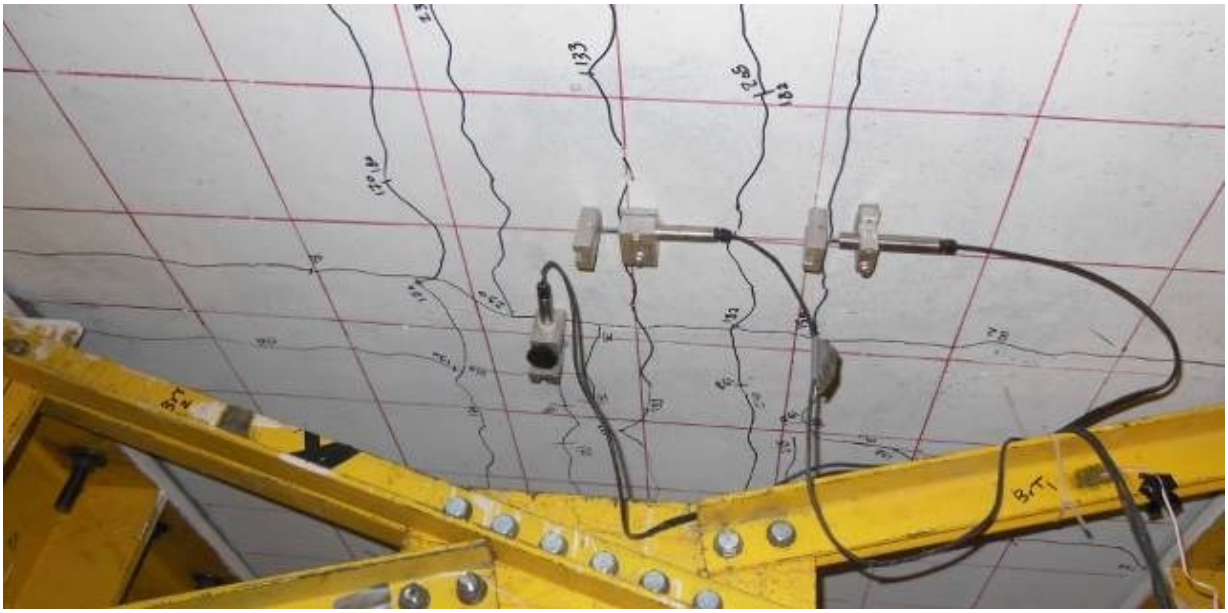

Figure 3–28: LVDTs to record the crack widths

3.3.5 Test Setup and Procedures

Each slab was loaded up to failure over a center-to-center span of 2000 mm under monotonic single concentrated load, using a hydraulic jack controlled by a manually operated pump monitored with a pressure dial gauge. The load was applied to the slab center with a contact area of 600 × 250 mm, using a 70 mm thick steel plate to simulate the footprint of a sustained truck wheel load (87.5 kN-CL-625 truck) as specified in CAN/CSA S6 (2014). To create uniform stresses over the loading area, a 10 mm thick neoprene sheet was used between the loading plate and the concrete surface. The slabs were supported on two steel girders simulating the setup of El-Gamal et al. (2005) to resist the maximum applied load without exceeding the permissible stresses and deflections. To insure full contact between the bottom surface of concrete slab and top surface of steel girders, neoprene pads of 3 mm thickness and 100 mm wide were inserted on the steel girders underneath the concrete slab. The two steel girders were braced together with three steel cross frames spaced at 1500 mm. The steel girders were supported by two steel cross beams spaced 3000 mm in longitudinal direction. The loads were transferred to the laboratory strong floor through four steel legs at the edge of the cross beams. **Figure 3–29** shows the test setup under the loading frame. To facilitate monitoring of the crack propagation and crack widths; the slab surface was painted with white color before the testing and verified that no initial crack signs on the slab surface.

Six of seven slabs were tested after being restrained along the longitudinal edges while the last slab was simply supported. The restrained slabs were tied to the top flange of steel girder in the longitudinal direction with 22 mm diameter threaded anchors, which were fitted into pre-prepared holes through the slab thickness, as shown in **Figure 3–29** and **Figure 3–30**. These steel anchors were used to partially restrain the slab edges. The steel anchors represent the shear connectors between the girder and deck slab in an actual slab-on-girder bridges. All anchors were hand tightened with a torque wrench to a torque moment of 160 N.m in order to make a constant partially edges restrain for all slabs and make it uniform along the slab edges. The torque moment was calculated to generate horizontal shear friction between the steel girder and bottom surface of the slab higher than the horizontal component of the arching stress and to prevent lateral movement between the slab and girder. The bridge-deck slabs were tested similarly to past tests at the University of Sherbrooke by El-Gamal et al. (2005). Steel channels were used along the top face of the concrete slab to prevent stress concentration around the holes along the slab edges. In addition, 10 mm thick and 100 mm wide neoprene strips were placed between the concrete slab and the steel channel to ensure full contact until the end of the test. A hydraulic jack with a capacity of 1000 kN and a ±250 mm stroke was used to apply the monotonic load up to failure at a load control rate of 5 kN/min. The hydraulic jack was controlled manually with a hand pump monitored with a pressure dial gauge connected to the data-acquisition system and monitored by a computer. **Figure 3–29** and **Figure 3–30** provide overview of the test setup. During the test, the slabs were observed until the first three cracks appeared in the transverse direction; the corresponding load was recorded. The test was paused when each of the first three cracks appeared. The initial crack widths were measured manually by a 50X handheld electronic microscope and LVDTs were installed at crack locations to record crack widths with load increasing. The cracking load was also verified in terms of the change in stiffness of the load-deflection and load-strain relationships. The load was continuously increased until slab failure. The formation of the cracks on the sides and bottom surface of the deck slabs and corresponding loads were marked and recorded during the test.

(a) Loading system

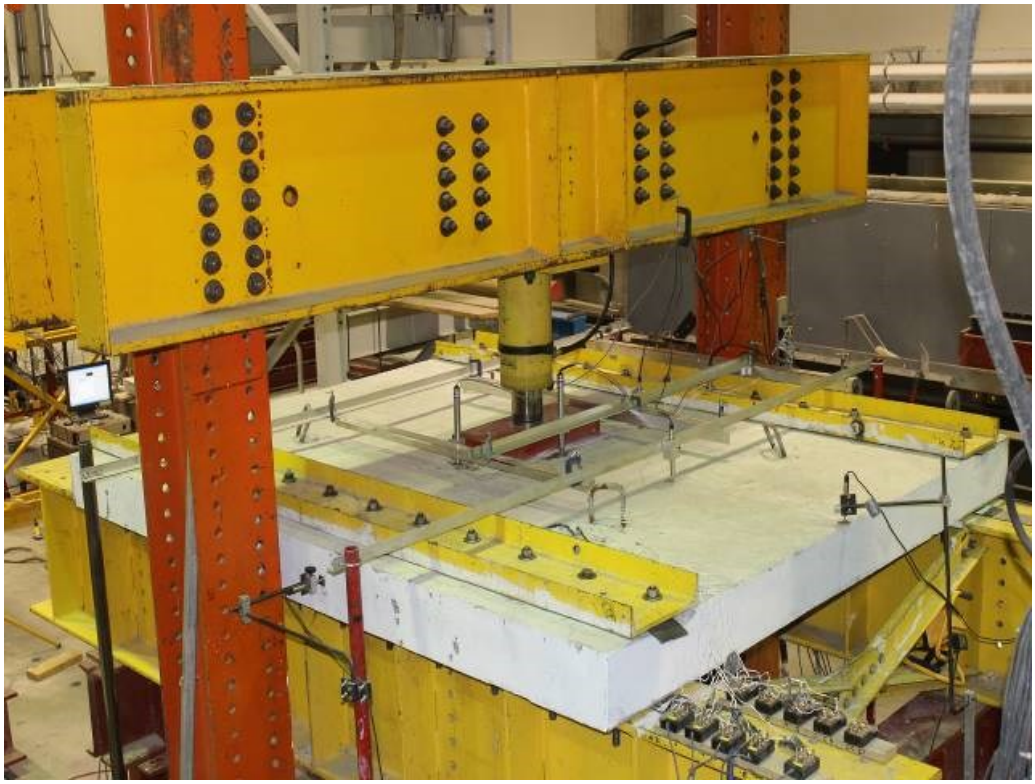

(b) Deck slab ready for testing

Figure 3–29: Overview of the test setup

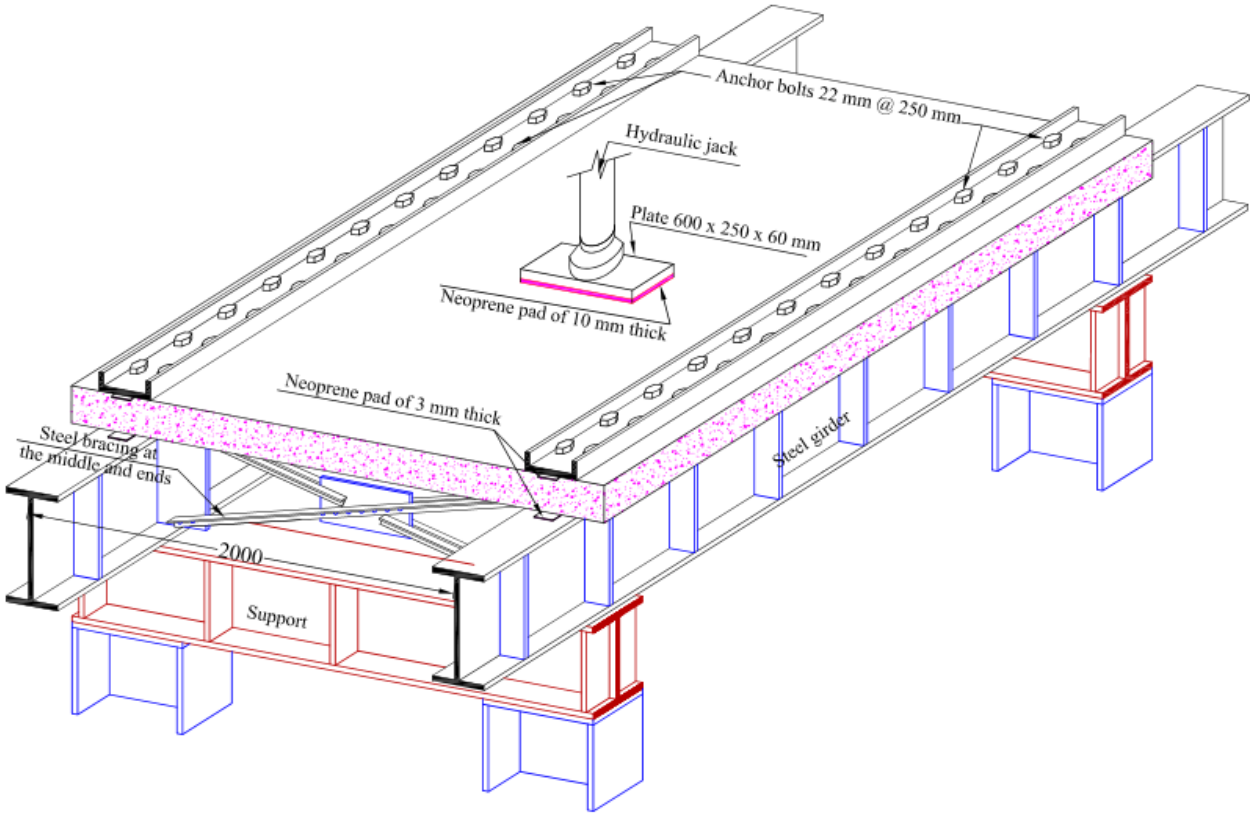

Figure 3–30: Schematic drawing for test setup

3.4 Part III: Performance Evaluation of Concrete Beams Reinforced with BFRP Bars under Flexure Load

The third part of the current study presents an experimental study investigated the effect of the surface configurations (sand-coated and ribbed bars) and mechanical properties (tensile strength and modulus of elasticity) of BFRP bar as well as the reinforcement ratio on the serviceability of concrete beams reinforced with BFRP bars in terms of crack width, deflection and ultimate capacity. Moreover, this part determines the bond-dependent coefficient (k_b) of the newly developed BFRP bars. A total of fourteen concrete beams were constructed and tested up to failure. Six beams were reinforced with sand-coated BFRP bars (Described in details in **Chapter 6**), as well as six beams were reinforced with ribbed BFRP bars and two reference beams were reinforced with steel bars (Described in details in **Chapter 7**). The main difference between chapters 6 and 7 are the mechanical properties and surface configuration of basalt FRP bars. The effect of reinforcement ratio and surface type on the ultimate capacity summarized in appendix B. The beam

specimens were designed in accordance with CAN/CSA S806 (2012), Annex S "*Test Method for Determining the Bond-Dependent Coefficient of Fiber-Reinforced Polymer (FRP) Bars*. This section provides full description of the experimental work related to this part.

3.4.1 Material Properties

Reinforcing bars: Two different products of BFRP bars with different mechanical properties and surface configurations were used as tension reinforcements in the tested beams. The BFRP bars were manufactured from continuous basalt fibers impregnated in vinyl-ester resins using the pultrusion process. The basalt fibers had a diameter of 10 to 22 microns and were given a surface treatment consisting of a silane coupling agent. The tensile properties of the BFRP bars were determined by testing five representative specimens of each diameter according to ASTM D7205 (2011). The BFRP bars used in **Chapter 6** were 10, 12 and 16 mm diameter and had a sand-coated surface over helical wire wrapping, as shown in **Figure 3–31**, to enhance the bond between the bars and the surrounding concrete. The fiber contents of the sand-coated BFRP bars were 87.2%, 90.6%, and 89.9% (by weight) for the 10, 12, and 16 mm diameters, respectively. These bars were known as MagmaTech (produced by MagmaTech Ltd, UK). On the other hand, the BFRP bars used in **Chapter 7** were 8, 12, and 16 mm diameter and had a ribbed surface with helical rips, as shown in **Figure 3–31,** to enhance the bond between the bars and the surrounding concrete. The fiber contents of the ribbed BFRP bars were 77.4%, 79.2%, and 80.0% for the 8, 12, and 16 mm diameters, respectively. These bars were known ASA.TEC (produced by Asamer Basaltic Fibers GmbH, Austria). In addition, 10M and 15M steel bars of ribbed surface were used for the reference beams. In addition, 10M steel bars were used as transverse and top reinforcement in the test specimens. **Table 3–6** summarizes the tensile properties of the BFRP and steel bars and the bond strength between the BFRP bars and concrete. It should be mentioned that, the mechanical properties of BFRP bars were determined using nominal cross-section areas of 50, 79, 113, and 201 mm^2 for the 8, 10, 12, and 16 mm diameters, respectively.

Concrete: The beams were made with ready-mixed, normal-strength concrete with a 28-day target compressive strength of 40 MPa. A cubic meter of concrete contained 350 kg of cement, 813 kg of natural sand, 1032 kg of aggregate (20 mm maximum nominal size), 155 L of water (water–cement ratio, *w/c*, of 44%) and an air-entrained ratio of 5% to 8%. The concrete mix had slump of 80±30 mm. The fourteen beams were cast from four concrete batches. The curing process started

two hours after the concrete was cast by covering the concrete surface with wet burlap and polythene sheeting for 10 days. The concrete compressive strength of each batch was determined by testing three 150 × 300 mm cylinders on the day of beam testing in accordance with ASTM C39 (2015). The tensile strength was also determined from split-cylinder testing on 150 × 300 mm cylinders in accordance with ASTM C496 (2011). **Table 3–7** shows the compressive and tensile strengths of the different concrete batches.

Table 3–6: Tensile properties, bond strength and surface configurations of the reinforcing bars

Chapter No.	RFT Type	d_b (mm)	A_f [a] (mm²)	E_f (GPa)	f_{fu} (MPa)	ε_{fu} (%)	f_b (MPa)	Surface configuration
Six	BFRP	10	79	44.4±0.3	1189±74	2.68±0.16	18.0±0.2	Sand coated
		12	113	45.3±0.1	1162±26	2.56±0.05	13.8±1.9	
		16	201	48.7±0.4	1173±49	2.41±0.10	13.5±1.6	
Seven	BFRP	8	50	64.6±1.4	1655±95	2.56±0.17	25.4±2.3	Ribbed
		12	113	69.3±0.5	1760±39	2.54±0.10	17.7±1.3	
		16	201	64.8±3.3	1724±64	2.67±0.17	16.8±1.4	
	Steel[b]	10M	100	200.0	f_y [c] = 450	ε_y [c] = 0.2	---	Ribbed
		15M	200					

[a] Nominal cross-sectional area.

[b] Tensile properties of steel bars were provided by the manufacturer.

[c] f_y and ε_y are yield strength and strain of steel bars, respectively.

Notes: properties calculated based on the nominal cross-sectional area.

BFRP bars used in Chapter 6 BFRP bars used in Chapter 7 Steel bars used in Chapter 7

Figure 3–31: Basalt-FRP and steel bars

Table 3–7: Mechanical properties of concrete

Chapter No.	Beam ID	f'_c (MPa)	f_t (MPa)
Six	B-2#10mm, B-4#10mm, B-2#12mm, B-4#12mm, B-2#16mm, B-4#16mm	42.5±0.40	2.8±0.05
Seven	B-3#8mm, B-5#8mm	52.7±1.28	4.7±0.40
	B-2#12mm, B-3#12mm B-2#10M, B-2#15M	44.7±2.00	4.3±0.28
	B-2#16mm, B-3#16mm	50.8±1.65	4.2±0.26

3.4.2 Test Specimens

This investigation included fourteen rectangular concrete beams of 200 mm wide × 300 mm deep × 3100 mm total length, made with normal-strength concrete. Six beams were reinforced with sand-coated BFRP bars, six beams were reinforced with ribbed BFRP bars, and two reference beams were reinforced with steel bars. The tested specimens were designed in accordance with CAN/CSA S806 (2012), Annex S "*Test Method for Determining the Bond-Dependent Coefficient of Fibre-Reinforced Polymer (FRP) Bars*". The beams were tested under four-point bending over a clear span of 2700 mm. The beams had a clear shear span of 1100 mm (corresponding to a shear-span-to-depth ratio of about 4.3), while the distance between the two loading points was 500 mm (constant moment zone). The beams were reinforced with two 10M rebar as top reinforcement, while the bottom reinforcement were BFRP and steel bars in different configurations, as shown in **Table 3–8**. 10M steel stirrups spaced at 100 mm were used as shear reinforcement in both shear spans to avoid shear failure. To minimize the confining effect of the shear reinforcement on the flexure behavior, no stirrups were used in the constant moment zone. The clear concrete cover was 38 mm, which was set in accordance with Annex S of CAN/CSA S806 (2012). The BFRP-RC beams were designed to fail by concrete crushing in the constant moment zone. This was achieved by using a reinforcement ratio (ρ_f) greater than the balanced reinforcement ratio (ρ_{fb}), as shown in **Table 3–8**, where the balanced reinforced reinforcement ratio (ρ_{fb}) was calculated considering the actual concrete strength. The ratio between the actual and balanced reinforcement ratios for the BFRP-RC beams ranged from 1.35 to 6.87 according to ACI 440.1R (2015) and from 1.09 to 5.52 according to CAN/CSA S806 (2012). In contrast, the steel-RC beams were designed to fail due to

steel yielding (under-reinforcement), which is common for steel-RC members. **Figure 3–32** shows the dimensions and reinforcement details of the tested beams. The test parameters investigated herein were: (i) reinforcement type [steel and BFRP bars]; (ii) reinforcement ratio [0.29% up to 1.54%]; (iii) bar size [8, 10, 12 and 16 mm]; and (vi) surface configuration of reinforcing bars [sand-coated and ribbed reinforcing bars].

Table 3–8: Summary of the reinforcement details of tested beams

Chapter	Beam ID [a]	f_c' [b] (MPa)	ρ_f	ρ_f/ρ_{fb} [c]		$E_f \times A_f$ (kN)	Reinforcement configuration
				ACI 440 (2015)	CAN/CSA S806 (2012)		
Six	B-2#10	42.5 ±0.40	0.0030	1.35	1.09	6677	One layer
	B-4#10		0.0060	2.89	2.34	13954	Two layers
	B-2#12		0.0044	1.83	1.48	10251	One layer
	B-4#12		0.0086	3.95	3.20	20501	Two layers
	B-2#16		0.0078	3.13	2.54	19591	One layer
	B-4#16		0.0154	6.81	5.52	39183	Two layers
Seven	B-3#8	52.7 ±1.28	0.0030	1.54	1.18	9745	One layer
	B-5#8		0.0052	2.72	2.08	16242	Two layers
	B-2#12	44.7 ±2.00	0.0044	2.67	2.14	15682	One layer
	B-3#12		0.0066	4.00	3.21	23552	One layer
	B-2#16	50.8 ±1.65	0.0078	4.58	3.55	26068	One layer
	B-3#16		0.0119	6.87	5.14	39102	One layer
	B-2#10M	44.7 ±2.00	0.0039	0.103	0.096	40000	One layer
	B-2#15M		0.0079	0.207	0.194	80000	One layer

[a] The first letter "B" indicates concrete beam; the second number "2, 3, 4, or 5" indicates the number of reinforcing bars; the last number (#8, #10, #12, #16, 10M, or 15M) indicates the bar size (in mm).

[b] f_c': concrete compressive strength.

[c] ρ_{fb}: balanced reinforcement was calculated based on the actual concrete compressive strength.

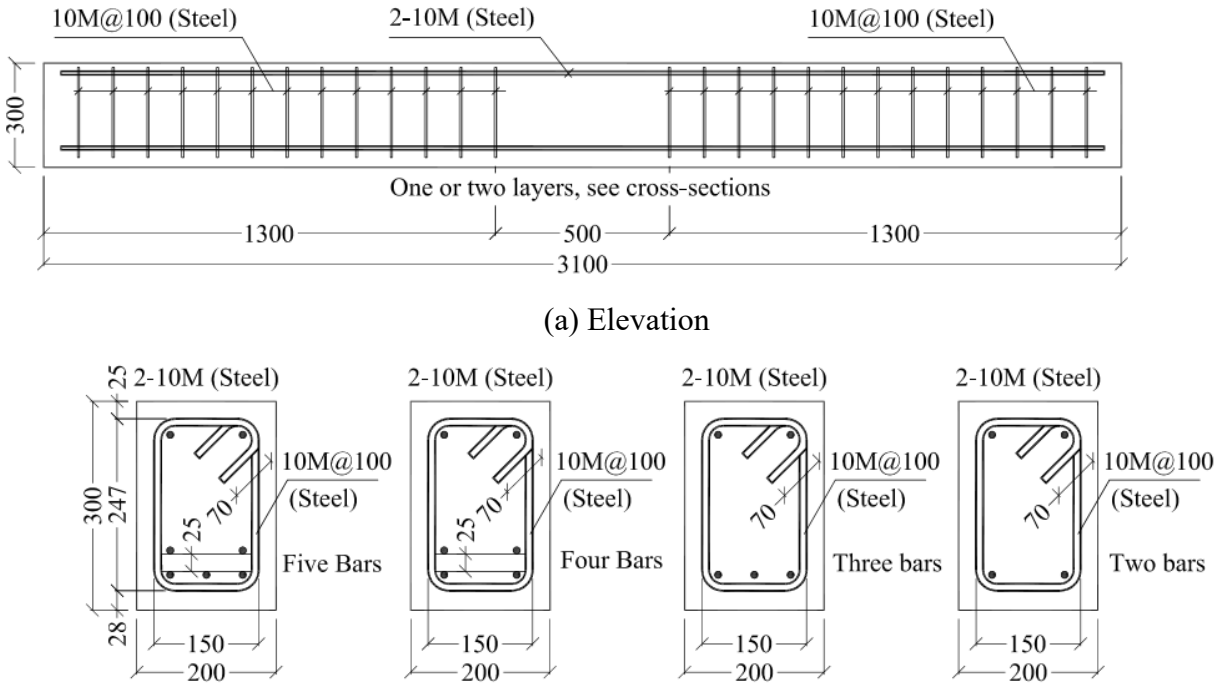

Figure 3–32: Dimensions and reinforcement details of tested beams

3.4.3 Preparation of the Specimens

3.4.3.1 The Formwork

A wooden formwork was fabricated and used for casting the beams. The formwork consists of six cells of 200 mm wide × 300 mm deep × 3100 mm total length (internal dimensions) for casting six beams at the same time. Before placing the cages, the formwork was painted with oil to protect the formwork and to facilitate the de-molding of the specimens from the formwork after concrete hardening, as shown in **Figure 3–33**.

Figure 3–33: Painting of the wooden formwork with oil

3.4.3.2 Preparing of the Reinforcement and Concrete Casting

Steel and BFRP bars were cut to the required lengths. Then the strain gauges were installed on the surface of the reinforcing bars before cage assemblage. Steel stirrups were arranged and tied to the top and bottom reinforcement using plastic tie-wraps to keep the spacing as required (**Figure 3–34**). Then the reinforcing cages were placed inside the formwork, as shown in **Figure 3–35**. Plastic chairs were used to ensure the bottom concrete cover.

A normal-weight ready mixed concrete with 28-days target compressive strength of 40 MPa was used. Once the concrete was poured, the concrete was compacted using electrical vibrator and leveled manually. After two hours, curing process started by covering the concrete surface with wet burlap and polythene sheet for ten days. After that, the beams were removed from the forms and kept in the ambient temperature until testing. Nine standard cylinder specimens (150 × 300 mm) from each batch were prepared during the concrete casting. The standard cylinders were subjected to the same environmental conditions as their correspondent beams. The concrete compressive strength and tensile strength for each batch was determined by testing three standard cylinders at the same day of beam testing. **Figure 3–36** to **Figure 3–39** show the casting, surfacing, curing and de-molding of the concrete beams, respectively. While **Figure 3–40** shows the concrete beams after construction.

Figure 3–34: Assembled cages

Figure 3–35: Cages of the beams inside the formwork (Before concrete casting)

Figure 3–36: Beams during concrete casting

Figure 3–37: Leveling of concrete surface

Figure 3–38: Curing of the concrete beams

Figure 3–39: De-molding of concrete beams

Figure 3–40: Concrete beams after de-molding

3.4.4 Instrumentations

Figure 3–41 provides the instrumentation details. The deflection along the beam's span was monitored using four linear variable differential transducers (LVDTs) accurate to 0.001 mm, labeled D1 to D4 (D2 and D3 at mid-span, and D1 and D4 at quarter-span). Crack propagation was also monitored during testing until failure, and the crack widths of the first three flexural cracks were monitored with three horizontal LVDTs (D5 to D7). The strains of the longitudinal BFRP reinforcing bars were captured with four electrical-resistance strain gauges 6 mm in length (S1 to S4). The compressive concrete strains at the mid-span section were measured with two electrical-resistance strain gauges 60 mm in length (C1 and C2). To facilitate crack monitoring, the beams were painted white prior to testing. In addition, an automatic data-acquisition system connected to a computer was used to monitor loading, deflections, and strains in the concrete and reinforcement. The formation of beam cracks and the corresponding loads were marked and recorded during testing until failure.

3.4.5 Test Setup and Procedures

The simply supported beams were tested under monotonic load in four-point bending until failure. **Figure 3–42** shows the dimensions and locations of the applied loads, while **Figure 3–43** provides a photo of the test setup for beam specimens. The load was applied at a stroke-controlled rate of 1.2 mm/min. During testing, the beams were observed visually until the first crack appeared and the corresponding load was recorded. The test was paused when each of the first three cracks appeared. The initial crack width of the first three cracks was measured manually with a 50X handheld electronic microscope; LVDTs were installed at crack locations to measure crack width electronically with increasing load. The load continuously increased until beam failure.

The cracking load was also verified based on the change in stiffness of the load–deflection and load–strain relationships. The concrete and reinforcement strain gauges and deflection and cracking LVDTs were connected to an automatic data-acquisition system connected to a computer to record their readings.

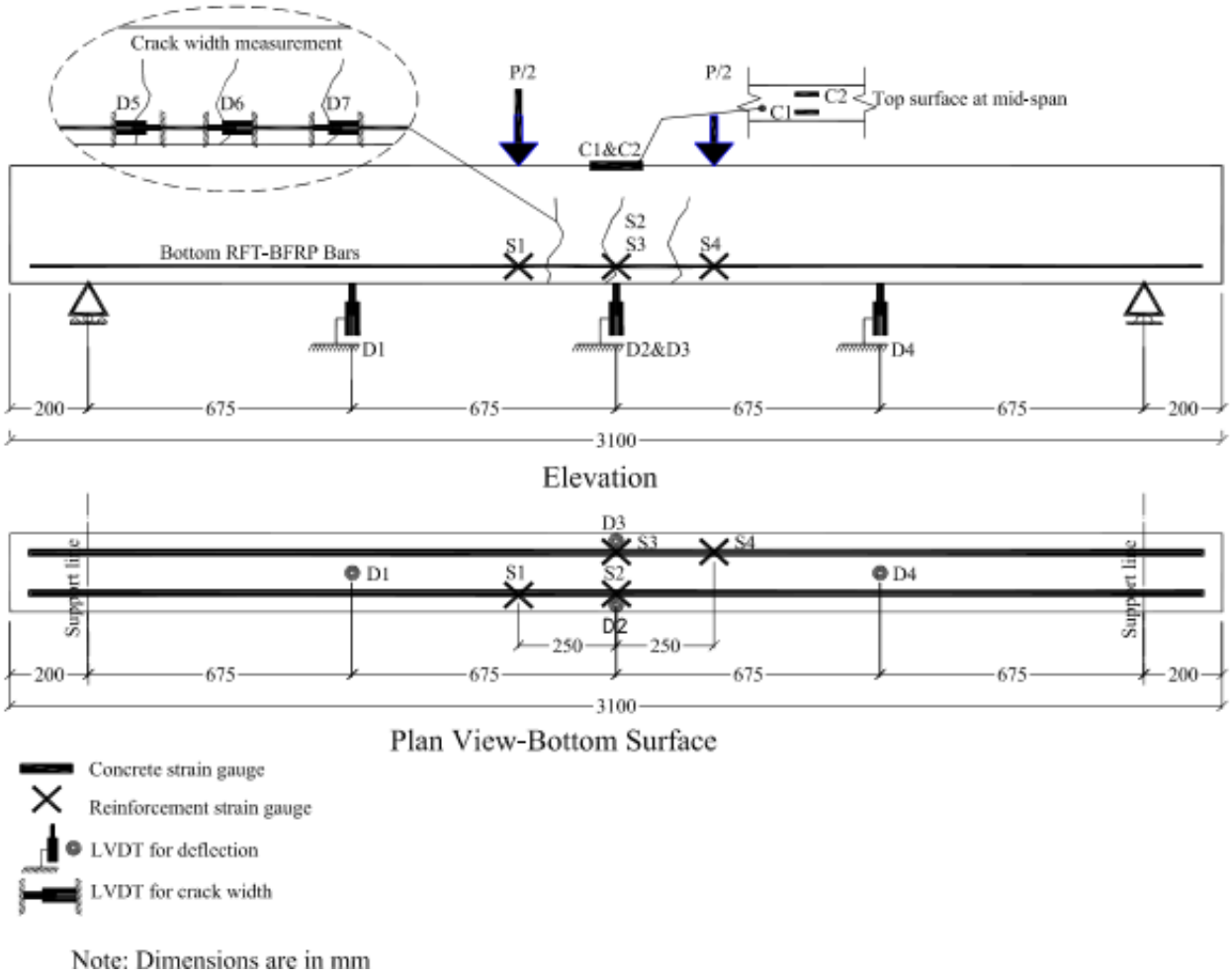

Figure 3–41: Schematic drawing of instrumentations

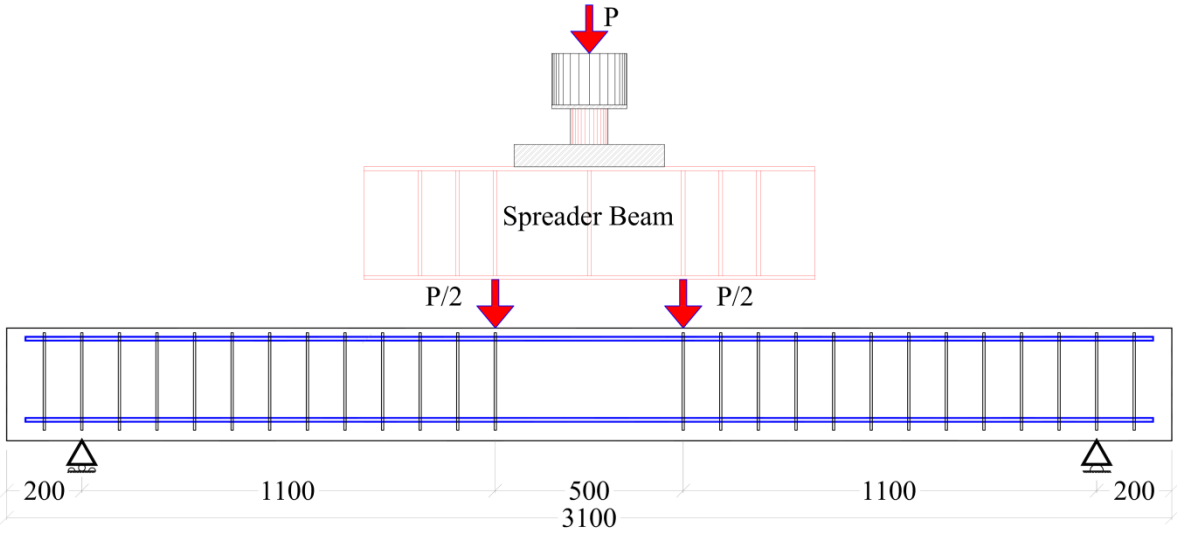

Figure 3–42: Schematic drawing for test setup

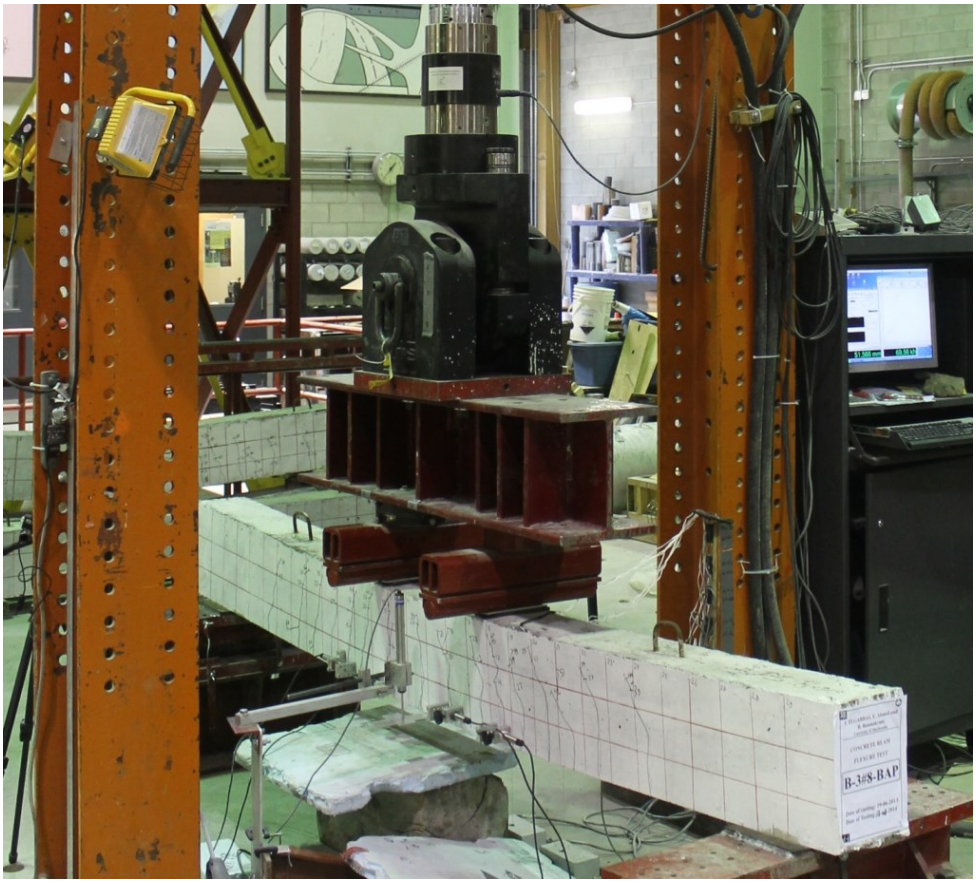

Figure 3–43: Overview of the test setup

CHAPTER 4
PHYSICAL AND MECHANICAL CHARACTERISTICS OF NEW BASALT-FRP BARS FOR REINFORCING CONCRETE STRUCTURES

Abstract

This paper introduces an experimental study that investigated the physical, mechanical, and durability characteristics of basalt fiber-reinforced polymer (BFRP) bars. Durability and long-term performance were assessed by conditioning the BFRP bars in an alkaline solution simulating the concrete environment (up to 3000 h at 60 °C) to determine their suitability as internal reinforcement for concrete elements. Thereafter, the properties were assessed and compared with the unconditioned (reference) values. In this study, three types of BFRP bars were investigated. The test results revealed that the BFRP bars had good mechanical behavior and could be placed in the same category as grade II and grade III GFRP bars (according to tensile modulus of elasticity). Their tensile strength, however, was higher than that provided by CAN/CSA S807 (2010) for CFRP bars. On the other hand, the BFRP bars showed poor alkali resistance and exhibited a remarkable reduction in mechanical properties due to the resin–fiber interface issues, which needs to be remedied to achieve the desired durability characteristics.

***Keywords*:** Fiber Reinforced Polymer (FRP); basalt fiber; FRP bar, physical; mechanical; characterization; durability; alkaline; accelerated aging; microstructural; SEM; FTIR; concrete, material specification.

4.1 Introduction

Premature degradation of concrete structures due to the corrosion of embedded steel reinforcement bars is a well-known and well-documented problem, particularly where deicing salts are routinely used, such as on concrete deck slabs and in parking garages (Tighiouart et al. 1999). The use of fiber-reinforced polymer (FRP) composite materials, for concrete structures located in severe adverse environments, has achieved worldwide acceptance because of their non-corrodible nature, higher tensile strength, and lower weight relative to conventional steel reinforcing bars. FRPs are available with a wide range of mechanical properties (tensile strength, bond strength, and modulus of elasticity) and are made with high-tensile-strength fibers such as carbon, glass, and aramid embedded in polymer matrices such as vinylester and epoxy. Moreover, FRPs can be produced as bars, ropes, tendons, and grids in a wide variety of shapes and surface configurations as well as with varied characteristics.

In a continuous effort to develop FRP technology and innovate, new types of fibers—such as basalt fibers—are being introduced to manufacture basalt-fiber-reinforced polymers (BFRPs). BFRP is the most recently FRP composite, appearing within the last decade. BFRP has good potential to provide benefits that are comparable or superior to other FRP types and provide significantly better cost-effectiveness compared to carbon FRP (CFRP). Basalt fibers show high tensile strength and modulus, good chemical resistance, extended operating-temperature range, and good environmental friendliness. Therefore, basalt fibers are ideally suited for applications involving high temperature, chemical resistance, durability, mechanical strength, and low water absorption (InfoMine Research Group 2007). In comparison to E-glass FRP, BFRP has higher strength and modulus, similar cost, and greater chemical stability. Moreover, it exhibits over five times the strength and around one-third the density of commonly used low-carbon steel bars (Zhishen et al. 2012). Few studies, however, have investigated the performance of BFRP bars, which underscores the importance of assessing their physical, mechanical properties, and durability characteristics in order to understand their behavior and generate higher confidence in these newly developed materials.

4.2 Literature Review

Basalt fiber is an inorganic fiber made from quarried basalt rock by melting the rocks at 1400 °C. The molten rocks are then extruded through small nozzles to produce continuous filaments of basalt fibers. The fibers typically have diameters ranging from 9 to 13 µm (Ross 2015). Basalt fibers have many excellent characteristics: energy-saving; environmentally friendly; natural green fiber; high tensile strength and modulus; a wide range of working temperatures (-269 to 700 °C); good acid, salt, and alkali resistance; anti-ultraviolet; low moisture absorption; good insulation; anti-radiation; and sound wave-transparent properties (Patnaik et al. 2004; Sim et al. 2005; Palmieri et al. 2009; Lopresto et al. 2011; Zhishen et al. 2012). The chemical composition of basalt fibers closely resembles that of the commonly used E- and S-glass fibers, except that basalt contains a high ratio of iron, which yields its brown color, as shown in **Table 4–1** (Parnas et al. 2007). **Figure 4–1** shows some basalt fibers. The mechanical properties of basalt fibers from different sources are also different (Sim et al. 2005), probably due to different chemical components and processing conditions, such as drawing temperature. The tensile strength of basalt fibers tends to increase with increasing drawing temperatures. This is due to increasing proportions of crystal basalt nuclei at lower temperatures, as proved by scanning electron microscopy (SEM) (Subramanian et al. 1977).

Table 4–1: Chemical composition comparison between basalt and glass FRP

Chemical Composition (%)	Basalt FRP	E-Glass FRP	S-Glass FRP
Silicon dioxide, SiO_2	48.8–51.0	52–56	64–66
Aluminum oxide, Al_2O_3	14.0–15.6	12–16	24–26
Iron oxide, $FeO+Fe_2O_3$	7.3–13.3	0.05–0.40	0–0.3
Calcium oxide, CaO	10.0	16–25	0–0.3
Magnesium oxide, MgO	6.2–16.0	0–5	9–11
Sodium oxide & potassium oxide, Na_2O+K_2O	1.9–2.2	0–2	0–0.3
Titanium oxide, TiO_2	0.9–1.6	0–0.8	--
MnO	0.10–0.16	--	--
Fluorides	--	0–1	--
Boron oxide	--	5–10	--

Figure 4–1: Basalt fibers

Wu et al. (2014) assessed the residual tensile properties of unstressed and stressed BFRP bars exposed to four types of simulated harsh environments: alkaline solution, salt solution, acid solution, and deionized water at 25, 40, and 55 °C. Microstructural analysis by scanning electronic microscopy (SEM) was also performed to reveal the inherent degradation mechanism of BFRP bars in an alkaline environment. The residual tensile strength of unstressed BFRP bars exposed to an alkaline solution was used to predict long-term performance based on the Arrhenius theory. The results showed that the effect on the durability of BFRP bars exposed to acid, salt, and deionized water was less than that for bars exposed to alkaline solution. The effects of sustained stress on the degradation of BFRP bars were not obvious when the stress level was less than 20% of ultimate strength, but the degradation processes accelerated when the stress exceeded this level. Considering a mean annual temperature of 5.7 °C (which represents an area with a northern latitude of 50°), the predicted exposure time to produce a 50% reduction in strength was estimated at approximately 16.1 years for the 6 mm BFRP bar.

Sim et al. (2005) investigated the durability and elevated-temperature performance of basalt, glass, and carbon fibers. They reported that when the fibers were immersed in an alkali solution, the basalt and glass fibers lost volume and strength (50% at 7 days and more than 80% at 28 days) with a reaction product on the surface, but the carbon fiber did not show significant strength reduction (about 13%). Nevertheless, the basalt fiber maintained its volumetric integrity and 90% of its strength after exposure to high-temperature at over 600 °C for 2 hours. Mingchao et al. (2008) studied the chemical durability and mechanical properties of basalt fiber and its epoxy resin composites. The experimental results showed that, after the BFRP was exposed to alkali solutions (including saturated Na_2CO_3 solution, 10% NaOH, and 10% $NH_3.H_2O$) for 3 months, the modulus remained unaffected, although the strength decreased by 40%. Li et al. (2012) studied the durability

and fatigue performance of basalt-fiber / epoxy-FRP bars exposed to hygrothermal and alkaline environments. The bare basalt fibers (no resin protection) immersed in these environments exhibited a severe degradation of tensile properties due to significant fiber corrosion, as revealed by SEM. In contrast, the BFRP bars evidenced higher durability when subjected to the same conditions.

This paper presents an experimental investigation aimed at assessing the physical and mechanical characteristics of newly developed BFRP bars. It also aimed at assessing their long-term durability through conditioning in an alkaline solution simulating a moist concrete environment at high temperature. Since BFRPs have not been included in design standards and specifications yet, the results of this experimental study will contribute to integrating BFRP into FRP standards and guides.

4.3 Experimental Program

This experimental work was carried out on newly developed BFRP bars to investigate their short- and long-term characteristics. This research work is a part of an extensive research project being conducted at the University of Sherbrooke through NSERC Research Chair activities to develop and introduce new FRP reinforcement for concrete infrastructure especially that subjected to harsh environmental conditions, such as marine structures, parking garages, and bridge-deck slabs. The findings of this research project will contribute to integrating BFRP into FRP standards and guides, such as ACI 440.1R (2015), ACI 440.6M (2008), CAN/CSA S807 (2010), CAN/CSA S6S1 (2010), and CAN/CSA S806 (2012).

The experimental program involved three types of BFRP bars: A, B, and C. Type A has a 7 mm diameter and is manufactured for prestressing purposes. Its physical and mechanical properties as well as durability in a concrete environment were investigated. Further study to investigate prestressing-related characteristics such as relaxation under sustained loads and creep–rupture will be conducted in another research project. Types B and C bars are 8 mm in diameter with similar surface configurations. They were provided by the manufacturer with an expected tensile modulus close to 50 and 60 GPa, simulating grade II and III GFRP bars in accordance with CAN/CSA S807 (2010). The research program was divided into three phases. Phase I focused on physical characterization of the BFRP bars. The physical properties determined in this phase served as

references for physical properties after conditioning. Phase II focused on mechanical characterization of the BFRP bars. The tensile strength, tensile modulus of elasticity, ultimate tensile strain, transverse-shear strength, flexural strength, flexural modulus of elasticity, interlaminar-shear strength, and bond strength were determined according to the appropriate test methods. The test results also served as references for calculating the residual strengths after conditioning. Phase III assessed the durability and long-term performance of the conditioned BFRP bars. The durability was assessed by immersing the BFRP specimens in an alkaline solution at high temperature (60 °C) for different lengths of time (3000 hours for Type A and 2160 hours for Types B and C) designed to simulate a concrete environment so as to validate the performance of the BFRP bars as internal reinforcement for concrete elements. Changes in the physical and mechanical characteristics were assessed by comparing the characteristics of the conditioned BFRP bars to the reference ones from Phases I and II.

4.4 Materials and Test Procedures

Three types of BFRP bars were used in this study. Type A has a 7 mm diameter (nominal cross-sectional area of 38.46 mm^2) with a woven surface, while Types B and C have a 8 mm diameter (nominal cross-sectional area of 50.24 mm^2) with a deformed surface. The BFRP bars were made of continuous basalt fibers impregnated in vinylester resin according to the pultrusion process. **Figure 4–2** shows the BFRP bars. The basalt fibers used herein were known ASA.TEC (produced by Asamer Basaltic Fibers GmbH, Austria). The fibers were produced from volcanic material with organic surface coating and had a diameter of 10 to 19 μm.

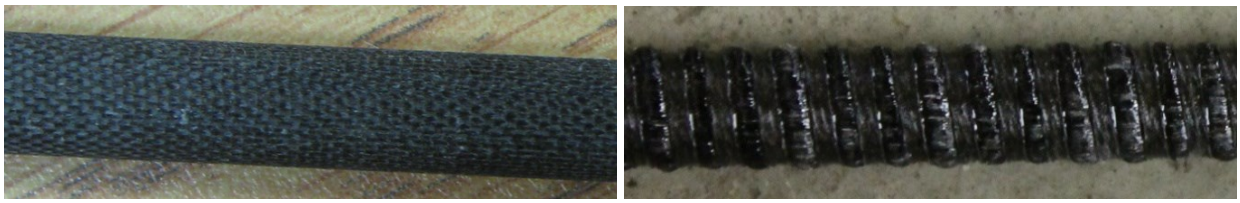

Type A BFRP Types B and C BFRP

Figure 4–2: Tested BFRP bars

The tests in Phase I (physical characterization) were conducted in accordance with ACI 440.6M (2008) and CAN/CSA S807 (2010) and the relevant ASTM standards. The relative density was determined according to ASTM D792 (2008), fiber content according to ASTM D3171 (2011), transverse coefficient of thermal expansion according to ASTM E831 (2012), water absorption according to ASTM D570 (2010), cure ratio according to ASTM D5028 (2009), and glass-transition temperature (T_g) according to ASTM D3418 (2012). In addition, microstructural analysis was performed for all three types of BFRP specimens using scanning electron microscopy (SEM) for both the unconditioned (reference) and conditioned specimens to assess changes and/or degradation. The effects of conditioning on the glass-transition temperatures (T_g) and on BFRP-bar chemical composition were also determined with differential scanning calorimetry (DSC) and Fourier transform infrared spectroscopy (FTIR), respectively.

The Phase II mechanical-characterization tests were tensile strength (ASTM D7205, 2011), transverse-shear testing (ASTM D7617, 2011), flexural testing (ASTM D4476, 2009), short-beam shear testing (ASTM D4475, 2008), and bond strength using the pullout test (ACI 440.3R, 2012, B.3 Test Method). The mechanical properties reported herein were calculated using the nominal cross-sectional areas.

Furthermore, a pilot investigation was also conducted to evaluate the effects of chemicals on the basalt fibers used in manufacturing the BFRP bars tested herein. The tests were conducted according to Owens Corning (2011) guide for glass fibers and the results are reported.

4.5 Chemical Resistance Evaluation of Bare Basalt Fibers

Chemical resistance tests were conducted on the basalt fibers utilized in manufacturing the tested BFRP bars, in parallel to the main study conducted herein to investigate the physical and mechanical characteristics of new BFRP bars. These tests were conducted to clarify the effect of the different chemicals on the bare basalt fibers. The tests were conducted following Owens Corning (2011) guide for evaluating the chemical resistance of glass fibers. Basalt fibers were heated to 540 °C overnight to remove any sizing and provide a proper clean surface for chemical-resistance investigation. Samples were then cut and carefully weighed before immersion in different corrosive aqueous solutions at 96 °C for 1 (24 h) and 7 days (168 h). The solutions were deionized water, an acidic solution (10% HCl), a saline solution (10% NaCl), and an alkaline

solution (3.2 g NaOH per liter). After conditioning, the samples were thoroughly washed, dried, and weighed again. **Table 4–2** presents the mass losses after 1 and 7 days of conditioning in deionized water, acidic solution, saline solution, and alkaline solution. The mass losses were less than 1.0% (wt) after immersion in water and saline solution, whereas the alkaline solution caused a mass loss of about 3% (wt) and the acidic solution caused a mass loss of 7.0% (wt). It should be mentioned that the color of the acidic solution turned green after conditioning, which may indicate some leaching of iron oxide.

Table 4–2: Mass loss (wt %) of basalt fibers after conditioning in water, acidic, saline, and alkaline solutions at 96 °C

Conditioning period (days)	Mass loss by weight (%)			
	Water	Acidic	Saline	Alkaline
1	0.3	5.9	-0.6	0.7
7	0.6	7.0	0.2	2.6

Furthermore, the conditioned fibers were then analyzed using SEM to detect any changes in microstructure. **Figure 4–3** presents typical micrographs obtained on unconditioned (reference) and conditioned samples (acidic, saline, and alkaline solutions). The basalt fiber conditioned in the different solutions showed tiny signs of corrosion.

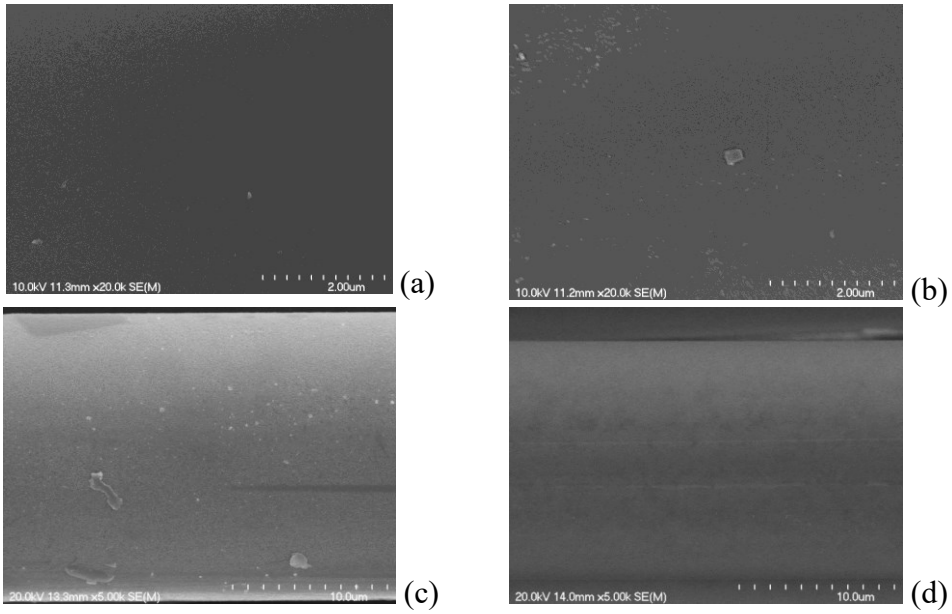

Figure 4–3: SEM micrographs of basalt fibers: (a) before condition (reference); (b) conditioned in acidic solution; (c) conditioned in saline solution; and (d) conditioned in alkaline solution

4.6 Testing, Results, and Discussion

4.6.1 Phase I: Physical Characterization

The physical properties of the reference (unconditioned) BFRP bars were determined according to ACI 440.6M (2008) and CAN/CSA S807 (2010) test methods. Since BFRP bars are not included in any FRP standard yet, the physical properties of the investigated BFRP bars and tendons were compared to the specified limits for FRP bars. **Table 4–3** presents the results of those physical characterization tests and compares them to the limits specified in ACI 440.6M (2008) and CAN/CSA S807 (2010) for FRP bars. **Table 4–3** shows that the fiber content of the BFRP bars was 85.1%, 77.4%, and 81.1% for BFRP Types A, B, and C, respectively, thereby satisfying the ACI 440.6M (2008) limits (55% by volume) and CAN/CSA S807 (2010) limits (70% by weight). The cure ratio of Type A BFRP was 97.5%, while the curing ratio of Types B and C was 100%. The BFRP specimens had a transverse coefficient of thermal expansion (CTE) ranging from 18.4×10^{-6} to 26.8×10^{-6} ºC, which is less than 40×10^{-6} ºC as stated by CAN/CSA S807 (2010). Type B's higher transverse CTE as compared to Types A and C may be due to the lower fiber content (higher resin content).

Differential scanning calorimetry (DSC) is used to obtain information about the thermal behavior and characteristics of polymer materials and composites, such as the glass-transition temperature (T_g) and curing process. In this study, 30-50 mg specimens from both the unconditioned and conditioned specimens were sealed in aluminum pans and heated in a TA Instruments DSC Q10 calorimeter to 200 °C at a rate of 20 ºC/min. The glass-transition temperature (T_g) was determined in accordance with ASTM D3418 (2012). Two scans were performed for each BFRP type. **Figure 4–4** presents the DSC scans for the T_g, while **Table 4–3** presents the T_g values. Since the cure ratio of BFRP type A was 97.5%, this indicates the presence of uncured resin. Consequently, BFRP type A showed a T_g of 105 °C in the first run and 123 °C in the second run because of the post-polymerization of uncured resin. BFRP types B and C evidenced a T_g of 118 and 127 ºC, respectively, with no post-polymerization, since the T_g in the second run was almost the same as in the first. It should be mentioned that the higher T_g of the specimens after the second scan is an indicative of a reversible chemical reaction and consequently not caused by any chemical degradation of the resin (such as hydrolysis).

The moisture uptake at saturation was determined. The test was carried out in accordance with ASTM D570 (2010). Five 100 mm long specimens for each type of BFRP were cut, dried, and weighed. They were then immersed in water at 50 °C for 3 weeks. The samples were periodically removed from the water, surface dried, and weighed. The water content as a percentage of weight was calculated with Eq. (4-1).

$$W = \frac{(P_s - P_d)}{P_d} \times 100 \tag{4-1}$$

where P_s and P_d are the bar weights in the saturated and dried states, respectively. The percentage of moisture uptake was calculated. The gain in mass was corrected to account for specimen mass loss due to a possible dissolution phenomenon. This correction was achieved by completely drying the immersed specimens in an oven at 100 °C for 24 h and comparing their masses to their initial masses. The moisture uptake was 0.15%, 0.56%, and 0.62% for types A, B, and C, respectively. This difference is due to delamination and/or debonding of the fiber–resin interface or due to the presence of continuous voids, which will be discussed later in this paper.

It should be mentioned that the BFRP bars met the requirements of D1 FRP bars (FRP bars with high durability) in accordance with CAN/CSA S807 (2010) with respect to cure ratio, T_g, and moisture uptake. Regardless of the differences between the results for the three BFRP products tested, they still meet the physical-property requirements of ACI 440.6M (2008) and CAN/CSA S807 (2010).

Table 4–3: Results for physical properties of BFRP bars and the specified limits for FRPs

Property	Type (A)	Type (B)	Type (C)	Specified Limits for FRP Bars	
				ACI 440.6M (2008)	CAN/CSA S807 (2010)
Relative density (ρ)	2.167	1.998	2.046	--	--
Fiber content by weight (%)	85.1	77.4	81.1	55% (by vol.)	70% (by weight)
Transverse CTE ($\times 10^{-6}$ °C^{-1})	18.7	26.8	18.4	NA	40
Cure ratio (%)	97.5	100	100	NA	≥ 93 (D2)[a]; 95 (D1)[a]
T_g (°C) – Run 1	105	118	127	100	≥ 80 (D2)[a]; 100 (D1)[a]
Run 2	123	119	129		
Moisture uptake (%)	0.15	0.56	0.62	1.0	1.0 (D2)[a]; 0.75 (D1)[a]

[a] Classification based on durability: FRPs with high durability shall be classified as D1; FRPs with moderate durability shall be classified as D2; FRPs made with vinylester and epoxy shall be classified as D1 or D2; FRPs made with polyester matrix shall be classified as D2.

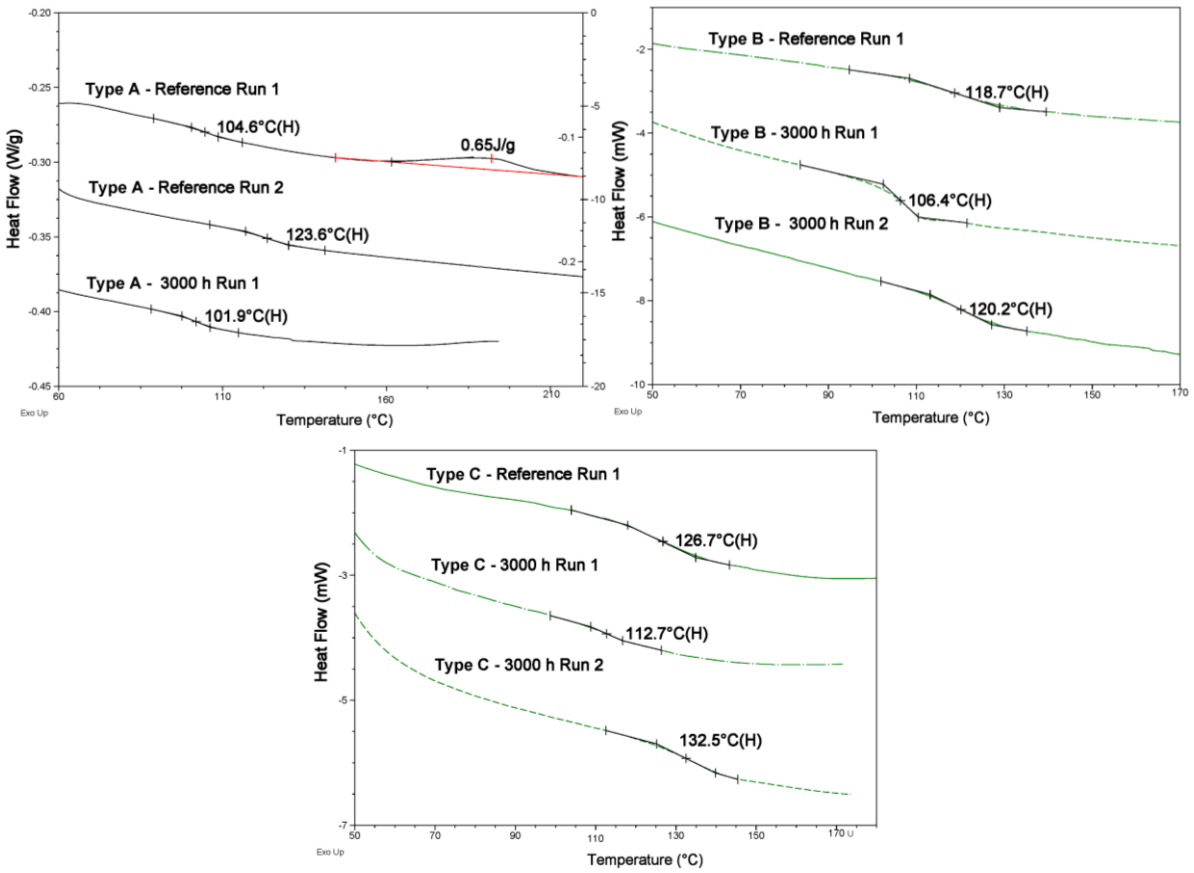

Figure 4–4: DSC graphs for glass-transition temperature (T_g)

4.6.2 Phase II: Mechanical Characterization

The mechanical characterization included testing of representative BFRP specimens to determine their tensile properties in accordance with ASTM D7205 (2011), transverse-shear strength in accordance with ASTM D7617 (2011), flexural properties in accordance with ASTM D4476 (2009), interlaminate shear strength in accordance with ASTM D4475 (2008), and bond strength in accordance with ACI 440.3R (2012), B.3 Test Method, and CAN/CSA S806 (2012), Annex G. **Figure 4–5** to **Figure 4–9** show the mechanical characterization tests and the tested specimens at failure, while **Table 4–4** lists the results. The following sections provide brief descriptions and interpretation of those results.

4.6.2.1 Tensile Properties of the Reference BFRP Bars

The tensile properties of FRP bars are among the most important parameters affecting the design of FRP-reinforced concrete sections, since tensile strength governs section capacity and the tensile modulus of elasticity governs the serviceability limit state. The tensile properties of the investigated BFRP bars were determined by testing five representative specimens for each type in accordance with ASTM D7205 (2011). The specimens were cut to the desired lengths and prepared by installing the steel tube (anchors) with expansive cement grout commercially known as Bustar Expanding Grout. The specimens were instrumented with a 200 mm LVDT to capture specimen elongation during testing. The tests were conducted with a Baldwin testing machine in which the applied load and specimen elongation were electronically recorded during the test. **Figure 4–5 (a)** shows the test setup. The tensile strength and tensile modulus of the BFRP bars were determined with Eqns. (4-2) and (4-3), respectively,

$$f_u = F_u / A \tag{4-2}$$

where f_u is the tensile strength (MPa), F_u is the tensile capacity (N), and A is the bar's cross-sectional area (mm^2).

$$E = (F_1 - F_2) / ((\varepsilon_1 - \varepsilon_2) A) \tag{4-3}$$

where E is the tensile modulus of elasticity (MPa); A is the cross-sectional area (mm^2); F_1 and ε_1 are the load and corresponding strain, respectively, at approximately 50% of the ultimate tensile

capacity; and F_2 and ε_2 are the load and corresponding strain, respectively, at approximately 25% of the ultimate tensile capacity. The tensile properties of the tested specimens are listed in **Table 4–4** and the failure is shown in **Figure 4–5 (b)**.

Like all FRP products, the tested specimens showed a linear elastic stress–strain relationship up to failure. The tested bars showed very high tensile strength exceeding 1500 MPa, which meets the requirements of GFRP (750 MPa for 8 mm diameter) and CFRP (1350 MPa for 8 mm diameter) bars according to CAN/CSA S807 (2010). On the other hand, Types A and B showed tensile moduli of elasticity of 69.0 and 64.6 GPa, respectively, which correspond to grade III (GIII) for GFRP bars according to CAN/CSA S807 (2010) classification. Type C, however, had tensile modulus of elasticity of 59.5 GPa, which corresponds to grade II (GII) for GFRP bars according to CAN/CSA S807 (2010) classification. Furthermore, the tested specimens showed a strain at failure ranging from 2.43% to 2.64%, both higher than the 1.2% provided by CAN/CSA S807 (2010) for GFRP bars.

It should be mentioned that the design of FRP-reinforced members is based on guaranteed tensile strength (the mean tensile strength minus three times the standard deviation in according to ACI 440.1R (2006)).

Table 4–4: Mechanical properties of tested BFRP bars (reference/unconditioned)

BFRP Type	Tensile Properties			Transverse-Shear Strength	Interlaminar-Shear Strength	Flexural Properties			Bond Strength
	f_u (MPa)	E (GPa)	ε_u (%)	τ_u (MPa)	S_u (MPa)	f_u (MPa)	E (GPa)	ε_u (%)	f_b (MPa)
A	1680 ±133	69.0 ±0.7	2.43	344 ±18	63 ±2.7	1790 ±91	90.4 ±3.8	1.98	7.0 ±0.9
B	1655 ±95	64.6 ±1.4	2.56	315 ±38	72 ±2.9	2061 ±216	84.6 ±8.6	2.47	25.4 ± 2.3
C	1567 ±115	59.5 ±3.3	2.64	293 ±28	60 ±2.4	1587 ±111	74.0 ±4.2	2.15	27.2 ± 2.4

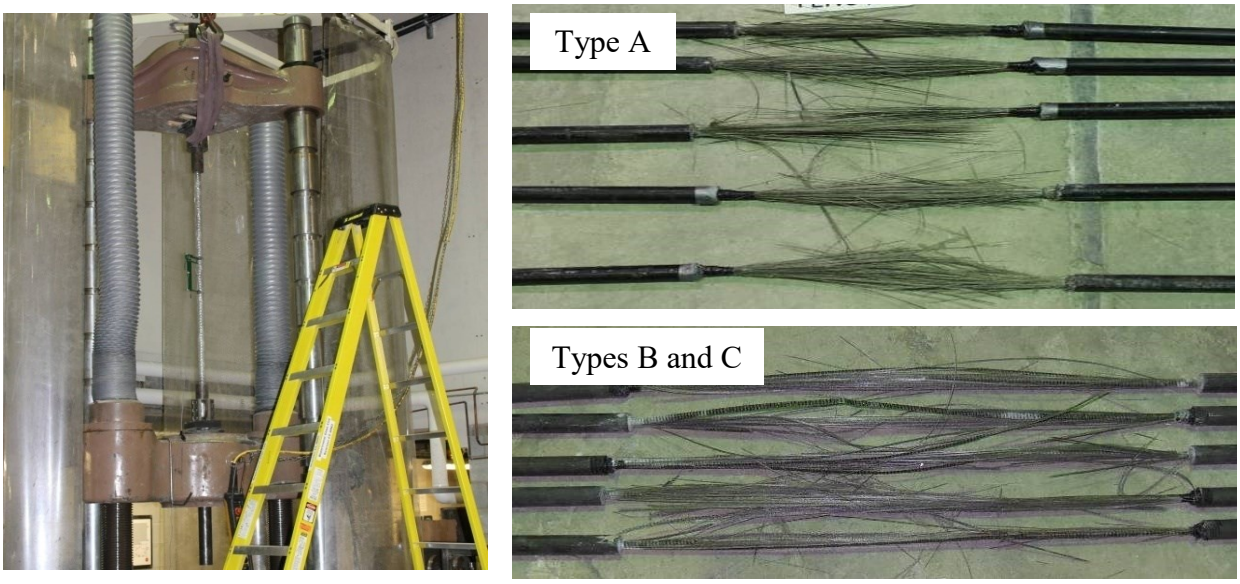

(a) Typical test setup (b) Failure mode (rupture)

Figure 4–5: Typical tensile-strength test and failure mode

4.6.2.2 Transverse-Shear Strength of the Reference BFRP Bars

Transverse-shear tests were conducted according to ASTM D7617 (2011). The setup consisted of a 230 × 100 × 110 mm steel base equipped with lower blades spaced at 50 mm face to face, allowing for the double transverse-shear failure of the specimen caused by an upper blade, as shown in **Figure 4–6 (a)**.

For each type of BFRP bar, five unconditioned specimens of 200 mm length were tested under laboratory conditions with an MTS 810 testing machine equipped with a 500 kN load cell. A displacement-controlled rate of 1.3 mm/min was used during the test, which yielded between 30 and 60 MPa/min until specimen failure. The loading was performed without subjecting the test specimens to any shock. **Figure 4–6 (b)** shows the specimens at failure. The transverse-shear strength was calculated with Eq. (4-4):

$$\tau_u = P_s/(2A) \tag{4-4}$$

where τ_u is the transverse-shear strength (MPa), P_s is the failure load (N), and A is the cross-sectional area of the FRP bar (mm²).

As shown in **Table 4–4**, the transverse-shear strength of the BFRP specimens ranged from 293 to 344 MPa, with an average of 317 MPa. These values meet the requirements of CAN/CSA S807 (2010), which specifies a minimum transverse-shear strength of 160 MPa for FRP bars. These results were expected, since the transverse-shear strength resulted mainly from the resin with a small contribution from the fiber–resin interface (Montaigu et al. 2013).

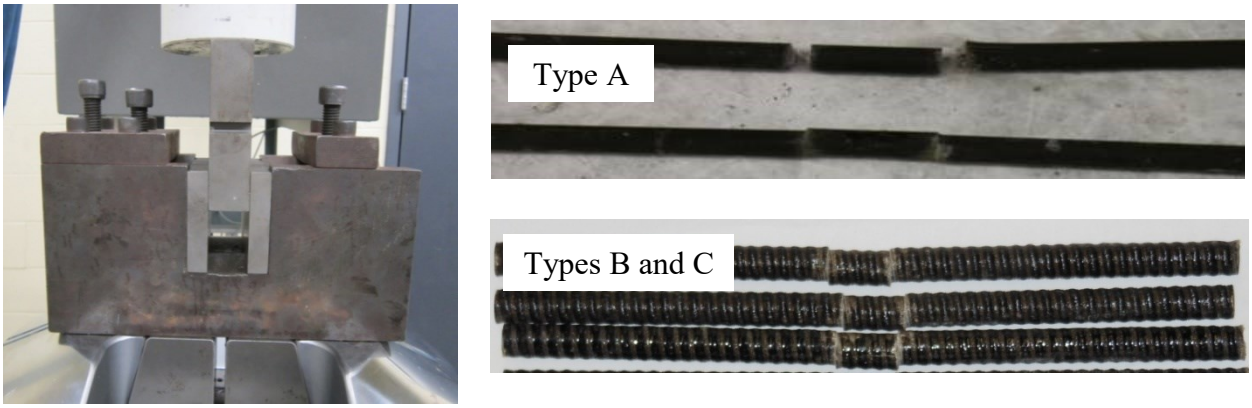

(a) Test setup (b) Specimens at failure

Figure 4–6: Typical transverse-shear strength and specimens at failure

4.6.2.3 Interlaminar-Shear Strength of the Reference BFRP Bars (Short-Beam Shear Test)

In pultruded FRP bars in which the fibers are arranged unidirectionally and bonded with the polymer matrix, the horizontal stresses would be more conducive to inducing interface degradation than transverse-shear stresses (Park et al. 2008). The short-beam shear test was conducted on five specimens of each type of FRP bar according to ASTM D4475 (2008) in order to calculate the interlaminar-shear strength, which is governed by the fiber–matrix interface. The tests were carried out with a 500-kN MTS 810 testing machine. The distance between the shear planes was set to 6 times the nominal diameter of the FRP bars. **Figure 4–7** shows the test setup and typical mode of failure of the tested specimens. A displacement-controlled rate of 1.3 mm/min was used during the test. The applied load was recorded with a computer-monitored data-acquisition system.

The interlaminar-shear strength, S_u, of the FRP bars was calculated with Eq. (4-5).

$$S_u = 0.849P/d^2 \qquad (4\text{-}5)$$

where S_u is the interlaminar-shear strength (MPa), P is the shear failure load (N), and d is the bar diameter (mm).

Table 4–4 shows the interlaminar-shear strength of BFRP bars. BFRP Type B exhibited the highest interlaminar-shear strength (72 MPa), followed by Type A (63 MPa) and Type C (60 MPa). It is worth mentioning that the high values of the interlaminar-shear strength indicate a sound interface between the resins and reinforcing fibers. The difference between the highest (Type B) and the lowest (Type C) interlaminar-shear strength was 20%. This difference may have been affected by fiber–resin interface issue, which will be clarified in the SEM analysis.

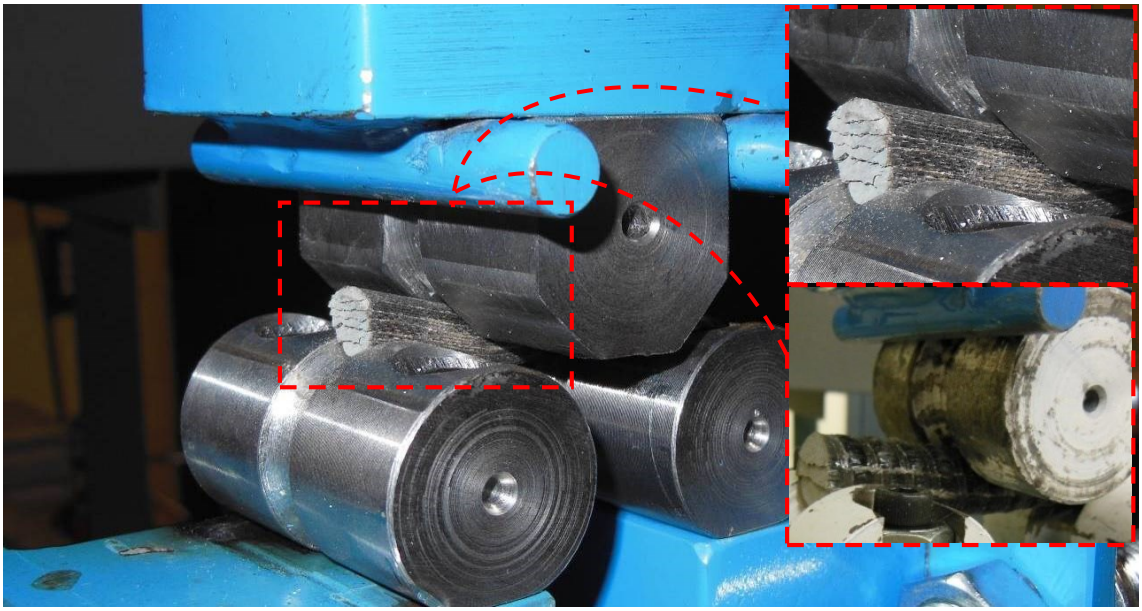

(a) Test setup for the short-beam shear test

(b) Specimens at failure

Figure 4–7: Interlaminar-shear-strength test (short-beam test) and specimens at failure

4.6.2.4 Flexural Properties of the Reference BFRP Bars (Three-Point Flexural Test)

Flexural testing is especially useful for quality control and specification purposes. Flexural properties may vary with specimen diameter, temperature, weather conditions, and differences in rates of straining. The flexural properties obtained according to ASTM D4476 (2009) cannot be used for design purposes, but are appropriate for the comparative testing of composite materials. The test was conducted on specimens of 180 mm long over a simply supported span equal to 20 times the bar diameter, as shown in **Figure 4–8 (a)**. Five unconditioned specimens were tested under laboratory conditions on an MTS 810 testing machine equipped with a 500 kN load cell as references for each type. The specimens were loaded at the mid-span with a circular nose; the specimen ends rested on two circular supports that allowed the specimens to bend. A displacement-controlled rate of 3.0 mm/min was used during the test. The rate of loading occurred without subjecting the test specimen to any shock. The applied load and deflection were recorded during the test on a computer- monitored data-acquisition system.

The flexural strength of tested FRP specimens was calculated with Eq. (4-6). Flexural modulus of elasticity is the ratio, within elastic limit, of stress to corresponding strain. It was calculated with Eq. (4-7):

$$f_u = P\,L\,C/(4\,I) \tag{4-6}$$

$$E = P\,L^3/(48\,I\,Y) \tag{4-7}$$

where f_u is the flexural strength in the outer fibers at mid-span (N/mm^2), P is the failure load (N), L is the clear span (mm), I is the moment of inertia (mm^4), C is the distance from the centroid to the extremities (mm), E is the flexural modulus of elasticity in bending (N/mm^2), and Y is the mid-span deflection at load P (mm).

The maximum outer-fiber strain (ε_u) was calculated from Eq. (4-8).

$$\varepsilon_u = f_u/E \tag{4-8}$$

Table 4–4 provides test results of three-point loading test for the BFRP specimens in terms of flexural strength, flexural modulus of elasticity, and ultimate strain. The elastic behavior of all the specimens was retained until flexural failure, which occurred due to compression at the top fibers,

as shown in **Figure 4–8 (b)**. The moduli of elasticity from the flexural test were 24% to 31% higher than those from the tensile test. Since the ASTM D4476 (2009) test method is designated for FRP bars with a diameter of at least 0.5 in. (12.7 mm), this may have impacted the flexural testing results.

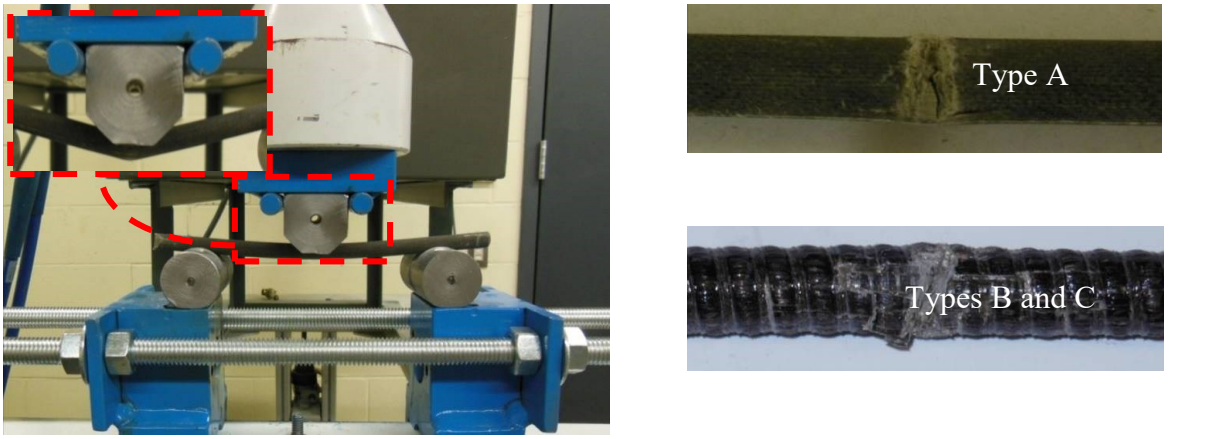

(a) Test setup (b) Specimens at failure (compression failure)

Figure 4–8: Typical flexural-strength test and specimens at failure

4.6.2.5 Bond Strength of the Reference BFRP Bars (Pullout Test)

The bond strength of the BFRP bars was assessed with the pullout test. The pullout tests were carried out in normal-strength concrete with a designated strength of 35 MPa after 28 days according to the ACI 440.3R (2012), B.3 Test Method, and CAN/CSA S806 (2012), Annex G. The bonded length was kept constant at $5d_b$, where d_b is the nominal diameter of FRP bars. The pullout blocks measured 200 × 200 × 200 mm. **Figure 4–9** shows the geometry of the pullout specimens, test setup, and modes of failure, while **Figure 4–10** shows the typical bond stress-free slip relationship of the tested BFRP bars. **Table 4–4** presents the bond strength of the tested BFRP bars.

The BFRP Type A (manufactured for prestressing purposes) showed an average bond strength of 7.0 MPa. According to CEB-FIP (1978), the bond strength of prestressing steel bars of a diameter smaller than 32 mm in normal-weight concrete with compressive strength of 35 MPa is about 4 MPa for deformed bars and 2.0 MPa for smooth bars. Thus, the bond strength obtained herein is in agreement with what has been reported for steel tendons. On the other hand, the pullout tests of the Types B and C (with similar surface configurations) showed an average bond strength of 24.5 and 27.2 MPa, respectively, which is higher than 8.0 MPa as specified by CAN/CSA S807 (2010).

Thus, it could be concluded that Types B and C meet the mechanical-property requirements of CAN/CSA S807 (2010).

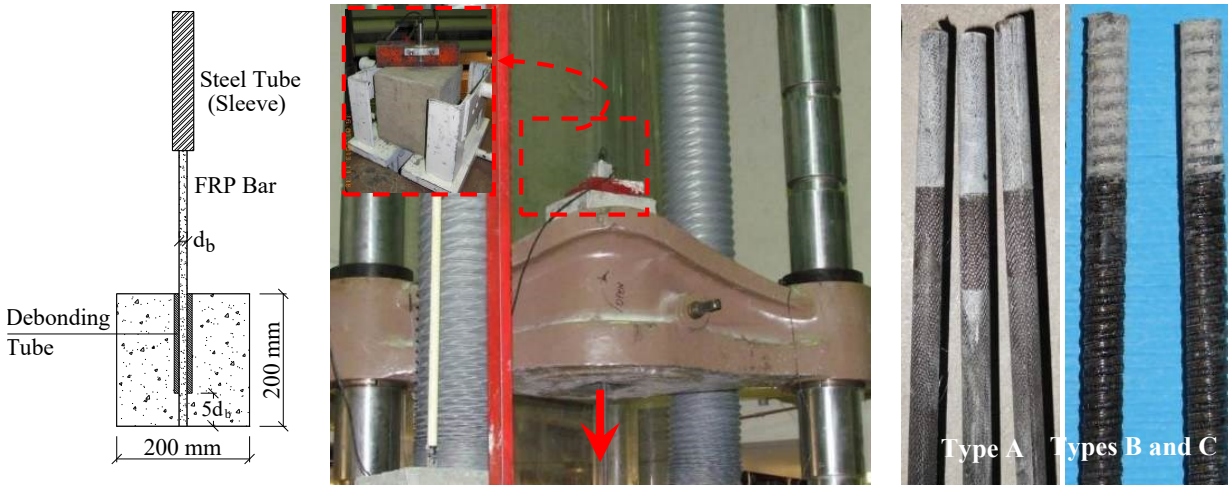

(a) (b) (c)

Figure 4–9: Pullout test: (a) Specimen geometry; (b) Test setup; (c) Typical pullout bond failure

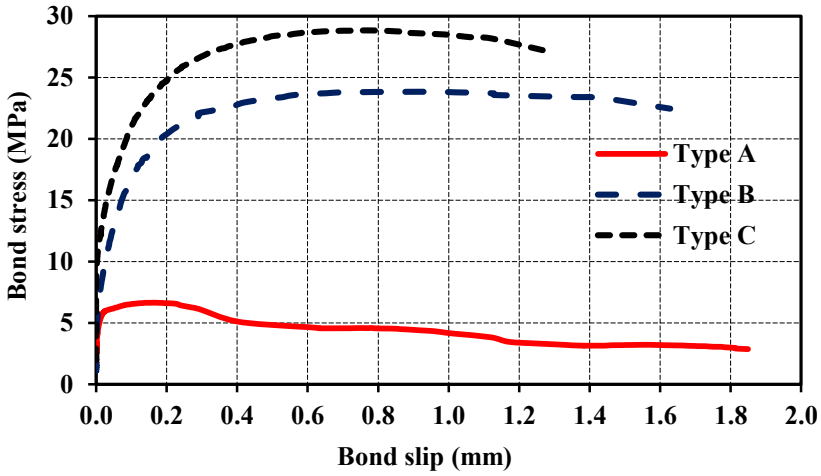

Figure 4–10: Bond stress-free slip relationships of the tested BFRP bars

4.6.3 Phase III: Durability Study and Long-Term Performance Assessment

4.6.3.1 Conditioning of the BFRP Specimens

This phase was conducted to assess the durability and long-term performance of the BFRP bars conditioned in an alkaline solution simulating concrete pore solution. Accelerated aging tests were conducted in accordance with ASTM D7705 (2012). The conditioning of the FRP bars included a combined exposure to an alkaline environment and elevated temperature. Immersion in an aqueous

media (alkaline solution) at high temperature accelerates degradation. The alkaline solution was prepared to have a composition representative of the pore water inside Portland-cement concrete, specifically, 118.5 g of $Ca(OH)_2$, 0.9 g of NaOH, and 4.2 g of KOH per liter of deionized water. The solution had a pH of 12.6-13.0, which is representative of a mature concrete pore solution. The three types of BFRP bars were immersed in this solution at 60 °C. The BFRP specimens were conditioned for different lengths of time (1000 and 3000 h for BFRP Type A; 720 and 2160 h for BFRP Types B and C). The conditioning time started once the solution had reached the prescribed temperature. Robert et al. (2009) reported that the increase in degradation reaction rate was almost linear between room temperature and 50 °C, whereas, at higher temperatures (over 60 °C), the increase in the degradation reaction rate was exponential. Therefore, to avoid any thermal degradation, the maximum conditioning temperature used in this study was 60 °C, as specified in ASTM D7705 (2012).

The BFRP specimens were placed in hermetically sealed stainless-steel containers to prevent excessive evaporation and reaction of atmospheric CO_2 with calcium hydroxide. The containers were placed in an environmental chamber adjusted to the prescribed temperature (60 °C) under isothermal conditions. The BFRP bars were weighed and their diameters measured throughout the conditioning period to monitor water absorption and eventually characterize the mass and diameter changes. Observation revealed no changes in diameter during the conditioning periods. Specimens of each type of BFRP bar were removed from the solution and tested to determine their physical and mechanical properties after the exposure periods at 60 °C. Similar to as in Phase I, the effects of conditioning on the glass-transition temperatures (T_g) and chemical composition were also assessed with differential scanning calorimetry (DSC) and Fourier transform infrared spectroscopy (FTIR), respectively. The microstructure of all types of the BFRP bars was investigated with scanning electron microscopy (SEM) for both conditioned and unconditioned cases to assess changes and/or degradation. In addition, the mechanical properties of the conditioned specimens were assessed with tests similar to those in Phase II for tensile strength (ASTM D7205, 2011), transverse shear (ASTM D7617, 2011), flexural strength (ASTM D4476, 2009), and short-beam shear (ASTM D4475, 2008). The results for the conditioned specimens were compared to those of the reference ones. The change in the properties was selected as an indicator on the degradation of the BFRP materials.

4.6.3.2 Tensile Properties of the Conditioned BFRP Bars

Table 4–5 presents the ultimate tensile strength, tensile modulus of elasticity, and ultimate tensile strain of the conditioned specimens along with the retention ratios. The results indicate that the BFRP Type A bars were highly affected by accelerated aging with an ultimate tensile strength retention of 60.9% after 3000 h in an alkaline solution at 60 ºC. Types B and C were less affected by accelerated aging with ultimate tensile strength retentions of 77.0% and 76.5%, respectively, after 2160 h. Thus, BFRP Types B and C satisfied the 70% retention in accordance to CAN/CSA S807 (2010) for D2 bars, but these bars did not qualify for the 80% specified for D1 bars. On the other hand, as expected, the changes in the tensile moduli of elasticity were not significant for the tested BFRP specimens (less than 7.0%). **Figure 4–11 (a)** and **(b)** show the effect of the alkaline solution at high temperature (60 °C) on the tensile strength and modulus of elasticity of the BFRP specimens, respectively.

Table 4–5: Tensile properties and retention of the conditioned BFRP bars

BFRP Type	Cond. Period (h)	f_u (MPa)	Retention (%)	E (GPa)	Retention (%)	ε_u (%)
A	1000	1012±47.3	60.2	70.8±1.2	102.6	1.43±0.05
	3000	1023±177.0	60.9	69.1±0.4	100.0	1.48±0.26
B	720	1429±52.6	86.3	60.1±0.7	93.0	2.38±0.06
	2160	1275±4.0	77.0	61.5±0.9	95.2	2.07±0.03
C	720	1409±91.7	89.9	59.7±1.6	100.0	2.36±0.13
	2160	1198±31.7	76.5	56.6±0.9	95.1	2.12±0.02

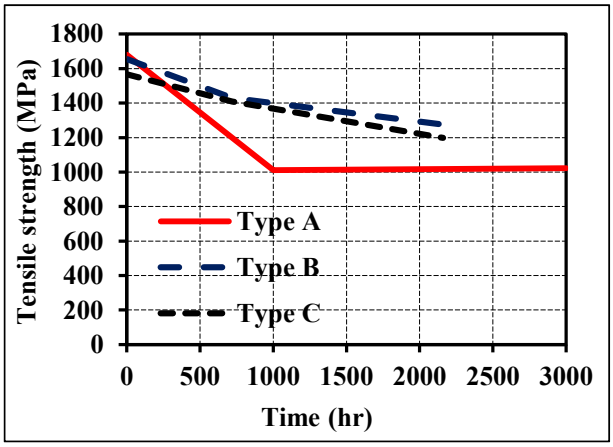

(a) Tensile strength

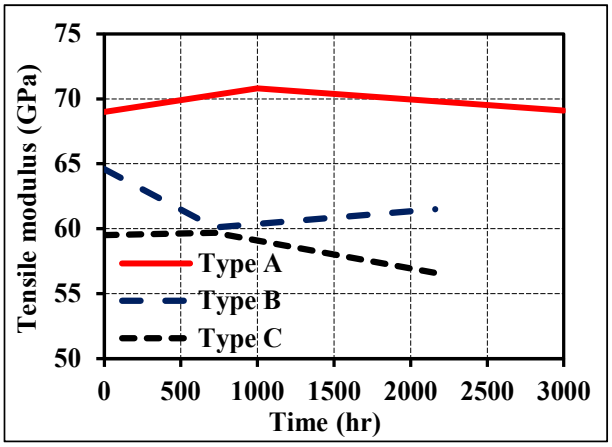

(b) Tensile modulus

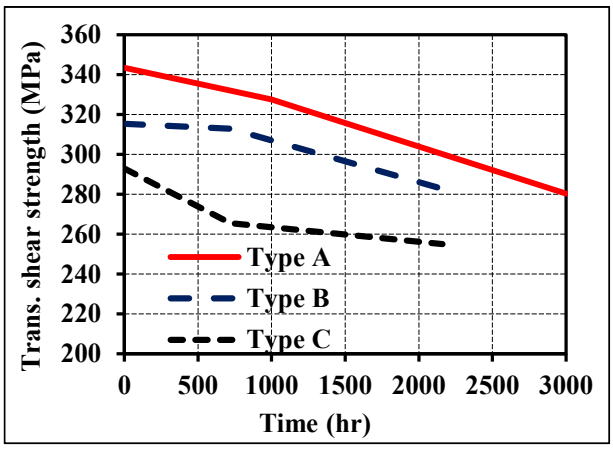

(c) Transverse-shear strength

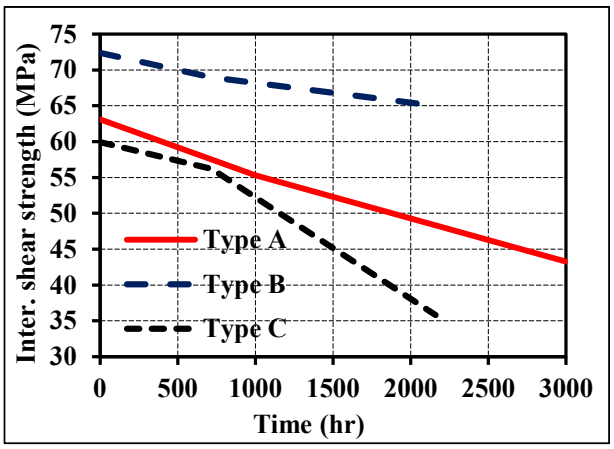

(d) Interlaminar-shear strength

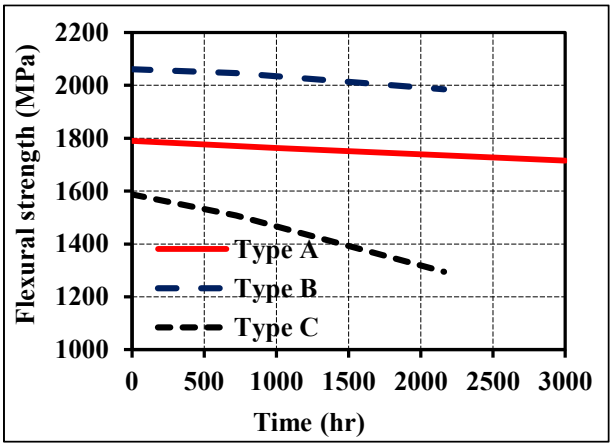

(e) Flexural strength

Figure 4–11: Effect of conditioning on the mechanical properties of the tested BFRP bars

4.6.3.3 Transverse-Shear Strength of the Conditioned BFRP Bars

Table 4–6 shows the ultimate transverse-shear strength and the retention strength of the BFRP bars after conditioning. The Type A bars were affected by accelerated aging and had a transverse-shear strength retention of 81.7% after 3000 h. The Type B and C bars were slightly affected by accelerated aging and evidenced strength retentions of 89.6% and 87.0%, respectively, after conditioning for 2160 hours. **Figure 4–11 (c)** shows the effect of the alkaline solution at high temperature (60 °C) on the transverse-shear strength of BFRP specimens.

4.6.3.4 Interlaminar-Shear Strength of the Conditioned BFRP Bars

Table 4–6 shows the interlaminar-shear strength of the conditioned BFRP bars and their retention-strength ratios. **Figure 4–11 (d)** shows the effect of the alkaline solution at high temperature (60 °C) on interlaminar-shear strength. Clearly, Type B has the highest interlaminar-shear strength and the lowest rate of degradation due to conditioning, followed by Types A and C. This observation coincides with the results for the reference specimens where Type B had an interlaminar-shear strength of 72 MPa compared to 63 MPa and 60 MPa for Types A and C, respectively. This indicates that the Type B bars had a better fiber–matrix interface, which minimized the degradation due to conditioning. The fiber–matrix interface was investigated, as described later, with SEM.

Table 4–6: Transverse- and interlaminar-shear strength and retention of the conditioned BFRP bars

BFRP Type	Cond. Period (h)	τ_u (MPa)	Retention (%)	S_u (MPa)	Retention (%)
A	1000	327.5±7.6	95.4	55.3±2.8	87.7
	3000	280.4±7.3	81.7	43.25±1.3	68.5
B	720	312.9±36.6	99.2	68.98±3.0	95.3
	2160	282.7±30.0	89.6	65.00±5.1	89.8
C	720	265.6±11.3	90.6	56.20±2.7	93.8
	2160	254.9±15.9	87.0	35.82±7.0	59.8

4.6.3.5 Flexural Properties of the Conditioned BFRP Bars

Table 4–7 shows the flexural properties of conditioned BFRP bars as well as their retention strengths and modulus ratios after conditioning. **Figure 4–11 (e)** shows the effect of the alkaline solution on flexural strength. Type B bars have the lowest degradation rate, followed by Type A bars and Type C bars, the latter being significantly affected by the conditioning. This observation confirms good bonding between the basalt fibers and resin (fiber–matrix interface) in Type B, followed by Types A and C, which minimized degradation due to conditioning.

Table 4–7: Flexural properties and retention of the conditioned BFRP Bars

BFRP Type	Cond. Period (h)	f_u (MPa)	Retention (%)	E (GPa)	Retention (%)
A	1000	1763.3±60.9	98.5	93.0±2.4	102.8
	3000	1715.2±100.7	95.6	90.8±1.0	100.0
B	720	2047.0±197.1	99.3	72.7±2.7	85.9
	2160	1985.2±77.9	96.3	66.7±4.4	78.8
C	720	1507.4±156.9	95.0	63.7±1.3	86.1
	2160	1295.5±153.5	81.6	63.0±1.7	85.1

4.6.3.6 Glass-Transition Temperature of the Conditioned BFRP Bars

Differential scanning calorimetry (DSC) was also conducted on the specimens conditioned in the alkaline solution at 60 °C for 3000 h; the glass-transition temperature was determined in accordance with ASTM D3418 (2012). Two scans were performed for each BFRP type. **Figure 4–4** presents the DSC scans for the T_g. The first scan was useful to determine the difference in T_g between the reference and conditioned specimens. A decrease in T_g for the conditioned specimens is indicative of a plasticizing effect or chemical degradation. A higher specimen T_g after the second scan is indicative of a reversible chemical reaction and consequently not caused by any chemical degradation of the resin (such as hydrolysis). The conditioned BFRP specimens showed first-run T_g values of 101, 108, and 113 °C for Types A, B, and C, respectively. The T_g values from the second run were 117, 121, and 134 °C for Types A, B, and C, respectively. The increased T_g in the second run can be explained by a reversible chemical reaction.

4.6.3.7 Moisture Uptake at Saturation of the Conditioned BFRP Bars

The moisture uptake at saturation was also determined for the specimens conditioned in the alkaline solution at 60 °C for 3000 h. The moisture-uptake ratios at saturation for the reference specimens were 0.15%, 0.56%, and 0.62% for Types A, B, and C, respectively. The moisture-uptake ratios at saturation for the conditioned specimens were 0.16%, 0.49%, and 0.59% for Types A, B, and C, respectively. Clearly, the conditioned and reference specimens had similar moisture uptakes.

4.6.3.8 Microstructural Analysis of the Reference and Conditioned BFRP Bars

Scanning-electron-microscopy (SEM) observations were performed to investigate microstructural changes in the BFRP bars before and after conditioning. The analysis was carried out on a JEOL JSM-840A microscope. The specimens were cut in one-inch lengths and placed in cylindrical molds, where epoxy resin was cast. After 24 h of curing at room temperature, the samples were removed and cut with a low-speed saw equipped with a diamond blade. Then, the specimens were polished and coated with a thin layer of gold/palladium in a vapor-deposit process. Thereafter, microstructural observations were performed with a JEOL JSM-840A microscope.

Figure 4–12 presents micrographs of the reference and conditioned BFRP specimens. SEM of the reference specimens revealed some delamination or gaps between fibers and the resin (fiber–matrix interface). The micrographs show that the worst fiber–matrix interface was observed in Type C, where complete separation between fibers and resin was evident. On the other hand, the micrographs of the Type A reference specimens revealed no significant issues with the fiber–matrix interface. These results can account for the highest moisture uptake measured at saturation for the Type C bars.

The initial status of the fiber–matrix interface (reference specimens) usually gave indications of the rate of degradation and the changes in mechanical properties related specifically to the fiber–matrix interface, such as interlaminar-shear strength. The presence of fiber–matrix delamination or voids accelerates degradation, since it allows the alkaline solution to penetrate between the fibers and resin, resulting in a higher diffusion of hydroxyl ions in the polymer matrix. **Figure 4–12** clearly shows the conditioning-related degradation of the fiber–matrix interface in the tested BFRP bars. Since the Type C reference specimens showed such significant delamination of the fiber–matrix interface, the degradation was noticeable in the properties related to the fiber–matrix

interface. The reduction in the interlaminar-shear strength of the conditioned Type C specimens was 40.2% (59.8% retention).

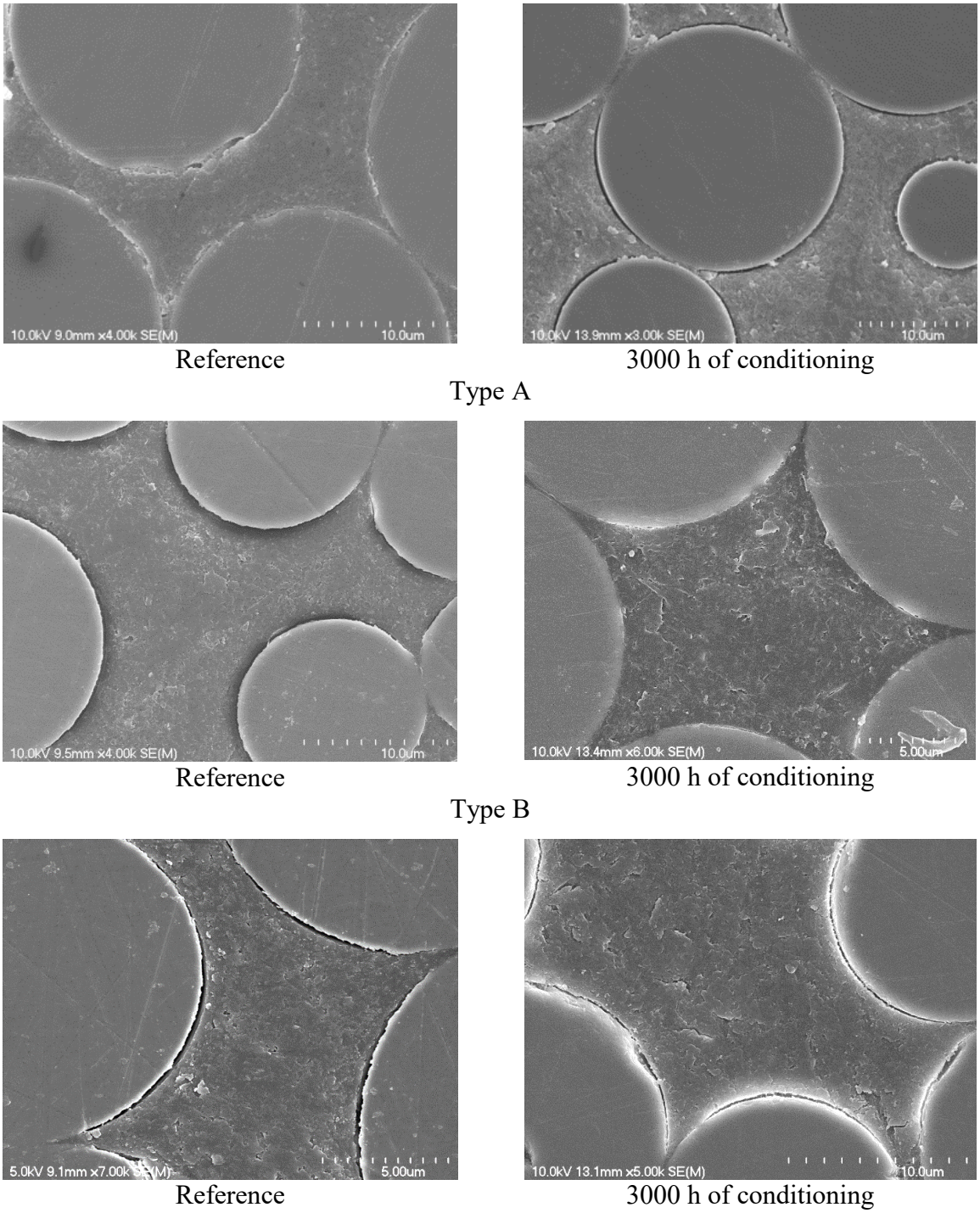

Figure 4–12: Micrograph of the unconditioned and conditioned BFRP bars

4.6.3.9 Chemical Changes in the BFRP Bars after Conditioning

Fourier transform infrared spectroscopy (FTIR) was used to identify any chemical change/degradation after conditioning. FTIR spectra were recorded with an ABB-Bomen (MB series) spectrometer equipped with an attenuated total reflectance device. Thirty-two scans were routinely acquired with an optical retardation of 0.25 cm to yield a resolution of 4 cm^{-1}. The reference and 3000 h conditioned specimens were investigated.

Figure 4–13 shows the FTIR analysis of the reference and conditioned BFRP bars. The Type A reference and conditioned specimens evidenced very similar spectra. The hydroxyl peak did not show any significant changes, which means that the amount of hydroxyl groups present in the resins had not increased. This observation confirms that the resins did not degrade chemically when the BFRP bars were immersed in the alkaline solution at 60 °C for 3000 h. In the case of Types B and C, a very small increase in the peak related to hydroxyl groups (-OH) around 3400 cm^{-1} was observed. This could be due to a slight chemical degradation of the resin matrix through a hydrolysis reaction or more probably the presence of alkalis or water from the conditioning solution.

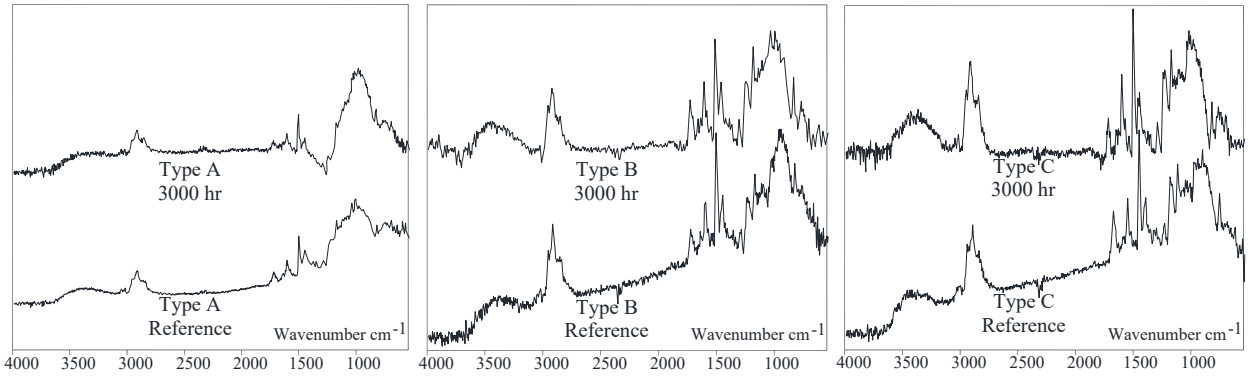

Figure 4–13: FTIR spectra of the BFRP specimens

4.7 Summary and Conclusions

This paper presented the result of an investigation conducted to characterize newly developed basalt-fiber-reinforced polymer (BFRP) bars. The experiments included physical and mechanical testing of reference and alkali-conditioned specimens. The testing was conducted according to ACI

440.6M (2008) and CAN/CSA S807 (2010) as well as relevant ASTM standard test methods. Based on the test results presented herein, the following conclusions can be drawn:

1. These results confirmed that the basalt-FRP (BFRP) bars meet the requirements of ACI 440.6M (2008) and CAN/CSA S807 (2010) with respect to physical and mechanical properties. The bond strength of the Type A BFRP bars (manufactured for prestressing purposes) obtained herein was in agreement with CEP-FIP (1978) values for steel tendons. The long-term testing, however, showed significant degradation and reduction in the mechanical properties of the alkali-conditioned specimens.

2. The results confirmed that the basalt fibers and resins used in this study were not affected by the conditioning. The strength degradation observed in the BFRP bars was attributed to the fiber–matrix interface (sizing), which evidenced poor bonding between the resin and basalt fibers, as confirmed by scanning electronic microscopy (SEM). Addressing this aspect is essential for producing durable BFRP bars that perform well in concrete environments.

3. The results obtained herein contribute to developing and enhancing the properties of BFRP bars. Further investigations on different BFRP products should be conducted to generate more confidence and encourage wider acceptance of this new material, which may lead to introducing the BFRP materials into the FRP design codes and standards.

CHAPTER 5
EXPERIMENTAL TESTING OF CONCRETE BRIDGE-DECK SLABS REINFORCED WITH BASALT-FRP BARS UNDER CONCENTRATED LOADS

Abstract

Advances in FRP technology have led to the introduction of new basalt-fiber-reinforced-polymer (BFRP) bars. This paper presents a research project investigating the behavior of edge-restrained concrete bridge-deck slabs reinforced with BFRP bars. The tests included six full-scale edge-restrained concrete deck slabs simulating a slab-on-girder bridge-deck commonly used in North America and one full-scale unrestrained concrete deck slab. The deck slabs measured 3000 mm long × 2500 mm wide × 200 mm thick. The test parameters investigated were (1) reinforcement type (BFRP and steel); (2) BFRP bar size (12 mm and 16 mm); (3) reinforcement ratio in each direction (0.4% to 1.2%); and (4) edge-restraining (restrained or unrestrained [free]). The slabs were tested up to failure over a center-to-center span of 2000 mm under single concentrated load acting on the center of each slab over a contact area of 600 × 250 mm to simulate the footprint of a sustained truck wheel load (87.5 kN CL-625 truck) as specified in Canadian Standards. The observed mode of failure for the edge-restrained deck slabs was punching-shear with carrying capacities exceeding the design factored load specified by CHBDC.

***Keywords*:** Fiber-reinforced polymers (FRP), basalt-FRP bars, concrete, bridge, deck slab, design, restrained, punching, strain, serviceability, code.

5.1 Introduction

Concrete deck slabs deteriorate faster than any other bridge element because of direct exposure to harsh environmental conditions such as freeze–thaw cycles, wet–dry cycles, deicing chemicals, and traffic loads, all of which result in the corrosion of steel reinforcement. The magnitude of deck cracking and delamination due to corrosion constitutes a major problem when measured in terms of rehabilitation costs and traffic disruption.

Because of their noncorrosive nature, fiber-reinforced-polymer (FRP) reinforcing bars help improve the durability of bridge-decks and reduce—if not eliminate—maintenance and repair costs. As FRP technology has evolved, it has been implemented in many bridge design codes as primary reinforcement. AASHTO (2009) allows the use of glass-FRP (GFRP) bars, while the CHBDC (CAN/CSA S6 2014) allows the use of glass-, carbon-, and aramid-FRP (GFRP, CFRP, AFRP) bars. The CAN/CSA S6 (2014) provides two different methods for designing bridge-deck slabs: (1) the empirical design method and (2) the flexural design method. They set the minimum diameter for the GFRP reinforcing bars at 16 mm and the maximum spacing at 300 mm (minimum reinforcement of 16 mm @ 300 mm). It should be mentioned that this minimum reinforcement (16 mm @ 300 mm) is based on many investigations and field applications using GFRP bars with a modulus of elasticity around 40 GPa. Some of the currently available GFRP bars and newly developed basalt-FRP (BFRP) bars have moduli of elasticity higher than 60 or 65 GPa. Developments may yield BFRP bars with moduli of elasticity as high as 70 or 75 GPa. This might impact the minimum reinforcement requirements in FRP design codes for bridge-deck slabs if the parameter of 16 mm GFRP bars @ 300 mm is replaced based on axial-reinforcement stiffness ($E_f A_f$). Since the current FRP design standards (ACI 440.1R 2015; AASHTO 2009; CAN/CSA S6 2014; CAN/CSA S806 2012) do not yet include any recommendations for BFRP bars, further investigation is needed to develop and provide material resistance factors and stress levels at the service limit state to optimize designs.

Several research projects have investigated GFRP reinforcement in concrete bridge-deck slabs under static and fatigue loading (El-Gamal et al. 2005; El-Ragaby et al. 2007; Bouguerra et al. 2011) and bridge barriers under static and impact loading (El-Salakawy et al. 2003b; Ahmed and Benmokrane 2011; Ahmed et al. 2013a&b). Moreover, several field applications have been carried

out in Quebec: the Joffre Bridge in Sherbrooke, the Wotton Bridge in Wotton, the Magog Bridge on Highway 55 North, the Cookshire–Eaton Bridge on Route 108, the Val-Alain Bridge on Highway 20 East, and the new bridges on the extension of Highway 410 (El-Salakawy et al. 2003a; El-Salakawy et al. 2005; Benmokrane et al. 2007; Ahmed et al. 2014a) and in the United States, such as the Morristown Bridge in Vermont (Benmokrane et al. 2006) and the bridges on Pierce Street in Lima (Ohio 1999), Salem Avenue in Dayton (Ohio 1999), Rollins Road in Rollinsford (New Hampshire 2000), Sierrita de la Cruz Creek in Potter County (Texas 2000), 53rd Avenue in Bettendorf (Iowa 2001), Bridge Street in Southfield (Michigan 2001), Highway 151 in Waupun (Wisconsin 2005), and Route Y in Boone County (Missouri 2007) (Eamon et al. 2012). Most of these projects focused on using GFRP bars for their relatively lower cost compared to other FRPs (carbon and aramid). Most of these bridges were constructed with GFRP with moduli of elasticity from 40 to 45 GPa. Some of these bridges have been in service for more than 10 years without any signs of deterioration or unexpected problems.

Basalt fibers have high tensile strength and modulus, good chemical resistance, extended operating-temperature range, and good environmental friendliness. Therefore, basalt fibers are ideally suited for applications involving high temperature, chemical resistance, durability, mechanical strength, and low water absorption (IinfoMine 2007). In comparison to E-glass FRP, BFRP has higher strength and modulus, similar cost, and greater chemical stability. Moreover, it exhibits over five times the strength and around one-third the density of commonly used low-carbon steel bars (Wu et al. 2012). Few studies, however, have investigated the performance of BFRP reinforcing bars in structural testing and field applications. Since the chemical composition of the basalt fibers is similar to that of glass fibers—except for the iron oxide that gives basalt fibers their brown/golden color—it is expected that the development of new BFRP bars will lead to many applications and may result in optimized and cost-effective designs because of BFRP's high mechanical and durability characteristics.

5.2 Literature Review

5.2.1 Lab Tests of Bridge-Deck Slabs Reinforced with FRP Bars

The behavior of steel-RC deck slabs system has been extensively investigated (Hewitt and Batchelor 1975; Perdikaris and Beim 1988; Kuang and Morely 1993; Mufti and Newhook 1998)

and several code provisions have been implemented. On the other hand, a few studies have investigated the behavior of restrained concrete deck slabs reinforced with glass- and carbon-FRP bars (Hassan and Rizkalla 2004; El-Gamal et al. 2005; El-Ragaby et al. 2007; Bouguerra et al. 2011; Zheng et al. 2012a&b). These studies concluded that the primary structural action of slabs that resist concentrated wheel loads is not flexion, as traditionally believed, but a complex internal membrane stress state referred to as an internal arch-action mechanism (Mufti and Newhook 1998). The arch-action creates an internal compressive dome and the resultant failure mode becomes punching-shear. **Figure 5–1** clarifies the arching action in restrained bridge-deck slabs. It was concluded that the reinforcement content in deck slabs can be reduced significantly and satisfy both serviceability and strength requirements. These studies, along with demonstration projects, contributed to incorporating FRP as the main reinforcement in bridges (AASHTO 2009; CAN/CSA S6 2014).

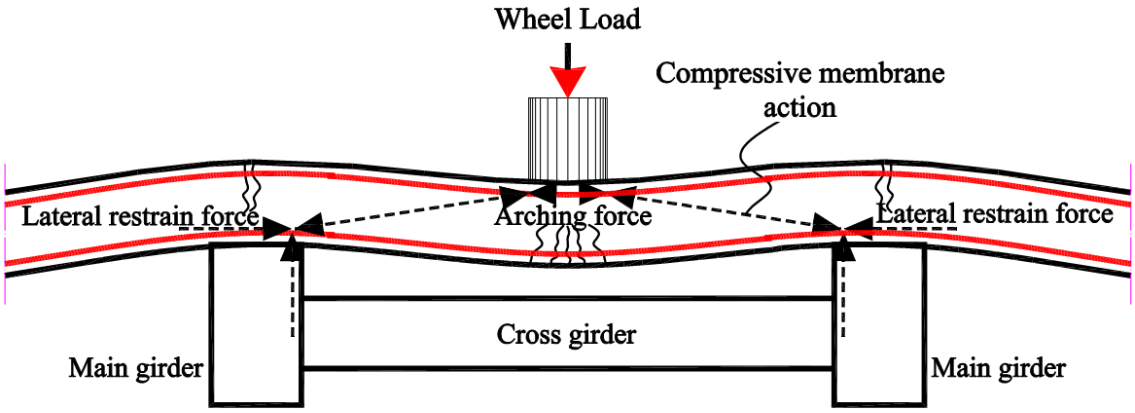

Figure 5–1: Arching action mechanism in slab-on-girder concrete deck slabs

Khanna et al. (2000) experimentally investigated the influence of each layer of reinforcement and reinforcement type (steel and GFRP) on the behavior of RC deck slabs. The test model was a 12.0 m long × 175 mm thick slab cast compositely on two steel beams spaced at 2.0 m. The slab model was conceptually divided into four segments (each 3.0 m long). All the segments had the same axial-reinforcement stiffness in the bottom transverse direction and different reinforcement configurations in the other directions. Each segment was tested under concentrated load, simulating the dual-tire footprint (250 × 500 mm) of a typical commercial vehicle. All the segments failed in a punching-shear mode at similar load values. The tested slabs confirmed that (i) only the bottom transverse reinforcement influences the load-carrying capacity and deflection behavior of a

reinforced concrete deck slab and (ii) the stiffness, not the strength, of the bottom transverse reinforcement is of paramount importance, (iii) the results validated and supported the competitiveness of the proposed FRP design compared to the conventional steel design. El-Gamal et al. (2005) investigated the behavior of restrained concrete bridge-deck slabs reinforced with GFRP, CFRP, and steel bars at different reinforcement ratios. Six full-scale deck slabs 3000 mm long × 2500 mm wide × 200 mm thick were constructed and tested to failure. The deck slabs were supported on two steel beams spaced 2000 mm center-to-center and were subjected to a monotonic single concentrated load over a contact area of 600 × 250 mm to simulate the footprint of sustained truck wheel load (87.5 kN CL-625 truck) acting on the center of each slab. It was observed that (i) the mode of failure for all deck slabs was punching-shear with carrying capacities more than three times the design factored load specified by the CHBDC (CAN/CSA S6 2014) and (ii) the maximum measured crack widths and deflections at service load were below the allowable code limits. Zheng et al. (2012a&b) studied the structural behaviors of GFRP reinforced concrete slabs with lateral restraining, such as bridge-deck slabs. The restrained slabs exhibited arching action or compressive membrane action (CMA), which positively impacts service behavior such as deflection, cracks width, and ultimate capacity. It is worth mentioning that the common mode of failure of the tested edge-restrained deck slabs is punching-shear failure similar to that of the two-way slabs such as those reported by Matthys and Taerwe (2000), El-Ghandour et al. (2003), Ospina et al. (2003), Zaghloul (2007), Lee et al. (2009), Nguyen-Minh and Rovnak (2013), Dulude et al. (2013), and Hassan et al. (2013a&b).

5.2.2 Basalt-FRP Bars for Concrete Structures and Bridge-Decks

Continuous efforts in development and innovation in the fiber-reinforced-polymer (FRP) technology are being deployed for using new types of fibers, such as basalt fibers, in addition to the commonly used glass and carbon fibers. Basalt-fiber-reinforced polymer (BFRP) is expected to provide benefits that are comparable or superior to other types of FRP, while being significantly cost effective (Parnas et al. 2007; Wei et al. 2010; Lopresto et al. 2011; Wang et al. 2012). An extensive experimental investigation is being conducted at the University of Sherbrooke (Quebec, Canada) to develop and investigate the short- and long-term performance of newly developed BFRP bars. The investigation includes five different types of BFRP bars and one type of BFRP tendon. The preliminary results of this investigation (Vincent et al. 2013; Elgabbas et al. 2013;

Elgabbas et al. 2014; Benmokrane et al. 2015) confirmed the feasibility of producing new BFRP bars for structural concrete elements with physical and mechanical properties that meet ACI 440.6M (2008) and CAN/CSA S807 (2010) requirements. The current FRP design codes and guides (ACI 440.1R 2015; AASHTO 2009; CAN/CSA S6 2014; CAN/CSA S806 2012), however, do not include any recommendations for the BFRP bars yet due to the lack of available studies and results.

The main objective of this paper is to experimentally investigate full-scale concrete bridge-deck slabs internally reinforced with BFRP bars under concentrated loads simulating truck wheel loads. This paper also highlights the overall performance of BFRP compared to the well-established results for steel, GFRP, and CFRP reinforcement in such structural elements.

5.3 Experimental Program

5.3.1 Material Properties

***Reinforcing bars*:** BFRP bars of 12 and 16 mm diameter, as shown in **Figure 5–2,** were used in this study. The BFRP bars were fabricated using a pultrusion process in a vinylester resin with fiber contents of 79.2% and 80.0% for 12 and 16 mm bars, respectively. The bars had a deformed surface with helical ribs to increase the bond between the bar surface and the surrounding concrete. The tensile properties of the BFRP bars were determined by testing five representative specimens of each diameter according to ASTM D7205 (2011). The mean tensile strength and the modulus of elasticity of the tested BFRP bars were 1760 and 1724 MPa, and 69.3 and 64.8 GPa for the 12 and 16 mm diameter bars, respectively. The reference slab was reinforced with 15M steel bars. **Table 5–1** summarizes the tensile properties of the FRP and steel bars.

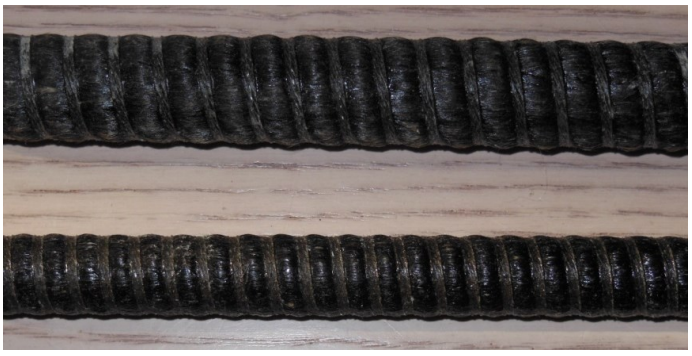

Figure 5–2: 12 and 16 mm diameter Basalt-FRP reinforcing bars

Table 5–1: Mechanical properties of BFRP and steel bars

Reinforcement	d_b (mm)	A_f (mm²)	E_f (GPa)	f_{fu} (MPa)	f_{fu} [c] (MPa)	ε_{fu} (%)	ε_{fu} [c] (%)
BFRP Bars	12.0	113.1	69.3±0.5	1760±38.8	1643	2.54±0.10	2.24
	16.0	201.1	64.8±3.3	1724±63.6	1633	2.67±0.17	2.16
Steel Bars[a]	15M	200.0	200.0	f_y [b] = 450	---	ε_y [b] = 0.20	---

[a] The tensile properties of the steel bars were provided by the manufacturer.

[b] f_y and ε_y are yield strength and strain of the steel bars, respectively.

[c] The guaranteed tensile strength and the guaranteed strain of BFRP bars (Mean value - 3× standard deviation) according to ACI 440.1R (2015).

Concrete: The slabs were constructed using ready-mix, normal-weight concrete with a target 28-day compressive strength of 40 MPa. The mix proportions for a cubic meter of concrete was 350 kg/m^3 of cement, 813 kg/m^3 of natural sand, 1032 kg/m^3 of aggregate in size ranging from 5 to 20 mm (20 mm maximum nominal size), a water-to-cement ratio (w/c) of 44%, and an air-entrainment ratio of 5% to 8%. Once poured, the concrete was compacted with an electrical vibrator and leveled manually. The curing process was initiated after two hours by covering the concrete surface with wet burlap and polythene sheet for 10 days. The concrete compressive strength for each batch was determined by testing three 150 × 300 mm cylinders. The tensile strength was determined from split-cylinder testing on three 150 × 300 mm cylinders. **Table 5–2** shows the concrete compressive and tensile strengths on the day of testing.

5.3.2 Test Specimens

The test specimens were designed to simulate commonly used slab-on-girder bridges. The geometry of the specimens depicts the deck slabs of the Wotton Bridge (Quebec, Canada) (El-Salakawy et al. 2003a) and was in agreement with past tests conducted at the University of Sherbrooke with GFRP and CFRP bars (Gamal et al. 2005). The experimental testing included seven full-scale concrete deck slabs measuring 3000 mm long × 2500 mm wide × 200 mm thick, as shown in **Figure 5–3**. The slab thickness was selected to keep the ratio of supporting-beam spacing to slab thickness to less than 18 and to represent the most commonly used dimensions for concrete bridge-deck slabs in Canada. Slab length, however, was selected to avoid one-way shear before punching failure and to include the slab area affected by the wheel load. This area was assumed to be based on the outer diameter of the wedge formed during punching failure (Newhook

1997; El-Gamal et al. 2005). Six slabs were provided with two holes of 27 mm in diameter and spaced 160 mm on centers with a 250 mm pitch in the longitudinal direction at the restrained edges. This edge restraining was needed to induce the arching action or compressive-membrane action (CMA), shown in **Figure 5–1**, as the case in actual bridges. On the other hand, one slab had no holes along the edges to be simply supported during the test. The concrete cover—constant for all the slabs—was equal to 30 mm and 25 mm at the top and bottom (CAN/CSA S6 2014). The test parameters investigated herein were: (i) reinforcement type (steel and BFRP); (ii) bar size (12 mm and 16 mm); (iii) reinforcement ratio in each direction (0.4% up to 1.2%); and (iv) edge restraining (restrained and unrestrained [free]). For comparison, two slabs reinforced with GFRP and CFRP (El-Gamal et al. 2005) with the same dimensions and loading procedure were presented.

Table 5–2 summarizes the concrete and reinforcement details. The first slab (S1-S) was reinforced, top and bottom, with 15M steel bars spaced at 150 mm in the main direction (transverse direction) and reinforced, top and bottom, with 15M steel bars spaced at 225 mm in the secondary direction (longitudinal direction). The slab had a reinforcement ratio of 0.80% in the bottom transverse direction. The slab's reinforcement was designed to simulate the deck slabs in the Wotton Bridge, Quebec, Canada (El-Salakawy et al. 2003a). The second slab (S2-B) was reinforced with 16 mm BFRP bars arranged exactly as in S1-S (same reinforcement ratio of BFRP and steel). The amount of reinforcement in this slab (S2-B, 16 mm @150 mm) satisfies the CHBDC's empirical and flexural design methods (CAN/CSA S6 2014), assuming that the material safety factor and the stress level in the BFRP bars at service load level are the same as GFRP bars as provided in Appendix A. The third slab (S3-B) was designed to have the same reinforcement ratio and approximately the same axial-reinforcement stiffness as S2-B by replacing the 16 mm BFRP bars with 12 mm BFRP bars. The fourth slab (S4-B) had the same bottom reinforcement as S2-B but without top reinforcement. The fifth slab (S5-B) was designed to have approximately the same axial-reinforcement stiffness as slabs G-S2 and C-S2 (El-Gamal et al. 2005). The last two slabs (S6-B and S7-B) were reinforced with the same BFRP bars: 16 mm spaced 300 mm in the orthogonal direction, top and bottom (minimum reinforcement as per the CHBDC (CAN/CSA S6 2014)). It should be mentioned that, if the minimum reinforcement (assume 16 mm @ 300 mm with a modulus of 40 GPa) in the CHBDC (CAN/CSA S6 2014) is replaced based on axial-reinforcement stiffness ($E_f A_f$) with 12 mm BFRP bars as used herein, the equivalent spacing becomes 300 mm (12 mm @ 300 mm with BFRP bars with a modulus of 70 GPa). All the slabs

were edge restrained except S7-B which was simply supported (free). **Figure 5–3** shows the geometry and the reinforcement details, while **Figure 5–4** shows the slab construction.

5.3.3 Instrumentation

Figure 5–5 illustrates the typical instrumentation on the slabs. Deflections were monitored using seven linear variable differential transducers (LVDTs), with a precision of 0.001 mm, installed on the top surface of the deck slabs (D1 to D7), as shown in **Figure 5–5 (a)**. This figure also shows that two LVDTs (D8 and D9) were installed on both sides of the slabs to monitor any movement of the slab edges during testing. The concrete compressive strains at different locations on the top surface of the slabs were measured with four electrical strain gauges. **Figure 5–5 (b)** shows the location of the gauges. Several electrical strain gauges were also installed on the reinforcing bars to record the strains. **Figure 5–5 (b)** also shows the position of strain gauges on the top and bottom reinforcing bars. The initial crack widths were measured using a 50X handheld microscope. High-precision LVDTs (0.001 mm) were installed at the position of the first three cracks to record crack-width propagation with increasing load, as depicted in **Figure 5–5 (c).** Moreover, six electrical strain gauges were used to measure strains at different positions on the steel cross frame at the top and bottom, as shown in **Figure 5–5 (d)**. An automatic data-acquisition system connected to a computer was used to monitor loading, deflections, and strains in concrete and reinforcing bars.

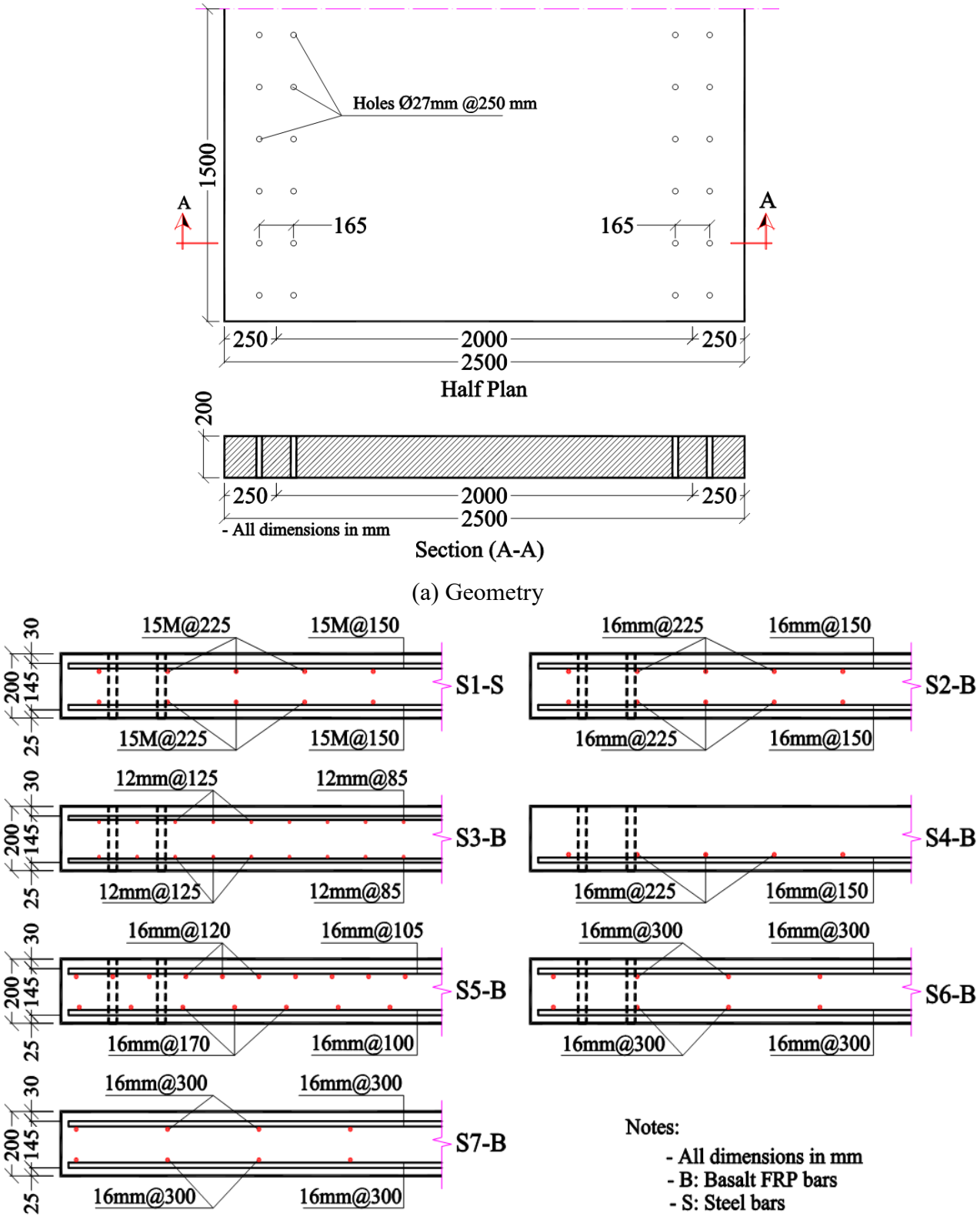

Figure 5–3: Geometry and reinforcement details of the tested concrete deck slabs

(a) Formwork

(b) Cages

(c) Assembly

(d) Casting

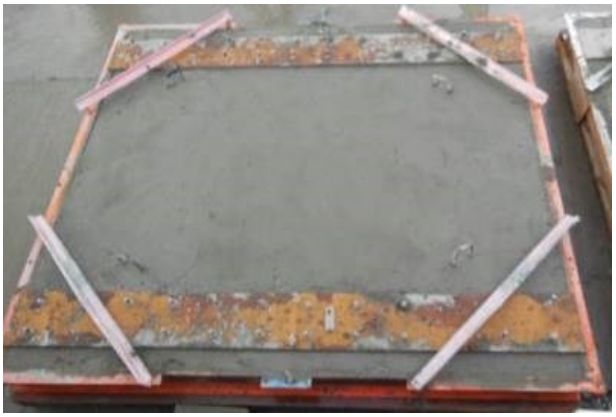

(e) Surfacing

(f) De-molding

Figure 5–4: Construction of the deck slabs

Table 5–2: Concrete and reinforcement details of the bridge-deck slabs

ID[a]	f'_c[c] (MPa)	f_t[d] (MPa)	Bottom Reinforcement						Top Reinforcement					
			Transverse direction			Longitudinal direction			Transverse direction			Longitudinal direction		
			Reinforcement[e]	ρ (%)	$\rho \times E$ (MPa)	Reinforcement[e]	ρ (%)	$\rho \times E$ (MPa)	Reinforcement[e]	ρ (%)	$\rho \times E$ (MPa)	Reinforcement[e]	ρ (%)	$\rho \times E$ (MPa)
S1-S	48.81 ±1.43	4.70 ±0.17	15M@150 mm	0.80	1606	15M@225 mm	0.59	1184	15M@150 mm	0.83	1655	15M@225 mm	0.61	1225
S2-B			16 mm@150 mm	0.80	520	16 mm@225 mm	0.59	383	16 mm@150 mm	0.83	536	16 mm@225 mm	0.61	396
S3-B	42.20 ±1.58	4.24 ±0.06	12 mm@85 mm	0.79	523	12 mm@125 mm	0.58	383	12 mm@85 mm	0.81	539	12 mm@125 mm	0.60	395
S4-B			16 mm@150 mm	0.80	520	16 mm@225 mm	0.59	383	--	--	--	--	--	--
S5-B	47.90 ±1.14	4.44 ±0.09	16 mm@100 mm	1.20	780	16 mm@170 mm	0.78	507	16 mm@105 mm	1.18	766	16 mm@120 mm	1.15	743
S6-B			16 mm@300 mm	0.40	260	16 mm@300 mm	0.44	288	16 mm@300 mm	0.41	268	16 mm@300 mm	0.46	297
S7-B[b]			16 mm@300 mm	0.40	260	16 mm@300 mm	0.44	288	16 mm @300 mm	0.41	268	16 mm@300 mm	0.46	297

[a] Slab number (S1 to S7) followed by reinforcement type (S: steel; B: basalt FRP).

[b] Simply supported slab.

[c] f'_c: Concrete compressive strength.

[d] f_t Concrete tensile strength.

[e] Bar diameter and spacing in mm (diameter in mm @ spacing in mm).

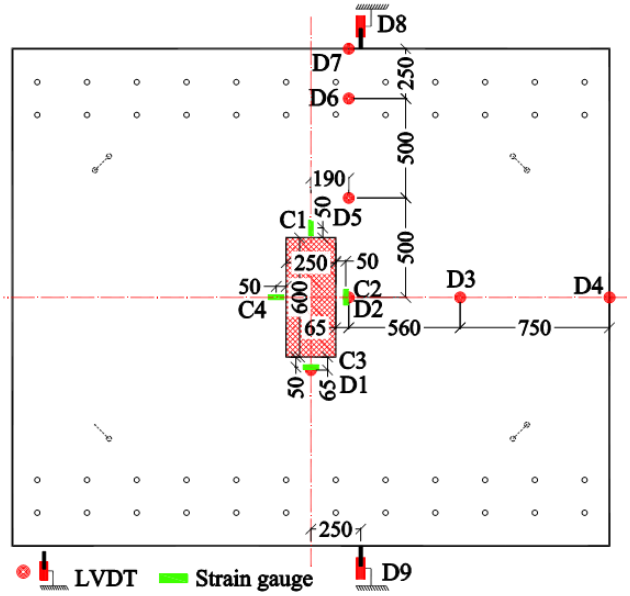

a) LVDTs and strain gauges on the top concrete surface

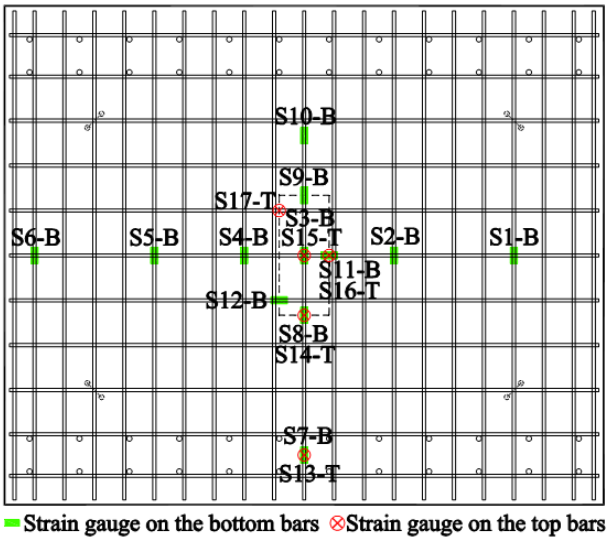

c) Strain gauges on the top (T) and bottom (B) reinforcing bars

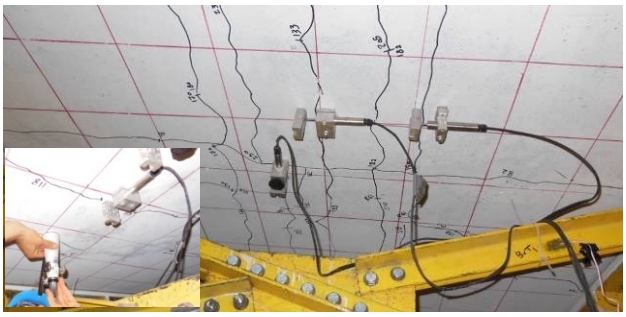

b) 50X handheld microscope and LVDTs for measuring the crack widths

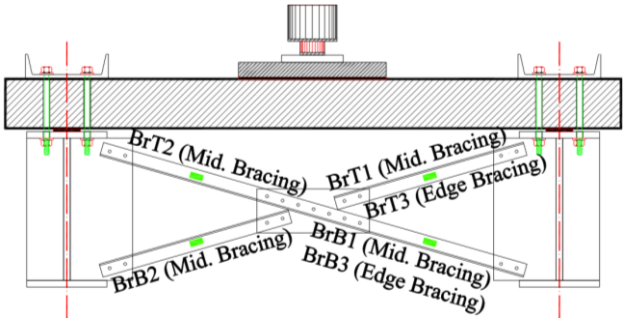

d) Strain gauges on the cross frames

Figure 5–5: Typical instrumentation of test slabs

5.3.4 Test Setup and Procedure

The slabs were loaded up to failure over a center-to-center span of 2000 mm under monotonic single concentrated load, using a hydraulic jack controlled by a manually operated pump monitored with a pressure dial gauge. The load was applied to the slab center with a contact area of 600 × 250 mm, using a 70 mm thick steel plate to simulate the footprint of a sustained truck wheel load (87.5 kN-CL-625 truck) as specified by the CHBDC (CAN/CSA S6 2014). To create uniform stresses over the loading area, a 10 mm thick neoprene sheet was placed between the loading plate and concrete surface. The slabs were supported on two steel girders simulating the setup used by

El-Gamal et al. (2005) to resist the maximum applied load without exceeding the permissible stresses and deflections. To ensure full contact between the bottom surface of concrete slab and top surface of the steel girders, neoprene pads of 3 mm thick and 100 mm wide were inserted between them. The two steel girders were braced together with three steel cross frames (bracing) spaced at 1500 mm. The steel girders were supported by two steel cross beams spaced 3000 mm in the longitudinal direction. The loads were transferred to the laboratory strong floor through four steel legs at the edge of the cross beams. **Figure 5–6 (a)** shows the test setup under the loading frame.

Six of the seven slabs were tested after being restrained on the longitudinal edges and the last slab was simply supported. The restrained slabs were tied to the top flange of the steel girder in the longitudinal direction with 22 mm diameter threaded anchors, which were fitted into holes through the slab thickness, as shown in **Figure 5–6 (b)**. The steel anchors represent the shear connectors between the girder and deck slab in the actual bridge. All anchors were hand tightened with a torque wrench to a torque moment of 160 N.m in order to make a constant partially edges restrain for all slabs and make it uniform along the slab edges. The torque moment was calculated to generate horizontal shear friction between the steel girder and bottom surface of the slab higher than the horizontal component of the arching stress and to prevent lateral movement between the slab and girder. The bridge-deck slabs were tested similarly to past tests at the University of Sherbrooke by El-Gamal et al. (2005). Steel channels were used on the top face of the concrete slab to prevent stress concentration around the holes on the slab edges. In addition, 10 mm thick and 100 mm wide neoprene strips were placed between the concrete slab and the steel channel to ensure full contact until the end of the test. A hydraulic jack with a capacity of 1000 kN and a ±250 mm stroke was used to apply the monotonic load up to failure at a load control rate of 5 kN/min. The hydraulic jack was controlled manually with a hand pump monitored with a pressure dial gauge connected to the data-acquisition system and monitored with a computer. **Figure 5–6** provides an overview of the test setup. During the test, the slabs were observed until the first three cracks appeared in the transverse direction; the corresponding loads were recorded. The test was paused when each of the first three cracks appeared. The initial crack widths were measured manually with a 50X handheld electronic microscope and LVDTs were installed at the crack locations. The cracking load was also verified in terms of the change in the stiffness of load–deflection and load–strain relationships. The load was continuously increased until slab failure. The formation of cracks on the sides and bottom surface of the deck slabs and corresponding loads were marked and recorded during the test.

(a) Loading system (b) Deck slab ready for testing

Figure 5–6: Overview of the test setup

5.4 Test Results and Discussion

The test results are presented in terms of the cracking load, cracking pattern, deflections, strains in reinforcing bars and concrete, ultimate capacity, and mode of failure. **Table 5–3** summarizes the test results. In this section, the design service load (P_{ser}) and design factored load (P_f) were calculated according to the CHBDC (CAN/CSA S6 2014). The design service load of the deck slabs was taken as 1.4 × 0.9 × 87.5 = 110.25 kN, where 87.5 is the maximum wheel load of the design truck (87.5 kN CL-625 truck), 1.4 is the impact coefficient, and 0.9 is the live-load combination factor. The design factored load was taken as 1.4 × 1.7 × 87.5 = 208.25 kN, where 1.7 is the live-load combination factor. Axial-reinforcement stiffness ($\rho \times E$) was also used when comparing different reinforcing materials.

5.4.1 Cracking Load and Pattern

Some transverse cracks were observed in S2-B, S3-B, S4-B, and S6-B as the anchor bolts were tightened. These cracks appeared in the slab bottom surface between bolts, then propagated to the middle of the slab. These cracks were mainly due to slab deformation in the longitudinal direction during anchor tightening. They had no significant effect on slab behavior. Therefore, the cracking load was considered to be the applied load corresponding to the appearance of the first longitudinal crack.

The overall crack patterns at failure for all the slabs were almost similar, despite the different reinforcement types and ratios. **Figure 5–7** shows the typical crack pattern of selected slabs at failure. The first longitudinal cracks on the bottom surface (tension side) appeared directly under the loaded area and were oriented in the longitudinal direction parallel to the supporting beams. The subsequent cracks propagated in the radial direction away from the loaded area. The cracks on the top surface, except for S7-B (simply supported), however, appeared beside the steel channel and propagated in arcs far from the slab center with a distance equal to half the supporting span.

The cracking load ranged between 73.1 to 134.8 kN with average value of 110.7 kN, as listed in **Table 5–3**. It can be noted that the average cracking load was approximately the same as the design service load level (110.25 kN) specified in the CHBDC (CAN/CSA S6 2014). The low cracking load for S6-B may be related to preexisting cracks that may have occurred during slab handling and transportation. Excluding S6-B yielded an average cracking load of 117.03 kN.

Figure 5–8 provides the crack widths for all the slabs versus the applied load. **Table 5–3** gives the values of the measured crack widths on the bottom surface at the service and factored load levels, as specified in the CHBDC (CAN/CSA S6 2014), as well as at load just before the failure. The crack width in S6-B was measured up to 220 kN, at which point, the LVDT malfunctioned. At the service load level, the maximum measured crack widths were 0.10 mm, 0.10 mm and 0.35 mm for S2-B, S5-B, and S6-B, respectively. These are less than the allowable limits specified by ACI 440.1R (2015) and the CHBDC (CAN/CSA S6 2014) of 0.5 mm for exterior exposure. The other slabs, however, were not cracked at the service load (cracking load was higher than the service load).

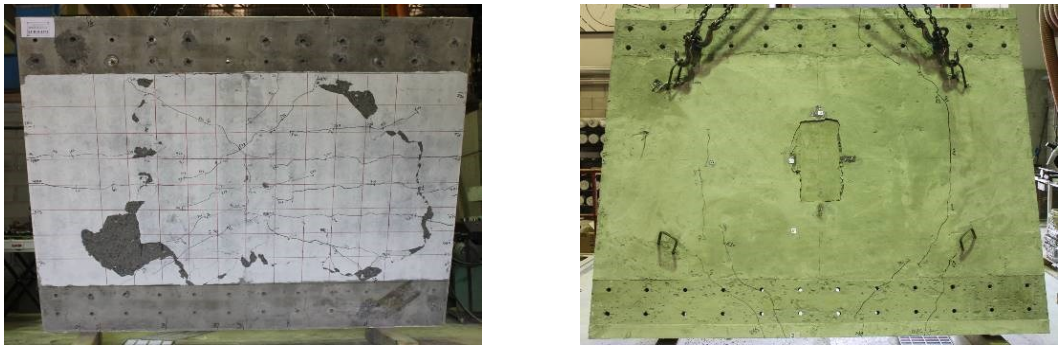

(a) S1-S

(b) S2-B

(c) S6-B

(d) S7-B

Figure 5–7: Cracks pattern at failure

Table 5–3 and **Figure 5–8** show that S1-S (15M steel bars @ 150 mm) exhibited the smallest crack width and the lowest number of cracks as a result of having the highest axial-reinforcement stiffness ($\rho \times E$). S3-B (12 mm BFRP bars @ 85 mm) and S5-B (16 mm BFRP bars @ 100 mm) showed very close load-to-crack-width relationships to that of S1-S, regardless of the significant difference in the reinforcement's axial stiffness (1606 MPa for S1-S, 523 MPa for S3-B, and 780 MPa for S5-B). This confirms the effect of decreasing the reinforcement spacing on reducing crack widths, even when reinforcing bars of low modulus of elasticity are used. Moreover, S2-B and S3-B, which had the same axial-reinforcement stiffness, exhibited different load-to-crack-width relationships. Using 12 mm diameter BFRP bars every 85 mm enhanced the cracking performance more than did 16 mm diameter bars spaced at 150 mm. Furthermore, S2-B and S4-B—which had the same bottom reinforcement ratio and diameter, but S4-B didn't have top reinforcement—showed the same load-to-crack-width relationship, which indicates that top reinforcement had no effect on cracking characteristics.

In S6-B, which had the minimum reinforcement according the CHBDC (CAN/CSA S6 2014), the crack width at the factored load level was 0.52 mm, which is wider than those in S1-S and S2-B to S5-B. This was attributed to the larger spacing between bars and the lower cracking load observed in this slab. The effect of edge restraining on crack width can be easily identified by comparing S6-B (with edge restraining) and S7-B (without edge restraining), which have the same reinforcement. At the design factored load, S7-B evidenced a crack width of 0.93 mm, which exceeds that in S6-B with edge restraining by 79%. The slope of the load-to-crack-width relationships can also clarify the contribution of edge restraining in enhancing the cracking performance of the deck slabs, as evidenced in **Figure 5–8.**

The comparison of S5-B, G-S2, and C-S2 also indicates that the surface and bundle configurations of the bar arrangements impacted on crack width. S5-B showed smaller crack widths than G-S2 and C-S2 with similar or higher axial-reinforcement stiffness.

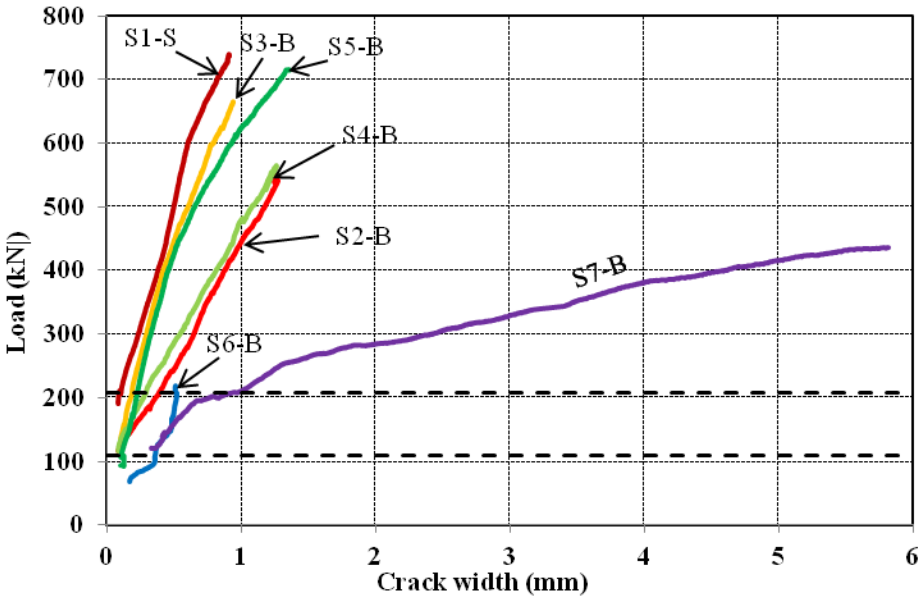

Figure 5–8: Load-average crack width curves

5.4.2 Ultimate Capacity and Failure Mode

Figure 5–7 shows the crack patterns on the bottom and top surfaces of the tested slabs after failure. All the slabs showed a brittle punching-shear failure mode around the loaded area where the steel loading plate penetrated through the top surface of the slab, creating an elliptical shape passing through the corners of the loaded area. The bottom surface had a roughly circular shape with a diameter equal to the spacing between the two steel girders. No signs of concrete crushing or bar rupture were evidenced, which confirms punching-shear as the failure mode. The ultimate punching-shear strengths were 739.6, 548.3, 664.6, 565.9, 716.4, and 575.8 kN for the restrained slabs S1-S, S2-B, S3-B, S4-B, S5-B and S6-B, respectively. As expected, the unrestrained slab S7-B showed a lower punching-shear capacity of 436.4 kN. The values of punching-shear strength for the restrained slabs ranged from 2.63 to 3.55 times the factored design load of 208.25 kN recommended by the CHBDC (CAN/CSA S6 2014). This was attributed to the fact that the section's design was based on flexural failure, while the actual failure mode was shear. Moreover, the high level of conservativeness is due to the general behavior of the restrained bridge-deck slabs and mode of failure. These findings are in agreement with the results reported by Hewitt and Btchelor (1975), Perdikaris and Beim (1988), El-Gamal et al. (2005), El-Gamal et al. (2007), and Bouguerra et al. (2011) for GFRP- and CFRP-reinforced concrete bridge-deck slabs. The failure mode was punching-shear under the concentrated wheel loads rather than flexural failure as

assumed in conventional designs. Furthermore, Hewitt and Batchelor (1975) reported that when a deck slab is restrained, there is no need for reinforcement to resist the wheel load due to the compression membrane action, which is similar to the arching action in reinforced-concrete beams. A minimum amount of reinforcement was proposed for serviceability reasons. This concept was adopted by the CHBDC (CAN/CSA S6 2014) through its empirical method. This method does not, however, account for any design parameters other than slab effective depth and the modulus of elasticity of the reinforcing bars. Ahmed and Benmokrane (2012) concluded that the empirical method usually overestimates the bottom transverse reinforcement required.

Table 5–3 provides the punching-shear capacities for all the tested slabs. S1-S (reinforced with 15M steel bars @ 150 mm) showed the highest punching-shear capacity (739.6 kN) due to the highest axial-reinforcement stiffness (1606 MPa). S5-B (reinforced with 16 mm diameter BFRP bars @ 100 mm) showed a punching-shear capacity of 716.4 kN, which is about 97% of that of the steel-reinforced counterpart, regardless of the lower axial-reinforcement stiffness (780 MPa). The results also confirm that the punching-shear capacity is proportional to the axial-reinforcement stiffness: the higher the axial-reinforcement stiffness, the higher the punching-shear capacity. This is because increasing the reinforcement ratio (or axial-reinforcement stiffness) controls crack width, enhances aggregate interlock, and increases the concrete compression zone (uncracked concrete). Since the axial-reinforcement stiffness of S5-B was almost the same as that of G-S2 (GFRP bars), the punching-shear capacity was almost the same (716.4 kN for S5-B and 712 for G-S2). S5-B also evidenced a punching-shear capacity close to that of C-S2 (CFRP bars), where the axial-reinforcement stiffness was close. On the other hand, S2-B and S4-B (without top reinforcement but with the same bottom reinforcement) showed approximately the same ultimate capacity, which implies that the top reinforcement did not impact the punching-shear capacity of the deck slabs. This confirms the findings of Khanna et al. (2000) and El-Gamal et al. (2005).

The effect of membrane action can be determined by comparing the restrained slab (S6-B) with the unrestrained slab (S7-B) that had the same concrete strength and reinforcement. The edge restraining increased the ultimate capacity by 31.9 % because of the compressive membrane forces. It also contributed to reducing deflection and crack width.

5.4.3 Reinforcement and Concrete Strains

Figure 5–9 shows the applied load versus the maximum measured strains in the bottom transverse reinforcement as well as in the top surface of concrete in the vicinity of the loading area. **Table 5–3** provides the strain values at the service design load and factored design load. S1-S (reinforced with steel bars) exhibited a yield plateau after 2620 με up to failure. This means the slab failed due to punching-shear initiated by the steel yielding. The strains in the deck slabs reinforced with BFRP bars, however, varied linearly with increasing load after concrete cracking up to failure. On the other hand, the reinforcement strain distribution along the cross section in the middle section of the slab in the transverse direction using the strain gauges shown in **Figure 5–5(c)** is presented in **Figure 5–10**. In **Figure 5–10**, the strains were typically high in the middle of the slab underneath the applied load. The strains decreased proportionally towards the slab supports. The strains reached zero or very small compressive values due to the edge restraining at the supports. This typical distribution confirms that no debonding of the reinforcement occurred.

Generally, **Figure 5–9** confirms that increasing the reinforcement ratio reduced both tensile and compression strains in the bottom reinforcement and concrete top surface, respectively. The effect of the reinforcement ratio can be seen in S2-B, S5-B, and S6-B, which had reinforcement ratios of 0.8%, 1.2%, and 0.4%, respectively. At a load of 576 kN, the strains in the bottom reinforcement were 5650, 5039, and 7932 με for S2-B, S5-B, and S6-B, respectively. Increasing the bottom transverse-reinforcement ratio by two and three times significantly reduced the measured strains by 28.8% and 36.5%, respectively.

Table 5–3 shows that the measured strains at service load ranged from 92 με to 575 με (tension) and -68 με to -425 με (compression) in the bottom transverse reinforcement and top concrete surface, respectively. The maximum ratios of the strains at service load to strains at failure were approximately 7.2% and 23.3% for the reinforcing bars and concrete, respectively. At the factored design load, the strains ranged from 706 με to 4042 με and -240 με to -994 με, respectively. The maximum ratios of the strains at the factored load to strains at failure were approximately 37.4% and 69.2% for the reinforcing bars and concrete, respectively. This provides a significant warning before failure and a safety factor ranging from 3.6 to 8.3 for the restrained slabs and 2.7 for the unrestrained slab (S7-B). At failure, the tensile strains in the BFRP reinforcement in the restrained deck slabs were less than the guaranteed strains (27.3% to 36.7% of guaranteed strain); the concrete

compressive strains were less than 3500 με (CAN/CSA S806 2012) (29.5% to 52.9% of the maximum concrete strain). This confirms that neither the rupture of the BFRP reinforcement nor concrete crushing occurred before punching-shear failure.

The maximum measured strains in the BFRP reinforcement in S6-B and S7-B at 436.4 kN (failure load of S7-B) were 5904 με and 10816 με, respectively. This represents 27.3% and 50.1% of the guaranteed strain of the BFRP bars. This result confirms the significant effect of edge restraining on reducing the strain in BFRP bars by 45.4% compared to the unrestrained slab. S2-B and S4-B (no top reinforcement but the same reinforcement ratio) showed approximately the same tensile strain up to failure. This confirms that the top reinforcement had no significant effect on the measured strains.

On the other hand, a comparison of S2-B and S3-B (same reinforcement ratio with 12 mm and 16 mm diameter bars) reveals nearly identical load–strain relationships up to about 400 kN. Before failure, the smaller reinforcing bars with closer spacing (S2-B) helped control the strains in the reinforcing bars and the crack width. In addition, S5-B (BFRP), G-S2 (GFRP), and C-S2 (CFRP), which had similar axial-reinforcement stiffness, displayed the same load–strain relationships up to failure.

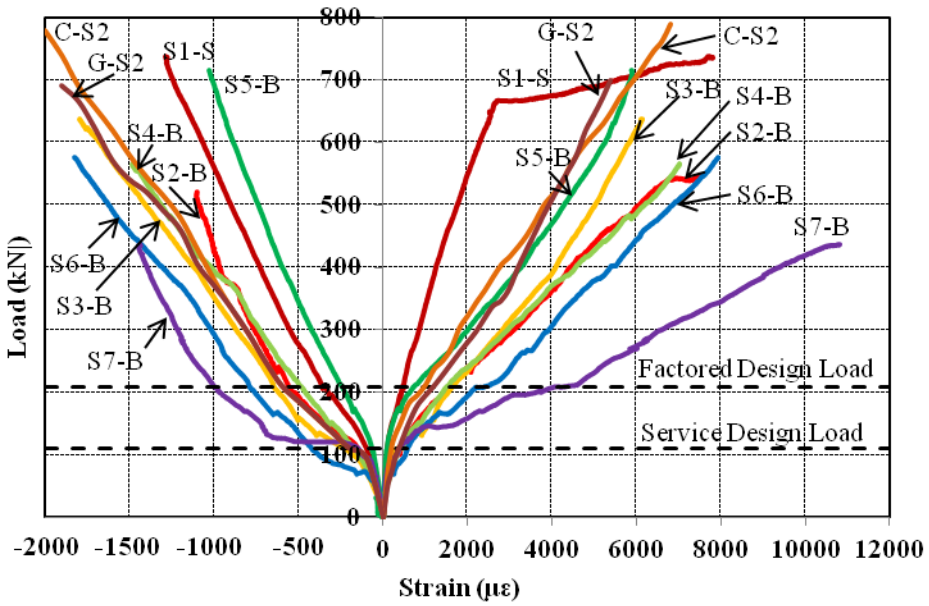

Figure 5–9: Load-strains on the top surface of the concrete and bottom reinforcement

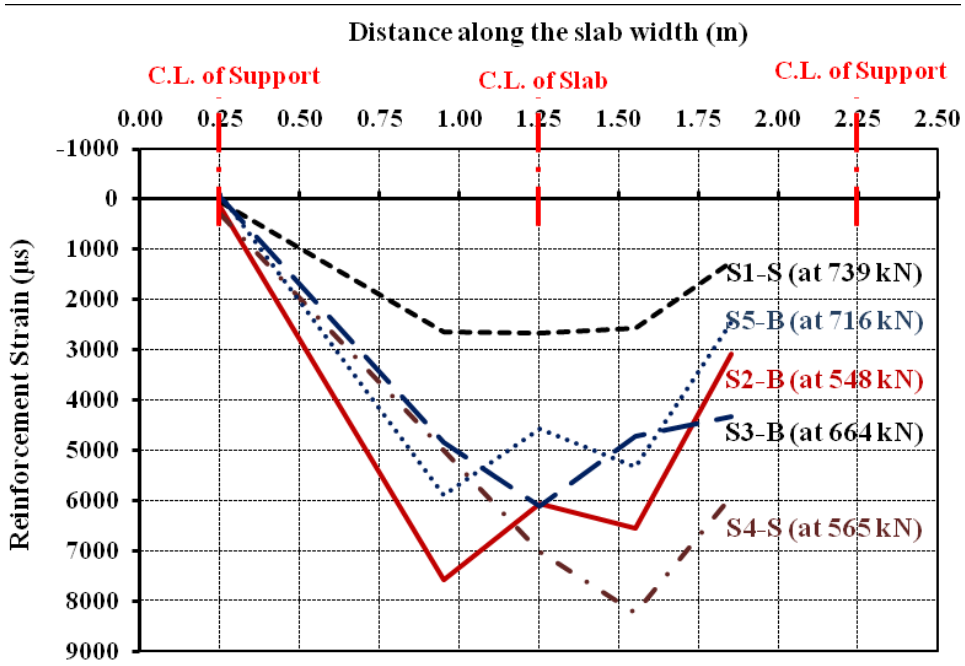

Figure 5–10: Distribution of the reinforcement strains at the middle section of the slabs

5.4.4 Deflection Behavior

Figure 5–11 provides the applied load versus the maximum deflection at position D2 for all the slabs. Neither the vertical load nor the deflection values include the effects of slab self-weight. The slabs behaved similarly up to failure and the load–deflection curves were almost bilinear. The pre-cracking behavior of all the slabs was similar, regardless of reinforcement type, diameter, or ratio. This was due to the negligible effect of the reinforcement on the gross moment of inertia in the slabs. Unlike the pre-cracking stage, the axial-reinforcement stiffness significant influenced slab post-cracking responses until failure. At the same load level, S1-S (reinforced with steel) exhibited a lower deflection and higher rigidity than S2-B, S3-B, and S4-B (BFRP bottom reinforcement in the transverse direction with the same reinforcement ratio as S1-S). This can be attributed to higher axial-reinforcement stiffness, which reduced crack width.

At the service load level, the maximum measured deflections for S2-B, S5-B, and S6-B (reinforcement ratios of 0.8%, 1.20% and 0.40%, respectively) were 1.25, 0.87, and 1.86 mm, respectively. At failure, however, the maximum measured deflections for the same slabs were 19.83, 16.96, and 24.86 mm, respectively, as given in **Table 5–3**. Increasing reinforcement ratio two and three times reduced the deflection by 32.8% and 53.2% at service load, respectively, and by 20.2% and 31.8% at failure, respectively.

In addition, S5-B (BFRP) had deflection values less than G-S2 (GFRP) with similar axial-reinforcement stiffness. This may be attributed to the closer bar spacing in S5-B and the bundled bar configuration of G-S2. Furthermore, S6-B and S7-B showed a remarkable difference in their behavior, with S7-B exhibiting higher deflection and lower rigidity compared to the other slab due to the absence of end restraining.

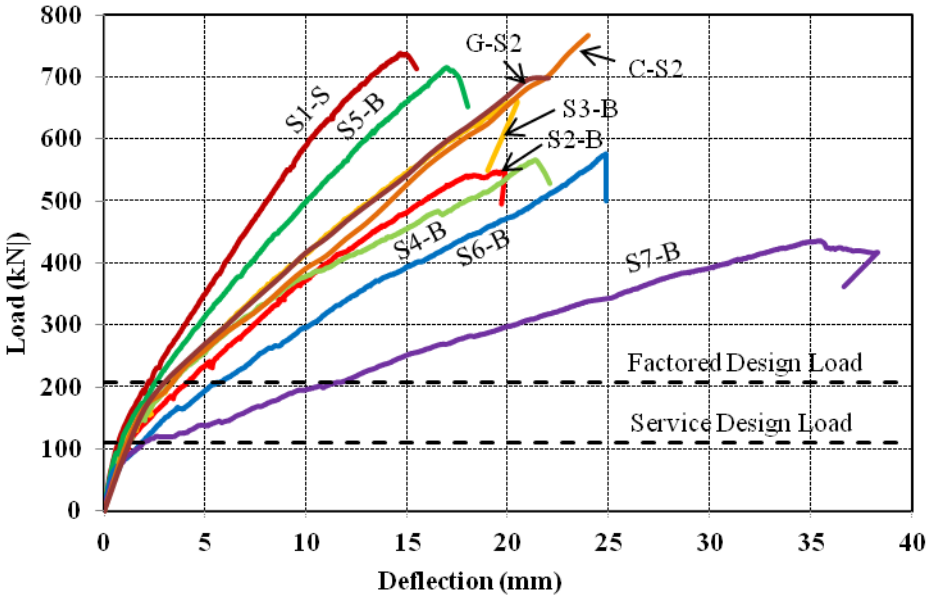

Figure 5–11: Load-maximum deflection curves

Table 5–3: Summary of the test results and comparison with theoretical prediction of the punching-shear capacities

ID	f'_c (MPa)	P_{cr} (kN)	P_{max} (kN)	Deflection (mm)			FRP Strain (με)			Concrete Strain (με)			Crack Width (mm)			$P_{max.\ exp.}/P_{max.\ pred.}$	
				P_{serv}	P_{Fact}	P_{max}	P_{serv}	P_{Fact}	P_{max}	P_{serv}	P_{Fact}	P_{max}	P_{serv}	P_{Fact}	P_{max}	CSA (2012)	ACI (2015)
S1-S	48.81	112.0	739.6	0.69	2.19	14.68	149	627	2645	-96	-340	-1285	--	0.09	1.16	--	--
S2-B		105.3	548.3	1.25	4.14	19.83	424	1595	7563	-149	-555	-1104 [b]	0.10	0.42	1.82	0.92	1.53
S3-B	42.20	134.8	664.6	0.94	3.34	20.36	340	1640	6109	-233	-647	-1851	--	0.19	0.94	1.13	1.86
S4-B		120.5	565.9	1.08	3.41	21.37	396	1497	7017	-171	-485	-1486	--	0.29	1.26	1.00	1.64
S5-B	47.90	108.6	716.4	0.87	2.53	16.96	92	706	5888	-68	-240	-1032	0.10	0.19	1.16	1.06	1.67
S6-B		73.1	575.8	1.86	5.58	24.86	575	2186	7932	-425	-788	-1826	0.35	0.52	N.A [c]	1.22	2.23
S7-B		121.0	436.4	1.93	11.56	35.49	381	4042	10815	-149	-994	-1437	--	0.93	5.81	0.93	1.69
G-S2 [a]	44.30	132	712	1.20	3.02	21.58	329	1317	5403	-189	-470	-1914	0.30	0.46	1.47	--	--
C-S2 [a]		145	799	1.14	3.62	24.59	177	91041	6814	-165	-574	-2000	0.25	0.36	1.36	--	--

P_{cr} and P_{max} are cracking and failure loads, Service (P_{serv}) and factored (P_{Fact}) design loads = 110.25 and 208.25 kN, respectively, [CL-625 Truck] (CAN/CSA S6 2014).

[a] Slabs G-S2 and C-S2 were tested by El-Gamal et al. (2005).

[b] Strain gauges malfunctioned after that load.

[c] Strain at 514.5 kN (LDVT malfunctioned before failure).

5.5 Comparison of Measured and Predicted Punching Capacities

The punching-shear capacities of the BFRP-reinforced slabs were predicted using the available punching-shear equations in CAN/CSA S806 (2012) and ACI 440.1R (2015) and compared against the experimental results.

According to CAN/CSA S806 (2012), the punching-shear strength is the smallest of Eqns. (5-1) to (5-3).

$$V_c = \left(1+\frac{2}{\beta_c}\right)\left[0.028\lambda\varphi_c\left(E_f\rho_f f_c^{'}\right)^{\frac{1}{3}}\right]b_o d \tag{5-1}$$

$$V_c = \left[\left(\frac{\alpha_s d}{b_o}\right)+0.19\right]0.147\lambda\varphi_c\left(E_f\rho_f f_c^{'}\right)^{\frac{1}{3}} b_o d \tag{5-2}$$

$$V_c = 0.056\lambda\varphi_c\left(E_f\rho_f f_c^{'}\right)^{\frac{1}{3}} b_o d \tag{5-3}$$

where $f_c^{'}$ is the specified concrete compressive strength; b_o is the perimeter of the critical section at a distance of $d/2$ from the concentrated load; and d is the distance from the extreme compression fiber to the centroid of the tension reinforcement; λ is a factor to account for concrete density; α_s is a factor that adjusts V_c for support location; and β_c is the ratio of the long side to short side of the concentrated load or reaction area.

ACI 440.1R (2015) provided Eq. (5-4) to calculate the punching-shear capacity of concrete slabs reinforced with FRP bars or grids. This equation considers the effect of reinforcement stiffness to account for the punching-shear capacity of concrete slabs as follows:

$$V_c = \frac{4}{5}\sqrt{f_c^{'}}b_o c \tag{5-4}$$

$$k = \sqrt{2\rho_f n_f + \left(\rho_f n_f\right)^2} - \rho_f n_f \tag{5-5}$$

where c is the neutral axis depth (mm) of the cracked transformed section; $c = k\,d$; and n_f is the modular ratio.

Table 5–3 provides the ratios between the experimentally measured and predicted punching-shear capacities. The punching-shear predictions with the ACI 440.1R (2015) equation yielded very conservative predictions with an average experimental-to-predicted ratio of 1.77±0.25. A similar high level of conservativeness was reported for GFRP reinforced-concrete deck slabs (Bouguerra et al. 2011) and two-way slabs (Dulude et al. 2013). Conversely, CAN/CSA S806 (2012) equations yielded reasonable yet conservative predictions with an average experimental-to-predicted ratio of 1.04±0.12. Dulude et al. (2013) and Hassan et al. (2013a&b) determined that CAN/CSA S806 (2012) accurately predicted the punching-shear capacity of FRP-RC slabs. Thus, it can be concluded that, similar to slabs reinforced with carbon-, glass-, and aramid-FRP reinforcement, the punching-shear capacity of concrete slabs with BFRP reinforcement can be predicted with current FRP design provisions.

5.6 Summary and Conclusion

This paper presents a research project aimed at investigating the performance of full-scale edge-restrained concrete bridge-deck slabs reinforced with basalt-fiber-reinforced-polymer (BFRP) bars. The tests included six full-scale, edge-restrained concrete deck slabs simulating an actual slab-on-girder bridge-deck commonly used in North America and one full-scale unrestrained concrete deck slab. The deck slabs measured 3000 mm long × 2500 mm wide × 200 mm thick. The slabs were tested up to failure over a center-to-center span of 2000 mm under a single concentrated load acting on the center of each slab over a contact area of 600 × 250 mm to simulate the footprint of sustained truck wheel load (87.5 kN CL-625 truck, CAN/CSA S6 2014). Based on the test results presented and discussed herein, the following conclusions have been drawn:

1. Similar to past findings for steel-, GFRP-, and CFRP-reinforced concrete bridge-deck slabs, the BFRP-reinforced concrete bridge-deck slabs evidenced punching-shear failure at corresponding loads higher than the factored designed loads provided by the CHBDC (CAN/CSA S6 2014).

2. The bottom transverse-reinforcement ratio was the main parameter affecting the general behavior (strains, crack width, deflection). Increasing the bottom-transverse reinforcement ratio significantly enhanced the performance and reduced strains, deflection, and crack width at the same load level.

3. Regardless of the role of the top reinforcement in actual bridges in controlling the shrinkage cracking, the top reinforcement had no significant effect on the structural behavior and punching-shear strength of the deck slabs.

4. Deck slabs with the same reinforcement ratio and axial-reinforcement stiffness ($E_f A_f$), reducing BFRP bar size and spacing improved the cracking performance and the induced strains by improving the bond between the concrete and reinforcing bars. The use of smaller diameters of FRP reinforcement is recommended, assuming that the code's requirements concerning the minimum diameters and maximum bar spacing are satisfied.

5. Bridge-deck slabs with the same axial-reinforcement stiffness nearly exhibit the same behavior and punching-shear capacity.

6. The design of deck slabs using the flexural method was governed in most cases by the crack-width limit. Thus, using FRP bars with a high modulus of elasticity, such as BFRP bars, will significantly reduce the required amount of reinforcement.

7. The test results showed that an edge-restraining system increased the ultimate capacity by 31.9% and reduced the crack widths, deflection, and FRP strains compared to the unrestrained slab. This provides evidence of the development of compressive membrane action (CMA) in the laterally restrained concrete deck slabs.

8. At failure, the tensile strains in the BFRP reinforcement in the restrained deck slabs ranged from 27.3% to 36.7% of the guaranteed strains of the BFRP bars.

9. The current punching-shear provisions in CAN/CSA S806 (2012) provided reasonable yet conservative predictions for the punching-shear capacity of BFRP-RC deck slabs. On the other hand, the current guide of ACI 440.1R (2015) underestimated the punching-shear strength of the tested slabs. These findings are in agreement with past work conducted on glass- and carbon-FRP bars.

10. Considering the results and interpretations presented herein, basalt-FRP (BFRP) reinforcing bars can be used in bridge-deck slabs. Such slabs can be conservatively designed according to

the flexural design method, assuming a material safety factor and stress level at service limit state similar to those of glass-FRP (GFRP) bars until new information is obtained.

CHAPTER 6
EXPEIMENTAL TESTING OF BASALT-FIBER-REINFORCED POLYMER BARS IN CONCRETE BEAMS

Abstract

The advances in fiber-reinforced-polymer (FRP) technology have spurred interest in introducing new fibers, such as basalt, in addition to the commonly used glass, carbon, and aramid. Recently, new basalt-FRP (BFRP) bars have been developed, but research is needed to characterize and understand how BFRP bars would behave in concrete members. This paper presents an experimental study aimed at determining the bond-dependent coefficient (k_b) and investigating the structural performance of newly developed BFRPs in concrete beams. A total of six concrete beams reinforced with BFRP bars were built and tested up to failure. The test beams measured 200 mm wide, 300 mm high, and 3100 mm long. Ten, 12, and 16 mm BFRP bars with sand-coated surfaces over helical wrapping were used. The beam specimens were designed in accordance with Annex S of CAN/CSA S806 (2012) and tested under four-point bending over a clear span of 2700 mm until failure. The beam test results are introduced and discussed in terms of cracking behavior, deflection, and failure modes. The test results yielded an average bond-dependent coefficient (k_b) of 0.76, which is in agreement with the CAN/CSA S6 (2014) recommendation of 0.8 for sand-coated bars. Moreover, comparing the results to code provisions showed that CAN/CSA S806 (2012) may yield reasonable yet conservative deflection predictions at service load for the beams reinforced with BFRP bars.

***Keywords*:** Beams, basalt-fiber-reinforced polymer (BFRP), sand-coated, deflection, flexure, crack width, bond-dependent coefficient, and serviceability.

6.1 Introduction

The service life of reinforced-concrete (RC) structures may be shortened due to the corrosion of steel reinforcement and related types of deterioration. Although routine maintenance is needed to counter durability-related deterioration, the cost of repairing, rehabilitating, or strengthening of steel RC structures can be high (Nkurunziza et al. 2005; Banibayat and Patnaik 2015). New materials, such as fiber-reinforced polymer (FRP), which is noncorrodible by nature, can be used, especially in harsh environmental conditions, to eliminate corrosion problems.

The use of glass-, carbon-, and aramid-FRP (GFRP, CFRP, and AFRP) reinforcement has been extensively investigated and used as reinforcement in concrete structures. The current design codes and guidelines such as ACI 440.1R (2015), CAN/CSA S6 (2014), and CAN/CSA S806 (2012) allow the use of GFRP, CFRP, and AFRP as the main reinforcement in concrete structures and provide design recommendations for using these bars. Advances in FRP technology, however, have resulted in increasing demand to introduce new types of fibers such as basalt fibers. Wu et al. (2012) reported that basalt-FRP (BFRP) bars are the most recent FRP composite materials developed to enhance the safety and reliability of structural systems compared to GFRP, CFRP, and AFRP composites. Nevertheless, fundamental studies on and relevant applications of BFRP are still limited because the technology is relatively recent compared to other FRP composites. Besides, the current FRP material specifications and design codes do not include BFRP as an FRP alternative.

6.2 Background

Basalt is a natural inorganic material that is found in volcanic rocks originating from frozen lava, with a melting temperature between 1500°C and 1700°C (Militký and Kovačič 1996; Militký et al. 2002). The molten rocks are then extruded through small nozzles to produce continuous filaments of basalt fiber with diameters ranging from 13 to 20 μm (Pantanik, 2009). BFRP fibers lie between glass and carbon for both stiffness and strength (Brik 2003; Sim et al. 2005). The good properties of basalt fiber (Patnaik et al. 2004), combined with cost-effective manufacturing, have led to the development of BFRP bars as internal reinforcement for concrete structures (Brik 2003; Sim et al. 2005; Patnaik et al. 2009; Banibayat and Patnaik 2015).

BFRP bars have attracted attention due to their cost effectiveness (Sim et al. 2005; Wu et al. 2012), high temperature resistance (Brik 2003; Sim et al. 2005), freeze–thaw performance (Wu et al. 2010; Shi et al. 2011a&b), and ease of manufacture (Sim et al. 2005). They have also been shown to perform better in acidic environments than GFRP (Wei et al. 2010). Like GFRP, however, BFRP has a low elastic modulus relative to steel and undergoes degradation from alkali solutions (Sim et al. 2005). Moreover, basalt fibers can be used for very low temperatures (i.e. about -200°C) up to comparatively high temperatures (i.e., in the range of 600°C to 800°C) (Sim et al. 2005; Scheffler et al. 2009; Deák and Czigány 2009; Cao et al. 2009; Wu et al. 2012) and has better fatigue performance (Wu et al. 2010). In addition, BFRP composites showed potential use in a number of areas such as national defense, aerospace, civil construction, transport infrastructure, energy infrastructure, petrochemical, fire protection, automobile, shipbuilding, water conservation, and hydropower (Wu et al. 2012).

The flexural performance of concrete beams (80 × 120 × 1200 mm) reinforced with BFRP bars 8 mm in diameter with a tensile modulus of elasticity of 39.05 GPa was investigated (Urbański et al. 2013; Lapko and Urbański 2015). The results showed that the BFRP-RC beams did not fail suddenly since the beams transformed into a tie system because flexural reinforcement did not rupture. The deflection and crack width of the BFRP-RC beams were significantly higher than that of a steel-reinforced beam, due to the lower modulus of BFRP bars compared to that of steel bars. The deflection predictions using CAN/CSA S806 (2002) showed good convergence with the experimental values in the initial level of load.

Tomlinson (2015) assessed the flexural and shear performances of concrete beams (150 × 300 × 3100 mm) reinforced with BFRP bars and stirrups. The test results showed that the standard provisions performed well in predicting the capacity of beams failing in flexure. For beams failing in shear, standards were both conservative and nonconservative.

6.3 Research Project

With the main objective of integrating BFRP reinforcement into current FRP design codes and standards, an extensive research project is being conducted at the University of Sherbrooke, Quebec, through the activities of the NSERC Research Chair in FRP Reinforcement for Concrete

Infrastructure. The project includes (i) Part I: short- and long-term characterization of newly developed BFRP bars; (ii) Part II: structural testing of full-scale concrete bridge-deck slabs reinforced with BFRP bars, and (iii) Part III: performance evaluation and bond characteristics of BFRP bars in concrete beams.

Part I included the complete physical and mechanical characterization of different products of BFRP bars. It also included long-term durability characterization using accelerated aging techniques in different chemical solutions at high temperatures for certain periods of time in accordance with ACI 440.6M (2008) and CAN/CSA S807 (2010). The findings of this part (Vincent et al. 2013; Elgabbas et al. 2014; Benmokrane at al. 2015; Elgabbas et al. 2015a) concluded that it was feasible to produce BFRP bars that would meet the requirements of current FRP standards. These findings also contributed to introduce new generations of BFRP with enhanced characteristics used for structural testing in the other parts of the study. Parts II and III are in progress and the preliminary results of testing the full-scale bridge-deck slabs reinforced with BFRP (Elgabbas et al. 2015b) revealed that the structural performance meeting the requirements of the *Canadian Highway Bridge Design Code* (CHBDC) (CAN/CSA S6 2014).

This paper presents the results of the first set of experimental testing (Part III) of BFRP bars in beams. The main objectives of the work presented herein were to investigate the bars' flexural behavior at service and ultimate limit states to evaluate the bond-dependent coefficient (k_b) of the sand-coated BFRP bars, as the crack-width predictions include k_b to account for the bond between the FRP bars and the surrounding concrete.

6.4 Experimental Program

6.4.1 Material Properties

Reinforcing bars: Basalt-fiber-reinforced polymer (BFRP) bars (Magmatech Inc.) 10, 12, and 16 mm in diameter were used as tension reinforcement in the tested beams. The bars had a sand-coated surface over helical wire wrapping, as shown in **Figure 6–1**, to enhance the bond between the bars and the surrounding concrete. The fiber content of the BFRP bars was 87.2%, 90.6%, and 89.9% (by weight) for the 10, 12, and 16 mm diameters, respectively. The physical characterization of the tested BFRP bars can be found elsewhere (Vincent et al. 2013). On the other hand, 10M

steel bars were used as transverse and top reinforcement in the test specimens. **Table 6–1** provides the mechanical properties of the BFRP and steel bars. It should be mentioned that, the mechanical properties of BFRP bars were determined using nominal cross-section areas of 79, 113, and 201 mm^2 for the 10, 12, and 16 mm diameters, respectively.

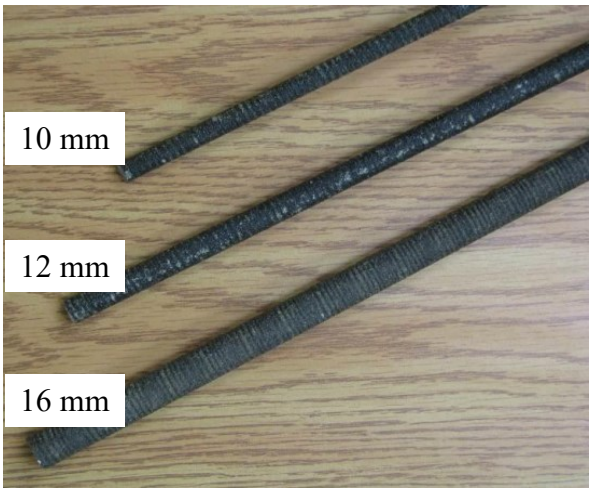

Figure 6–1: BFRP bars of different diameters

Table 6–1: Tensile properties and bond strength of BFRP and steel bars

Type	d_b (mm)	A_f (mm^2)	E_f (GPa)	f_{fu} (MPa)	ε_{fu} (%)	τ_{max} (MPa)
BFRP [a]	10	79	44.4 ± 1	1189 ± 74	2.7 ± 0.2	18.0 ± 0.2
	12	113	45.3 ± 1	1162 ± 26	2.6 ± 0.1	13.8 ± 1.9
	16	201	48.7 ± 1	1173 ± 49	2.4 ± 0.1	13.5 ± 1.6
Steel [b]	10M	100	200	450	0.2	---

[a] Mechanical properties determined based on nominal cross-sectional areas (A_f) shown in this table.

[b] Tensile properties of the steel bars were provided by the manufacturer.

Concrete: The beam specimens were made with ready-mixed, normal-strength concrete with a target compressive strength of 40 MPa. A cubic meter of the concrete contained 350 kg of cement, 813 kg of sand, and 1032 kg of aggregate with a water/cement ratio (w/c) of 44% and an entrained-air ratio of 5% to 8%. The maximum aggregate size was 20 mm. The six beams were cast using the same concrete batch. The concrete strength was determined by testing three 150×300 mm

cylinders on the day of beam testing. The average compressive strength was 42.5±0.4 MPa. The average tensile strength from split-cylinder testing on 150×300 mm cylinders was 2.83±0.05 MPa.

6.4.2 Test Specimens

This investigation included six rectangular concrete beams reinforced with BFRP bars designed in accordance with the geometry requirements in Annex S of CAN/CSA S806 (2012). The beams measured 200 mm wide, 300 mm high, and 3100 mm long. The beams were fabricated using normal-strength concrete and were tested under four-point bending over a clear span of 2700 mm. The beams had a clear shear span of 1100 mm (corresponding to a shear-span-to-depth ratio of about 4.3), while the distance between the two loading points was 500 mm (constant moment zone). The beams were reinforced with two 10M rebar as top reinforcement, while the bottom reinforcement was BFRP bars in different configurations (2 or 4 BFRP bars), as shown in **Table 6–2**. 10M steel stirrups spaced at 100 mm were used as shear reinforcement in both shear spans to avoid shear failure. To minimize the confining effect of the shear reinforcement on the flexural behavior, no stirrups were used in the constant moment zone. The clear concrete cover was 38 mm, which was set in accordance with Annex S of CAN/CSA S806 (2012). **Figure 6–2** shows the dimensions and reinforcement details of the tested beams. The test specimens were designed to fail by concrete crushing in the constant moment zone. This was accomplished by using a reinforcement ratio (ρ_f) greater than the balanced reinforcement ratio (ρ_{fb}), as shown in **Table 6–2**, where the balanced reinforced reinforcement ratio (ρ_{fb}) is calculated from Eq. (6-1):

$$\rho_{fb} = \alpha_1 \beta_1 \frac{f_c^{'}}{f_{fu}} \frac{\varepsilon_{cu}}{\varepsilon_{cu} + \varepsilon_{fu}} \tag{6-1}$$

$$\alpha_1 = 0.85 \tag{6-2a}$$

$$\beta_1 = 0.85 - 0.05\left(f_c^{'} - 27.6\right)/6.9 \tag{6-2b}$$

$$\alpha_1 = 0.85 - 0.0015 f_c^{'} \geq 0.67 \tag{6-3a}$$

$$\beta_1 = 0.97 - 0.0025 f_c^{'} \geq 0.67 \tag{6-3b}$$

The ratio between the actual and balanced reinforcement ratios ranged from 1.35 to 6.81 according to ACI 440.1R (2015) and from 1.09 to 5.52 according to CAN/CSA S806 (2012). The differences between actual and balanced reinforcement ratios in ACI 440.1R (2015) and CAN/CSA S806

(2012) for the same beams were due to the differences in the stress-block parameters (α_1 and β_1 as shown in Eq. (6-2) for ACI 440.1R (2015) and Eq. (6-3) for CAN/CSA S806 (2012)) and the ultimate compressive strain of the concrete (0.003 for ACI 440.1R (2015) and 0.0035 for CAN/CSA S806 (2012)).

Table 6–2: Reinforcement details of beam specimens

Beam ID[a]	ρ_f	ACI 440.1R (2015)		CAN/CSA S806 (2012)		$(E_f \times A_f)$ (kN)	Reinforcement Configuration
		ρ_{fb}[b]	ρ_f/ρ_{fb}	ρ_{fb}[b]	ρ_f/ρ_{fb}		
B-2#10mm	0.0030	0.0023	1.35	0.0028	1.09	6677	2-10 mm - 1 layer
B-4#10mm	0.0060	0.0023	2.89	0.0028	2.34	13954	4-10 mm - 2 layers
B-2#12mm	0.0044	0.0024	1.83	0.0030	1.48	10251	2-12 mm - 1 layer
B-4#12mm	0.0086	0.0024	3.95	0.0030	3.20	20501	4-12 mm - 2 layers
B-2#16mm	0.0078	0.0025	3.13	0.0031	2.54	19591	2-16 mm - 1 layer
B-4#16mm	0.0154	0.0025	6.81	0.0031	5.52	39183	4-16 mm - 2 layers

[a] The first letter "B" indicates concrete beam; the second number "2 or 4" indicates the number of BFRP bars; the last number (#10, #12 or #16) indicates the BFRP bar size (in mm).

[b] ρ_{fb} was calculated based on the concrete compressive strength of 42.5 MPa.

6.4.3 Instrumentation of Beam Specimens

Table 6–3 provides instrumentation details. The deflection along the beam's span was monitored using four linear variable differential transducers (LVDTs) with 0.001 mm accuracy, labeled D1 to D4 (D2 and D3 at mid-span and D1 and D4 at quarter-span). Crack propagation was also monitored during testing until failure, and the crack widths of the first three flexural cracks were monitored with three LVDTs (D5 to D7). The strains of the longitudinal BFRP reinforcing bars were captured with four electrical-resistance strain gauges 6 mm in length (S1 to S4). The compressive concrete strains at the mid-span section were measured with two electrical-resistance strain gauges 60 mm in length (C1 and C2). To facilitate monitoring the cracks, the beams were painted white before the test, revealing pre-existing cracks on the beams.

In addition, an automatic-data acquisition system connected to a computer was used to monitor loading, deflections, and strains in the concrete and reinforcement. The formation of beam cracks and the corresponding loads were marked and recorded during testing until failure.

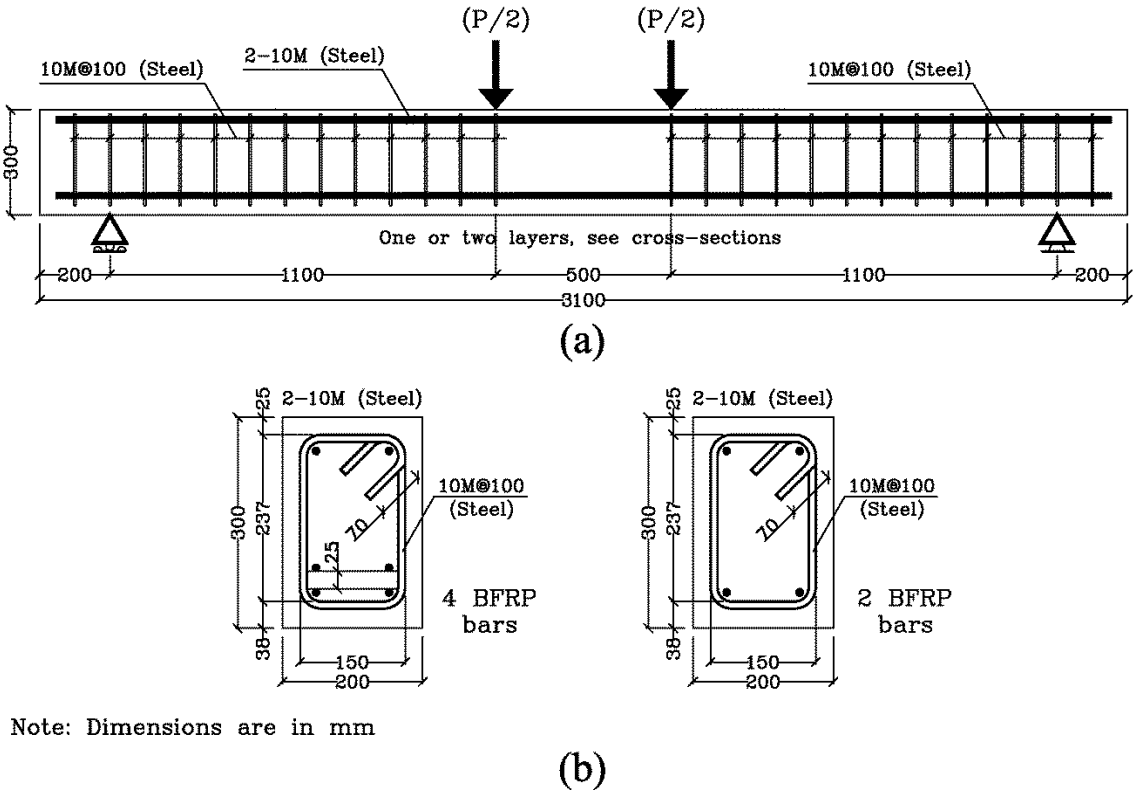

Figure 6–2: Dimensions and reinforcement details of tested beams: a) elevation; b) cross section

6.4.4 Test Setup and Procedure

The simply supported beams were tested under monotonic load in four-point bending until failure. **Figure 6–3** shows the dimensions and locations of the applied loads, while **Figure 6–4** provides a photo of the test setup for beam specimens. The load was applied at a stroke-controlled rate of 1.2 mm/min. During testing, the beams were observed visually until the first crack appeared and the corresponding load was recorded. The test was paused when each of the first three cracks appeared. The initial crack width of the first three cracks was measured manually with a 50X handheld electronic microscope; LVDTs were installed at crack locations to measure crack width electronically with increasing load. The load continuously increased until beam failure.

The cracking load was also verified based on the change in stiffness of the load–deflection and load–strain relationships. The concrete and reinforcement strain gauges and deflection and

cracking LVDTs were connected to an automatic-data acquisition system connected to a computer to record their readings.

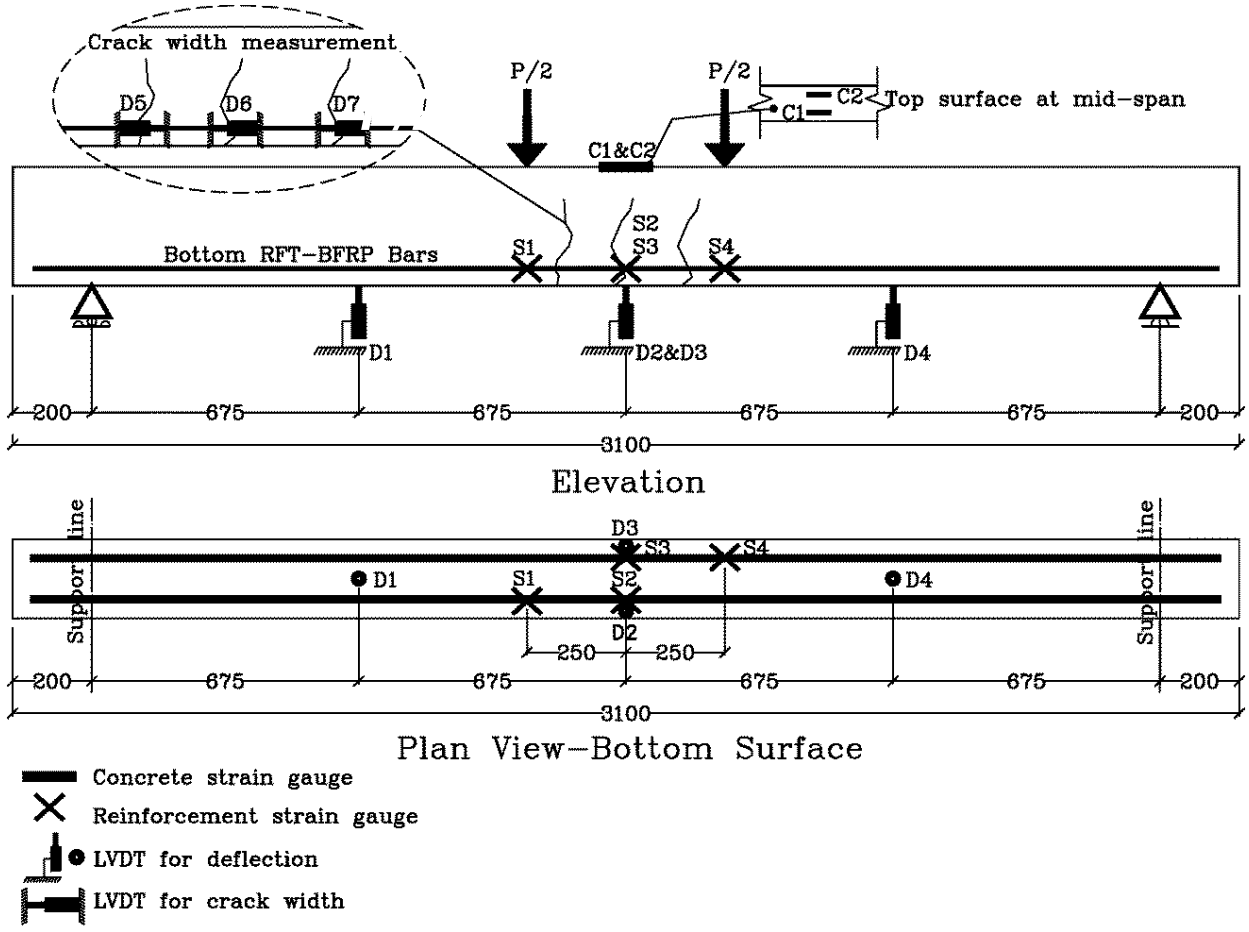

Figure 6–3: Schematic drawing of instrumentation

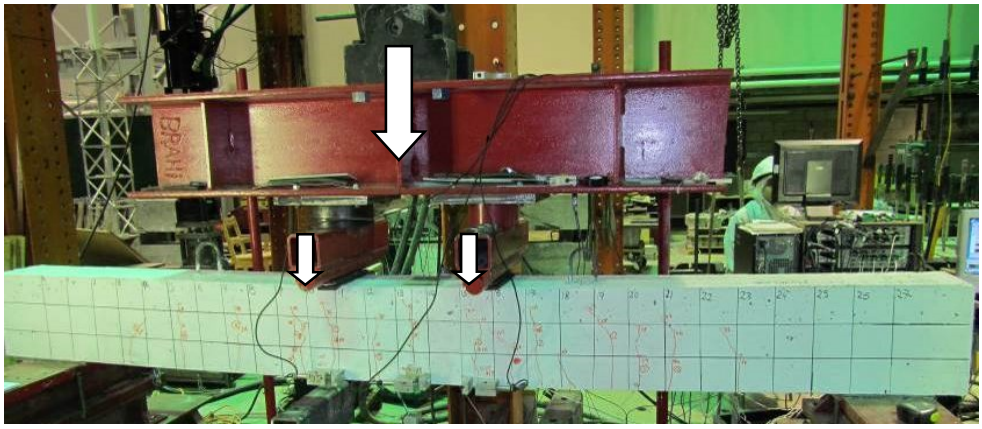

Figure 6–4: Overview of the test setup

6.5 Test Results and Discussion

6.5.1 First Cracking Moment

All beams behaved similarly until first cracking. Their cracking loads and pre-cracked stiffness were essentially the same regardless of reinforcement ratio.

Table 6–3 provides the cracking moments of all tested beams. The reported cracking moment, excluding the self-weight of the beams, ranged from 7.24 to 9.87 kN.m with an average of 8.84 kN.m. This value is approximately 13.5% of the average ultimate moment capacity. The cracking moments, M_{cr}, were predicted using Eq. (6-4):

$$M_{cr} = \frac{f_r \times I_g}{y_t} \tag{6-4}$$

where the modulus of rupture of concrete, f_r, is calculated from Eq. (6-5a) in accordance with ACI 440.1R (2015) and Eq. (6-5b) in accordance with CAN/CSA S806 (2012) for normal-density concrete.

$$f_r = 0.62\sqrt{f_c'} \tag{6-5a}$$

$$f_r = 0.60\sqrt{f_c'} \tag{6-5b}$$

Table 6–3 compares the experimental and predicted values of the cracking moments, M_{cr}. It should be noted that the controlling variable for predicting the cracking moment is the modulus of rupture of concrete, f_r, which varies according to the design codes and guidelines. As shown in **Table 6–3**, the cracking moment of the BFRP-RC beams was generally 27% and 24% lower, respectively, than those predicted with ACI 440.1R (2015) and CAN/CSA S806 (2012). CAN/CSA S806 (2012) yielded slightly better predictions of cracking moments than ACI 440.1R (2015) because of the former's smaller modulus of rupture. Similar observations were reported for the cracking moments of GFRP-RC beams (El-Nemr et al. 2013) where the predicted cracking moments were higher than the measured cracking moments for normal- and high-strength concrete. It is worth mentioning that FRP-RC members may crack over time as additional stresses developed from shrinkage, temperature effect (Bischoff 2001) and the freezing and melting of

water inside the concrete, causing hair cracks and therefore reducing the cracking load. The cracks resulting from shrinkage, however, did not significantly affect crack-width prediction (Bischoff 2001).

Table 6–3: Cracking, ultimate moments and mode of failure; experimental and theoretical

Beam	Experimental (kN.m)			ACI 440.1R (2015)			CAN/CSA S806 (2012)		
	M_{cr}	M_n	MOF[a]	$\frac{M_{cr,Exp.}}{M_{cr,Pre.}}$	$\frac{M_{n,Exp.}}{M_{n,Pre.}}$	MOF[b]	$\frac{M_{cr,Exp.}}{M_{cr,Pre.}}$	$\frac{M_{n,Exp.}}{M_{n,Pre.}}$	MOF[a]
B-2#10mm	9.03	52.84	B.F.	0.75	1.36	C.C.	0.77	1.22	C.C.
B-4#10mm	7.24	58.30	C.C.	0.60	1.27	C.C.	0.62	1.11	C.C.
B-2#12mm	9.87	53.72	C.C.	0.81	1.17	C.C.	0.84	1.05	C.C.
B-4#12mm	9.00	76.89	C.C.	0.74	1.45	C.C.	0.77	1.27	C.C.
B-2#16mm	8.09	69.74	C.C.	0.67	1.17	C.C.	0.69	1.05	C.C.
B-4#16mm	9.81	82.06	C.C.	0.81	1.24	C.C.	0.84	1.09	C.C.
Average				0.73	1.28	---	0.76	1.13	---
Standard deviation				0.08	0.11	---	0.09	0.09	---

[a] B.F. denotes balanced failure and C.C. denotes crushing of concrete.

6.5.2 Bond-Dependent Coefficient (k_b) Prediction

Extensive analysis of the bond-dependent coefficient (k_b) was conducted by an ACI committee on a variety of concrete sections and FRP bars considering the fiber type, resin formulations, and surface treatments. Through this study, the average k_b values ranged from 0.60 to 1.72, with an average of 1.10 reported ACI 440.1R (2015). Data for rough sand-coated FRP-bar surface treatments trended toward the lower end of this range. In the absence of experimental test data for k_b, ACI 440.1R (2015) suggests a conservative value of 1.4 should be used. On the other hand, ISIS (2007) recommends a k_b of 1.2 in the absence of significant test data, while CAN/CSA S6 (2014) recommends a k_b of 0.8 for sand-coated bars and 1.0 for deformed FRP bars.

The test results were used to assess the bond-dependent coefficient values (k_b). The k_b was calculated in accordance with Annex S of CAN/CSA S806 (2012) from Eq. (6-6). The calculations were based on the first three cracks in each beam. The k_b was calculated from each beam at 30%

of the nominal capacity, $0.3M_n$, (assumed service load) of the tested specimens. This value was reported as the service load level by many researchers (Mota at al. 2006; Bischoff 2009; and El-Nemr et al. 2013). For the calculations, however, the upper crack-width limit of 0.7 mm proposed in Annex S of CAN/CSA S806 (2012) was not considered. This was expected to provide more conservative k_b values. The individual and average k_b measured from each beam is presented in **Table 6–4**. The average k_b value was 0.76 for BFRP bars having a sand-coated over helical wire wrapping surface. This value is in agreement with the 0.8 for sand-coated FRP bars provided in the *Canadian Highway Bridge Design Code* (CAN/CSA S6 2014). It is worth mentioning that, if the upper limit of 0.7 mm for the crack width was considered in the calculations, the average k_b values would be 0.70.

$$w_{cr} = 2\frac{f_f}{E_f}\frac{h_2}{h_1}k_b\sqrt{d_c{}^2 + (s/2)^2} \qquad (6\text{-}6)$$

Table 6–4: Experimentally determined bond-dependent coefficient (k_b) for sand-coated BFRP bars

Beam	Crack #1	Crack #2	Crack #3	Average
B-2#10mm	0.82	0.79	0.71	0.77
B-4#10mm	0.59	1.02	0.68	0.76
B-2#12mm	1.14	0.46	0.75	0.78
B-4#12mm	0.65	0.73	0.77	0.72
B-2#16mm	0.67	0.66	0.91	0.75
B-4#16mm	0.57	0.66	1.17	0.80
Average				0.76
Standard deviation				0.03

6.5.3 Crack Propagation and Crack Width

The crack propagation in the tested beams followed the traditional flexural-cracking patterns in simply supported beams, as shown in **Figure 6–5**. The first cracks always appeared in the constant-moment region of the beams, starting from the beam bottom surface and extending vertically toward the compression zone. As the load increased, the cracks extended further away from the constant-moment region towards the supports. Cracks outside the constant-moment region were

affected by a combination of flexural and shear stresses, so the cracks tended to gain a horizontal component. At high loads approaching to beam nominal capacity, some longitudinal cracks at the level of the reinforcement appeared between two cracks, but did not affect the failure mode. These cracks are mainly due to the high deformation of the bars and the incompatibility of the deformations between two cracks, which led to slippage between the reinforcement bars and surrounding concrete (i.e., bond failure). This phenomenon has been reported in past research on concrete beams reinforced with FRP bars (Tomlinson and Fam 2015; El-Mogy et al. 2010). Moreover, no shear cracks were observed in any of the beams as the overall section capacity was less than the expected load that would cause shear cracks to form. Moreover, a horizontal crack appeared at the nominal-moment level between the two loading points at the beam top surface due to the high strain level in the concrete, which leads to concrete crushing, as shown in **Figure 6–5**.

The crack patterns in **Figure 6–5** confirm that beams with higher reinforcement ratios exhibited improved patterns characterized by better distribution and smaller crack widths, which could be captured by comparing the crack patterns of the tested beams to that of beam B-2#10mm (lowest reinforcement ratio, B-2#10mm BFRP bars). As expected, increasing the reinforcement ratio while keeping the mechanical properties unchanged helped enhance the cracking performance (distribution and widths), since it increased beam axial stiffness.

Unlike steel reinforcement, which can easily corrode when exposed to environmental and harsh conditions, FRP reinforcement does not corrode. Consequently, the crack width for FRP-reinforced concrete (FRP-RC) sections is provided for esthetic considerations rather than corrosion prevention. In addition, the allowable crack widths in FRP-RC are normally larger than those of steel-reinforced sections. CAN/CSA S806 (2012) and CAN/CSA S6 (2014) specify a service-limiting flexural-crack width of 0.5 mm for exterior exposure (or aggressive environmental conditions) and 0.7 mm for interior exposure. In addition, ACI 440.1R (2015) recommends using CAN/CSA S806 (2012) limits in most cases. On the other hand, since there is a direct relationship between the strain in the reinforcing bars and crack width, ISIS-M3 (2007) specified 2000 με as a strain limit in FRP reinforcing bars to control crack width.

Table 6–5 provides the initial and maximum crack widths at $0.30M_n$ and at $0.67M_n$ for the first three cracks in each beam**.** The initial crack width decreased as the reinforcement ratio increased.

It should be mentioned that, in beam B-2#10mm and B-2#12mm, the LVDTs stopped recording the data due to a technical problem, which prevented crack widths at $0.67M_n$ from being recorded.

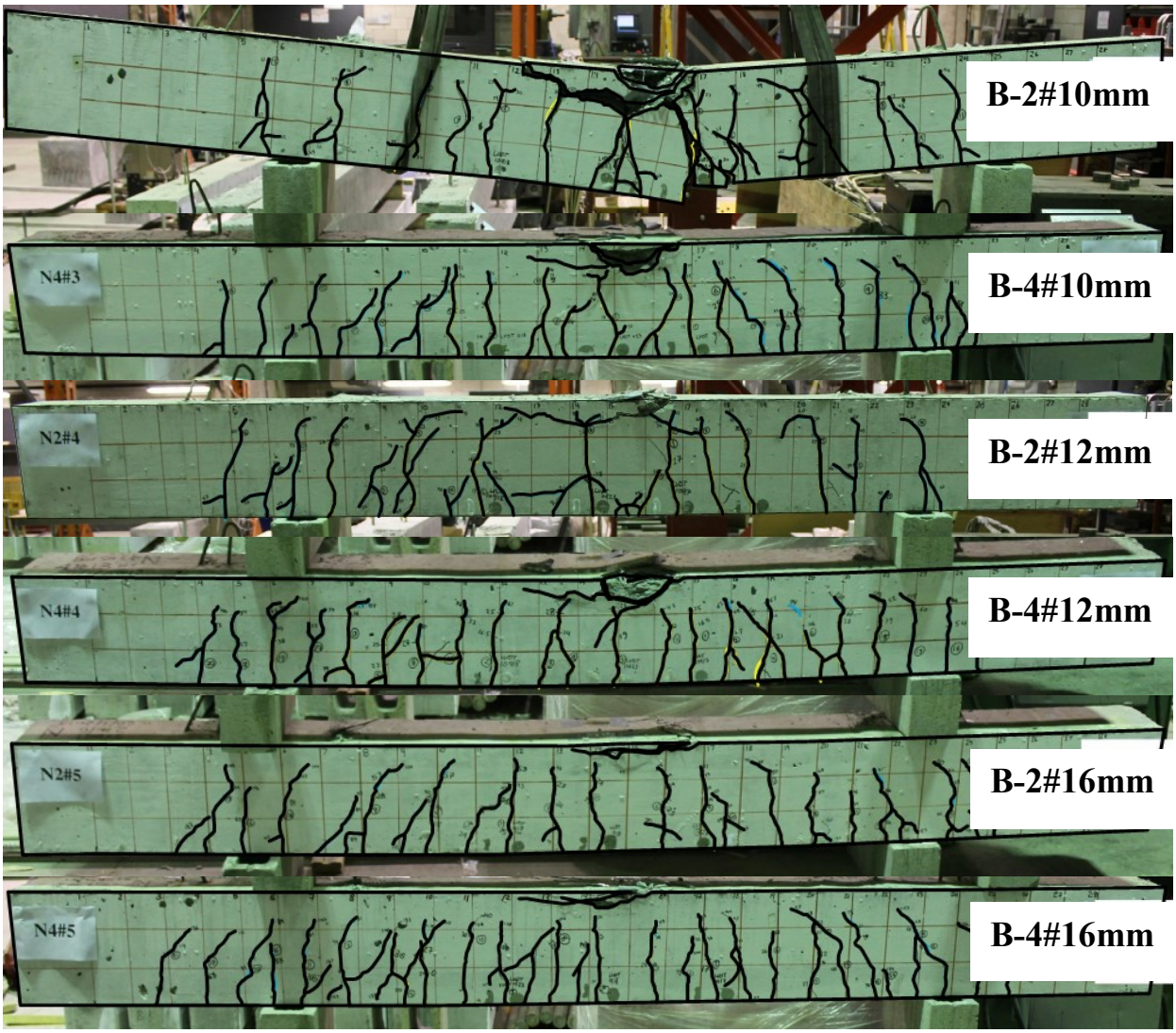

Figure 6–5: Crack patterns and failure modes of the tested beams

Table 6–5: Experimentally and predicted crack widths

Beam	$w_{exp.}$ (mm)			$w_{exp.}/w_{pred.}$			
				k_b=1.4 ACI 440.1R (2006)		k_b=0.8 CAN/CSA S6 (2014)	
	$w_{initial}$	$w_{0.30Mn}$	$w_{0.67Mn}$	$0.30M_n$	$0.67M_n$	$0.30M_n$	$0.67M_n$
B-2#10mm	0.22	1.44	N/A	0.60	N/A	1.04	N/A
B-4#10mm	0.12	1.20	2.70	0.73	0.76	1.28	1.33
B-2#12mm	0.22	1.36	N/A	0.82	N/A	1.42	N/A
B-4#12mm	0.10	0.78	1.86	0.52	0.55	0.92	0.96
B-2#16mm	0.17	0.81	2.02	0.66	0.75	1.16	1.31
B-4#16mm	0.05	0.69	1.27	0.69	0.56	1.21	0.98
Average				0.67	0.65	1.17	1.15
Standard deviation				0.10	0.12	0.18	0.20

6.5.4 Flexural Capacity and Mode of Failure

The concrete beams were designed to fail by concrete crushing when the concrete reached its maximum compressive strain of $\varepsilon_{cu} \approx 0.0030$ and 0.0035 according to ACI 440.1R (2015) and CAN/CSA S806 (2012), respectively, before the tensile stress in the FRP bars (f_f) reached the ultimate capacity (f_{fu}). Consequently, the actual reinforcement ratio (ρ_f) was greater than the balanced reinforcement ratio (over-reinforcement section). This is the most commonly used design concepts for concrete section reinforced with FRP bars. The balanced reinforcement ratios (ρ_{fb}) were calculated with Eq. (6-1). The terms (α_1) and (β_1) were calculated from Eq. (6-2) for ACI 440.1R (2015) and from Eq. (6-3) for CAN/CSA S806 (2012).

Table 6–3 presents the flexural capacity (M_n) and mode of failure of the tested beams. The tested beams failed by concrete crushing, except beam B-2#10mm, in which the actual reinforcement ratio was close to the balanced ratio as calculated according to CAN/CSA S806 (2012). The measured compressive strain in the concrete at failure was 3316 με, while the BFRP bars ruptured at 26205 με, which is almost equal to the ultimate strain of the BFRP bars (27000 με). These strain measurements imply a balanced failure in which the concrete and BFRP failed simultaneously (compressive failure in the concrete and rupture of the BFRP bars).

Moreover, **Table 6–3** shows that the higher reinforcement ratio led to an increase in the ultimate capacity. Beam B-2#10mm (ρ_f = 0.3%) failed at 52.84 kN.m by balanced failure, while B-4#10mm (ρ_f = 0.6%) failed at 58.3 kN.m (10.3% higher than B-2#10mm) due to concrete crushing. Doubling the reinforcement ratio in B-4#12mm, compared to B-2#12mm, increased the capacity from 53.72 to 76.89 kN.m (increased by 43.13 %) where both beams failed due to concrete crushing. Similarly, B-2#16mm and B-4#16mm failed at 69.74 and 82.06 kN.m, respectively, (increased by 17.67%). It should be mentioned that the effective depth of the beams with 4 BFRP bars in tension was less than those with 2 BFRP bars as the 4 BFRP bars were placed in two layers. These reinforcement configurations have an effect on specimen flexural capacity.

Considering the beams with one reinforcing layer of BFRP bars (B-2#10mm, B-2#12mm, and B-2#16mm), the ultimate capacities were 52.84, 53.72, and 69.74 kN.m for B-2#10mm (ρ_f = 0.3%), B-2#12mm (ρ_f = 0.43%), and B-2#16mm (ρ_f = 0.77%), respectively. Compared to B-2#10mm, the increases in the flexural capacities were 1.67% and 31.98% for B-2#12mm and B-2#16mm, respectively. Similar behavior was observed for the beams with two layers of BFRP bars (B-4#10mm, B-4#12mm, and B-4#16mm). The ultimate capacities were 58.30, 76.89, and 82.06 kN.m for B-4#10mm (ρ_f = 0.6%), B-4#12mm (ρ_f = 0.86%), and B-4#16mm (ρ_f = 1.54%), respectively. Compared to B-4#10mm, the increases in the flexural capacities were 31.89% and 40.75% for B-4#12mm and B-4#16mm, respectively. El-Nemr et al. (2013) reported similar behavior for GFRP bars when increasing ρ_f by 3 to 4 times resulted in an average increase of 83.5% in the load-carrying capacity.

Furthermore, B-4#12mm and B-2#16mm with close axial reinforcement stiffness (E_f A_f) (20501 kN and 19591 kN, respectively) exhibited similar flexural capacities (76.89 kN and 69.74 kN). The difference between the flexural strengths of both beams was 10%, which implies that beams with similar E_f A_f should exhibit similar behavior and flexural capacity (assuming the surface configuration of the bars have not been changed). This has been reported by many authors for other performances such as shear (El-Sayed et al. 2006; Ahmed et al. 2010a&b); such, however, is beyond the scope of this manuscript.

The ultimate capacity of the test specimens was predicted using the strain compatibility approach in ACI 440.1R (2015) and CAN/CSA S806 (2012) and compared to the measured values.

Table 6–3 shows the experimental-to-predicted ultimate capacity of the tested beams. Generally, both the ACI 440.1R (2015) and CAN/CSA S806 (2012) prediction equations underestimated the flexure capacity of BFRP-RC beams. The average experimental-to-predicted ultimate capacities were 1.28±0.11 and 1.13±0.09 for ACI 440.1R (2015) and CAN/CSA S806 (2012), respectively. The difference between the experimental ultimate capacities and the predicted capacities of ACI 440.1R (2015) and CAN/CSA S806 (2012) was related to the negligence of the compression strength contribution of the top steel bars (Maranan et al. 2015). Moreover, the difference between ACI 440.1R (2015) and CAN/CSA S806 (2012) was related to the β_1 factor and the assumed strain at ultimate which is 0.003 for ACI 440.1R (2015) and 0.0035 for CAN/CSA S806 (2012).

6.5.5 FRP Reinforcement and Concrete Strain

Table 6–6 presents the average mid-span tensile strains in the BFRP bars at positions (S3) and (S4), and the average compressive strains in concrete at positions (C1) and (C2) versus the applied moment until failure. The relationships were typical bilinear curves with a sharp increase in the reinforcement strains, especially in the beams with low reinforcement ratios, which reflects the sudden change in the stiffness at cracking. This is in agreement with the results reported for different types of FRP bars in concrete beams (Kassem et al. 2011; El-Nemr et al. 2013). **Figure 6–6** shows the similar pre-cracking responses of all the tested beams, as well as the significant post-cracking increases in the BFRP tensile strains until failure due to the reduced post-cracking stiffness of the beams. Moreover, the plotted data shows that, after beam cracking, the reinforcement tensile strains varied linearly with the increased load up to failure.

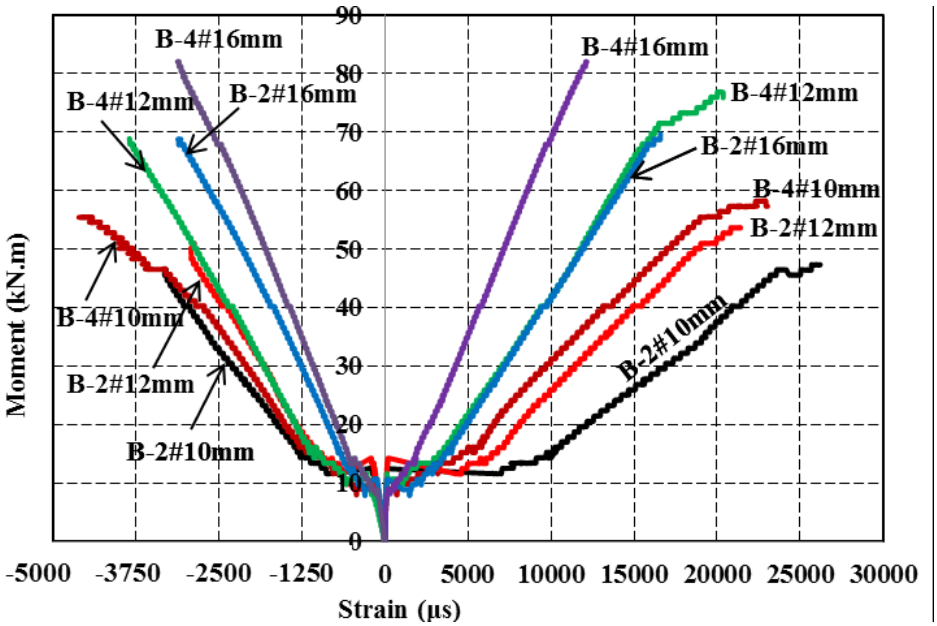

Figure 6–6: Moment reinforcement and concrete-strain relationships

Table 6–6 shows the strains of BFRP bars and concrete at 30% of the nominal capacity ($0.3M_n$) and nominal capacity (M_n). The tested beams failed by concrete crushing, except beam B-2#10mm, in which the actual reinforcement ratio was close to the balanced ratio calculated according to CAN/CSA S806 (2012). It is worth mentioning that over-reinforced section design is the most common and recommended design for FRP-RC sections (CAN/CSA S806 2012, and ACI 440.1R 2015). In some instances, however, under-reinforced sections may be used, assuming that the design requirements are met such as recommended by CAN/CSA S6 (2014). **Figure 6–6** shows that the higher the reinforcement ratio, the lower the reinforcement strains at the same load level. For beams B-4#12mm and B-2#16mm with $E_f A_f$ = 20501 kN and 19591 kN, respectively, the moment–reinforcement-strain relationships were almost the same, which supports that beams with similar $E_f A_f$ for the same FRP reinforcing bars exhibited similar strains at the same load level.

The measured strains were used in determining the c/d at $0.30M_n$ and M_n (see **Table 6–6**). The c/d did not change much between $0.30M_n$ and M_n, which indicates that the sections were totally cracked and the location of the neutral axis was not changed significantly between $0.30M_n$ and M_n. In addition, the neutral-axis depth increased as the reinforcement ratio increased, since the equilibrium of forces required a larger compression block. The c/d were also determined theoretically based on strain compatibility in a cracked section (see **Table 6–6**), which shows good agreement between the theoretical and experimental results.

Table 6–6: BFRP and concrete strains neutral axis-to-depth ratio and curvature of test specimens

Beam	FRP Strain (με)			Conc. Strain (με)		$(c/d)_{exper.}$			$(c/d)_{pred.}$	Curvature, Ψ x 10^{-2}, m^{-1}			Deform.
	ε_c=1000 με	0.30M_n	M_n	0.30M_n	M_n	ε_c=1000 με	0.30M_n	M_n	M_n	ε_c=1000 με	0.30M_n	M_n	factor (J)
B-2#10mm	7976	10082	26205	-1252	-3316	0.11	0.11	0.11	0.12	3.49	4.41	11.17	12.87
B-4#10mm	4987	6063	22720	-1315	-4608	0.17	0.18	0.17	0.17	2.50	3.08	11.40	17.42
B-2#12mm	6686	7001	21434	-1071	-2922	0.13	0.13	0.12	0.12	3.00	3.15	9.51	11.22
B-4#12mm	4344	6219	20370	-1476	-3846	0.19	0.19	0.16	0.17	2.25	3.34	10.20	22.83
B-2#16mm	5737	5124	16762	-895	-3115	0.15	0.15	0.15	0.13	2.65	2.37	7.83	8.53
B-4#16mm	3934	2913	12207	-891	-3251	0.20	0.21	0.21	0.18	2.11	1.63	6.61	9.43

6.5.6 Ductility and Deformability

Ductility can be defined as the capacity of a structure to absorb energy without suffering failure (Naaman and Jeong 1995; Jaeger et al. 1995; Vijay and GangaRao 1996), and is generally related to the amount of inelastic deformation that takes place before complete failure. In other words, it could be represented as the ability to sustain inelastic deformations without loss of load-carrying capacity prior to failure. For steel-RC members, ductility is defined as the ratio of deflection or curvature or rotation values at ultimate to those at yielding of steel. This way of estimating ductility, however, cannot be applied to the concrete structures reinforced with FRP bars because of the linear elastic behavior of FRP until failure, whether compressive or tensile. The ductility of an FRP-reinforced beam depends on uniform elongation of FRP bars at different locations as compared with localized steel bar yielding; confinement effect; uniform crack location and spacing in the case of FRP-reinforced concrete beams; the bond between bar and concrete; the plastic-hinge formation in concrete; and frictional-force development along diagonal and wedge cracks (Vijay and GangaRao 2001).

Jaeger et al. (1997) and Newhook et al. (2002) proposed an alternative concept based on deformability rather than ductility for FRP-RC members to ensure that FRP-RC exhibited significant deformation before failure (at ultimate). The *Canadian Highway Bridge Design Code* (CAN/CSA S6 2014) adopted this concept and provided Eq. (6-7) to determine the deformability factor *J*.

$$j = \frac{\psi_u M_u}{\psi_c M_c} \tag{6-7}$$

where M is the bending moment and Ψ is the curvature. The subscripts u and c refer to ultimate state and a concrete strain equal to 0.001, respectively. The moment and curvature at a concrete strain of 0.001 may depict the moment and curvature at service limit state. CAN/CSA S6 (2014) state that the deformability factor, *J*, should be at least 4.0 for rectangular sections and 6.0 for T-sections. **Table 6–6** presents the deformability factor *J* of the tested beams, which ranged from 8.53 to 22.83 to meet CAN/CSA S6 (2014) requirements.

Vijay and GangaRao (2001) used experimental results in determining that *c/d* ranging from 0.15 to 0.30 appeared to be a reasonable design choice for concrete beams and slabs reinforced with

FRP bars in order to achieve a deformability factor of 6 or higher. The tested beams showed a *c/d* at failure ranging from 0.11 to 0.21 with corresponding deformability factors higher than 6. This may be in acceptable agreement with the findings of Vijay and GangaRao (2001) but more investigation is needed to define a specific range for BFRP-RC members.

6.5.7 Deflection Responses

Figure 6–7 shows the applied load versus the average mid-span deflection responses at positions D2 and D3 (see **Figure 6–3**) for all tested beams, while **Table 6–7** provides the average measured deflections at different load levels. As expected, the beams' responses are nearly similar before cracking due to the non-significant effect of the reinforcement ratio on the beams' gross moment of inertia. The identical slopes of the load–deflection curves indicate the similar stiffness of the beams at this stage.

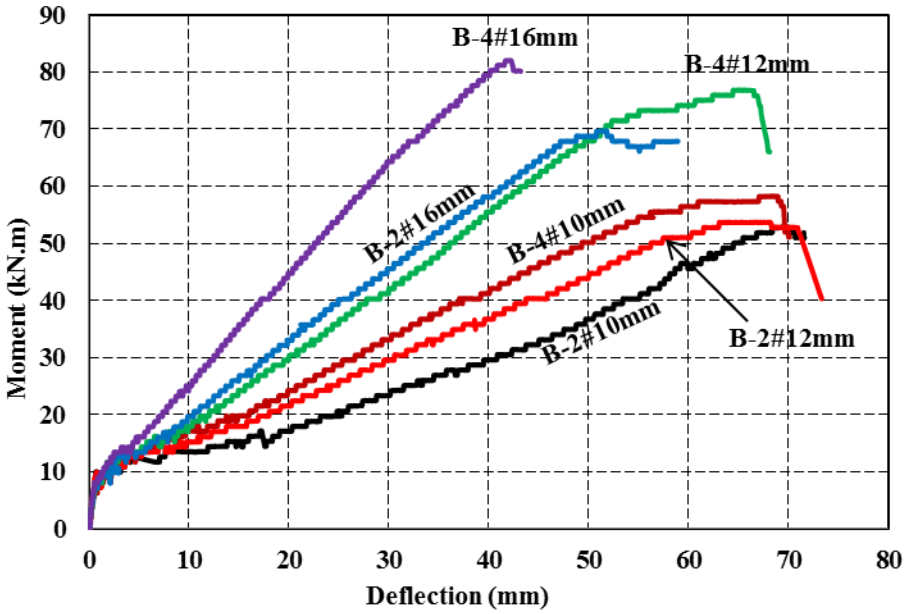

Figure 6–7: Load–mid-span deflection relationships

Unlike in the pre-cracking stage, the BFRP-RC beams exhibited reduced post-cracking stiffness until failure. When the applied moment exceeded the cracking moment, the cracking occurred in the constant-moment zone, causing a reduction in stiffness and drop in slope. The reinforcement ratio (ρ_f) appears to have significantly influenced the post-cracking stiffness of the beams until failure and, therefore, the load–deflection behavior. As expected, the higher the reinforcement

ratio, the higher the post-cracking stiffness and, consequently, the lower the deflection values. Beam B-2#10mm with the lowest reinforcement ratio and an axial stiffness ($E_f A_f$) of 0.3% and 6677 kN, respectively, exhibited the lowest post-cracking stiffness until failure at a nominal capacity of 52.84 kN.m. The average mid-span deflection of B-2#10mm at failure was 69.33 mm, while B-4#16mm, with the highest reinforcement ratio and axial stiffness ($E_f A_f$) of 1.54% and 39183 kN, respectively, exhibited the highest post-cracking stiffness and showed an average mid-span deflection value of 23.00 mm at 52.84 kN.m (capacity of B-2#10mm), which represents 33% that of B-2#10mm. The average mid-span deflection of B-4#16mm at failure (82.06 kN.m) was 42.10 mm. It is worth mentioning that the beams with low reinforcement ratios (as B-2#10mm) exhibited sharp increases in deflection at cracking, which is in agreement with the sharp increase in reinforcement strains at cracking (see **Figure 6–6**). This behavior was enhanced by increasing the reinforcement ratio. Similar behavior was reported for GFRP bars (El-Nemr et al. 2011).

Furthermore, B-4#12mm and B-2#16mm with $E_f A_f$ = 20501 kN and 19591 kN, respectively, demonstrated very close moment–deflection relationships (see **Figure 6–7**), which implies similar post-cracking stiffness. Thus, beams with similar $E_f A_f$ may show the same moment–deflection relationship.

6.6 Comparison between the Experimental and Predicted Results

6.6.1 Crack Width

The average k_b value calculated based on the beam test results was used in predicting the crack width of each beam. The crack width was calculated using Eq. (6-6). **Table 6–5** provides a comparison between the average measured crack widths of the first three flexural cracks and the predicted crack widths at $0.3M_n$ and $0.67M_n$ using CAN/CSA S6 (2014) (Eq. 6-6). Since the crack width equation of ACI 440.1R (2006) is the same as that of CAN/CSA S806 (2012), it was also used in predicting the crack width of the tested beams. The recommended k_b values for sand-coated FRP bars were 0.8 and 1.4 for CAN/CSA S6 (2014) and ACI 440.1R (2015), respectively.

The reported values in **Table 6–5** confirm that using k_b = 0.8 as provided by CAN/CSA S6 (2014) underestimated the crack widths by 16%, on average, at $0.3M_n$ and $0.67M_n$. On the other hand, the k_b = 1.4 in ACI 440.1R (2006) overestimated the crack widths by 34%, on average, at $0.3M_n$ and

0.67M_n. **Figure 6–8** shows the experimental and predicted moment–crack-width relationships for all tested beams. It is worth mentioning that the average measured k_b was 0.76, which justifies the reasonable agreement between the crack-width prediction in CAN/CSA S6 (2014) and the measured values.

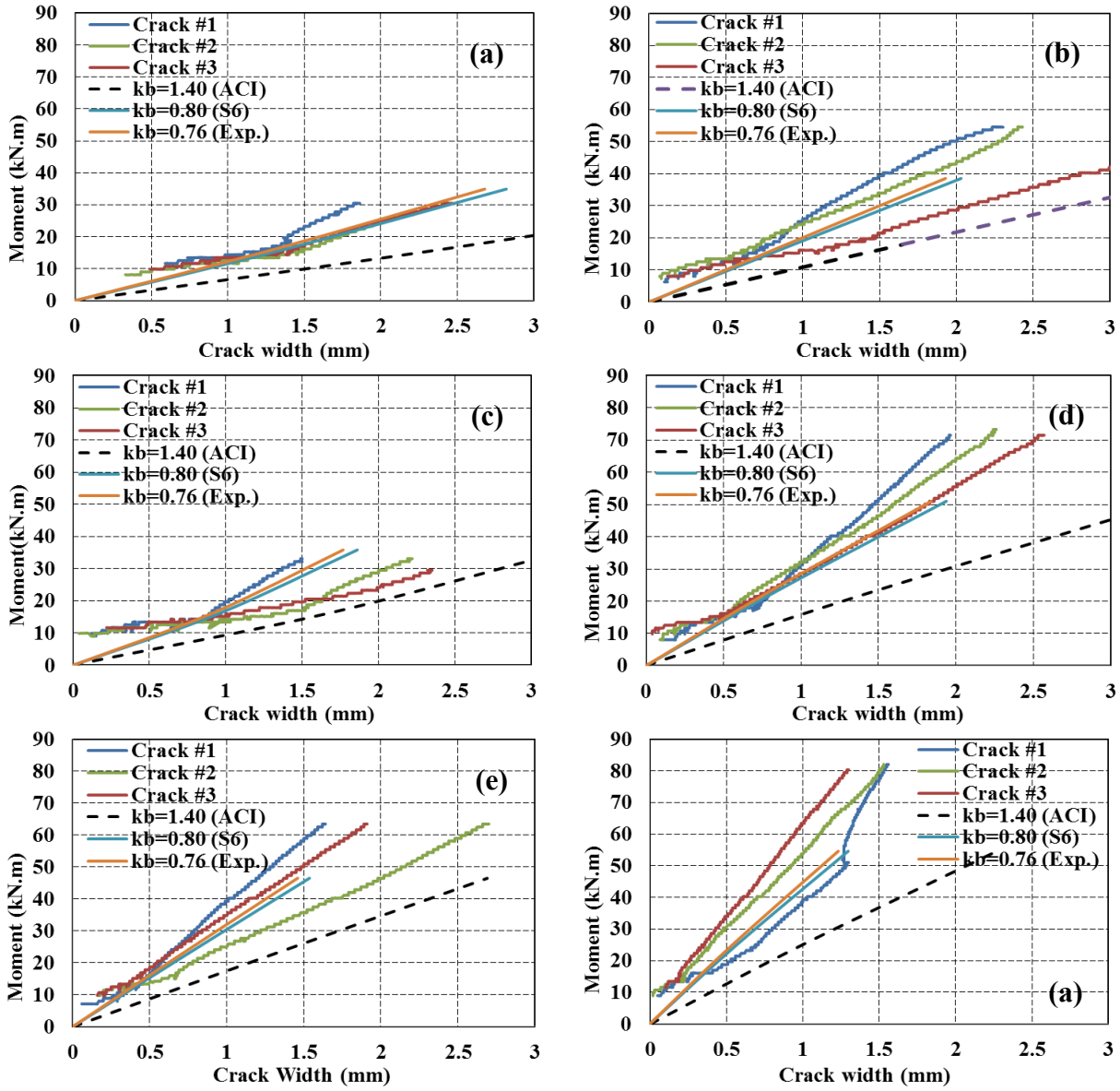

Figure 6–8: Experimental and predicted moment–crack-width relationships of all tested beams: (a) B-2#10mm; (b) B-4#10mm; (c) B-2#12mm; (d) B-4#12mm; (e) B-2#16mm; (f) B-4#16mm

6.6.2 Mid-Span Deflection

The deflection behavior of reinforced-concrete elements subject to flexure moment can be divided into two separate stages: before and after cracking. The first stage, in which the section is not cracked, according to ACI 440.1R (2006&2015) and the CAN/CSA S806 (2012), the behavior of the concrete element is controlled by the section's gross moment of inertia (I_g). The second stage starts when the applied moment (M_a) exceeds the cracking moment (M_{cr}) and crack propagation occurs; which reduces stiffness.

The ACI 440.1R (2006) equation is based on the effective moment of inertia (I_e), which is determined through modification of the Branson (1968) equation. The modification, shown in Eq. (6-8a), introduced (β_d) to account for FRP instead of steel, where (β_d) is proportional to the ratio between the actual and balanced reinforcement ratio of the section (Eq. 6-8b). While ACI 440.1R (2015) recommended another formula to calculate I_e, which was based on Bischoff et al. (2009) (Eq. 6-9a). This formula includes an additional factor γ to account for the variation in stiffness along the length of the member as shown in Eq. (6-9b) which was introduced by Bischoff and Gross (2011). The deflection prediction entails calculating a uniform moment of inertia throughout the beam length and uses deflection equations derived from linear elastic analysis, as shown in Eq. (6-10), for a simply supported member subjected to two-point loading.

$$I_e = \left(\frac{M_{cr}}{M_a}\right)^3 \beta_d I_g + \left[1 - \left(\frac{M_{cr}}{M_a}\right)^3\right] I_{cr} \le I_g \tag{6-8a}$$

$$\beta_d = \frac{1}{5}\left(\frac{\rho_f}{\rho_{fb}}\right) \le 1.0 \tag{6-8b}$$

$$I_e = \frac{I_{cr}}{1 - \gamma\left(\frac{M_{cr}}{M_a}\right)^2\left[1 - \frac{I_{cr}}{I_g}\right]} \le I_g \tag{6-9a}$$

$$\gamma = 1.72 - 0.72\left(\frac{M_{cr}}{M_a}\right) \tag{6-9b}$$

$$\delta_{max} = \frac{PL^3}{24E_cI_e}\left[3L^2 - 4a^2\right] \tag{6-10}$$

CAN/CSA S806 (2012) recommends curvature integration along the span to determine the deflection of a concrete member at any point, assuming the section is fully cracked with no contribution of tension stiffness in the beam's cracked regions. Therefore, the moment–curvature relation of FRP concrete members can be assumed to be bilinear, where the curvature (Ψ) is given by ($M_a/(E_cI_g)$) for the uncracked parts of the beam, followed by an increase in curvature at a constant moment value (transition from uncracked to cracked stage) and ($M_a/(E_cI_{cr})$) for the cracked part when the applied moment (M_a) is higher than the cracking moment (M_{cr}). CAN/CSA S806 (2012) provides deflection equations for simple loading cases, such as Eq. (6-11), for a simply supported member subjected to two-point loading where the cracked moment of inertia (I_{cr}) is calculated from Eq. (6-12).

$$\delta = \frac{PL^3}{24E_cI_{cr}}\left[3\left(\frac{a}{L}\right) - 4\left(\frac{a}{L}\right)^3 - 8\left(1-\frac{I_{cr}}{I_g}\right)\left(\frac{L_g}{L}\right)^3\right] \quad (6\text{-}11)$$

$$I_{cr} = \frac{bd^3}{3}k^3 + n_fA_fd^2(1-k)^2 \quad (6\text{-}12)$$

Table 6–7 provides the experimental mid-span deflections measured at 30% and 67% of the nominal capacity (0.3M_n and 0.67M_n), respectively. It also provides the experimental-to-predicted deflection ratios ($\delta_{exp}/\delta_{pred}$) for all tested beams at 0.3M_n and 0.67M_n based on ACI 440.1R (2006), ACI 440.1R (2015) and CAN/CSA S806 (2012) provisions. **Figure 6–9** shows the correlation between the experimental and predicted responses. Besides, **Table 6–7** confirms that ACI 440.1R (2006) underestimated the deflection of the beams at 0.30M_n (expected service load) where the average $\delta_{exp}/\delta_{pred}$ was 2.10±0.37. Similarly, at 0.67M_n, it underestimated the deflection values with an average $\delta_{exp}/\delta_{pred}$ of 1.08±0.04. While ACI 440.1R (2015) showed better predictions than ACI 440.1R (2006) at both 0.3M_n and 0.67M_n, with an average $\delta_{exp}/\delta_{pred}$ of 1.35±0.15 and 1.03±0.05, respectively. On the other hand, CAN/CSA S806 (2012) overestimated the deflection predictions at 0.30M_n and 0.67M_n, where the average $\delta_{exp}/\delta_{pred}$ was 0.80±0.09 and 0.92±0.08, respectively. Thus, CAN/CSA S806 (2012) may provide reasonable yet conservative deflections for the beams reinforced with BFRP bars.

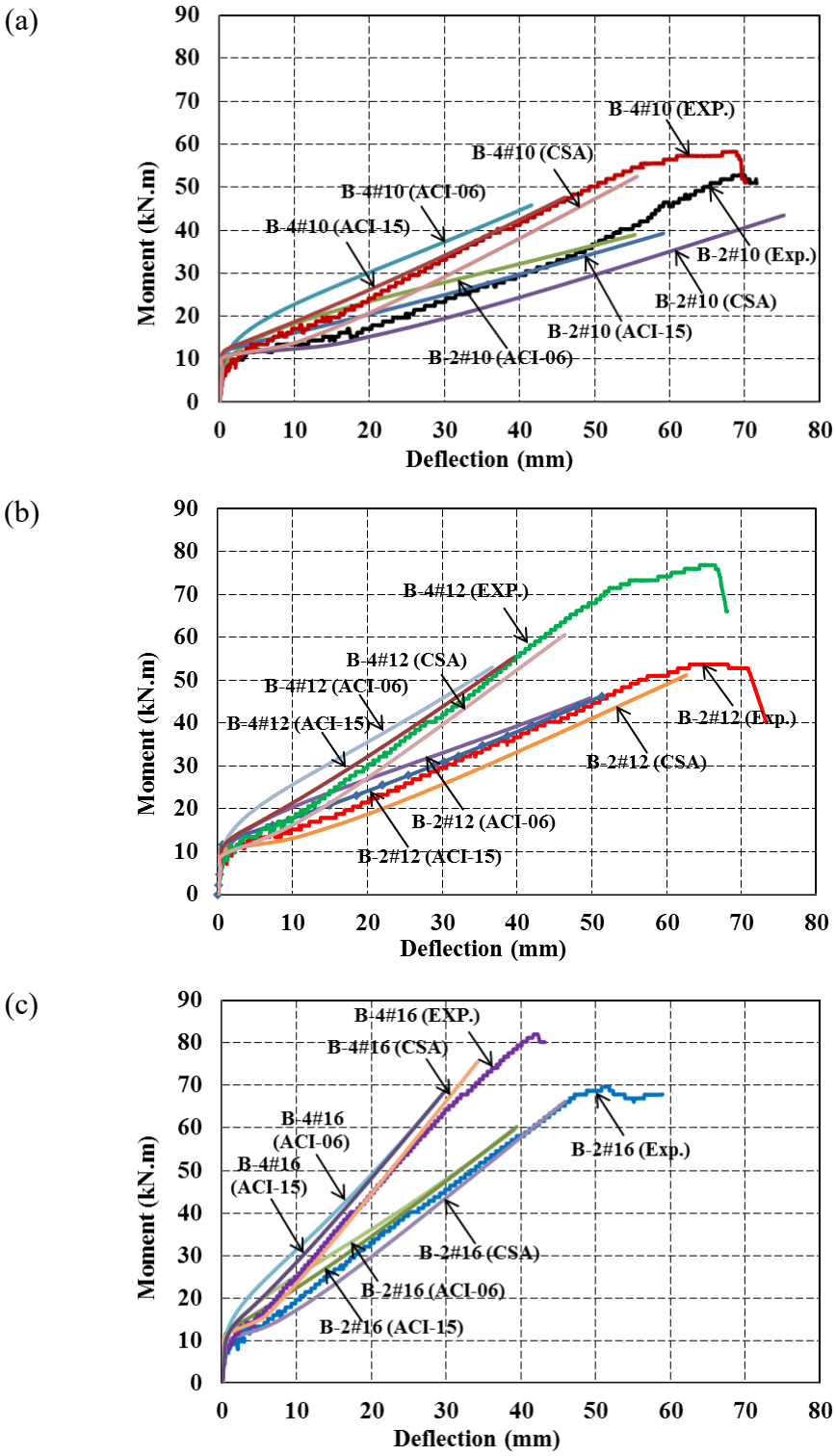

Figure 6–9: Comparison between the experimental and predicted deflection: (a) B-2#10mm and B-4#10mm; (b) B-2#12mm and B-4#12mm; (c) B-2#16mm and B-4#16mm

Table 6–7: Comparison between the experimental and predicted deflections of tested beams

Beam	δ_{exp} (mm)				$\delta_{exp}/\delta_{pred}$					
					ACI 440.1R (2006)		ACI 440.1R (2015)		CAN/CSA S806 (2012)	
	M_{cr}	$0.30M_n$	$0.67M_n$	M_n	$0.30M_n$	$0.67M_n$	$0.30M_n$	$0.67M_n$	$0.30M_n$	$0.67M_n$
B-2#10mm	1.45	16.00	48.71	69.33	2.52	1.03	1.43	0.95	0.75	0.80
B-4#10mm	0.64	10.74	36.08	68.34	2.37	1.11	1.30	1.00	0.69	0.88
B-2#12mm	0.75	11.65	39.56	67.50	2.38	1.14	1.62	1.06	0.75	0.91
B-4#12mm	1.12	14.29	37.24	57.81	1.88	1.05	1.23	1.02	0.87	0.95
B-2#16mm	0.75	11.14	31.20	51.48	1.79	1.08	1.29	1.06	0.85	0.97
B-4#16mm	1.20	9.70	25.28	42.10	1.64	1.10	1.23	1.09	0.92	1.02
Average					2.10	1.08	1.35	1.03	0.80	0.92
Standard deviation					0.37	0.04	0.15	0.05	0.09	0.08
Coefficient of variation (%)					17.74	3.68	11.23	4.99	11.03	8.21

According to ACI 440.1R (2015) and CAN/CSA S806 (2012), the deflection at service load should not exceed Span/180 = 15.0 mm (Flat roofs not supporting and not attached to non-structural elements likely to be damaged by large deflections).

6.7 Summary and Conclusion

This experimental study aimed at determining the bond-dependent coefficient (k_b) and investigating the structural performance of newly developed sand-coated BFRPs bars in normal-strength concrete beams. A total of six concrete beams reinforced with BFRP bars were constructed and tested up to failure. The tested beams measured 200 mm wide, 300 mm high, and 3100 mm long. BFRP bars sizes of 10, 12, and 16 mm with sand-coated surfaces over helical wrapping were used. The beam specimens were tested under four-point bending over a clear span of 2700 mm until failure. The experimental results were compared against the predictions using FRP design codes and guidelines. Based on the test results and discussion presented herein, the following conclusions are drawn:

1. The tested BFRP-RC beams showed cracking moments lower than the predicted values using ACI 440.1R (2015) and CAN/CSA S806 (2012) equations. ACI 440.1R (2015) and CAN/CSA S806 (2012) overestimated the cracking moment of the tested beam by 27% and 24%, respectively. Similar findings were reported for beams reinforced with GFRP bars (El-Nemr et al. 2011&2013).

2. The average bond-dependent coefficient (k_b), determined from the three first cracks in each beam, was 0.76±0.03 for the BFRP bars with sand-coated surface over helical wire wrapping. This is in agreement with the recommendation of the CHBDC (CAN/CSA S6 2014), where k_b = 0.8 for the sand-coated FRP bars.

3. The BFRP-RC beams showed typical bilinear behavior for strain and deflection until failure. The pre-cracking response and cracking loads of all the beams were nearly unaffected by the reinforcement ratio, since they are governed by the gross concrete section. After cracking, however, the increase in stiffness or reduction in reinforcement strains was proportional to the reinforcement ratio. The higher the reinforcement ratio, the higher the stiffness and the lower the strain at the same load level.

4. The BFRP-RC beams with low reinforcement ratios showed sharp increases in strains and deflection at cracking. The sudden increase in strains resulted in wider and deeper cracks, which is reflected on the stiffness and the location of the neutral axis of the cracked section. Increasing the reinforcement ratio, however, increased the amount of absorbed energy at the

first crack, which enhanced the behavior, as it controls the immediate increase in strain and initial crack width.

5. The axial stiffness of the flexural reinforcement (E_f A_f) significantly affected the general behavior of the BFRP-RC beams. The higher the axial stiffness, the better the performance (lower deflection, lower strain, and lower crack width at the same load level). Beams with the same reinforcement axial stiffness are expected to show similar behavior. More investigation, however, is needed to quantify the effect of bar surface configuration, if changed.

6. ACI 440.1R (2006) underestimated the deflection of the beams at 0.30M_n, where the average $\delta_{exp}/\delta_{pred}$ was 2.10±0.37. Similarly, at 0.67M_n, it underestimated the deflection values with an average $\delta_{exp}/\delta_{pred}$ of 1.08±0.04, while ACI 440.1R (2015) showed better predictions than ACI 440.1R (2006) at both 0.3M_n and 0.67M_n, with an average $\delta_{exp}/\delta_{pred}$ of 1.35±0.15 and 1.03±0.05, respectively. On the other hand, CAN/CSA S806 (2012) overestimated the deflection predictions at 0.30M_n and 0.67M_n, where the average $\delta_{exp}/\delta_{pred}$ was 0.80±0.09 and 0.92±0.08, respectively. Thus, CAN/CSA S806 (2012) may provide reasonable yet conservative deflection values for beams reinforced with BFRP bars.

6.8 Nomenclature

The following symbols are used in this paper:

a = shear span (mm)

a = shear span (mm)

A_f = nominal area of FRP tension reinforcement (mm^2)

b = beam effective width (mm)

c = neutral-axis depth (mm)

d = distance from the extreme compression fiber to the centroid of tension force (mm)

d_b = bar diameter (mm)

d_c = distance from extreme tension fiber to the center of the longitudinal bar (mm)

E_f = modulus of elasticity of longitudinal reinforcement (MPa)

f'_c = compressive strength of concrete (MPa)

f_f = stress in FRP reinforcement under specified loads (MPa)

f_{fu} = ultimate strength of FRP longitudinal reinforcement (MPa)

f_r = modulus of rupture (kN/m^2)
h_1 = distance from neutral axis to center of tensile reinforcement (mm)
h_2 = distance from neutral axis to extreme tension fiber (mm)
I_{cr} = transformed moment of inertia of cracked reinforced-concrete section (mm^4)
I_e = effective moment of inertia (mm^4)
I_g = gross moment of inertia of uncracked section (mm^4)
J = deformability factor
k = ratio of depth of neutral axis to reinforcement depth
k_b = bond-dependent coefficient
L = length of clear span (mm)
L_g = length of the uncracked section (mm)
M_a = applied moment (kN.m)
M_{cr} = cracking moment (kN.m)
M_n = nominal moment of the reinforced-concrete section (kN.m)
n_f = ratio of modulus of elasticity of FRP bars to modulus of elasticity of concrete
P = applied load (kN)
s = spacing between the longitudinal reinforcement bars (mm)
w_{cr} = maximum crack width (mm)
y_t = distance from centroid axis of cross section to the extreme fiber in tension (mm)
γ = parameter to account for the variation of stiffness along the length of the member
δ = mid-span deflection (mm)
ε_{cu} = ultimate concrete strain
ε_{fu} = ultimate FRP strain
ρ_f = actual longitudinal reinforcement ratio
ρ_{fb} = balanced longitudinal reinforcement ratio
τ = bond strength
ψ = curvature

CHAPTER 7
FLEXURE BEHAVIOR OF CONCRETE BEAMS REINFORCED WITH RIBBED BASALT-FRP BARS UNDER STATIC LOADS

Abstract

Recently, basalt-fiber-reinforced-polymer (BFRP) reinforcement emerged as a new FRP type, in addition to the commonly used glass, carbon, and aramid. Research is needed, however, to understand how BFRP bars behave in concrete members. This paper presents an experimental study aimed at investigating the flexural behavior and serviceability performance of concrete beams reinforced with ribbed BFRP bars. A total of eight concrete beams measuring 3100 mm in length, 200 mm in width and 300 mm in depth were constructed and tested up to failure. Six beams were reinforced with 8, 12, and 16 mm BFRP bars with ribbed surfaces and two reference beams were reinforced with 10M and 15M steel bars. The beam specimens were designed in accordance with Annex S of CAN/CSA S806 (2012) and tested under four-point bending over a clear span of 2700 mm until failure. The beam test results are presented and discussed in terms of cracking behavior, deflection, and failure modes. The test results yielded an average bond-dependent coefficient (k_b) of 0.83, which is lower than the CAN/CSA S6 (2014) recommendation of 1.0 for ribbed FRP bars. Moreover, comparing the test results to the design provisions showed that ACI 440.1R (2006) and ACI 440.1R (2015) underestimated the deflections at service load for the beams reinforced with ribbed BFRP bars, while CAN/CSA S806 (2012) yielded reasonable and conservative deflections.

***Keywords*:** Basalt, fiber-reinforced polymer (FRP), ribbed surface, beams, service load, deflection, crack width, bond-dependent coefficient, and flexure.

7.1 Introduction

Recently, extensive efforts in development of fiber-reinforced-polymer (FRP) technology have focused on using new types of fibers, such as basalt fibers, in addition to the commonly used glass, carbon and aramid fibers. Basalt-fiber-reinforced polymer (BFRP) is expected to provide benefits that are comparable or superior to other FRP types, while being significantly more cost-effective (Wei et al. 2010; Lopresto et al. 2011; Serbescu et al. 2015; Zhang et al. 2015). BFRP has proven to have advantageous characteristics compared to other fiber-reinforced polymers, such as carbon, glass, and aramid (CFRP, GFRP, and AFRP). For instance, BFRP has higher strength and modulus, and more chemical stability than E-glass FRP. It also has a wider range of working temperatures and much lower cost than CFRP (Wu et al. 2012). The current FRP design codes (ACI 440.1R 2015; CAN/CSA S6 2014; CAN/CSA S806 2012) and material specifications (ACI 440.6M 2008; CAN/CSA S807 2010), however, do not provide any recommendations for structural elements reinforced with BFRP bars.

Preliminary studies concluded the feasibility of producing BFRP reinforcing bars with enhanced physical and mechanical properties (Benmokrane et al. 2015; Elgabbas et al. 2015a). In addition, a few studies were conducted to investigate the behavior of BFRP bars in reinforced-concrete (RC) beams. Ovitigala (2012) tested eight over-reinforced concrete beams (203 × 305 × 3658 mm) reinforced with BFRP reinforcement in flexure up to failure. The beams failed by concrete crushing and it was concluded that the serviceability criteria (deflection) can be achieved by increasing the BFRP reinforcement. The ultimate failure, however, would be brittle in nature without prior warning due to lower deflection when the area of BFRP reinforcement increased.

Urbański et al. (2013) and Lapko and Urbański, (2015) investigated the flexural performance of concrete beams (80 × 120 × 1200 mm) reinforced with 8 mm BFRP bars. The results showed that the failure of BFRP-RC beams did not occur suddenly due to the beam transforming into a tie system, since the flexural reinforcement did not rupture. The deflection and crack width of the BFRP-RC beams were significantly higher than that of the steel-reinforced beam, due to the BFRP bars having a lower modulus than the steel bars. The deflection predictions according to CAN/CSA S806 (2002) showed good convergence with the experimental values in the initial loading stage.

Rizkalla (2013) tested six one-way concrete slabs (152 × 610 × 3658 mm) reinforced with BFRP bars under four-point bending. The test results indicate that the measured failure loads compared well with the nominal flexural capacities predicted using the ACI 440.1R (2006) equation and detailed layered-sectional analyses. The measured short-term deflections at service load level were higher than the values predicted by ACI 440.1R (2006). The test results indicate that ACI 440.1R (2006) equations can be safely used to predict the nominal moment capacity of concrete flexural members reinforced with BFRP bars. ACI 440.1R (2006), however, underestimated the deflection at service load level by 20% to 60%.

Tomlinson (2015) assessed the flexural and shear performances of concrete beams (150 × 300 × 3100 mm) reinforced with BFRP bars and stirrups. The test results showed that ACI 440.1R (2006) and CAN/CSA S806 (2012) provisions predicted well the capacity of beams failing in flexure. Zhang et al. (2015) investigated the deflection behavior of six concrete beams (180 × 230 × 1800 mm) reinforced with BFRP bars. The results showed that the flexural capacities equations in ACI 440.1R (2006) code were suitable for BFRP-reinforced beams, while the effective moment rigidity predicted using ACI 440.1R (2006) was higher than the experimental one. Elgabbas et al. (2015c) investigated the bond-dependent coefficient (k_b) and the structural performance of sand-coated BFRP in concrete beams. They concluded that the average k_b was 0.76±0.03 for the sand-coated BFRP bars. This is in agreement with the CAN/CSA S6 (2014) recommendation of k_b = 0.8 for sand-coated FRP bars.

Considering the limited research work conducted on BFRP bars in concrete structures and the continuous effort to develop new BFRP bars, there is a need for more structural testing to understand their structural behavior at ultimate and service limit states. With the main objective of integrating BFRP reinforcement into current FRP design codes and standards, an extensive research project is being conducted at the University of Sherbrooke, Quebec, through the activities of the NSERC Research Chair in FRP Reinforcement for Concrete Infrastructure. The project has three parts. Part I included the complete physical and mechanical characterization of different BFRP bars. It also included long-term durability characterization using accelerated aging techniques in different chemical solutions at high temperatures for certain periods of time in accordance with ACI 440.6M (2008) and CAN/CSA S807 (2010). The findings of this part (Vincent et al. 2013; Benmokrane at al. 2015; Elgabbas et al. 2015a) concluded that it was feasible

to produce BFRP bars that would meet the requirements of current FRP standards. Part II investigated the structural behavior of full-scale concrete bridge-deck slabs reinforced with BFRP bars under truck wheel loads (Elgabbas et al. 2015b). The preliminary results of the slab testing revealed structural performance meeting the requirements of the Canadian Highway Bridge Design Code (CHBDC) (CAN/CSA S6 2014). Finally, Part III focuses on the performance assessment and bond characteristics of BFRP bars in concrete beams. The preliminary testing of sand-coated BFRP bars in concrete beams indicated a bond-dependent coefficient (k_b) in agreement with CAN/CSA S6 (2014) (Elgabbas et al. 2015c).

This paper presents an experimental study aimed at investigating the flexural behavior and serviceability performance of BFRP bars in concrete beams. The study also aimed at assessing the performance of BFRP-reinforced beams with respect to the reference beams reinforced with steel bars. In addition, the test results were compared to current design provisions and recommendations.

7.2 Experimental Program

7.2.1 Material Properties

***Reinforcing bars*:** Basalt-fiber-reinforced-polymer (BFRP) bars 8, 12, and 16 mm in diameter were used as tension reinforcement in the tested beams. The BFRP bars were manufactured from continuous basalt fibers impregnated in vinyl-ester resins using the pultrusion process. The basalt fibers had a diameter of 10 to 22 microns and were given a surface treatment consisting of a silane coupling agent. BFRP bars had a fiber content of 77.4%, 79.2%, and 80.0% for the 8, 12, and 16 mm diameters, respectively. The BFRP bars were fabricated with open-die pultrusion to allow for placement of helical fibers on the bar surface, as shown in **Figure 7–1**, to increase the bond between the bars and surrounding concrete. The tensile properties of the BFRP bars were determined by testing five representative specimens of each diameter according to ASTM D7205 (2011), while the bond strength was determined in accordance with ASTM D7913 (2014). It should be mentioned that the mechanical properties were calculated using nominal cross-sectional areas of 50, 113, and 201 mm^2 for the 8, 12 and 16 mm diameters, respectively. The immersed (measured) cross-sectional areas (ASTM D7205), however, were 69, 156, and 275 mm^2 for the 8, 12 and 16 mm diameters, respectively. On the other hand, the reference beams were reinforced in

tension with 10M and 15M steel bars (**Figure 7–1**). **Table 7–1** summarizes the tensile properties of the BFRP and steel bars and the bond strength of the BFRP bars.

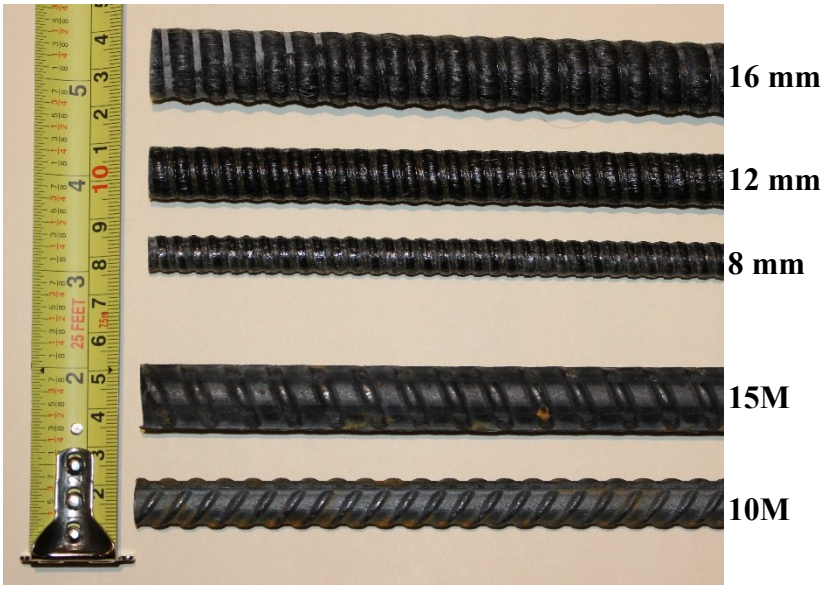

Figure 7–1: Basalt FRP versus steel bars

Table 7–1: Tensile properties and bond strength the reinforcing bars

RFT Type	d_b (mm)	A_f [a] (mm²)	A_{im} [d] (mm²)	E_f (GPa)	f_{fu} (MPa)	ε_{fu} (%)	τ_{max} (MPa)	Surface Configuration
Basalt	8	50	69	64.6±1.4	1655±95	2.56±0.17	25.4±2.3	Ribbed
	12	113	156	69.3±0.5	1760±39	2.54±0.10	17.7±1.3	
	16	201	275	64.8±3.3	1724±64	2.67±0.17	16.8±1.4	
Steel [b]	10M	100	---	200.0	f_y [c] = 450	ε_y [c] = 0.2	---	Ribbed
	15M	200						

[a] Nominal cross-sectional area.

[b] Tensile properties of steel bars were provided by the manufacturer.

[c] f_y and ε_y are the yield strength and strain of the steel bars, respectively.

[d] Immersed cross-sectional area (measured).

Note: properties calculated based on the nominal cross-sectional area.

Concrete: The beams were made with ready-mixed, normal-strength concrete with a 28-day target compressive strength of 40 MPa. A cubic meter of concrete contained 350 kg of cement, 813 kg of natural sand, 1032 kg of aggregate (20 mm maximum nominal size), 155 L of water (water–cement

ratio, *w/c*, of 44%) and an air-entrained ratio of 5% to 8%. The concrete mix had slump of 80±30 mm. The eight beams were cast from three concrete batches. The curing process started two hours after the concrete was cast by covering the concrete surface with wet burlap and polythene sheeting for 10 days. The concrete compressive strength of each batch was determined by testing three 150 × 300 mm cylinders on the day of beam testing. The tensile strength was also determined from split-cylinder testing on 150 × 300 mm cylinders. **Table 7–2** shows the compressive and tensile strengths of the different concrete batches.

7.2.2 Test Specimens

This study included six concrete beams reinforced with ribbed BFRP bars and two concrete beams reinforced with steel bars designed according to the geometry recommendations in Annex S of CAN/CSA S806 (2012). The beams measured 3100 mm long × 200 mm wide × 300 mm deep. As shown in **Table 7–2**, the beams had two 10M steel bars as top reinforcement, while the bottom reinforcement was either BFRP or steel bars. Shear reinforcement consisting of 10M steel stirrups spaced at 100 mm were used in both shear spans to avoid shear failure. To minimize the confining effect of the shear reinforcement on the flexural behavior, no stirrups were used in the constant moment zone. The clear concrete cover was 38 mm, which was set in accordance with Annex S of CAN/CSA S806 (2012). **Figure 7–2** shows the dimensions and reinforcement details of the tested beams. The BFRP-RC beams were designed to fail by concrete crushing in the constant moment zone. This was achieved by using a reinforcement ratio (ρ_f) greater than the balanced reinforcement ratio (ρ_{fb}), as shown in **Table 7–2**, where the balanced reinforced reinforcement ratio (ρ_{fb}) was calculated considering the actual concrete strength. The ratio between the actual and balanced reinforcement ratios for the BFRP-RC beams ranged from 1.543 to 6.865 according to ACI 440.1R (2015) and from 1.183 to 5.138 according to CAN/CSA S806 (2012). The differences between actual and balanced reinforcement ratios in ACI 440.1R (2015) and CAN/CSA S806 (2012) for the same beams were due to the differences in the stress-block parameters and the compressive strain of the concrete at ultimate. In contrast, the steel-RC beams were designed to fail due to steel yielding (under-reinforcement), which is common for steel-RC members.

Table 7–2: Concrete properties and reinforcement details

Beam ID[a]	f_c [b] (MPa)	f_t [c] (MPa)	ρ_f	ρ_f/ρ_{fb} [d]		$(E_f \times A_f)$ (kN)
				ACI 440.1R (2015)	CAN/CSA S806 (2012)	
B-3#8mm	52.7	4.7	0.0030	1.543	1.183	9745
B-5#8mm			0.0052	2.719	2.084	16242
B-2#12mm	44.7	4.3	0.0044	2.669	2.138	15682
B-3#12mm			0.0066	4.003	3.207	23552
B-2#16mm	50.8	4.2	0.0078	4.577	3.545	26068
B-3#16mm			0.0119	6.865	5.138	39102
B-2#10M	44.7	4.3	0.0039	0.103	0.096	40000
B-2#15M			0.0079	0.207	0.194	80000

[a] The first letter "B" indicates concrete beam; the second number "2, 3 or 5" indicates the number of reinforcing bars; the last number (#8, #12, #16, 10M or 15M) indicates the bar size (in mm).

[b] f'_c: concrete compressive strength.

[c] f_t: concrete tensile strength.

[d] ρ_{fb}: balanced reinforcement was calculated based on the actual concrete compressive strength.

7.2.3 Instrumentation

Figure 7–2 provides the instrumentation details. The deflection along the beam's span was monitored using four linear variable differential transducers (LVDTs) accurate to 0.001 mm, labeled D1 to D4 (D2 and D3 at mid-span, and D1 and D4 at quarter-span). Crack propagation was also monitored during testing until failure, and the crack widths of the first three flexural cracks were monitored with three horizontal LVDTs (D5 to D7). The strains of the longitudinal BFRP reinforcing bars were captured with four electrical-resistance strain gauges 6 mm in length (S1 to S4). The compressive concrete strains at the mid-span section were measured with two electrical-resistance strain gauges 60 mm in length (C1 and C2). To facilitate crack monitoring, the beams were painted white prior to testing. In addition, an automatic data-acquisition system connected to a computer was used to monitor loading, deflections, and strains in the concrete and reinforcement. The formation of beam cracks and the corresponding loads were marked and recorded during testing until failure.

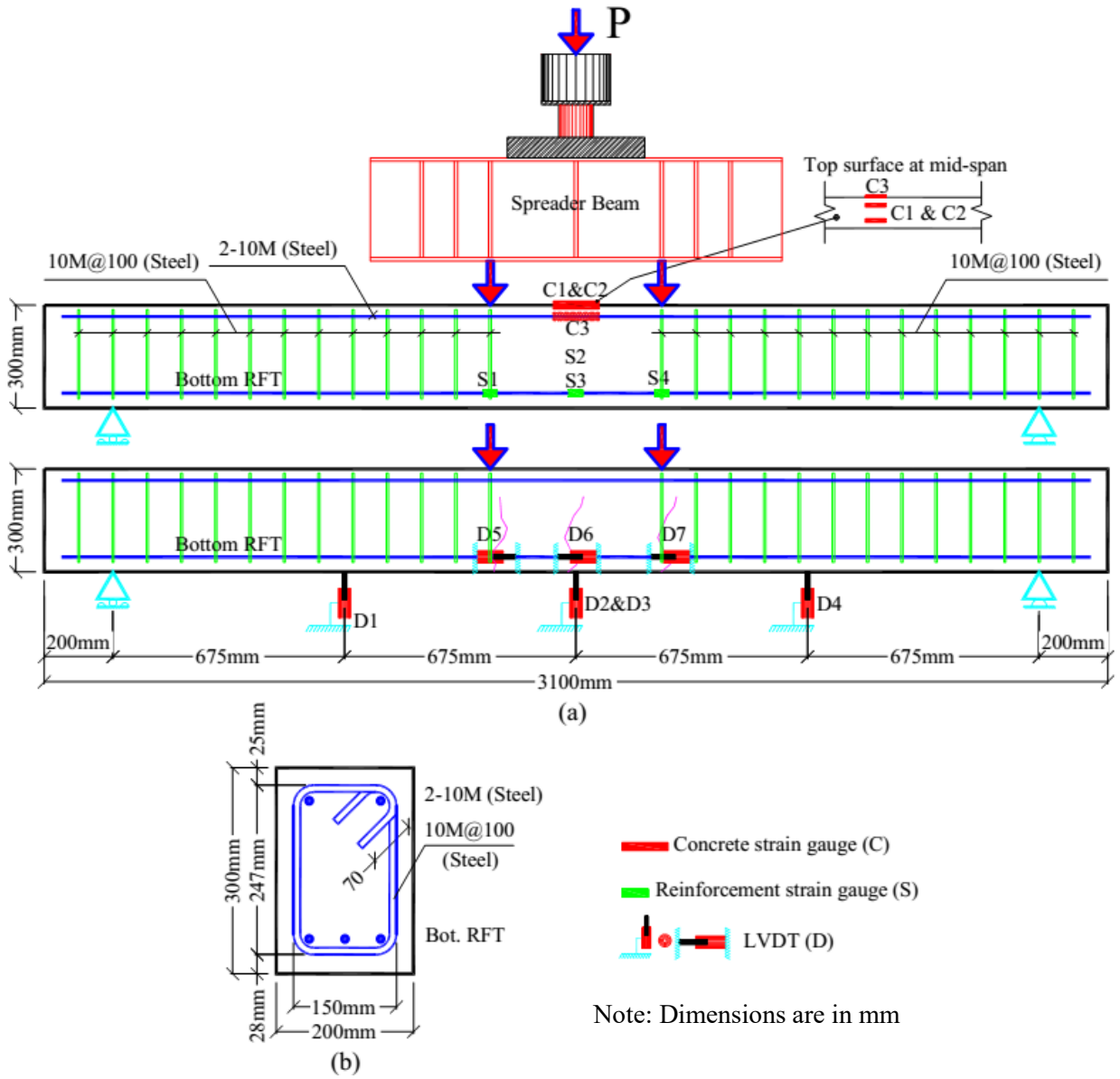

Figure 7–2: Schematic drawing for concrete dimensions, reinforcement details, typical location of instrumentation and test setup: (a) Elevation; (b) Cross- sections

7.2.4 Test Setup and Procedure

The simply supported beams were monotonically loaded under four-point bending until failure. **Figure 7–2** shows the dimensions and locations of the applied loads, while **Figure 7–3** provides a photo of the test setup. The load was applied at a stroke-controlled rate of 1.2 mm/min. During testing, the beams were observed visually until the first crack appeared, and the corresponding load was recorded. The test was paused when each of the first three cracks appeared. The initial crack width of the first three cracks was measured manually with a 50X handheld electronic microscope;

LVDTs were installed at crack locations to measure crack width electronically with increasing load. The load continuously increased until beam failure.

The cracking load was also verified based on the change in stiffness of the load–deflection and load–strain relationships. The concrete and reinforcement strain gauges and deflection and cracking LVDTs were connected to an automatic data-acquisition system connected to a computer to record their readings.

Figure 7–3: Overview of the test setup

7.3 Test Results and Discussion

7.3.1 Cracking Load and Pattern

The crack propagation in all the tested beams followed the flexural cracking patterns traditionally observed in simply supported beams, as shown in **Figure 7–4**. Crack formation was initiated in the constant flexural moment zone between the two concentrated loads. The cracks were vertical, perpendicular to the direction of the maximum principle tensile stress induced by pure bending. As the load increased, additional flexural cracks appeared and the crack spacing decreased. The beams with higher reinforcement ratios, however, evidenced more tensile cracks of smaller width extending away from the constant moment region towards the supports. The cracking moment of all the tested beams ranged from 6.94 to 8.51 kN.m with an average value of 7.69±0.56 kN.m (beam self-weight excluded). The cracking moments were also calculated with Eq. (7-1). **Table 7–3** provides the cracking moments (M_{cr}) of all the tested beams as well as a comparison between the experimental and predicted values of the cracking moments. It is worth mentioning that the reinforcement type and the modulus of elasticity had no significant effect on the cracking moment and that the controlling variable for predicting cracking moment was the modulus of rupture of concrete (f_r), which varies from one code to the next.

$$M_{cr} = \frac{f_r \times I_g}{y_t} \tag{7-1}$$

where the modulus of rupture of concrete (f_r) is calculated from Eq. (7-2a) according to ACI 440.1R (2015) and Eq. (2b) according to CAN/CSA S806 (2012) for normal-density concrete.

$$f_r = 0.62\sqrt{f_c'} \tag{7-2a}$$

$$f_r = 0.60\sqrt{f_c'} \tag{7-2b}$$

As shown in **Table 7–3**, the average cracking moments of the BFRP- and steel-RC concrete beams were generally lower than those predicted with ACI 440.1R (2015) and CAN/CSA S806 (2012) (by 40% and 38%, respectively). CAN/CSA S806 (2012) yielded slightly better predictions of cracking moments than ACI 440.1R (2015) because of the former's smaller modulus of rupture.

Bischoff (2001) stated that additional stresses developed from shrinkage, temperature effect, and the freezing and melting of water inside the concrete may cause hair cracks and therefore reduce the cracking load. Shrinkage cracks had no significant effect on predicting the crack widths.

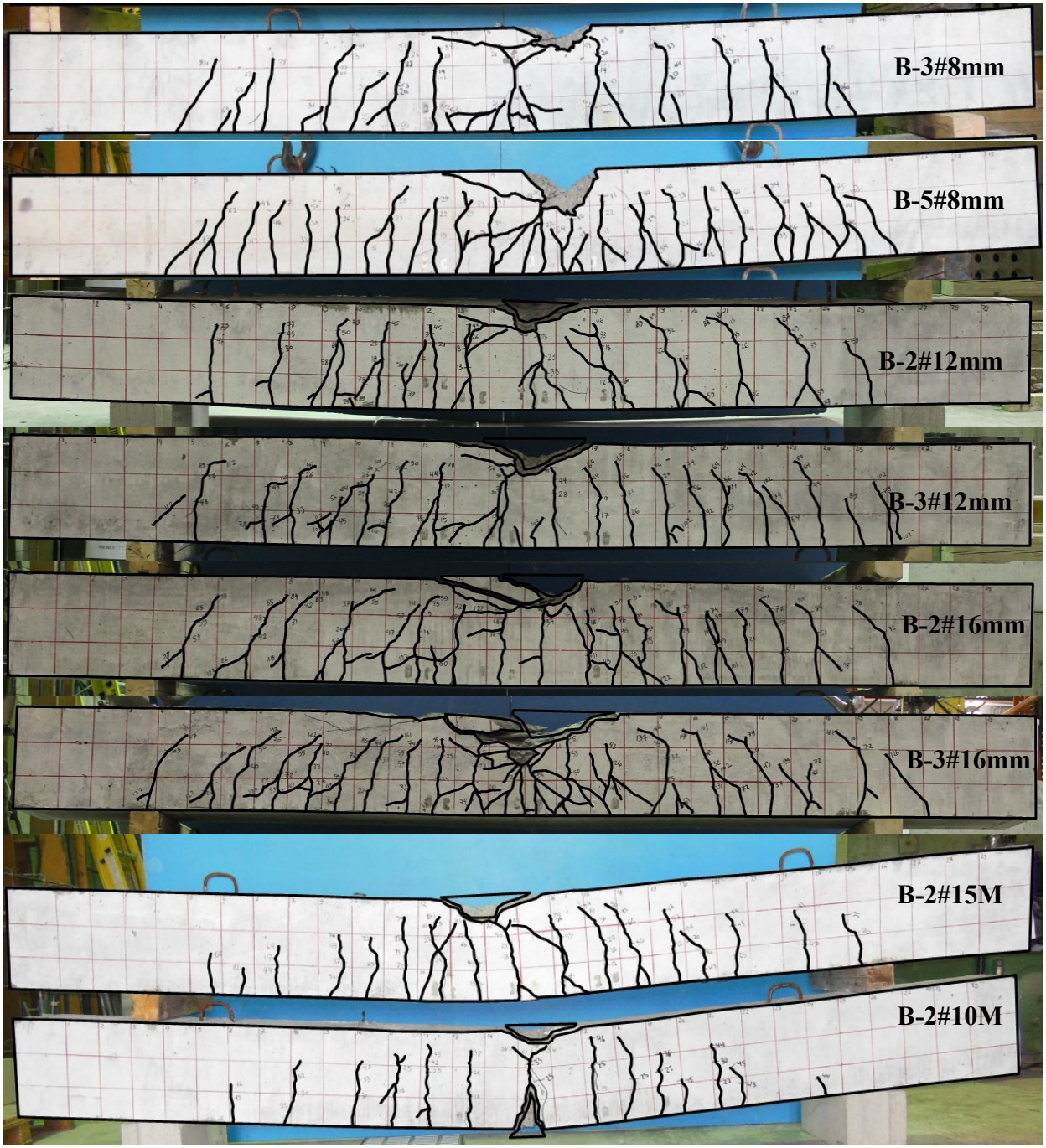

Figure 7–4: Crack pattern and failure modes of tested beams

Table 7–3: Cracking and ultimate moments and mode of failure

Beam ID	Experimental (kN.m)			ACI 440.1R (2015)		CAN/CSA S806 (2012)	
	M_{cr}	M_n	MOF [a]	$\frac{M_{cr,Exp.}}{M_{cr,Pre.}}$	$\frac{M_{n,Exp.}}{M_{n,Pre.}}$	$\frac{M_{cr,Exp.}}{M_{cr,Pre.}}$	$\frac{M_{n,Exp.}}{M_{n,Pre.}}$
B-3#8mm	8.51	51.59	CC	0.63	1.05	0.65	0.93
B-5#8mm	7.03	64.19	CC	0.52	1.14	0.54	1.01
B-2#12mm	6.94	53.14	CC	0.56	0.94	0.58	0.85
B-3#12mm	7.86	65.76	CC	0.63	0.98	0.65	0.89
B-2#16mm	7.62	69.83	CC	0.57	0.97	0.59	0.86
B-3#16mm	7.67	89.77	CC	0.58	1.06	0.60	0.95
B-2#10M	8.38	23.57 [b]	SY+CC	0.68	---	0.70	---
B-2#15M	7.55	40.19 [b]	SY+CC	0.60	---	0.62	---
Average				0.60	1.02[c]	0.62	0.91[c]
Standard deviation				0.05	0.08[c]	0.05	0.06[c]

[a] CC: crushing of concrete; R: rupture of FRP bars; SY+CC: yielding of steel followed by concrete crushing.

[b] Yielding moment.

[c] Beams reinforced with steel bars were excluded from the statistical analysis at M_n.

7.3.2 Bond-Dependent Coefficient (k_b) Prediction

Extensive analysis of the bond-dependent coefficient (k_b) was conducted by an ACI committee on a variety of concrete sections and FRP bars considering the fiber type, resin formulations, and surface treatments with the average k_b values ranging from 0.60 to 1.72, with an average of 1.10 (ACI 440.1R 2015). In the absence of experimental test data for k_b, ACI 440.1R (2015) suggests a conservative value of 1.4 should be used. On the other hand, in the absence of significant test data, CAN/CSA S6 (2014) recommends a k_b of 1.0 for ribbed FRP bars.

The test results were used to assess the bond-dependent coefficient values (k_b). The k_b was calculated in accordance with Annex S of CAN/CSA S806 (2012) with Eq. (7-3). The calculations were based on the first three cracks in each beam. The k_b was calculated for each beam at 30% of the nominal capacity, $0.3M_n$, (assumed service load) of the tested specimens. This value was reported as the service-load level by many researchers (Mota at al. 2006; Bischoff 2009; El-Nemr

et al. 2013). The k_b values were also determined at 0.67M_n, where no more cracks were appeared after this load level and only widening of the existing cracks could be observed, and at a crack width of 0.70 mm (upper crack-width limit provided by CAN/CSA S806 2012). **Table 7–4** presents the average k_b measured for each beam. The results did show differences between k_b determined at the different load levels. The average k_b value was 0.83 for BFRP bars with ribbed surfaces. This value is lower than the 1.0 for ribbed FRP bars provided in the CHBDC (CAN/CSA S6 2014).

$$w_{cr} = 2\frac{f_f}{E_f}\frac{h_2}{h_1}k_b\sqrt{d_c{}^2 + (s/2)^2} \tag{7-3}$$

Table 7–4: Bond-dependent coefficient, k_b

Beam ID	k_b [a]		
	0.3 M_n	0.67 M_n	0.7 mm
B-3#8mm	0.77	0.89	0.80
B-5#8mm	0.83	0.71	0.82
B-2#12mm	0.67	0.73	0.71
B-3#12mm	1.04	1.09	1.03
B-2#16mm	0.73	0.59	0.69
B-3#16mm	0.96	0.92	0.91
Average	0.83	0.83	0.83
Standard deviation	0.14	0.18	0.13

[a] Each of the reported value represents the average of 3 values (3 cracks).

7.3.3 Ultimate Capacity and Failure Mode

All the BFRP-RC beams were designed to fail by concrete crushing when the concrete reached its maximum compressive strain (ε_{cu}) of 0.30% or 0.35% according to ACI 440.1R (2015) and CAN/CSA S806 (2012), respectively, before the tensile stress in BFRP bars (f_f) achieved ultimate capacity (f_{fu}) (over-reinforced section). This is the common design concept for concrete sections reinforced with FRP bars. In contrast, the steel-RC beams were designed to fail due to steel yielding (under-reinforced section). The balanced reinforcement ratios were calculated with Eq. (7-4). The

terms (α_1) and (β_1) were calculated with Eq. (7-5) for ACI 440.1R (2015) and Eq. (7-6) for CAN/CSA S806 (2012).

$$\rho_{fb} = \alpha_1 \beta_1 \frac{f_c^{'}}{f_{fu}} \frac{\varepsilon_{cu}}{\varepsilon_{cu} + \varepsilon_{fu}} \tag{7-4}$$

$$\alpha_1 = 0.85 \tag{7-5a}$$

$$\beta_1 = 0.85 - 0.05\left(f_c^{'} - 27.6\right) / 6.9 \tag{7-5b}$$

$$\alpha_1 = 0.85 - 0.0015 f_c^{'} \geq 0.67 \tag{7-6a}$$

$$\beta_1 = 0.97 - 0.0025 f_c^{'} \geq 0.67 \tag{7-6b}$$

Table 7–3 presents the flexural capacity (M_n) for all the tested beams. The BFRP-RC beams failed by concrete crushing. They evidenced several cracks distributed around the mid-span, as a result of the beam transforming into a tie system, since the flexural BFRP bars did not rupture. On the other hand, the beams reinforced with steel bars (B-2#10M and B-2#15M) failed due to yielding of the steel bars, followed by concrete crushing at the top. This occurred because they were designed under-reinforced, which is commonly the case with steel-RC members. It is worth mentioning that none of the tested beams showed any slippage of the tension reinforcement.

Moreover, **Table 7–3** indicates that increasing the actual reinforcement ratio-to-balanced ratio (ρ_f/ρ_{fb}) lead to an increase in the ultimate load-carrying capacity. For B-3#8mm and B-5#8mm, increasing the reinforcement ratio from 0.29% to 0.52% increased the ultimate capacity from 51.59 kN.m to 64.19 kN.m, respectively (24.4% increase). Similarly, increasing the reinforcement ratio from 0.44% to 0.66% in B-2#12mm and B-3#12mm and from 0.79% to 1.19% in B-2#16mm and B-3#16mm increased the ultimate capacity by 21.8% and 28.5%, respectively. Thus, increasing the reinforcement ratio by about 50% increased the ultimate capacity by about 28.5%. Kassem et al. (2011) reported that a maximum increase in ultimate capacity of 4% and 16% was observed as a result of increasing the GFRP reinforcement ratio by 50% and 100%, respectively. Moreover, El-Nemr et al. (2013) concluded that increasing ρ_f by 3 to 4 times resulted in an average increase of 83.5% in the load-carrying capacity of GFRP-RC beams. The higher tensile properties for BFRP bars compared with GFRP bars resulted in an increase in the reinforcement axial stiffness ($E_f A_f$),

and accordingly, a significant reduction in reinforcing-bar and concrete strains at the same load level, which delayed the concrete crushing until higher loads were achieved.

The comparison of close axial stiffness ($E_f A_f$) of B-5#8mm and B-2#12mm revealed that the former's capacity was 21% higher than the latter's, despite the lower effective depth. This is attributed to B-5#8mm's higher concrete strength (52.7 MPa) compared to B-2#12mm (44.7 MPa). The BFRP bar diameter and arrangement may have contributed to the ultimate capacity; further investigation is required to quantify this effect.

The ultimate capacity of the test specimens was predicted using the strain compatibility approach in ACI 440.1R (2015) and CAN/CSA S806 (2012) (Eqns. (7-7) and (7-8)) and compared to the measured values. **Table 7–3** shows the experimental-to-predicted ultimate capacity of the tested beams. The ACI 440.1R (2015) approach yielded an average experimental-to-predicted ultimate capacity of 1.02±0.08, while the CAN/CSA S806 (2012) approach gave a conservative experimental-to-predicted ultimate capacity with an average of 0.91±0.06. The difference between ACI 440.1R (2015) and CAN/CSA S806 (2012) was related to the β_1 factor and the assumed strain at ultimate, which is 0.003 for ACI 440.1R (2015) and 0.0035 for CAN/CSA S806 (2012).

$$f_f = \left(\sqrt{\frac{\left(E_f \varepsilon_{cu}\right)^2}{4} + \frac{0.85\beta_1 f_c^{'}}{\rho_f} E_f \varepsilon_{cu}} - 0.5 E_f \varepsilon_{cu} \right) \le f_{fu} \tag{7-7}$$

$$M_n = \rho_f f_f \left(1 - \frac{\rho_f f_f}{2\alpha_1 f_c^{'}}\right) b d^2 \tag{7-8}$$

On the other hand, B-2#10M and B2-2#15M failed at 23.57 kN.m and 40.19 kN.m, respectively, which is lower than the capacities of B-3#8mm and B-2#16mm with similar reinforcement ratios. The ultimate capacity of the BFRP-RC beams was 1.74–2.19 times greater than that of the steel-RC beams with similar reinforcement ratios. This was attributed to the higher tensile strength and strain capacity of the BFRP bars compared to the yield stress and strain of the steel bars.

7.3.4 Reinforcement and Concrete Strains

Figure 7–5 shows the average mid-span tensile strains in the reinforcing bars at positions (S2) and (S3), as well as the average compressive strains in the concrete at positions (C1) and (C2) versus

the applied moment until failure. The BFRP- and steel-RC beams showed similar pre-cracking responses and significant strain increases after cracking until failure due to the reduced post-cracking stiffness. The tested BFRP-RC beams exhibited typical bilinear moment–average strain relationships (concrete and reinforcement), while the steel-RC beams showed similar responses followed by a yield plateau. Once the steel-RC beams reached the yielding load (corresponding strain of about 2500 μs; see **Figure 7–5**) the yield plateau initiated and the concrete strains increased rapidly, which led to concrete crushing after steel yielding. **Figure 7–5** also shows that, at the same load level, increasing the reinforcement ratio (ρ_f) decreased both the tensile strains in the reinforcing bars and the compressive strains in the concrete. In addition, BFRP-RC beams with close axial stiffness ($E_f\ A_f$) yielded approximately the same moment–strain relationship, as evidenced in B-5#8mm and B-2#12mm, and B-3#12mm and B-2#16mm.

Moreover, **Figure 7–5** shows that B-3#8mm, which had the lowest reinforcement ratio of 0.29%, experienced very high and sharp tensile strain increases when the first crack appeared. The sharp increase at the first crack was more than 4000 μs. In contrast, B-2#16mm and B-3#16mm, which had the highest reinforcement ratios of 0.79% and 1.19%, respectively, showed much smaller jump in strain in the BFRP bars and concrete after cracking. This phenomenon is due to the low amount of absorbed energy by the BFRP bars compared to the steel bars, which caused a sudden reduction in stiffness after cracking. This was improved by increasing the reinforcement ratio. These results are in agreement with those reported for different types of FRP bars in concrete beams (Kassem et al. 2011; El-Nemr et al. 2013; Elgabbas et al. 2015c). An after-cracking comparison of B-2#10M and B-3#16mm, which had similar $E_f\ A_f$ values, showed approximately the same rate of strain increases, but without the sudden strain increase in the steel-RC beam after the first crack, due to the high energy absorption of the steel bars.

Despite the difference in concrete strengths for B-5#8mm and B-2#12mm, they exhibited the same moment–strain relationship until about 50% of B-2#12mm's failure moment. This was due to providing approximately the same axial stiffness ($E_f\ A_f$) for both beams. After that, B-5#8mm showed lower strains than B-2#12mm until failure. Using more BFRP bars of smaller diameter may be better than using fewer BFRP bars of larger diameter, as this enhanced the cracking and bond performance. This can be confirmed again with **Figure 7–5**, since B-5#8mm showed the same moment–strain relationship as B-2#12mm until failure, regardless of the low $E_f\ A_f$ compared to

that of B-2#12mm (9745 compared to 15682 kN, respectively). It is worth mentioning that the bond strength of the 8 mm BFRP bars was 25.4 MPa, compared to 17.7 MPa and 16.8 MPa for the 12 mm and 16 mm BFRP bars, respectively. In addition, providing approximately the same $E_f A_f$ for B-3#16mm and S-2#10M yielded the same moment–strain relationship up to yielding of the steel bars.

Table 7–5 shows the tensile and compressive strains of the reinforcement bars and concrete, respectively, at service load, which represents approximately 30% of the nominal capacity ($0.3M_n$), since this value has been reported as the service-load level by many researchers (Mota et al. 2006, Bischoff et al. 2009, and El-Nemr et al. 2013). ISIS (2007) recommended a value of 2000 με as a limit for the strain in FRP bars under service load. As shown in **Table 7–5**, the strains in the BFRP bars at $0.30M_n$ were high and ranged from 3907 to 6036 με. El-Nemr et al. (2013) reported high strain values up to 5349 με and Kassem et al. (2011) also reported strain values as high as 4119 με in GFRP bars at $0.3M_n$. This is also high and could not be considered as strains at service load. Therefore, in this study, the key results were presented at a load level corresponding to 2000 με in the BFRP bars, at $0.3M_n$, and $0.67M_n$, since some strain gauges on the FRP bars malfunctioned after this load. It is worth mentioning that the crack patterns often stabilized at $0.67M_n$ until failure.

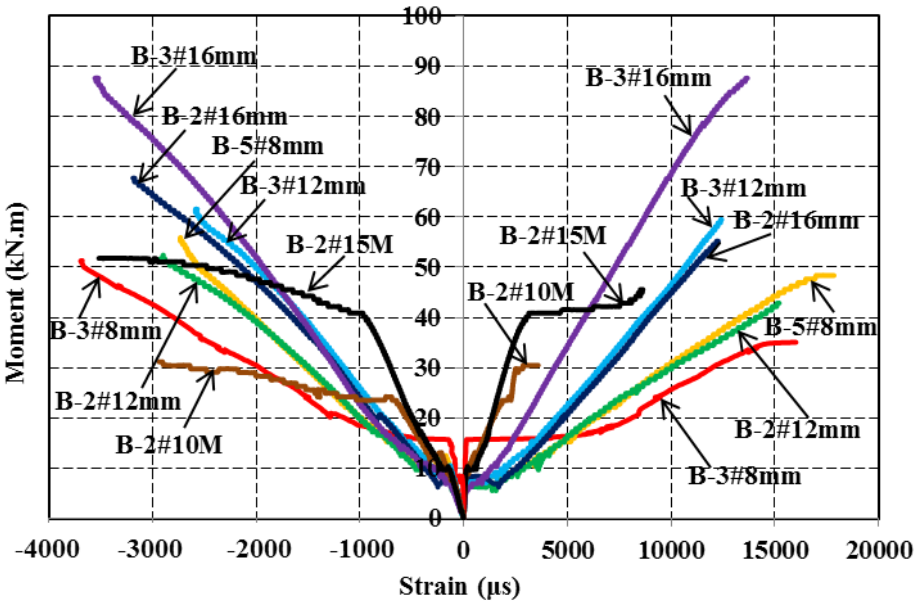

Figure 7–5: Moment-reinforcement and concrete-strain relationships

7.3.5 Crack Width

Figure 7–6 shows the moment-versus-average crack width for the tested beams. Increasing the reinforcement ratio reduced the crack widths, as shown in **Figure 7–4**. The steel-RC beams showed the smallest crack widths as they had very high reinforcement axial stiffness ($E_f\ A_f$) compared to the BFRP-RC beams. Moreover, at the yield load of steel-RC beams, the average cracks widths in BFRP-RC beams were about 2.4 times higher than steel-RC beams for the same reinforcement ratio (B-3#8mm against S-2#10M and B-2#16mm against S-2#15M). These results were expected due to the higher modulus of elasticity of steel bars compared to BFRP bars.

Figure 7–6 shows that B-5#8mm had the same moment–crack-width relationship as B-2#12mm, since they had the same reinforcement axial stiffness ($E_f A_f$). Similarly, B-3#12mm and B-2#16mm had very close $E_f A_f$ values. Thus, it may be concluded that reinforced-concrete beams with the same $E_f\ A_f$ may exhibit the same moment–crack-width relationships until failure.

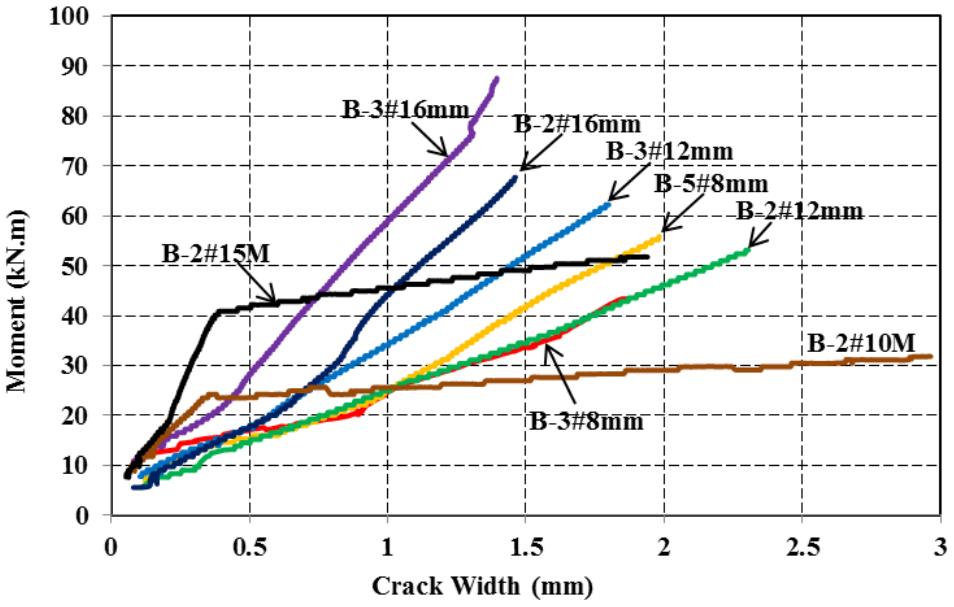

Figure 7–6: Applied moment–average crack width of all tested beams

Table 7–5: Strains, neutral axis-to-depth ratio, and curvature of BFRP-RC beams

Beam ID	Reinforcement Strain (με)			Concrete Strain (με)			$(c/d)_{exper.}$			$(c/d)_{pred.}$	Curvature, Ψ ($\times 1/d$)			Deform. factor (J) at 0.67 M_n
	ε_c=1000 με	0.30 M_n	0.67 M_n	ε_f= 2000 με	0.30 M_n	0.67 M_n	ε_f= 2000 με	0.30 M_n	0.67 M_n	Theo. at M_n	ε_f= 2000 με	0.30 M_n	0.67 M_n	
B-3#8mm	7223	5274	14376	732	764	2405	0.27	0.13	0.14	0.13	0.0027	0.0060	0.0168	6.21
B-5#8mm	6248	6036	14620	567	947	2181	0.22	0.14	0.13	0.17	0.0026	0.0070	0.0168	5.37
B-2#12mm	6070	4999	12383	711	759	1795	0.26	0.13	0.13	0.17	0.0027	0.0058	0.0142	5.50
B-3#12mm	5661	4414	9506	665	756	1723	0.25	0.15	0.15	0.21	0.0027	0.0052	0.0112	4.85
B-2#16mm	5634	5019	10355	583	895	1970	0.23	0.15	0.16	0.21	0.0026	0.0059	0.0123	4.65
B-3#16mm	3373	3907	8768	527	1130	2324	0.21	0.22	0.21	0.25	0.0025	0.0050	0.0111	4.91

7.3.6 Natural Axis-to-Depth Ratio (c/d) and Curvature

The measured strains were used to calculate the natural axis-to-depth ratio (c/d); the values are reported in **Table 7–5.** There were no significant changes in the c/d ratios at $0.30M_n$ or $0.67M_n$. The neutral axis depth increased as the reinforcement ratio increased, since the equilibrium of forces requires a larger compression block for a greater force. The theoretical neutral-axis depth-to-concrete depth (c/d) was calculated based on the strain-compatibility theory using a cracked-section analysis. Moreover, **Table 7–5** provides the calculated curvature as a function of $1/d$ at $0.30M_n$, $0.67M_n$ as well as at a load level corresponding to 2000 μs in the BFRP bars. The calculated values at $0.67M_n$ ranged from $0.0111/d$ to $0.0168/d$ for compression-controlled failure, which is higher than the range of $0.008/d$ to $0.015/d$ given by El-Nemr et al. (2013), the range of $0.0089/d$ to $0.012/d$ given by Gulbrandsen (2005), and the range of $0.009/d$ to $0.014/d$ given by Kassem et al. (2011) for GFRP bars.

7.3.7 Deflection Responses

Figure 7–7 shows the applied moment versus the average mid-span deflection responses at positions D2 and D3 for the tested beams. The figure provides typical bilinear moment–deflection relationships for the tested BFRP-RC beams and trilinear with a yielding plateau for the tested steel-RC beams. The beams showed nearly similar pre-cracking stiffness and cracking loads due to the negligible effect of the reinforcement ratio and modulus on the gross moment of inertia of the beams. Unlike in the pre-cracking stage, all the BFRP-RC beams exhibited lower post-cracking stiffness until failure. This is due to the wider crack openings in the BFRP-RC beams compared to the steel beams, which is attributed to the low modulus of elasticity of the BFRP bars. Clearly, the reinforcement ratio significantly influenced the beams' post-cracking responses until failure. As expected, larger deformations were observed for lower reinforcement ratios.

Table 7–6 summarizes the measured deflections at 30% and 67% of the nominal capacity ($0.3M_n$ and $0.67M_n$), respectively, as well as at 40 kN.m (the highest moment beams' achieved before failure). As expected, at the same moment (40 kN.m), lower deformations were noted with increasing reinforcement ratio. Increasing the reinforcement ratio by 50% (B-3#12 mm compared to B-2#12 mm and B-3#16mm compared to B-2#16mm) reduced the deflection by 30.82% and 25.40%, respectively.

Despite their differences in concrete strengths, B-5#8mm and B-2#12mm exhibited the same moment–deflection relationship until the failure moment of B-2#12mm. This was due to providing approximately the same axial stiffness ($E_f A_f$) in both beams. Thus, it can be generally stated that the deflection of BFRP-RC beams is proportional to $E_f A_f$ and that using similar reinforcement ratios of BFRP and steel will result in more deflection in BFRP-RC beams due to the lower modulus of elasticity. Assuming that the beam deflection limit at service load is span/240 (L/240), as provided by CAN/CSA S806 (2012)—which yields 11.25 mm—all the beams except B-3#8mm and B-5#8mm exhibited deflections of less than 11.25 mm at service load ($0.30M_n$).

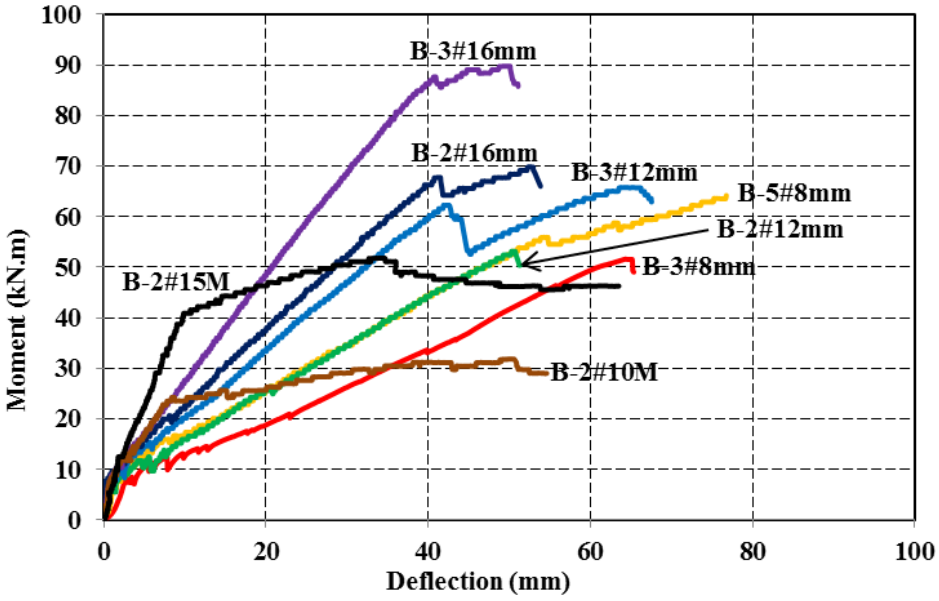

Figure 7–7: Applied moment–mid-span deflection relationships

Table 7–6: Experimental-to-predicted deflection ($\delta_{exp}/\delta_{pred}$) of the BFRP-RC beams

Beam ID	δ_{exp} (mm)				$\delta_{exp}/\delta_{pred}$					
					ACI 440.1R (2006)		ACI 440.1R (2015)		CAN/CSA S806 (2012)	
	40 kN.m	$0.30M_n$	$0.67M_n$	M_n	$0.30M_n$	$0.67M_n$	$0.30M_n$	$0.67M_n$	$0.30M_n$	$0.67M_n$
B-3#8mm	48.07	14.29	41.69	64.47	4.08	1.36	3.64	1.21	1.10	0.99
B-5#8mm	35.50	12.82	38.88	76.76	3.05	1.30	1.73	1.19	0.90	1.03
B-2#12mm	35.24	10.35	31.08	50.72	3.47	1.38	2.29	1.26	1.01	1.07
B-3#12mm	24.38	9.62	27.78	64.27	2.48	1.28	1.55	1.22	0.96	1.10
B-2#16mm	21.26	9.08	26.19	52.94	2.62	1.26	1.50	1.18	0.92	1.06
B-3#16mm	15.86	9.91	25.63	50.06	1.75	1.22	1.38	1.22	1.04	1.14
Average					2.91	1.30	2.02	1.21	0.99	1.07
Standard deviation					0.81	0.06	0.86	0.03	0.08	0.05
Coefficient of variation (%)					27.95	4.70	42.53	2.36	7.71	5.10

According to ACI 440.1R (2015) and CAN/CSA S806 (2012), the deflection at service load should not exceed Span/180 = 15.0 mm (Flat roofs not supporting and not attached to non-structural elements likely to be damaged by large deflections).

7.4 Comparison between the Experimental and Predicted Results

7.4.1 Crack Width

The average k_b value, calculated based on the beam test results, was used in predicting the crack width of each beam. The crack width was calculated with Eq. (7-3). Since the crack-width equation in ACI 440.1R (2006) is the same as in CAN/CSA S806 (2012), it was used in predicting the crack width of the tested beams. The recommended k_b values for ribbed FRP bars were 1.0 and 1.4 for CAN/CSA S6 (2014) and ACI 440.1R (2015), respectively.

Table 7–4 provides the calculated bond-dependent coefficient values (k_b) of each beam at 30% and 67% of the nominal capacity as well as at the permissible crack width of 0.70 mm in accordance with CAN/CSA S806 (2012). The k_b was calculated based on the measured crack widths and the corresponding strains in FRP bars using Eq. (7-3) (CAN/CSA S806 2012). The results showed that the k_b values ranged from 0.59 to 1.09 with an average value of 0.83 for the ribbed BFRP tested herein. The comparison confirms that the k_b=1.4 in ACI 440.1R (2015) is very conservative and overestimates the crack widths in the tested beams. On the other hand, the k_b=1.0 provided by CAN/CSA S6 (2014) yields a better prediction but still overestimates the crack widths.

7.4.2 Mid-Span Deflection

The deflection behavior of RC elements subject to flexural moment can be divided into two separate stages: before and after cracking. The first stage, in which the section is not cracked, the behavior of the concrete element is controlled by the section's gross moment of inertia (I_g). The second stage starts when the applied moment (M_a) exceeds the cracking moment (M_{cr}) and crack propagation occurs, which reduces stiffness.

The ACI 440.1R (2006) equation is based on the effective moment of inertia (I_e), which is determined by modifying the Branson (1968) equation. The modification, shown in Eq. (7-9a), introduced (β_d) to account for FRP instead of steel, where (β_d) is proportional to the ratio between the actual and balanced reinforcement ratio of the section (Eq. (7-9b)). ACI 440.1R (2015), however, recommended another formula to calculate I_e, which was based on Bischoff et al. (2009) (Eq. (7-10a)). This formula includes an additional factor γ to account for the variation in stiffness along the length of the member, as shown in Eq. (7-10b), which was introduced by Bischoff and

Gross (2011). The deflection prediction entails calculating a uniform moment of inertia throughout the beam length and uses deflection equations derived from linear elastic analysis, as shown in Eq. (7-11), for a simply supported member subjected to two-point loading.

$$I_e = \left(\frac{M_{cr}}{M_a}\right)^3 \beta_d I_g + \left[1 - \left(\frac{M_{cr}}{M_a}\right)^3\right] I_{cr} \le I_g \tag{7-9a}$$

$$\beta_d = \frac{1}{5}\left(\frac{\rho_f}{\rho_{fb}}\right) \le 1.0 \tag{7-9b}$$

$$I_e = \frac{I_{cr}}{1 - \gamma\left(\frac{M_{cr}}{M_a}\right)^2\left[1 - \frac{I_{cr}}{I_g}\right]} \le I_g \tag{7-10a}$$

$$\gamma = 1.72 - 0.72\left(\frac{M_{cr}}{M_a}\right) \tag{7-10b}$$

$$\delta_{max} = \frac{PL^3}{24E_cI_e}\left[3L^2 - 4a^2\right] \tag{7-11}$$

CAN/CSA S806 (2012) recommends curvature integration along the span to determine the deflection of a concrete member at any point, assuming the section is fully cracked with no contribution of tension stiffness in the beam's cracked regions. Therefore, the moment–curvature relation of FRP concrete members can be assumed to be bilinear, where the curvature (Ψ) is given by ($M_a/(E_cI_g)$) for the uncracked parts of the beam, followed by an increase in curvature at a constant moment value (transition from uncracked to cracked stage) and ($M_a/(E_cI_{cr})$) for the cracked part when the applied moment (M_a) is higher than the cracking moment (M_{cr}). CAN/CSA S806 (2012) provides deflection equations for simple loading cases, such as Eq. (7-12), for a simply supported member subjected to two-point loading where the cracked moment of inertia (I_{cr}) is calculated from Eq. (7-13).

$$\delta = \frac{PL^3}{24E_cI_{cr}}\left[3\left(\frac{a}{L}\right) - 4\left(\frac{a}{L}\right)^3 - 8\left(1 - \frac{I_{cr}}{I_g}\right)\left(\frac{L_g}{L}\right)^3\right] \tag{7-12}$$

$$I_{cr} = \frac{bd^3}{3}k^3 + n_fA_fd^2(1-k)^2 \tag{7-13}$$

Table 7–6 provides the experimental mid-span deflections measured at 30% and 67% of the nominal capacity ($0.3M_n$ and $0.67M_n$), respectively. It also provides the experimental-to-predicted deflection ratios ($\delta_{exp}/\delta_{pred}$) for all tested beams at $0.3M_n$ and $0.67M_n$ based on ACI 440.1R (2006), ACI 440.1R (2015) and CAN/CSA S806 (2012) provisions. **Figure 7–8** shows the correlation between the experimental and predicted responses. Moreover, **Table 7–6** confirms that ACI 440.1R (2006) underestimated the deflection of the beams at $0.30M_n$ (expected service load), where the average $\delta_{exp}/\delta_{pred}$ was 2.91±0.81. Similarly, at $0.67M_n$, it underestimated the deflection values with an average $\delta_{exp}/\delta_{pred}$ of 1.30±0.06. ACI 440.1R (2015) showed better predictions than ACI 440.1R (2006) at both $0.3M_n$ and $0.67M_n$, with an average $\delta_{exp}/\delta_{pred}$ of 2.02±0.86 and 1.21±0.03, respectively. On the other hand, CAN/CSA S806 (2012) has a reasonable prediction at $0.30M_n$ and overestimated the deflection prediction at $0.67M_n$, where the average $\delta_{exp}/\delta_{pred}$ were 0.99±0.08 and 1.07±0.05, respectively. Thus, CAN/CSA S806 (2012) may provide reasonable yet conservative deflections for beams reinforced with BFRP bars. It is worth mentioning that the large coefficient of variation for the results at the service-load level is related to the low reinforcement ratio in some beams, which have cracking loads close to the service-load level.

(a)

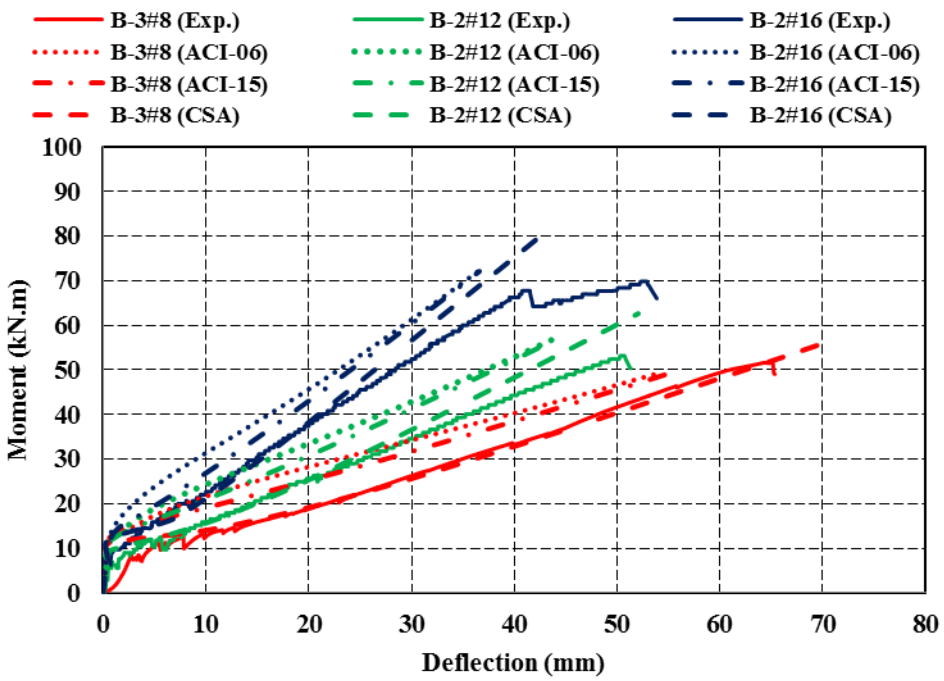

(b)

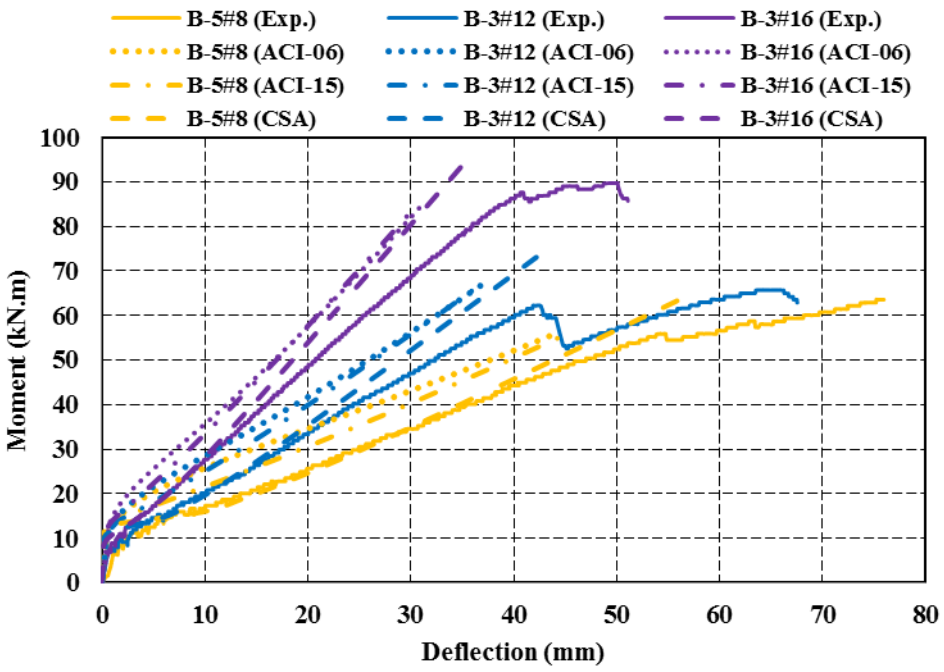

Figure 7–8: Comparison between the experimental and predicted deflection: (a) B-3#8mm, B-2#12mm and B-2#16mm; (b) B-5#8mm, B-3#12mm and B-3#16mm

6.5 Summary and Conclusion

This paper presented an experimental study aimed at investigating the flexural behavior of concrete beams reinforced with ribbed basalt-fiber-reinforced-polymer bars (BFRP). A total of eight concrete beams measuring 3100 mm long × 200 mm wide × 300 mm deep were constructed and tested up to failure. Six beams were reinforced with 8, 12, and 16 mm BFRP bars with ribbed surfaces and two reference beams were reinforced with 10M and 15M steel bars. The beams were tested under four-point bending over a clear span of 2700 mm until failure, and the experimental results were compared to design provisions. Based on the test results and the discussions presented herein, the following conclusions can be drawn:

1. The tested BFRP-RC beams failed due to concrete crushing as they were designed as over-reinforced sections. The beams showed distributed flexural cracks with no signs of slippage of the tensile reinforcement. The load-carrying capacity was higher than that of the steel-RC beams with the same reinforcement ratios due to the higher tensile strength and strain capacity of the BFRP bars compared to the steel bars.

2. The BFRP-RC beams showed typical bilinear behavior for strain and deflection until failure. The pre-cracking response and cracking loads of all the beams were nearly unaffected by the reinforcement ratio, since they are governed by the gross concrete section. After the beams crack, the increase in stiffness or reduction in reinforcement strains was proportional to the reinforcement ratio.

3. The average bond-dependent coefficient (k_b), determined from the three first flexural cracks in each beam, was 0.83±0.14 for the BFRP bars with ribbed surfaces, which is lower than the recommendation in the Canadian Highway Bridge Design Code (CAN/CSA S6 2014) (k_b = 1.0) for ribbed FRP bars.

4. The axial stiffness of the flexural reinforcement ($E_f A_f$) significantly affected the general behavior of the BFRP-RC beams. Beams with the same $E_f A_f$ are expected to show similar deflection and capacity, regardless the effect of the concrete strength and the variation in the effective depth. On the other hand, the use of smaller diameters of BFRP bars may result in better cracking behavior due to the higher bond strength of the bars, as evidenced by B-3#8mm

and B-2#12. Despite its low E_f A_f, B-3#8mm showed the same moment–crack width relationship as B2#12mm. More investigation is needed, however, to quantify the effect of bar diameter and bar spacing.

5. ACI 440.1R (2006) and ACI 440.1R (2015) underestimated the deflection of the beams at $0.30M_n$, where the average $\delta_{exp}/\delta_{pred}$ ratios were 2.91±0.81 and 2.02±0.86, respectively. Similarly, at $0.67M_n$, the average $\delta_{exp}/\delta_{pred}$ ratios were 1.30±0.06 and 1.21±0.03 using ACI 440.1R (2006) and ACI 440.1R (2015), respectively. On the other hand, CAN/CSA S806 (2012) provided reasonable yet conservative deflection values with average $\delta_{exp}/\delta_{pred}$ ratios of 0.99±0.08 and 1.07±0.05 at $0.30M_n$ and $0.67M_n$, respectively.

6.6 Nomenclature

The following symbols are used in this paper:

a = shear span (mm)
A_f = nominal area of FRP tension reinforcement (mm^2)
b = beam effective width (mm)
c = neutral-axis depth (mm)
d = distance from the extreme compression fiber to the centroid of tension force (mm)
d_b = bar diameter (mm)
d_c = distance from extreme tension fiber to the center of the longitudinal bar (mm)
E_f = modulus of elasticity of longitudinal reinforcement (MPa)
f'_c = compressive strength of concrete (MPa)
f_f = stress in FRP reinforcement under specified loads (MPa)
f_{fu} = ultimate strength of FRP longitudinal reinforcement (MPa)
f_r = modulus of rupture (kN/m^2)
h_1 = distance from neutral axis to center of tensile reinforcement (mm)
h_2 = distance from neutral axis to extreme tension fiber (mm)
I_{cr} = transformed moment of inertia of cracked reinforced-concrete section (mm^4)
I_e = effective moment of inertia (mm^4)
I_g = gross moment of inertia of uncracked section (mm^4)
J = deformability factor

k = ratio of depth of neutral axis to reinforcement depth

k_b = bond-dependent coefficient

L = length of clear span (mm)

L_g = length of the uncracked section (mm)

M_a = applied moment (kN.m)

M_{cr} = cracking moment (kN.m)

M_n = nominal moment of the reinforced-concrete section (kN.m)

n_f = ratio of modulus of elasticity of FRP bars to modulus of elasticity of concrete

P = applied load (kN)

s = spacing between the longitudinal reinforcement bars (mm)

w_{cr} = maximum crack width (mm)

y_t = distance from centroid axis of cross section to the extreme fiber in tension (mm)

γ = parameter to account for the variation of stiffness along the length of the member

δ = mid-span deflection (mm)

ε_{cu} = ultimate concrete strain

ε_{fu} = ultimate FRP strain

ρ_f = actual longitudinal-reinforcement ratio

CHAPTER 8
SUMMARY, CONCLUSIONS, AND RECOMMENDATIONS FOR FUTURE WORK

8.1 Summary

This experimental study aimed at developing a better understanding of basalt fiber-reinforced polymer (BFRP) reinforcing bars and their structural performance in concrete members. The experimental program consisted of three parts, designed to evaluate the short-and long-term characteristics and the structural performance of newly developed BFRP bars in concrete members. This section summarizes the different parts of the study as follows:

Part I: Characterization of BFRP Bars

This part aimed at investigating the physical, mechanical, and durability characteristics of three types of BFRP bars and tendons. Durability and long-term performance were assessed in accordance to CAN/CSA S807 (2010), ACI 440.6M (2008) and ASTM standards using accelerated aging techniques in different chemical solutions at high temperature for certain periods of time to determine their suitability as internal reinforcement for concrete elements.

Part II: Concrete Bridge-Deck Slabs Reinforced with BFRP Bars

This part aimed at investigating the performance of edge-restrained concrete bridge-deck slabs reinforced with BFRP bars. The tests included six full-scale, edge-restrained concrete deck slabs simulating an actual slab-on-girder bridge-deck commonly used in North America, and one full-scale unrestrained concrete deck slab. The deck slabs measured 3000 mm long × 2500 mm wide × 200 mm thick. The slabs were tested up to failure under a single concentrated load acting on the center of each slab to simulate the footprint of the sustained truck wheel load (87.5 kN for CL-625 truck, CAN/CSA S6.1S1, 2010). The punching shear capacities were predicted using the available equations and provisions and compared with the experimental results.

Part III: Concrete Beams Reinforced with BFRP Bars

This part aimed at investigating the flexural behavior and serviceability performance of concrete beams reinforced with sand-coated and ribbed BFRP bars. In addition, it investigated the bond-dependent coefficient (k_b) of the BFRP bars and compared the calculated values with the recommendations of the current FRP design codes and guidelines. The tests included twelve rectangular concrete beams of 3100 mm long × 200 mm wide × 300 mm deep reinforced with BFRP bars and two beams reinforced with steel bars. The beam specimens were designed in accordance with Annex S of CSA S806 (2012) and tested under four-point bending over a clear span of 2700 mm until failure. The beam test results are introduced and discussed in terms of cracking behavior, deflection, flexure capacity, and failure modes, and the experimental results were compared to design provisions.

8.2 Conclusion

Based on the experimental testing and the analysis of the results, the following conclusions were drawn:

Part I: Characterization of BFRP Bars

1. The test results confirmed that the BFRP bars meet the requirements of ACI 440.6M (2008) and CAN/CSA S807 (2010) with respect to physical and mechanical properties and could be placed in the same category as grades II and III GFRP bars (according to tensile modulus of elasticity). Their tensile strength, however, was higher than that provided by CAN/CSA S807 (2010) for CFRP bars.

2. The long-term testing showed significant degradation and reduction in the mechanical properties of the alkali-conditioned specimens. However, the basalt fibers and resins used in this study were not affected by the conditioning. The strength degradation observed in the BFRP bars was attributed to the fiber–matrix interface (sizing), which evidenced poor bonding between the resin and basalt fibers.

Part II: Concrete Bridge-Deck Slabs Reinforced with BFRP Bars

3. Similar to past findings for steel-, GFRP-, and CFRP-reinforced concrete bridge-deck slabs, the BFRP-reinforced concrete bridge-deck slabs evidenced punching-shear failure at corresponding loads higher than the factored designed loads provided by the CHBDC (CAN/CSA S6 2014).

4. The bottom transverse-reinforcement ratio was the main parameter affecting the general behavior (strains, crack width, deflection). Increasing the bottom-transverse reinforcement ratio significantly enhanced the performance and reduced strain, deflection, and crack width at the same load level.

5. Deck slabs with the same reinforcement ratio and axial-reinforcement stiffness nearly exhibit the same behavior and punching-shear capacity. Reducing BFRP bar size and spacing improved the cracking performance and the induced strains by improving the bond between the concrete and reinforcing bars.

6. The design of deck slabs using the flexural method was governed in most cases by the crack-width limit. Thus, using FRP bars with a high modulus of elasticity, such as BFRP bars, will significantly reduce the required amount of reinforcement.

7. The test results showed that an edge-restraining system increased the ultimate capacity by 31.9% and reduced the crack widths, deflection, and FRP strains compared to the unrestrained slab. This provides evidence of the development of compressive membrane action (CMA) in the laterally restrained concrete deck slabs.

8. The current punching-shear provisions in CAN/CSA S806 (2012) provided reasonable yet conservative predictions for the punching-shear capacity of BFRP-RC deck slabs. On the other hand, the current guide of ACI 440.1R (2015) underestimated the punching-shear strength of the tested slabs. These findings are in agreement with past work conducted on glass- and carbon-FRP bars.

Part III: Concrete Beams Reinforced with BFRP Bars

9. The tested BFRP-RC beams failed due concrete crushing as they were designed as over-reinforced sections. The beams showed distributed flexural cracks with no signs of slippage of the tensile reinforcement. The load-carrying capacity was higher than that of the steel-RC beams with the same reinforcement ratios due to the higher tensile strength and strain capacity of the BFRP bars compared to the steel bars.

10. Beams reinforced with sand-coated and ribbed BFRP bars exhibited similar behavior. However, the former showed a higher number of cracks and lower crack width due to better bond distribution between the bar and concrete.

11. The average bond-dependent coefficients (k_b), determined from the three first cracks in each beam, were 0.76±0.03 and 0.83±0.14 for the sand-coated and ribbed BFRP bars, respectively.

12. The BFRP-RC beams showed typical bilinear behavior for strain and deflection until failure. The pre-cracking response and cracking loads of all the beams were nearly unaffected by the reinforcement ratio, since they are governed by the gross concrete section. After the beams crack, the increase in stiffness or reduction in reinforcement strains was proportional to the reinforcement ratio.

13. The BFRP-RC beams with low reinforcement ratios showed sharp increases in strains and deflection at cracking. The sudden increase in strains resulted in wider and deeper cracks, which is reflected on the stiffness and the location of the neutral axis of the cracked section. Increasing the reinforcement ratio, however, increased the amount of absorbed energy at the first crack, which enhanced the behavior, as it controls the immediate increase in strain and initial crack width.

14. The axial stiffness of the flexural reinforcement ($E_f A_f$) significantly affected the general behavior of the BFRP-RC beams. The higher axial stiffness, the better performance (lower deflection, lower strain, and lower crack width at the same load level). Beams with the same axial stiffness are expected to show similar behavior. On the other hand, the use of smaller diameters of BFRP bars may result in better cracking behavior due to the higher bond strength of the bars.

15. ACI 440.1R (2006) underestimated the deflection of the beams at service load level (0.30M_n), where the average $\delta_{exp}/\delta_{pred}$ were 2.10±0.37 and 2.91±0.81 for sand-coated and ribbed BFRP bars, respectively, while ACI 440.1R (2015) showed better predictions than ACI 440.1R (2006) with an average $\delta_{exp}/\delta_{pred}$ of 1.35±0.15 and 2.02±0.86 for sand-coated and ribbed BFRP bars, respectively. On the other hand, CAN/CSA S806 (2012) overestimated the deflection predictions at 0.30M_n, where the average $\delta_{exp}/\delta_{pred}$ were 0.80±0.09 and 0.99±0.08 for sand-coated and ribbed BFRP bars, respectively. Thus, CAN/CSA S806 (2012) may provide reasonable yet conservative deflection values for beams reinforced with BFRP bars.

8.3 Conclusion en Francais

Suite aux essais expérimentaux et à l'analyse des résultats, les conclusions suivantes ont été tirées:

Partie I: Caractérisation des barres de PRFB

1. Les résultats confirment que les barres de PRFB remplissent les conditions des normes ACI 440.6M (2008) et CAN/CSA S807 (2010) en respectant les propriétés physiques et mécaniques et pourrait être placées dans les mêmes catégories que les barres de PRFV de grade II et III (en fonction du module élastique en traction). Cependant, leurs résistances à la traction étaient plus élevées que ce qui est mentionné dans la norme CAN/CSA S807 (2010) pour des barres de PRFC.

2. Les essais à long terme sous conditionnement alcalin ont montré une dégradation significative et une réduction des propriétés mécaniques des spécimens. Cependant, les fibres de basalte et les résines utilisées dans cette étude n'ont pas été affectées par ce conditionnement. La dégradation de la résistance observée dans les barres de PRFB était attribuée à l'interface fibre-matrice (dimension), ce qui pointait à de faibles liaisons entre la résine et les fibres.

Partie II: Dalle de pont en béton armé de barres de PRFB

3. Comme pour les dernières conclusions sur les dalles de pont en béton armé de barres d'acier, PRFV et PRFC; les dalles de pont en béton armé de barres de PRFB manifestent une rupture en poinçonnement correspondant à une charge plus élevé que la charge de dimensionnement pondérée prescrite par le CHBDC (CAN/CSA S6 2014).

4. Le ratio de renforcement transversal du bas était le paramètre principal qui affectait le comportement général (contraintes, largeur de fissure, déflexion). Augmenter le ratio de renforcement transversal du bas améliore significativement les performances et réduit les contraintes, la largeur de fissuration et la déflexion pour une même charge.

5. Les dalles ayant le même ratio de renforcement et rigidité de renforcement axial démontrent presque le même comportement et capacité en poinçonnement. Réduire le diamètre et l'espacement des barres de PRFB augmente les performances de fissuration et les contraintes induites en améliorant la liaison en le béton et les barres de renforcement.

6. La conception des dalles utilisant l'analyse en flexion était gouvernée, dans la majorité des cas, par la limite de largeur de fissuration. Par conséquent, l'utilisation de PRF avec un module d'élasticité élevé, comme pour le PRFB, réduirait significativement la quantité de renforcement requis.

7. Les résultats des essais ont montré qu'un système de retenue des bords augmente la capacité ultime de 31.9% et réduit la largeur de fissuration, la déflexion et les contraintes dans les PRF comparativement à une dalle non retenue. Cela fournit une preuve qu'il y a un développement d'une action de la membrane en compression dans une dalle retenue latéralement.

8. La disposition actuelle sur le poinçonnement dans la norme CAN/CSA S806 (2012) fourni des prédictions raisonnables, mais conservatrices vis-à-vis de la capacité en poinçonnement des dalles de béton renforcé de PRFB. D'un autre côté, le guide actuel du ACI 440.1R (2015) sous-estime la résistance au poinçonnement des dalles testé. Ces conclusions sont en accord avec les travaux passés conduits avec des barres PRFV et PRFC.

Partie III: Poutres en béton armé de barres de PRFB

9. Les poutres en béton armé de PRFB testées ont failli en compression du béton puisqu'elles ont été conçues comme une section surarmée. Les poutres montrent des fissurations en flexion distribuées avec aucun signe de glissement du renforcement en traction. La capacité de charge était plus grande que celle pour des poutres armées d'acier en considérant les mêmes ratios de renforcement. Cela était dû la une plus grande résistance à la traction et capacité de contrainte des barres de PRFB comparativement à des barres d'acier.

10. Les poutres renforcées avec des barres en PRFB enrobées de sable ou nervurées présentent un comportement similaire. La première présente un nombre plus élevé de fissures avec une ouverture moins important due à une meilleure distribution de la liaison entre la barre et le béton.

11. Le coefficient moyen dépendant de la liaison (k_b), déterminée avec les trois premières fissurations de chaque poutre, était de 0.76±0.03 et 0.83±0.14 pour les surfaces sablées et crénelées respectivement des barres de PRFB.

12. Les poutres en béton armées de PRFB démontrent un comportement bilinéaire typique pour les contraintes et les déflexions jusqu'à la rupture. Les réponses préfissuration et les charges de fissuration de toutes les poutres étaient presque infectées par le ratio de renforcement puisque c'est la section brute de béton qui gouvernait. Après la fissuration des poutres, l'augmentation en rigidité ou la réduction des contraintes dans le renforcement était directement proportionnelle au ratio de renforcement.

13. Les poutres en béton armé de PRFB avec un ratio de renforcement faible montraient une forte augmentation dans les contraintes et la déflexion au moment de la fissuration. Cette augmentation soudaine dans les contraintes a entraîné des fissurations plus larges et plus profondes; ce qui s'est reflété dans la rigidité et l'emplacement de l'axe neutre de la section fissurée. Cependant en augmentant le ratio de renforcement, cela a augmenté l'énergie absorbée lors de la première fissuration. Cela a eu pour effet de rehausser le comportement puisqu'il contrôle immédiatement l'augmentation de la contrainte et la largeur initiale de fissuration.

14. La rigidité axiale et le renforcement en flexion (E_f A_f) ont significativement affecté le comportement général des poutres en béton armé de PRFB. Plus la rigidité axiale est élevée, meilleur sont les performances (faible déflexion, faible contrainte, faible largeur de fissuration pour une même charge). Les poutres avec une rigidité axiale similaire sont attendues de montré des comportements similaires. D'un autre côté, l'utilisation de diamètre plus petit pour des barres de PRFB peut conduire à un meilleur comportement en fissuration en raison d'une plus grande résistance à la liaison des barres.

15. L'ACI 440.1R (2006) sous-estime la flèche des poutres pour la charge en service ($0.30M_n$), où la moyenne de $\delta_{exp}/\delta_{pred}$ est de 2.10±0.37 et 2.91±0.81 pour les surfaces sablées et crénelées respectivement. Par contre, L'ACI 440.1R (2015) montre des meilleures prédictions que l'ACI 440.1R (2006) avec une moyenne de 1.35±0.15 et 2.02±0.86 pour les surfaces sablées et crénelées respectivement. D'autre part, la norme CAN/CSA S806 (2012) surestime la prédiction de la flèche pour le même niveau de chargement, où la moyenne de $\delta_{exp}/\delta_{pred}$ est de 0.80±0.09 et 0.99±0.081 pour les surfaces sablées et crénelées respectivement. Ainsi, la norme CAN/CSA S806 (2012) donne des résultats conservateurs pour les poutres renforcées avec des barres de PRFB.

8.4 Recommendations for Future Work

Based on the findings and conclusions of the current study, further investigations on different BFRP products should be conducted to generate more confidence and encourage wider acceptance of this new material, which may lead to introducing the BFRP materials into the FRP design codes and standards. Some of the recommendations for future research are to:

1. Investigate the durability of the BFRP bars subjected to water, salts and acids for a long time, as well as the fire resistance.

2. Investigate the serviceability and structural performance of BFRP-RC beams and bridge-deck slabs using different types of concrete, such as high-strength, high-performance and self-consolidated concrete.

3. Investigate the serviceability and structural performance of BFRP-RC beams and bridge-deck slabs under fatigue load.

4. Investigate the performance of prestressed concrete elements reinforced with BFRP tendons.

5. Investigate the shear behavior of BFRP-RC beams.

6. For the flexure test, the authors recommend not to use top reinforcement at the maximum moment region of the beam, to reduce the effect of compression reinforcement on the beam behavior.

REFERENCES

AASHTO (1996). “Standard Specifications for Highway Bridges.” American Association of State Highway and Transportation Officials, Washington, D.C.

ACI Committee 318. (1999). “Building Code Requirements for Structural Concrete (ACI 318-99) and Commentary (ACI 318 R-99)”, *ACI*, Farmington Hills, Michigan, USA.

ACI Committee 318. (2005). “Building Code Requirements for Structural Concrete (ACI 318-05) and Commentary (ACI 318R-05).” *ACI*, Farmington Hills, Michigan, USA.

ACI Committee 440 (2006). “Guide for the Design and Construction of Concrete Reinforced with FRP Bars (ACI 440.1R-06).” *ACI*, Farmington Hills, Michigan, USA.

ACI Committee 440 (2015). “Guide for the Design and Construction of Concrete Reinforced with FRP Bars (ACI 440.1R-15).” *ACI*, Farmington Hills, Michigan, USA.

ACI Committee 440. (2008). “Specification for Carbon and Glass Fiber-Reinforced Polymer Bar Materials for Concrete Reinforcement (ACI 440.6M-08).” *ACI*, Farmington Hills, Michigan, USA.

ACI Committee 440. (2012). “Guide Test Methods for Fiber-Reinforced Polymers (FRPs) for Reinforcing or Strengthening Concrete Structures (ACI 440.3R-12).” *ACI*, Farmington Hills, Michigan, USA.

Adhikari, S. (2009). “Mechanical Properties and Flexural Applications of Basalt Fiber Reinforced Polymer (BFRP) Bars.” *MSc Thesis*, Department of Civil Engineering, University of Akron, Ohio, USA.

Ahmad, S.H., Zia, P., Yu, T., and Xie, Y. (1993). “Punching Shear Tests of Slabs Reinforced with 3-D Carbon Fiber Fabric.” *ACI Concrete International*, 16 (6), 36–41.

Ahmed, E. and Benmokrane, B. (2010). “Design of Concrete Bridge Deck Slabs Reinforced with GFRP Bars According to the CHBDC S6-06.” *Proceedings of the 8th International Conference*

on Short and Medium Span Bridges (*SMSB*), Niagara Falls, Ontario, Canada, August 3-6, 10 pp.

Ahmed, E., and Benmokrane, B. (2011). "Static Testing of Full-Scale Concrete Bridge Barriers Reinforced with GFRP Bars." *Proceedings of the 10th International Symposium on Fiber-Reinforced Polymer Reinforcement for Concrete Structures* (*FRPRCS-10*), *ACI Special Publication*, SP-275, 20 pp.

Ahmed, E., and Benmokrane, B. (2012). "Design, Construction, and Testing of Hybrid-Reinforced Concrete Bridge Deck, 410 Overpass Bridge." *Proceedings of the 6th International Conference on FRP Composites in Civil Engineering*, Rome, Italy, June 13–15, 8 pp.

Ahmed, E., and Benmokrane, B. (2014b). "Design of Bridge Deck Slabs using Glass Fiber-Reinforced Polymer (GFRP) Bars of Different Grades." *Proceedings of the Ninth International Conference on Short and Medium Span Bridges* (*SMSB*), Calgary, Alberta, Canada, 10 pp.

Ahmed, E., Dulude, C., and Benmokrane, B. (2013a). "Concrete Bridge Barriers Reinforced with Glass Fibre-Reinforced Rolymer: Static Tests and Pendulum Impacts." *Canadian Journal of Civil Engineering*, 41, 1051-1059.

Ahmed, E., El-Salakawy, E., Benmokrane, B. (2010a). "Performance Evaluation of GFRP Shear Reinforcement for Concrete Beams." *ACI Structural Journal*, 107(1), 53-62.

Ahmed, E., Matta, F., and Benmokrane, B. (2013b). "Steel Post-and-Beam Barrier with FRP Reinforced Concrete Curb and Bridge Deck Connection." *ASCE Journal of Bridge Engineering*, 18 (11), 1189-1197.

Ahmed, E., Settecasi, F., and Benmokrane, B. (2014a). "Construction and Testing of GFRP Steel Hybrid-Reinforced Concrete Bridge-Deck Slabs of Sainte-Catherine Overpass Bridges." *ASCE Journal of Bridge Engineering*, 19 (6), 04014011, 11 pp.

Ahmed, E., El-Salakawy, E., and Benmokrane, B. (2010b). "Shear Performance of RC Bridge Girders Reinforced with Carbon FRP Stirrups." *Journal of Bridge Engineering*, 15(1), 44–54.

Alsayed, S.H., Al-Salloum, Y.A., and Almusallam, T.H. (2000). "Performance of Glass Fiber Reinforced Plastic Bars as a Reinforcing Material for Concrete Structures." *Journal of Composites: Part B: Engineering*, 31, 555–567.

Alsharif, F. (2014). "Structural Behavior of Lightweight Concrete Bridge Deck Slabs Reinforced with Basalt FRP Bars." *MSc Thesis*, University of Illinois, Chicago.

Altalmas, A., El Refai, A., and Abed, F. (2015). "Bond Degradation of Basalt Fiber-Reinforced Polymer (BFRP) Bars Exposed to Accelerated Aging Conditions." *Journal of Construction and Building Materials*, 81, 162–171.

American Association of State Highway and Transportation Officials (AASTO LRFD). (2010). "LRFD Bridge Design Specifications." 5th ed., AASHTO, Washington, D.C.

American Association of State Highway and Transportation Officials (AASTO LRFD). (2009). "LRFD Bridge Design Guide Specifications for GFRP-Reinforced Concrete Bridge Decks and Traffic Railings." 1st ed., AASHTO, Washington, D.C.

Artemenko, S. (2003). "Polymer Composite Materials Made From Carbon, Basalt, and Glass Fibers. Structure and Properties." *Journal of Fiber Chemistry*, 35 (3), 226–229.

ASTM A615/A615M (2006). "Standard Specification for Deformed and Plain Carbon-Steel for Concrete Reinforcement." *American Society for Testing and Materials*, Conshohocken, USA, 6 pp.

ASTM C39 (2015). "Standard Test Methods for Compressive Strength of Cylindrical Concrete Specimens." *American Society for Testing and Materials*, Conshohocken, USA. 7 pp.

ASTM C496 (2011). "Standard Test Methods for Splitting Tensile Strength of Cylindrical Concrete Specimens." *American Society for Testing and Materials*, Conshohocken, USA. 5 pp.

ASTM D3171 (2011). "Standard Test Method for Constituent Content of Composite Materials." *American Society for Testing and Material*, Conshohocken, USA, 11 pp.

ASTM D3418 (2012). "Standard Test Method for Transition Temperatures and Enthalpies of Fusion and Crystallization of Polymers by Differential Scanning Calorimetry." *American Society for Testing and Materials*, Conshohocken, USA, 7 p.

ASTM D4475 (2008). "Standard Test Method for Apparent Horizontal Shear Strength of Pultruded Reinforced Plastic Bars by the Short Beam Method." *American Society for Testing and Materials*, Conshohocken, USA, 4 pp.

ASTM D4476 (2009). "Standard Test Method for Flexural Properties of Fiber Reinforced Pultruded Plastic Bars." *American Society for Testing and Material*, Conshohocken, USA, 5 pp.

ASTM D5028 (1990). "Standard Test Method for Curing Properties of Pultrusion Resin by Thermal Analysis." *American Society for Testing and Material*, Conshohocken, USA, 4 pp.

ASTM D570 (2010). "Standard Test Method for Water Absorption of Plastics." *American Society for Testing and Material*, Conshohocken, USA, 4 pp.

ASTM D7205 (2011). "Standard Test Method for Tensile Properties of Fiber-Reinforced Polymer Matrix Composite Bars." *American Society for Testing and Materials*, Conshohocken, USA, 13 pp.

ASTM D7617 (2011). "Standard Test Method for Transverse Shear Strength of Fiber-Reinforced Polymer Matrix Composite Bars." *American Society for Testing and Materials*, Conshohocken, USA, 12 pp.

ASTM D7705 (2012). "Standard Test Method for Alkali Resistance of Fiber Reinforced Polymer (FRP) Matrix Composite Bars used in Concrete Construction." *American Society for Testing and Material*, Conshohocken, USA, 5 pp.

ASTM D7913 (2014). "Standard Test Method for Bond Strength of Fiber Reinforced Polymer Matrix Composite Bars to Concrete by Pullout Testing." *American Society for Testing and Material*, Conshohocken, USA, 9 pp.

ASTM D792 (2008). "Standard Test Methods for Density and Specific Gravity (Relative Density) of Plastics by Displacement." *American Society for Testing and Materials*, Conshohocken, USA. 6 pp.

ASTM E1356 (2008). "Standard Test Method for Assignment of the Glass Transition Temperatures by Differential Scanning Calorimetry." *American Society for Testing and Material*, Conshohocken, USA, 4 pp.

ASTM E831 (2012). "Standard Test Method for Linear Thermal Expansion of Solids Materials by Thermo-Mechanical Analysis (TMA)." *American Society for Testing and Material*, Conshohocken, USA, 4 pp.

Azimi, H., Sennah, K., Tropynina, E., Goremykin, S., Lucic, S., Lam, M. (2014). "Anchorage Capacity of Concrete Bridge Barriers Reinforced with GFRP Bars with Headed Ends." *ASCE Journal of Bridge Engineering*, 19 (9), 04014030.

Bakht, B., Lam, C. "Behavior of Transverse Confining Systems for Steel-Free Deck Slabs." *ASCE Journal of Bridge Engineering*, 5 (2), 139–147.

Bakis, C., Bank, L., Brown, V., Cosenza, E., Davalos, J., Lesko, J., Machida, A., Rizkalla, S., and Triantafillou, T. (2002). "Fiber-Reinforced Polymer Composites for Construction—State-of-the-Art Review." *ASCE Journal of Composites for Construction*, 6 (2), 73–87.

Banibayat, P. and Patnaik, A. (2015). "Creep Rupture Performance of Basalt Fiber Reinforced Polymer (BFRP) Bars." *ASCE Journal of Aerospace Engineering*, 28 (3), 04014074.

Banthia, N., Al-Asaly, M., and Ma, S. (1995). "Behavior of Concrete Slabs Reinforced with Fiber-Reinforced Plastic Grid," *ASCE Journal of Materials in Civil Engineering*, 7 (4), 643–652.

Basaltex. (2015). "The Thread of Stone." ⟨http://www.basaltex.com ⟩ (April 30, 2015).

Batchelor, B., Hewitt, B. Csagoly, P., and Holowka, M. (1978). "Investigation of the Ultimate Strength of Deck Slabs of Composite Steel/Concrete Bridges." *Proceedings of Bridge Engineering Conference,* Conducted by the Transportation Research Board, Washington, D.C, Research Record No. 664, 162-170.

Benmokrane, B., and EI-Salakawy, E. (2002). "Durability of Fiber-Reinforced Polymer (FRP) Composites for Construction." *Proceedings of the 2nd International Conference* (*CDCC*), Montréal, Québec, Canada, 715 pp.

Benmokrane, B., Elgabbas, F., Ahmed, E., and Cousin, P. (2015). "Characterization and Comparative Durability Study of Glass/Vinylester, Basalt/Vinylester, and Basalt/Epoxy FRP Bars." *ASCE Journal of Composites for Construction*, 19 (6), 04015008.

Benmokrane, B., El-Salakawy, E., Cherrak, Z., and Wiseman, A., (2004b). "Fiber Reinforced Polymer Composite Concrete Slabs of a Public Works and Government Services Canada Parking Garage." *Canadian Journal of Civil Engineers*, 31, 732–748.

Benmokrane, B., El-Salakawy, E., Desgagné, G., and Lackey, T. (2004a). "Building a New Generation of Concrete Bridge Decks using FRP Bars for Bridges." *ACI Concrete International*, 26 (8), 84–90.

Benmokrane, B., El-Salakawy, E., El-Gamal, S., and Goulet, S. (2007) "Construction and Testing of an Innovative Concrete Bridge Deck Totally Reinforced with Glass FRP Bars: Val-Alain Bridge on Highway 20 East." *ASCE Journal of Bridge Engineering*, 12 (5), 632–645.

Benmokrane, B., El-Salakawy, E., El-Ragaby, A., and Lackey, T. (2006). "Designing and Testing of Concrete Bridge Decks Reinforced with Glass FRP Bars." *ASCE Journal of Bridge Engineering*, 11 (2), 217–229.

Benmokrane, B., Masmoudi, R., and Chaallal, O. (1996). "Flexural Response of Concrete Beams Reinforced with FRP Rebars." *ACI Structural Journal*, 93 (1), 46–55.

Benmokrane, B., Rahman, H., Mukhopadhyaya, R., Masmoudi, R., Zhang, B., Lord, I., and Tadros, G. (2001). "Fiber-Optic Sensors Monitor FRP-Reinforced Bridge." *ACI Concrete International*, 23 (6), 33–38.

Benmokrane, B., Wang, P., Ton-That, T.M., Rahman, H., and Robert, J.F. (2002). "Durability of Glass Fiber-Reinforced Polymer Reinforcing Bars in Concrete Environment." *ASCE Journal of Composites for Construction*, 6 (3), 143–153.

BFCMTD. (2015). "Basalt Fiber and Composite Materials Technology Development." ⟨http://www.basaltfm.com⟩ (May 5, 2015).

Bi, Q., Wang, Q., Wang, H. (2011). "Study on Bond Properties of BFRP Bars to Basalt Fiber-Reinforced Concrete." *Advanced Material Research*, 163-167, 1251–1256.

Bischoff, P. (2001). "Effects of Shrinkage on Tension Stiffening and Cracking in Reinforced Concrete." *Canadian Journal of Civil Engineering*, 28(3), 363–374.

Bischoff, P. and Gross, S. (2011). "Equivalent Moment of Inertia Based on Integration of Curvature." *Journal of Composites for Construction*, 15(3), 263–273.

Bischoff, P., (2007). "Rational Model for Calculating Deflection of Reinforced Concrete Beams and Slabs." *Canadian Journal of Civil Engineering*, 34 (8), 992–1002.

Bischoff, P., Gross, S., and Ospina, C. (2009). "The Story behind Proposed Changes to the ACI 440 Deflection Requirements for FRP-Reinforced Concrete." *ACI Special Publication*, SP-264, 53–76.

Bouguerra, K., Ahmed, E., El-Gamal, S., and Benmokrane, B. (2011). "Testing of Full-Scale Concrete Bridge Deck Slabs Reinforced with Fiber-Reinforced Polymer (FRP) Bars." *Journal of Construction and Building Materials*, 25 (10), 3956–3965.

Boyle, H.C. and Karbhari, V.M. (1994). "Investigation of Bond Behavior between Glass Fiber Composite Reinforcements and Concrete." Polymer-Plastics Technology and Engineering, 33(6), 733-753.

Branson, D.E. (1968). "Design Procedures for Computing Deflections." *ACI Journal Proceedings*, 65 (9), 730–742.

Brik, V.B. (1997). "Basalt Fiber Composite Reinforcement for Concrete." *Final report*, Deserving Exploratory Analysis Programs (IDEA), Transportation Research Board, National Research Council, Contract No. NCHRP-96 IDO25.

Brik, V.B. (2003). "Advanced Concept Concrete Using Basalt Fiber/BF Composite Rebar Reinforcement." *Final Report for Highway*, Innovations Deserving Exploratory Analysis Programs (IDEA), Transportation Research Board of National Academies, Project No. 86.

British Standards Institution. (1997). "Structural Use of Concrete, BS8110: Part 1-Code of Practice for Design and Construction." London, UK, 172 pp.

Canadian Standards Association (2000). "Canadian Highway Bridge Design Code (CAN/CSA S6–00)." Rexdale, ON, Canada.

Canadian Standards Association (2002). "Design and Construction of Building Structures with Fiber Reinforced Polymers (CAN/CSA S806-02)." Rexdale, ON, Canada.

Canadian Standards Association (2004). "Design of Concrete Structures (CAN/CSA A23.3-04)." Rexdale, ON, Canada.

Canadian Standards Association (2010). "Canadian Highway Bridge Design Code (CAN/CSA S6.1S1–10)." Rexdale, ON, Canada.

Canadian Standards Association (2010). "Specification for Fiber-Reinforced Polymers (CAN/CSA-S807)." Rexdale, ON, Canada.

Canadian Standards Association (2012). "Design and Construction of Building Structures with Fiber Reinforced Polymers (CAN/CSA S806-12)." Rexdale, ON, Canada.

Canadian Standards Association (2014). "Canadian Highway Bridge Design Code (CAN/CSA S6–14)." Rexdale, ON, Canada.

Cao, S.H., Wu, Z.S., and Wang, X. (2009). "Tensile Properties of CFRP and Hybrid FRP Composites at Elevated Temperatures." *Journal of Composite Materials*, 43 (4), 315–330.

De Luca, A., Matta, F., and Nanni, A. (2010). "Behavior of Full-Scale GFRP Reinforced Concrete Columns under Axial Load." *ACI Structural Journal*, 107 (5), 589–596.

Deák, T., and Czigány, T. (2009). "Chemical Composition and Mechanical Properties of Basalt and Glass Fibers: A Comparison." *Textile Research Journal*, 79 (7), 645–651.

Dhand, V., Mittal, G., Rhee, K.Y., Park, S.J., and Hui, D. (2015). "A Short Review on Basalt Fiber Reinforced Polymer Composites." *Journal of Composites Part B: Engineering*, 73, 166–180.

Dulude, C., Hassan, M., Ahmed E., and Benmokrane, B. (2013). "Punching Shear Behavior of Flat Slabs Reinforced with Glass Fiber-Reinforced Polymer Bars." *ACI Structural Journal*, 110 (5), 723–734.

Eamon, D.C., Jensen, E.A., Grace, N.F., and Shi, X. (2012). "Life-Cycle Cost Analysis of Alternative Reinforcement Materials for Bridge Superstructures Considering Cost and Maintenance Uncertainties." *ASCE Journal of Materials in Civil Engineering*, 24 (4): 373–380.

Edalatmanesh, R., and Newhook, J.P. (2012). "Behavior of Externally Restrained Noncomposite Concrete Bridge Deck Panels." *ACI Structural Journal*, 109 (2), 161–170.

Eddie, D., Shalaby, A., Rizkalla, S. (1999). "FRP Dowels for Concrete Pavements." *MSc Thesis*, University of Manitoba, Winnipeg, Manitoba.

El Refai, A. (2013). "Durability and Fatigue of Basalt Fiber-Reinforced Polymer Bars Gripped with Steel Wedge Anchors." *ASCE Journal of Composites for Construction*, 17 (6), 04013006.

El Refai, A., Abed, F., and Altalmas, A. (2014b). "Bond Durability of Basalt Fiber–Reinforced Polymer Bars Embedded in Concrete under Direct Pullout Conditions." *ASCE Journal of Composites for Construction*, 19 (5), 04014078.

El Refai, A., Ammar, M., Masmoudi, R. (2014a). "Bond Performance of Basalt Fiber- Reinforced Polymer Bars to Concrete." *ASCE Journal of Composite for Construction*, 9 (3), 04014050.

El Safty, A., Benmokrane, B., and Rizkalla, S. (2014). "Degradation Assessment of Internal Continuous Fiber Reinforcement in Concrete Environment." *Report*, School of Engineering, College of Computing, Engineering, and Construction, University of North Florida, Report No. BDK82-977-05.

Elgabbas F, Ahmed E, Benmokrane B. (2015b). "Experimental Testing of Concrete Bridge-Deck Slabs Reinforced with Basalt-FRP Reinforcing Bars under Concentrated Loads." *ASCE Journal of Bridge Engineering*. (Accepted).

Elgabbas, F., Ahmed, E., and Benmokrane, B. (2013). "Basalt FRP Reinforcing Bars for Concrete Structures." *Proceedings of the 4th Asia-Pacific Conference on FRP in Structures* (*APFIS*), Melbourne, Australia. December 11–13, 6 pp.

Elgabbas, F., Ahmed, E., and Benmokrane, B. (2015a). "Physical and Mechanical Characteristics of New Basalt-FRP Bars for Reinforcing Concrete Structures." *Journal of Construction and Building Materials*, 95, 623–635.

Elgabbas, F., Cousin, P., Ahmed, E., and Benmokrane, B. (2014). "Development and Characterization of Basalt FRP Reinforcing Bars for Concrete Structures." *Proceedings of the 7th International Conference on FRP Composites in Civil Engineering* (*CICE*), Vancouver, Canada. August 20–22, 6 pp.

Elgabbas, F., Vincent, P., Ahmed, E., and Benmokrane, B. (2015c). "Experimental Testing of Basalt-Fiber-Reinforced Polymer Bars in Concrete Beams." Submitted to *Journal of Composite: Part B*, 91, 205-218.

El-Gamal, S., Benmokrane, B., and El-Salakawy, E. (2009). "Cracking and Deflection Behavior of One-Way Parking Garage Slabs Reinforced with CFRP Bars." *ACI Special Publication*, SP-264 (3), 33–52.

El-Gamal, S., El-Salakawy, E., and Benmokrane, B. (2007). "Influence of Reinforcement on the Behavior of Concrete Bridge Deck Slabs Reinforced with FRP Bars." *ASCE Journal of Composites of Construction*, 11 (5), 449–458.

El-Gamal, S., El-Salakawy, E.F., and Benmokrane, B. (2005). "Behavior of Concrete Bridge Deck Slabs Reinforced with FRP Bars under Concentrated Loads."*ACI Structural Journal*, 102 (5), 727–735.

El-Gendy, M., and El-Salakawy, E. (2014). "Effect of Flexural Reinforcement Type on the Punching Shear Strength of GFRP-RC Edge Slab-Column Connections*." Proceedings of the 4th International Structural Specialty Conference* (*CSCE*), Halifax, Nova Scotia, Canada, 9 pp.

El-Ghandour, A., Pilakoutas, K., and Waldron, P. (1999). "New Approach for Punching Shear Capacity Prediction of Fiber Reinforced Polymer Reinforced Concrete Flat Slabs." *ACI Special Publication*, SP-188-13, 135–144.

El-Mogy, M., El-Ragaby, A., El-Salakawy, E. (2010). "Flexural Behavior of Continuous FRP-Reinforced Concrete Beams." *ASCE Journal of Composites for Construction*, 14(6), 669–680.

El-Nemr, A., Ahmed, E. A, and Benmokrane, B. (2013). "Flexural Behavior and Serviceability of Normal- and High-Strength Concrete Beams Reinforced with Glass Fiber-Reinforced Polymer Bars." *ACI Structural Journal*, 110 (6), 1077–1088.

El-Nemr, A., Ahmed, E., and Benmokrane, B. (2011). "Instantaneous Deflection of Slender Concrete Beams Reinforced with GFRP Bars." *Proceedings of the 2nd International Engineering Mechanics and Materials Specialty Conference* (*CSCE*), Ottawa, Ontario, Canada, 10 pp.

El-Ragaby, A., El-Salakawy, E., and Benmokrane, B. (2007). "Fatigue Life Evaluation of Concrete Bridge Deck Slabs Reinforced with Glass FRP Composite Bars." *ASCE Journal of Composites for Construction*, 11 (3), 258–268.

El-Salakawy, E., Benmokrane, B., and Desgagné, G. (2003a). "Fiber-Reinforced Polymer Composite Bars for the Concrete Deck Slab of Wotton Bridge." *Canadian Journal of Civil Engineering*, 30 (5), 861–870.

El-Salakawy, E., Benmokrane, B., El-Ragaby, A., and Nadeau, D. (2005). "Field Investigation on the First Bridge Deck Slab Reinforced with Glass FRP Bars Constructed in Canada." *ASCE Journal of Composites for Construction*, 9 (6), 470–479.

El-Salakawy, E., Benmokrane, B., Masmoudi, R., Brière, F., and Breaumier, E. (2003b). "Concrete Bridge Barriers Reinforced with Glass Fiber-Reinforced Polymer Composite Bars." *ACI Structural Journal*, 100 (6), 815–824.

El-Sayed, A., El-Salakawy, E., and Benmokrane, B. (2005). "Shear Strength of One-Way Concrete Slabs Reinforced with Fiber-Reinforced Polymer Composite Bars." *ASCE Journal of Composites for Construction*, 9 (2), 147–157.

El-Sayed, A., El-Salakawy, E., and Benmokrane, B. (2006). "Shear Strength of FRP-Reinforced Concrete Beams without Transverse Reinforcement." *ACI Structural Journal*, 103(2), 235-243.

Ericson, C.A. (2012). "Basalt FRP Rebar." *Seminar on Corrosion Resistant Reinforcing Bar*, Florida Department of Transportation, Tallahassee, FL.

Erki, M.A. and Rizkalla, S. (1993). "FRP Reinforcement for Concrete Structures." *ACI Concrete International*, 15 (6), 48–53.

Fahmy, M., Wu, Z., and Wu, G. (2009). "Seismic Performance Assessment of Damage-Controlled FRP-Retrofitted RC Bridge Columns Using Residual Deformations." *ASCE Journal Composites for Construction*, 13 (6), 498–513.

Fang, I., Tsui, C., Burns, N., and Klingner, R. (1990). "Load Capacity of Isotropically Reinforced, Cast-in-Place and Precast Panel Bridge Deck." *PCI Journal*, 35, 104–113.

Fang, K.I. (1985). "Behavior of Ontario-Type Bridge Deck on Steel Girders." *PhD Thesis*, University of Texas, Austin, TX.

Fib. (2007). "FRP Reinforcement in RC Structures." Fédération International Du Béton, Fib Task Group 9.3, Fib Bulletin 40, Lausanne, Switzerland, 147 p.

Förster, T., Scheffler, C., Mäder, E., Heinrich, G., Jesson, D.A., and Watts, J.F. (2014). "Dissolution Behaviour of Model Basalt Fibres Studied by Surface Analysis Methods." *Journal of Applied Surface Science*, 322, 78–84.

GangaRao, H.V.S., and Vijay, P.V. (1997). "Design of Concrete Members Reinforced with GFRP Bars." *Proceedings of the 3rd International Symposium on Non-Metallic (FRP) Reinforcement for Concrete Structures* (*FRPRCS-3*), Japan Concrete Institute, Tokyo, Japan, 1 , 143-150.

Ghali, A., and Azarnejad, A. (1999). "Deflection Prediction of Members of any Concrete Strength." *ACI Structural Journal*, 96 (5), 807–816.

Ghali, E., Sastri, V.S., Elboujdaini, M. (2007). "Corrosion Prevention and Protection: Practical Solutions." John Wiley & Sons, UK, 574 pp.

Graddy, J., Kim, J., Whitt, J., Burns, N., and Klingner, R. (2002) "Punching Shear Behavior of Bridge Decks under Fatigue Loading." *ACI Structural Journal*, 99 (3), 257–266.

Gulbrandsen, P. (2005). "Reliability Analysis of the Flexural Capacity of Fiber Reinforced Polymer Bars in Concrete Beams." M.Sc. Thesis, University of Minnesota, USA, 80 pp.

Hassan, M., Ahmed, E.A., and Benmokrane, B. (2013a). "Punching-Shear Strength of Normal- and High-Strength Concrete Flat Slabs Reinforced with GFRP Bars." *ASCE Journal of Composites for Construction*, 17 (6), 12 pp.

Hassan, M., Ahmed, E.A., and Benmokrane, B. (2013b). "Punching-Shear Strength of Glass Fiber-Reinforced Polymer Reinforced Concrete Flat Slabs." *Canadian Journal of Civil Engineering*, 40 (10), 951-960.

Hassan, T., and Rizkalla, S.H. (2004). "Punching Shear Strength of GFRP Reinforced Deck Slabs in Slab-Girder Bridges." *Proceedings of the 4th International Conference on Advanced Composite Materials in Bridges and Structures* (*ACMBS*), Calgary, Alberta, 8 pp.

Hassan, T., Rizkalla, S., Abdelrahman, A., and Tadros, G. (2000) "Fiber Reinforced Polymer Reinforcing Bars for Bridge Decks." *Canadian Journal of Civil Engineering*, 27, 839–849.

Hewitt, B.E., and Batchelor, B. (1975). "Punching Shear Strength of Restrained Slabs." *ASCE Journal of the Structural Division*, 101 (9), 1837–1853.

Hill, C., Chiaw, C., and Harik, I. (2003). "Reinforcement Alternatives for Concrete Bridge Decks." *Research Report*, Kentucky Transportation Center, University of Kentucky, Report No. KTC-03-19/SPR215-00-1F.

Holowka, M., Dorton, R.A., and Csagoly, P.F. (1980). "Punching Shear Strength of Restrained Circular Slabs." Ministry of Transportation and Communication, Downsview, Ontario, Canada.

Hon, A., Taplin, G., and Al-Mahaidi, R. (2005). "Strength of Reinforced Concrete Bridge Decks under Compressive Membrane Action." *ACI Structural Journal*, 102 (3), 393–401.

Humar, J., and Razaqpur, G. (2000). "Advanced Composite Materials in Bridges and Structures." *Proceedings of the 3rd International Conference*, Ottawa, Ontario, Canada, 876 pp.

Hussein, A., Rashid, I., and Benmokrane, B. (2004). "Two-Way Concrete Slabs Reinforced with GFRP Bars." *Proceedings of the 4th International Conference on Advanced Composite Materials in Bridges and Structures* (*ACMBS*), Calgary, Alberta, Canada, 8 pp.

InfoMine Research Group. (2007). "Basalt Fiber-Based Thermal Insulating Materials Market Research in Russia." Moscow.

ISIS Canada (2007). "Reinforcing Concrete Structures with Fiber-Reinforced Polymers (Design Manual No. 3)." Manitoba, Canada.

Iyer, S.L. and Sen, R. (1991). "Advanced Composite Materials in Civil Engineering Structures." *Proceedings of the Specialty Conference*, *ASCE*, New Yourk, N.Y., 443 pp.

Jacobson, D., and Bank, L. (2005). "Punching Shear Capacity of Double Layer FRP Grid Reinforced Slabs." *ACI Special Publication*, SP-230, 857–876.

Jaeger, L.G., Mufti, A.A., and Tadros, G. (1997). "The Concept of the Overall Performance Factor in Rectangular-Section Reinforced Concrete Members." Proceedings of the 3rd International Symposium on Non-Metallic (FRP) Reinforcement for Concrete Structures (FRPRCS-3), Japan Concrete Institute, Tokyo, 2, 551–559.

Jaeger, L.G., Tadros, G., Mufti, A.A. (1995). "Balanced Section, Ductility and Deformability in Concrete with FRP Reinforcement." Research Report presented in Joint U.S.-Canadian Meeting at West Virginia University.

Japan Society of Civil Engineering (JSCE). (1997). "Recommendation for Design and Construction of Concrete Structures using Continuous Fiber Reinforcing Materials." Concrete Engineering Series, No. 23, Tokyo, Japan.

Kamenny Vek. (2015). "Advanced Basalt Fiber." ⟨http://www.basfiber.com/⟩ (May 5, 2015).

Karbhari, V.M. (2007). "Durability of Composites for Civil Structural Applications." Woodhead *Publishing in Materials and CRC Press*, Cambridge, England.

Kassem, C., Farghaly, A., and Benmokrane, B. (2011). "Evaluation of Flexural Behavior and Serviceability Performance of Concrete Beams Reinforced with FRP Bars." *ASCE Journal of Composites for Construction*, 15 (5), 682–695.

Katz, A. (2004). "Environmental Impact of Steel and Fiber–Reinforced Polymer Reinforced Pavements." *ASCE Journal of Composites for Construction*, 8 (6), 481–488.

Khanna, O., Mufti, A., and Bakht, B. (2000). "Experimental Investigation of the Role of Reinforcement in the Strength of Concrete Deck Slabs." *Canadian Journal of Civil Engineering*, 27, 475–480.

Khederzadeh, H., Sennah, K. (2014). "Development of Cost-Effective PL-3 Concrete Bridge Barrier Reinforced with Sand-Coated Glass Fibre Reinforced Polymer (GFRP) Bars: Static Load Tests." *Canadian Journal of Civil Engineering*, 41 (4), 368–379.

Koch, G.H., Payer, J.H., Brongers, M.P.H., Thompson, N.G., and Virmani, Y.P. Payer, J.H. (2002). "Corrosion Costs and Preventive Strategies in the United States." *Report*, *National Association of Corrosion Engineers* (*NACE*), Report No. FHWA-RD-01-156, 773 pp.

Kuang, J., and Morley C. (1993). "Punching Shear Behavior of Restrained Reinforced Concrete Slabs." *ACI Structural Journal*, 89 (1), 13–19.

Lapko, A., and Urbański, M. (2015). "Experimental and Theoretical Analysis of Deflections of Concrete Beams Reinforced with Basalt Rebar." *Journal of Archives of Civil and Mechanical Engineering*, 15 (1), 223–230.

Lee, J.H., Yoon, Y.S., and Mitchell, W.D. (2009). "Improving Punching Shear Behavior of Glass Fiber-Reinforced Polymer Reinforced Slabs." *ACI Structural Journal*, 106 (4), 427–434.

Li, H., XIAN, G., Ma, M., and WU, J. (2012). "Durability and Fatigue Performances of Basalt Fiber/Epoxy Reinforcing Bars." *Proceedings of the 6th International Conference on FRP Composites in Civil Engineering* (*CICE*), Rome, Italy, 8 pp.

Lopresto, V., Leone, C., and De Iorio, I. (2011). "Mechanical Characterization of Basalt Fiber Reinforced Plastic." *Journal of Composites Part B: Engineering*, 42 (4), 717–723.

Lu, Z., Xian, G., and Li, H. (2015). "Effects of Exposure to Elevated Temperatures and Subsequent Immersion in Water or Alkaline Solution on the Mechanical Properties of Pultruded BFRP Plates." *Journal of Composites Part B: Engineering*, 77, 421–430.

Mara, V., Haghani, R., and Harryson, P. (2014). "Bridge Decks of Fiber Reinforced Polymer (FRP): A sustainable Solution." *Journal of Construction and Building Materials*, 50, 190–199.

Maranan, G.B., Manalo, A.C., Benmokrane, B., Karunasena, W., and Mendis, P. (2015). "Evaluation of the Flexural Strength and Serviceability of Geopolymer Concrete Beams Reinforced with Glass-Fibre-Reinforced Polymer (GFRP) Bars." *Journal of Engineering Structures*, 101, 529–541.

Marzouk, H., Hussein A. (1991). "Experimental Investigation on the Behavior of High-Strength Concrete Slabs." *ACI Structural Journal*, 88 (6), 701–713.

Masmoudi, R., Theriault, M., and Benmokrane, B. (1998). "Flexural Behavior of Concrete Beams Reinforced with FRP C-BAR Reinforcing Bars." *ACI Structural Journal*, 95 (6), 665–676

Matta, F., and Nanni, A. (2009). "Connection of Concrete Railing Post and Bridge Deck with Internal FRP Reinforcement." *ASCE Journal of Bridge Engineering*, 14 (1), 66–76.

Matthys, S., and Taerwe, L. (2000). "Concrete Slabs Reinforced with FRP Grids-II: Punching Resistance." *ASCE Journal of Composites for Constructions*, 4 (3), 154–161.

Militký, J., and Kovačič, V. (1996). "Ultimate Mechanical Properties of Basalt Filaments." *Textile Research Journal*, 66 (4), 225–229.

Militký, J., Kovačič, V., and Rubnerová, J. (2002). "Influence of Thermal Treatment on Tensile Failure of Basalt." *Journal of Engineering Fracture Mechanics*, 69 (9), 1025–1033.

Mingchao, W., M., Zuoguang, Z., Yubin, L., Min, L., and Zhijie, S. (2008). "Chemical Durability and Mechanical Properties of Alkali-Proof Basalt Fiber and Its Reinforced Epoxy Composites." *Journal of Reinforced Plastics and Composites*, 27 (4), 393–407.

Morozov, N.N., Bakunov, V.S., Morozov, E.N., Aslanova, L.G., Granovskii, P.A., Prokshin, V.V. and Zemlyanitsyn, A.A. (2001). "Materials Based on Basalt from the European North of Russia." *Journal of Glass Ceram*, 58 (3-4), 100–104.

Mota, C., Alminar, S., and Svecova, D. (2006). "Critical Review of Deflection Formulas for FRP-RC Members." *ASCE Journal of Composites for Construction*, 3 (10), 183–194.

Mufti, A., and Newhook, J. (1998). "Punching Shear Strength of Restrained Concrete Bridge Deck Slabs." *ACI Structural Journal*, 95 (4), 375–381.

Naaman, A.E., Jeong, S.M. (1995). "Structural Ductility of Concrete Beams Prestressed with FRP Tendons." *Proceedings of the 2nd International RILEM Symposium* (*FRPRCS-2*), Non-metallic (FRP) Reinforcement for Concrete Structures, Nawy,

Nanni, A. (1993), "Flexural Behavior and Design of RC Members using FRP Reinforcement." *ASCE Journal of Structural Engineering*, 119 (11), 3344–3359.

Nanni, A., and Dolan, C.W. (1993). "Fiber-Reinforced- Plastic Reinforcement for Concrete Structures." *ACI Special Publication*, SP-138, International Symposium, Farmington Hills, Michigan, USA, 977 pp.

Nanni, A., and Faza, S. (2002). "Designing and Construction with FRP Bars: An Emerging Technology." *ACI Concrete International*, 24 (11), 53–58.

National Transportation Safety Board (2008). "Collapse of I-35W Highway Bridge." Minneapolis, Minnesota, August 1st, 2007. Highway Accident Report No. NTSB/HAR-08/03. Washington, DC.

Newhook, J. (1997). "The Behavior of Steel-Free Concrete Bridge Deck Slabs under Static Loading Conditions." *PhD Thesis*, Dalhousie University, Halifax, Nova Scotia, Canada.

Newhook, J., Gaudet, J., and Edalatmanesh, R. (2011). "Investigation of an Externally Restrained Concrete Bridge Deck Slab on a Multi-Girder Bridge Model." *Canadian Journal of Civil Engineering*, 38 (2), 233–241.

Newhook, J., Ghali, A., and Tadros, G. (2002). "Concrete Flexural Members Reinforced with Fiber-Reinforced Polymer: Design for Cracking and Deformability." *Canadian Journal of Civil Engineering*, 29 (1), 125–134.

Nguyen-Minh L., and Rovnak M. (2013). "Punching-Shear Resistance of Interior GFRP Reinforced Slab-Column Connection." *ASCE Journal of Composites for Constructions*, 17(1), 2–13.

Nkurunziza, G., Debaiky, A., Cousin, P., and Benmokrane, B. (2005). "Durability of GFRP Bars: A Critical Review of the Literature." *Progress in Structural Engineering and Materials*, 7(4), 194–209.

O'Connor, J., and Hooks J. (2003). "U.S.A.'s Experience using Fiber Reinforced Polymer (FRP) Composite Bridge Decks to Extend Bridge Service Life." Technical Momorandum of Public Works Research Institute.

Ospina, C.E., Alexander, S.D.B., and Cheng, J.J. (2003). "Punching of Two-Way Concrete Slabs with Fiber-Reinforced Polymer Reinforcing Bars or Grids." *ACI Structural Journal*, 100 (5), 589–598.

Ovitigala, T. (2012). "Structural Behavior of Concrete Beams Reinforced with Basalt Fiber Reinforced Polymer (BFRP) Bars." *PhD Thesis*, University of Illinois, Chicago.

Ovitigala, T., and Issa, M.A. (2013). "Mechanical and Bond Strength of Basalt Fiber-Reinforced Polymer (BFRP) Bars for Concrete Structures." *Proceedings of the 11th International Symposium on Fiber-Reinforced Polymer Reinforcement for Reinforced Concrete Structures* (*FRPRCS-11*), Guimarães, Portugal.

Palmieri, A., Matthys, S., Tierens, M., and Pikakoutas, K. (2009). "Basalt Fibers for Reinforcing and Strengthening Concrete." *Proceedings of the 9th International Symposium of the Fiber-Reinforced Polymer Reinforcement for Reinforced Concrete Structures* (*FRPRCS-9*), Sydney, Australia, 4 pp.

Park, C., Jang, C. Lee, S., and Won, J. (2008). "Microstructural Investigation of Long-Term Degradation Mechanisms in GFRP Dowel Bars for Jointed Concrete Pavement." *Journal of Applied Polymer Science*, 108 (5), 3128–3137.

Parnas, R., Shaw, M., and Liu, Q. (2007). "Basalt Fiber Reinforced Polymer Composites." *Technical Report No. NETCR63*, Prepared for the New England Transportation Consortium, Institute of Materials Science, University of Connecticut.

Patnaik, A. (2009). "Applications of Basalt Fiber Reinforced Polymer (BFRP) Reinforcement for Transportation Infrastructure." Developing a Research Agenda for Transportation Infrastructure – TRB, University of Akron , OH44325-3905, 5 pp

Patnaik, A. (2011). "Basalt Fiber Reinforced Polymer (BFRP) Materials for Reinforced Concrete Applications." Department of Defense Corrosion Conference, NACE International, Palm Springs, 15 pp.

Patnaik, A. (2013). "BasBar BFRP Design Guide." Design Guide Book for Structural Concrete Reinforced with Basalt Fiber Reinforced Polymer (BFRP) Bars, Published by ReforceTech AS (Royken, Norway), 35.

Patnaik, A., Puli, R., and Mylavarapu, R. (2004). "Basalt FRP: A New FRP Material for Infrastructure Market." *Proceedings of the 4th International Conference on Advanced Composite Materials in Bridges and Structures* (*ACMBS*), Calgary, Alberta.

Perdikaris P.C., and Beim S. (1988). "RC Bridge Decks under Pulsating and Moving Loads." *ASCE Journal of Structural Engineering*, 114 (3), 591–607.

Phillips, K. (2004). "Performance of a Bridge Deck with Glass Fiber Reinforced Polymer (GFRP) Bars as the Top Mat of Reinforcement." *MSc Thesis*, Blacksburg, Virginia.

Quagliarini, E., Monni, F., Lenci, S., and Bondioli, F. (2012). "Tensile Characterization of Basalt Fiber Bars and Ropes: A first Contribution." *Journal of Construction and Building Materials*, 34, 372–380.

Rahman, A., Kingsley, C., and Kobayashi. K., (2000). "Service and Ultimate Load Behavior of Bridge Deck Reinforced with Carbon FRP Grid." *ASCE Journal of Composites for Construction*, 4 (1), 16–23.

Rizkalla, S., and Tadros, G. (1994). "First Smart Bridge in Canada." *ACI Concrete International*, 16 (6), 42–44.

Rizkalla, S.H. (2013). "Flexural Behavior of Concrete Members Reinforced with BFRP Bars." Progress Report No. 6, North Carolina State University, Department of Civil, Construction, and Environmental Engineering, 34 pp.

Robert, M., Cousin, P. and Benmokrane, B. (2009). "Durability of GFRP Reinforcing Bars Embedded in Moist Concrete." *ASCE Journal of Composites for Construction*, 13 (2), 66–73.

Ross, A. (2006). "Basalt Fibers: Alternative to Glass?" Composites World. ⟨http://www.compositesworld.com/articles/basalt-fibers-alternative-to-glass⟩ (April 1, 2015).

Scheffler, C., Förster, T., Mäder, E., Heinrich, G., Hempel, S., Mechtcherine, V. (2009). "Aging of Alkali-Resistant Glass and Basalt Fibres in Alkaline Solutions: Evaluation of the Failure Stress by Weibull Distribution Function." *Journal of Non-Crystalline Solids*, 355 (52-54), 2588–2595.

Schwartz, M., (1997). "Non-destructive Testing and Repair." Book of Composite Materials Properties, Prentice Hall, NJ.

Seliem, H.M., Lucier, G., Rizkalla, S.H., and Zia, P. (2008). "Behavior of Concrete Bridge Decks Reinforced with High-Performance Steel." *ACI Structural Journal*, 105 (1), 78–86.

Serbescu, A., Guadagnini, M., and Pilakoutas, K. (2015). "Mechanical Characterization of Basalt FRP Rebars and Long-Term Strength Predictive Model." *ASCE Journal of Composites for Construction*, 19 (2), 04014037.

Shi, J., Zhu, H., Wu, Z., and Wu, G. (2011a). "Durability of BFRP and Hybrid FRP Sheets under Freeze-Thaw Cycling." *Journal of Advanced Materials Research*, 163–167, 3297–3300.

Shi, J., Zhu, H., Wu, Z., and Wu, G. (2011b). "Effects of Freeze-Thaw Cycles and Sustained Load on Bond Behavior between FRP Sheet and Concrete Substrate." *ACI Special Publication*, SP-275, 1–20.

Sim, J., Park, C., and Moon, D. (2005). "Characteristics of Basalt Fiber as a Strengthening Material for Concrete Structures." *Journal of Composites Part B: Engineering*, 36 (6-7), 504–512.

Subramanian, R., Tang, T. J. and Austin, H. (1977). "Reinforcement of Polymers by Basalt Fibers." *SAMPE Quarterly*, 8 (1), 1–10.

Subramanian, R.V. (1978). "Basalt Fiber – A New Cost Mineral Fiber for Composites." *Proceedings of Conference on Advanced Composite Technology*, California.

Sukhanov A., Dalinkevich A., Sisauri V., and Aseev A. (2004). "Continuous Basalt Fiber Composite Materials and Bridge Members." *Proceedings of the 4th International Conference on Advanced Composite Materials in Bridges and Structures* (*ACMBS*), Calgary, Alberta.

Theriault, M., and Benmokrane, B. (1998). "Effects of FRP Reinforcement Ratio and Concrete Strength on Flexural Behavior of Concrete Beams." *ASCE Journal of Composites for Construction*, 2 (1), 7–16.

Thorbum, J. (1998). "A Study of Externally Reinforced Fiber-Reinforced Concrete Bridge Decks on Steel Girgers)." *PhD Thesis*. Civil Engineering Department, Dalhousie University, Halifax, Nova Scotia, Canada.

Thorburn, J., and Mufti, A.A. (2001). "Design Recommendations for Externally Restrained Highway Bridge Decks." *ASCE Journal of Bridge Engineering*, 6 (4), 243–249.

Tighiouart B, Benmokrane B, and Mukhopadhyaya P. (1999). "Bond Strength of Glass FRP Rebar Splices in Beams under Static Loading." *Journal of Construction and Building Materials*, 13 (7), 383–392.

Tomlinson, D., and Fam, A. (2015). "Performance of Concrete Beams Reinforced with Basalt FRP for Flexure and Shear." *ASCE Journal of Composites for Construction*, 19 (2), 1–10.

Toutanji, H.A., and Saafi, M. (2000). "Flexural Behavior of Concrete Beams Reinforced with Glass Fiber-Reinforced Polymer (GFRP) Bars." *ACI Structural Journal*, 97 (5), 712-719.

Transportation for America. (2013). "The Fix We're In For: The State of Our Nation's Bridges 2013." Washington, USA, 8 pp.

Urbański, M., Lapko, A., and Garbacz, A. (2013). "Investigation on Concrete Beams Reinforced with Basalt Rebars as an Effective Alternative of Conventional R/C Structures." *Journal of Procedia Engineering (Modern Building Materials, Structures and Techniques)*, 57, 1183–1191.

Van de Velde, K., Kiekens, P., and Van Langenhove, L. (2015). "Basalt Fibers as Reinforcement for Composites." ⟨http://www.basaltex.com/files/cms1/Basalt-Fibres-as-reinforcement-for-composites_Ugent.pdf⟩ (March 2015)

Vijay P.V., and GangaRao H.V. (1996). "A unified Limit State Approach using Deformability Factors in Concrete Beams Reinforced with GFRP Bars." *ASCE Proceeding of the 4th Materials Engineering Conference*, Washington, DC, 1996, 657-665.

Vijay, P.V., and GangaRao H.V. (2001). "Bending Behavior and Deformability of Glass-Fiber-Reinforced Polymer Reinforced Concrete Members." *ACI Structural Journal*, 98 (6), 834–842.

Vincent, P. (2013). "Caractérsation Physico-Méchanique et Évaluation de la Performance Structurale de Nouvelle de Barres de Polyméres Renforés de Fibres de Basalte (BFRP) dans des Poutres en Béton. *MSc Thesis*, University of Sherbrooke, Canada.

Vincent, P., Ahmed, E., and Benmokrane, B. (2013). "Characterization of Basalt Fiber-Reinforced Polymer (BFRP) Reinforcing Bars for Concrete Structures." *Proceedings of the 3rd Specialty Conference on Material Engineering and Applied Mechanics* (*CSCE*), Montréal, Québec, Canada, 10 pp.

Waldron, P. (2004). "The Use of FRP as Embedment Reinforcement in Concrete." *Proceedings of the 2nd International Conference on FRP Composites in Civil Engineering* (*CICE*), Taylor and Francis Group, Adelaide, Australia, 83–92.

Wang, H., and Belarbi, A. (2005). "Flexural Behavior of Fiber-Reinforced-Concrete Beams Reinforced with FRP Rebars." *ACI Special Publication*, SP-230, 895–914.

Wang, X., Shi, J., Liu, J., Yang, L., and Wu, Z. (2014b) "Creep Behavior of Basalt Fiber Reinforced Polymer Tendons for Prestressing Application." *Journal of Materials and Design*, 59, 558–564.

Wang, X., Wu, G., and Wu, Z. (2012). "Tensile Property of Prestressing Basalt and Hybrid FRP Tendons under Salt Solution." Proceeding *of the 6th International Conference on FRP Composites in Civil Engineering* (*CICE*), Rome, Italy, 8 pp.

Wang, X., Wu, G., Wu, Z., Dong, Z., and Xie, Q. (2014a). "Evaluation of Prestressed Basalt Fiber and Hybrid Fiber Reinforced Polymer Tendons under Marine Environment." *Journal of Materials and Design*, 64, 721–728.

Wei, B., Cao, H., and Song, S. (2010). "Environmental Resistance and Mechanical Performance of Basalt and Glass Fibers." *Journal of Materials Science and Engineering: Part A*, 527, 4708–4715.

Wei, B., Cao, H.L., Song, S.H. (2011). "Degradation of Basalt Fibre and Glass Fibre/Epoxy Resin Composites in Seawater." *Journal of Corrosion Science*, 53 (1), 426–431.

Wu, G., Wang, X., Wu, Z., Dong, Z., and Zhang, G. (2015a). "Durability of Basalt Fibers and Composites in Corrosive Environments." *Journal of Composite Materials*, 49 (7), 873–887.

Wu, G., Dong, Z., Wang, X., Zhu, Y., and Wu, Z. (2015b). "Prediction of Long-Term Performance and Durability of BFRP Bars under the Combined Effect of Sustained Load and Corrosive Solutions." *ASCE Journal of Composites for Construction*, 19 (3), 04014058.

Wu, Z., Wang, X., and Wu, G. (2011). "Advancement of Basalt Fiber Composites Towards Infrastructural." *Proceedings of the International Symposium on Innovation & Sustainability of Structures in Civil Engineering* (*ISISS2011*), Xiamen, China.

Wu, Z., Wang, X., and Wu, G. (2012). "Advancement of Structural Safety and Sustainability with Basalt Fiber Reinforced Polymers." *Proceedings of 6th International Conference on FRP Composites in Civil Engineering* (*CICE*), Rome, Italy, 29 pp.

Wu, Z., Wang, X., Iwashita, K. (2007). "State-of-the-Art of Advanced FRP Applications in Civil Infrastructure in Japan." *Journal of Composites & Polycon*, American Composites Manufacturers Association, Tampa, FL USA.

Wu, Z., Wang, X., Iwashita, K., Sasaki, T., and Hamaguchi, Y. (2010). "Tensile Fatigue Behaviour of FRP and Hybrid FRP Sheets." *Journal of Composites: Part B*, 41 (5), 396–402.

Yost, J.R. (2002). "Structural Reinforcement of Bridge Decks Using Rigid FRP Grids." *Proceedings of the 6th International Conference on Short and Medium Span Bridges*, Vancouver, Canada, 201–208.

Yost, J.R., Gross, S.P., and Dinehart, D.W. (2001). "Shear Strength of Normal Strength Concrete Beams Reinforced with Deformed GFRP Bars." *ASCE Journal of Composites for Construction*, 5 (4), 268–275.

Yunovich, M., and Thompson, N. (2003). "Corrosion of Highway Bridges: Economic Impact and Control Methodologies." *ACI Concrete International*, 25, 52–57.

Zaghloul, A. (2007). "Punching Shear Strength of Interior and Edge Column Slab Connections in CFRP Reinforced Flat Plate Structures Transferring Shear and Moment." *PhD Thesis*, Department of Civil and Environmental Engineering, Carleton University, Ottawa, ON.

Zhang, L., Sun, Y., and Xiong, W. (2015). "Experimental Study on the Flexural Deflections of Concrete Beam Reinforced with Basalt FRP Bars." Journal of Materials and Structures, pp. 48, 3279–3293.

Zheng, Y., Fu, X., Lu, Z., and Pan, Y. (2013). "Investigation of Structural Behavior of GFRP Reinforced Concrete Deck Slabs through NLFEA." *Journal of Construction and Building Materials*, 45, 60–77.

Zheng, Y., Li, C., and Yu, G. (2012a). "Investigation of Structural Behaviors of Laterally Restrained GFRP Reinforced Concrete Slabs." *Journal of Composites Part B: Engineering*, 43 (3), 1586–1597.

Zheng, Y., Sun, C., Deng, T., Yang, J.B., and Lu, Z.Y. (2014). "Arching Action Contribution to Punching Failure of GFRP-Reinforced Concrete Bridge Deck Slabs." *Arabian Journal for Science and Engineering*, 39 (12), 8609–8625.

Zheng, Y., Yu, G., and Pan, Y. (2012b). "Investigation of Ultimate Strengths of Concrete Bridge Deck Slabs Reinforced with GFRP Bars." *Journal of Construction and Building Materials*, 28 (1), 482–492.

APPENDIX A: Design of Slab S2-B

This Appendix presents a typical design of slab S2-B according to the CHBDC CAN/CSA S6 (2014). The corresponding clause numbers (CAN/CSA S 2014) are provided, where applicable. **Figure A-1** shows the cross-section of the slab. The ultimate capacity of the used BFRP bars (f_{fu}) =1724 ± 63.6 MPa and the tensile modulus of elasticity (E_f) = 64.8 GPa.

Deck slab thickness, h = 200 mm (5-6)

Effective span of deck slab, S_e = 2000 mm (5-7)

Bottom concrete cover, $C.C.$ = 25 mm (5-8)

$$I_g = \frac{bh^3}{12} = \frac{1000 \times 200^3}{12} = 666.67 \times 10^6 \text{ mm}^4 \quad (5\text{-}9)$$

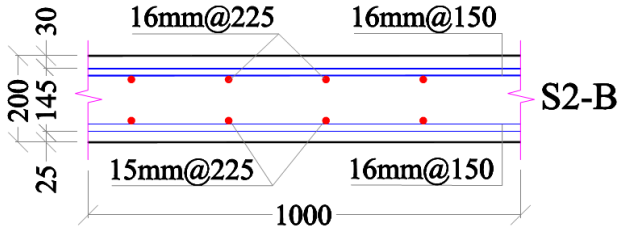

Figure A-1: Cross section of slab S2-B

The Empirical Design Method (Clause 16.8.8.1)

The bottom-transverse FRP reinforcing bars are determined according to the empirical design method as follows:

$$A_{f\ min.} = \frac{500\ d_s}{E_f} = \frac{500 \times 159}{64800} \times 1000 = 1227 \text{ mm}^2/\text{m} = 16 \text{ mm @ } 164 \text{ mm} \quad (5\text{-}10)$$

where $d_s = h - C.C.$ – bar diameter = 200 – 25 – 16 = 159 mm (5-11)

For the bottom transverse reinforcement, **use 16 mm BFRP @ 150 mm.**

The Flexural Design Method

The deck slab was designed using the flexural design method, considering the service and ultimate limit states. The design moments were based on a maximum wheel load of 87.5 kN (CL-625 truck), in addition to self-weight of the slab and pavement. The experimental results do not include the effects of slab self-weight, as mentioned before.

Concrete

$f_c^{'} = 40$ MPa (5-12)

$E_c = \left(3000\sqrt{f_c^{'}} + 6900\right)\left(\gamma_c / 2300\right)^{1.5} = 26.72$ MPa (Clause 8.4.1.7) (5-13)

$\phi_c = 0.75$ (Table 8-1) (5-14)

Reinforcement

Assume the bottom transverse direction is made of BFRP bars of 16 mm @ 150 mm.

$A_f = 1340.67$ mm^2/m (5-15)

$d = h - C.C. -$ bar diameter/2 = 200 – 25 – 16/2 = 167 mm (5-16)

$$\rho_f = \frac{A_f}{1000 \times d} \times 100 = \frac{1340.67}{1000 \times 167} \times 100 = 0.803\% \quad (5\text{-}17)$$

Specific tensile strength, f^*_u (Mean – 3×SD) = 1724 - 3 × 63.6 = 1533 MPa (5-18)

Bond-dependent coefficient, $k_b = 1.0$ (Clause 16.8.2.3, deformed bars) (5-19)

$\phi_f = 0.55$ (Assumed as GFRP bars, Table 16.2) (5-20)

Stress at service load level, $f_{SLS} = 0.25\, f^*_u$ (Assumed as GFRP bars, Clause 16.8.3) (5-21)

Cracking Moment

$f_r = 0.4\sqrt{f_c^{'}} = 0.4\sqrt{40} = 2.53$ MPa (Clause 8.4.1.8) (5-22)

$$M_{cr} = \frac{2 f_r I_g}{h} = \frac{2 \times 2.53 \times 666.67 \times 10^6}{200} \times 10^{-6} = 16.865 \text{ kN.m/m} \quad (5\text{-}23)$$

Load and Transverse Moment due to Uniform Load

Slab self-weight = 0.2×23.5 = 4.70 kN/m^2 (5-24)

Pavement self-weight = 0.065×24.0 = 1.56 kN/m^2 (5-25)

Service dead load, $W_{d\text{-}SLS} = 4.70+1.56 = 6.26$ kN/m^2 (5-26)

Factored dead load, $W_{d\text{-}ULS} = 1.2\times4.7+1.5\times1.56 = 7.98$ kN/m^2 (5-27)

Service moment due to dead load, $M_{d\text{-}SLS} = 0.071\ W_{d\text{-}SLS}\ S_e^2$ (5-28a)

$= 0.071 \times 6.26 \times 2.0^2 = 1.778$ kN.m/m (5-28b)

Factored moment due to dead load, $M_{d\text{-}ULS} = 0.071\ W_{du}\ S_e^2$ (5-29a)

$= 0.071 \times 7.98 \times 2.0^2 = 2.267$ kN.m/m (5-29b)

Load and Transverse Moment due to Wheel Load

The total transverse moment, $M_y = \dfrac{(S_e + 0.6)P}{10} = 22.75$ kN.m/m (Clause 5.7.1.7.1) (5-30)

Service moment due to wheel load, $M_{y\text{-}SLS} = 1.4 \times 22.75 \times 0.9 = 28.665$ kN.m/m (5-31)

Factored moment due to wheel load, $M_{y\text{-}ULS} = 1.4 \times 22.75 \times 1.7 = 54.145$ kN.m/m (5-32)

where 1.4 is the impact factor, while 0.9 and 1.7 are the service and ultimate load combination factors, respectively (Table 3.1).

Transverse Design Moment (Total Loads)

Total service moment, $M_{SLS} = 1.778 + 28.665 = 30.443$ kN.m/m (5-33)

Total factored moment, $M_{ULS} = 2.267 + 54.145 = 56.412$ kN.m/m (5-34)

Check for Crack Width and Stress Limit under Service Load

$$n_f = \frac{E_f}{E_c} = \frac{64.8}{26.72} = 2.425 \quad (5\text{-}35)$$

$$k = \sqrt{2\rho_f n_f + (\rho_f n_f)^2} - \rho_f n_f = 0.1788 \quad (5\text{-}36)$$

$$f_s = \frac{M_{SLS}}{A_f d\,(1 - k/3)} = 144.59 \text{ MPa} < 0.25 f_u^* = 0.25 \times 1533 = 383 \text{ MPa OK} \quad (5\text{-}37)$$

$h_2 = h - kd = 200 - 0.1788 \times 167 = 170.14$ mm (5-38)

$h_1 = d - kd = 167 - 0.1788 \times 167 = 137.14$ mm (5-39)

$d_c = h - d = 200 - 167 = 33$ mm (5-40)

$$w_{cr} = 2\frac{f_s}{E_f}\frac{h_2}{h_1} k_b \sqrt{d_c^{\,2} + (S/2)^2} \quad \text{(Clause 16.8.2.3)} \quad (5\text{-}41a)$$

$$= 2 \times \frac{144.59}{64800} \times \frac{170.14}{137.14} \times 1.0 \sqrt{33^2 + (150/2)^2} = 0.453 \text{ mm} < 0.50 \text{ mm (OK)} \quad (5\text{-}41b)$$

Check for Stress under Ultimate Load

$$\alpha_1 = 0.85 - 0.0015 f_c^{'} = 0.79 \geq 0.67 \text{ (Clause 8.8.3)} \quad (5\text{-}42)$$

$$\beta_1 = 0.97 - 0.0025 f_c^{'} = 0.87 \geq 0.67 \text{ (Clause 8.8.3)} \quad (5\text{-}43)$$

$$\phi_f A_f f_f = \alpha_1 \phi_c f_c^{'} ab \quad (5\text{-}44a)$$

$$0.55 \times 1340.6 \times \left(64800 \times \varepsilon_f\right) = 0.79 \times 0.75 \times 40 \times \left(0.87 \times c\right) \times 1000 \quad (5\text{-}44b)$$

$$c = 2317.2\ \varepsilon_f \quad (5\text{-}45)$$

$$\left(\frac{c}{0.0035}\right) = \left(\frac{d}{0.0035 + \varepsilon_f}\right) = \left(\frac{167}{0.0035 + \varepsilon_f}\right) \quad (5\text{-}46)$$

Solving (5-45) and (5-46)

$$\varepsilon_f = 0.0142 \quad (5\text{-}47)$$

$$c = 32.97 \text{ mm} \quad (5\text{-}48)$$

$$a = \beta_1 c = 28.86 \text{ mm} \quad (5\text{-}49)$$

$$f_f = E_f\ \varepsilon_f = 921.97 \text{ MPa} < f_u^* = 1533 \text{ MPa (Over-reinforced)} \quad (5\text{-}50)$$

$$M_r = \alpha_1 \phi_c f_c^{'} ab\left(d - a/2\right) \quad (5\text{-}51a)$$

$$= 103.78 \text{ kN.m} > 1.5 M_{cr} = 1.5 \times 16.865 = 25.30 \text{ kN.m (OK) (Clause 16.8.2.2)} \quad (5\text{-}51b)$$

$$> 1.5 M_u = 1.5 \times 56.412 = 84.62 \text{ kN.m (OK) (Clause 16.8.2.2)} \quad (5\text{-}51c)$$

Use 16 mm BFRP @ 150 mm.

APPENDIX B: Nominal Capacity-Reinforcement Ratio Relationship of Tested Beams

Figure B-1 shows the effect of the reinforcement ratio, ρ, on the on the nominal flexure capacity of beams reinforced with BFRP bar. The horizontal axis in Figure B-1 represents the normalized reinforcement ratio with respect to the ultimate tensile strength of BFRP bars, ρ/f_{fu}, while the vertical axis represents the experimental nominal capacity, M_n. As shown in the figure, the rate of increasing nominal capacity is decreasing as the reinforcement ratio increasing affected by the compression failure mode.

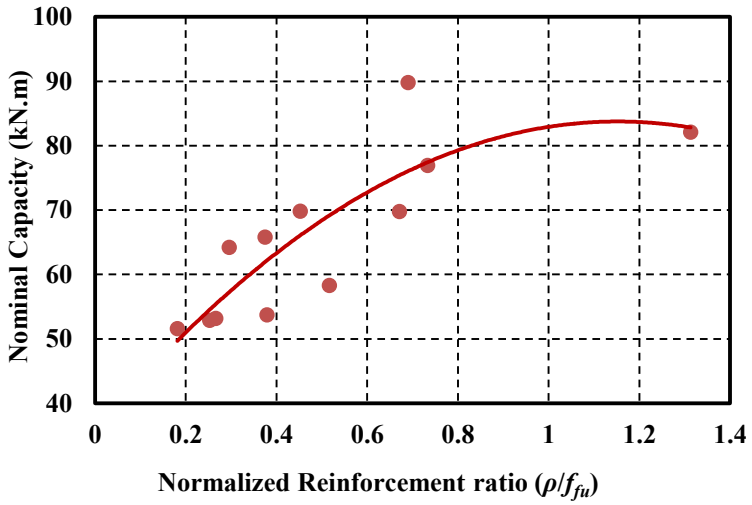

Figure B-1: Normalized relationship between the ultimate capacity and reinforcement ratio